High Entropy Oxides: Structure and Properties

Sarkar, Abhishek

(2020)

DOI (TUprints): https://doi.org/10.25534/tuprints-00014345

High Entropy Oxides: Structure and Properties

Hochentropie-Oxide: Struktur und Eigenschaften
Zur Erlangung des akademischen Grades Doktor-Ingenieur (Dr.-Ing.)
vorgelegte Dissertation von Abhishek Sarkar aus Kalyani
Tag der Einreichung: 15.07.2020, Tag der Prüfung: 21.10.2020

1. Gutachten: Prof. Dr.-Ing. Horst Hahn
2. Gutachten: Prof. Dr. Jürgen Janek
Darmstadt – D 17

TECHNISCHE UNIVERSITÄT DARMSTADT

Fachbereich Material- und Geowissenschaften

Gemeinschaftslabor Nanomaterialien

High Entropy Oxides: Structure and Properties
Hochentropie-Oxide: Struktur und Eigenschaften

vorgelegte Dissertation von Abhishek Sarkar

1. Gutachten: Prof. Dr.-Ing. Horst Hahn
2. Gutachten: Prof. Dr. Jürgen Janek

Tag der Einreichung: 15.07.2020
Tag der Prüfung: 21.10.2020

Darmstadt – D 17

Bitte zitieren Sie dieses Dokument als:
URN: urn:nbn:de:tuda-tuprints-143457
URL: http://tuprints.ulb.tu-darmstadt.de/id/eprint/14345

To Ma, Baba and Mum

Erklärungen laut Promotionsordnung

§8 Abs. 1 lit. c PromO

Ich versichere hiermit, dass die elektronische Version meiner Dissertation mit der schriftlichen Version übereinstimmt.

§8 Abs. 1 lit. d PromO

Ich versichere hiermit, dass zu einem vorherigen Zeitpunkt noch keine Promotion versucht wurde. In diesem Fall sind nähere Angaben über Zeitpunkt, Hochschule, Dissertationsthema und Ergebnis dieses Versuchs mitzuteilen.

§9 Abs. 1 PromO

Ich versichere hiermit, dass die vorliegende Dissertation selbstständig und nur unter Verwendung der angegebenen Quellen verfasst wurde.

§9 Abs. 2 PromO

Die Arbeit hat bisher noch nicht zu Prüfungszwecken gedient.

Darmstadt, 15.07.2020

Abhishek Sarkar

Abstract

Since the origin of humankind numerous approaches have been employed to develop new materials. Of these approaches, changing the composition of a given system, typically referred as alloying for metallic and doping for non-metallic systems, is undoubtedly the most common way of designing new materials. Conventionally, alloying or doping implies introduction of relatively small amounts of secondary elements to a base system. The base system typically consists of one major component, e.g., Fe for steels, while in yttria-stabilized zirconia, ZrO_2 is considered as the base system. The concept of high entropy materials (HEMs) can be considered as an extreme adaption of alloying or doping, where five or more elements all in (nearly) equal proportions are incorporated into a system. Hence, there is no base element ("baseless") as such in HEMs. Their unexpected tendency to form single phase solid solutions despite the high chemical complexity makes HEMs unique. Essentially, the combination of several elements in near equiatomic proportion enhances the configurational entropy of HEMs. It is believed, in some cases proven, that this enhanced configurational entropy drives the formation of a single phase solid solution. Due to these distinctive features, the high entropy based design concept is often considered as an original approach, and not a mere extension to alloying or doping.

The subject of studies in this doctoral thesis is high entropy oxides (HEOs). HEOs are phase-pure solid solutions arising from the inclusion of five or more elements into the cationic sub-lattice(s) of oxide materials. Building upon the initial reports on HEOs, the first one published in 2015, the main objective of this work is to investigate the unexplored regions of oxide compositions and structures offered by the high entropy based design approach.

The initial task was the identification and optimization of a suitable synthesis technique for fabrication of HEOs with rocksalt and fluorite structures. In this regard, several techniques, each possessing certain advantages and disadvantages, were explored. Out of these considered ones, aerosol based nebulized spray pyrolysis (NSP) was found to be the most versatile technique for preparation of HEOs on a laboratory scale and was used as the primary synthesis tool in this thesis. The exploration of new HEO systems with different compositions and crystallographic structures was the next challenge. Perovskite type HEOs (P-HEOs) were developed, in which up to 10 different cations in equiatomic proportion can be homogeneously incorporated into a single-phase orthorhombic structure. Besides the synthesis aspect, emphasis was placed on comprehensive understanding of the underlying phase stability mechanisms in different crystal types of HEOs, such as rocksalt, fluorite and perovskite. It was observed that the governing principles were rather distinct for different types of HEOs. In some cases, such as in rocksalt-HEOs (R-HEOs), an entropy-driven phase transformation is dominant, whereas in the other HEOs, aspects like

tolerance factors, oxidation state of the cations and related internal charge compensations play determining roles.

Apart from these structural investigations, a major part of this doctoral work is dedicated to explore the functional properties of HEOs. Oxides, in general, show rich structure-composition-property relationships. Hence, the properties of HEOs were explored based on their crystal structure and composition characteristics. Three different classes of properties were investigated: electrochemical, optical and magnetic. Transition metal (TM) based R-HEO was probed as electrode material for secondary Li-ion batteries (LIBs). Highly reversible lithium storage capacities (above 600 mAh/g for more than 900 cycles) were observed. A major part of the capacity is drawn from electrochemical reactions below 1 V (vs Li^+/Li), which warrants its possible use as an anode in LIBs. Importantly, a unique electrochemical reaction mechanism, possibly stemming from an entropy effect, was discovered. Rare earth (RE) based fluorite-HEOs (F-HEOs), on the other hand, showed interesting optical properties like narrow band gap of ∼2 eV, which could be reversibly tuned (from 2 – 3.2 eV) by conducting heat treatments under different atmospheres. Element specific techniques, like X-ray absorption spectroscopy (XAS) and energy electron loss spectroscopy (EELS), allowed to disentangle the individual effects of the constituent cations in complex F-HEOs and identify the relevant features in the electronic band structure underpinning the observed reversible changes in the optical behavior. The reason behind the change in band gap is closely associated with the presence of redox active multivalent cations, like $Pr^{3+,4+}$, which result in the formation of intermediate unoccupied energy states. Finally, P-HEOs comprising of multiple RE cations on the A-site and/or multiple TM cations on the B-site exhibited an interesting interplay between the magnetic exchange interactions and the high degree of chemical disorder in the systems. Additional ferromagnetic interactions in otherwise predominant antiferromagnetic environment leading to exchange anisotropy were observed in phase-pure P-HEOs, wherein the former could be attributed to either small ferromagnetic clusters or spin canting.

In brief, this doctoral work highlights the versatility of the high entropy based design concept in oxides by demonstrating the structure-property relationships in three different crystal structure types of HEOs. As the research on HEOs is still in its early state, a plethora of fundamental aspects of HEOs are yet to be explored to assess their full potential for practical applications.

Zusammenfassung

Seit Anbeginn der Menschheit wurden in allen Epochen unterschiedliche Ansätze entwickelt, um neuartige Materialien herzustellen. Der meist genutzte Grundgedanke, auch als „Legieren“ für metallische Systeme und „Dotieren“ für nicht-metallische Systeme bekannt, ändert die Zusammensetzung und erlaubt es somit, neuartige Materialien zu erschaffen. Der Begriff des Legierens und Dotierens beschreibt das Hinzufügen relativ kleiner Mengen Sekundärelemente in ein Grundsystem. Als Beispiele hierfür können Stahl und Yttriumoxid stabilisiertem Zirkonoxid genannt werden, im ersten Fall ist Fe das Grundelement, in zweiten Fall ist ZrO_2 die Basiskomponente. Das Konzept der Hochentropie-Materialien (engl. High-Entropy Materials, HEMs) kann als eine extreme Weiterentwicklung des Legierungsprinzips angesehen werden, da fünf oder mehr Elemente mit nahezu derselben Elementkonzentration eingesetzt werden, um einen Mischkristall zu bilden. Aufgrund der äquimolaren Verhältnisse der einzelnen Elemente besitzt das HEM kein Hauptlegierungselement mehr. Interessanterweise kristallisieren diese HEMs trotz der chemischen Komplexität oft in einer einphasigen Kristallstruktur; ein Verhalten, was diese Systeme zu einer einzigartigen Materialklasse macht. Die Konfigurationsentropie eines solchen Systems wird insbesondere durch die Äquimolarität der elementaren Bestandteile erhöht; in vielen Fällen wird diese Konfigurationsentropie als Triebkraft für die Bildung und die Stabilität der einphasigen Kristallstruktur gesehen. Aufgrund dieser Besonderheiten wird das Konzept der Hochentropie-Materialien häufig als eigenständiger Ansatz und nicht als bloße Erweiterung des Legierens oder Dotierens angesehen.

Diese Doktorarbeit beschäftigt sich mit Hochentropie-Oxide (HEOs). HEOs sind Mischkristalle, die sich aus dem Einbau von fünf oder mehr Elementen in ein oder mehrere kationische Untergitter der Oxidkristallstruktur ergeben. Aufbauend auf der ersten Arbeit an HEOs, die 2015 publiziert wurde, bestand das Hauptziel der vorliegenden Doktorarbeit darin, die bisher unerforschten Phasendiagramm-Bereiche der unterschiedlichen Materialzusammensetzungen zu untersuchen, die das Hochentropiekonzept ermöglicht.

Der erste Schritt war es, eine geeignete Synthesemethode für die Herstellung von HEOs zu finden und diese zu optimieren. Dazu wurden verschiedene Techniken mit ihren jeweiligen Vor- und Nachteilen untersucht. Als geeignetste und gleichzeitig vielseitigste Methode erwies sich hierbei die sogenannte „Nebulized Spray Pyrolysis“ (NSP) Methode, welche darauf basiert, ein Reagenzaerosol durch eine heiße Zone zu transportieren, welches dort zu dem gewünschten Oxid reagiert. Die nächste Herausforderung war die Erforschung und Entwicklung neuartiger HEO-Systeme; so wurden beispielsweise ein Perowskit Hochentropie-Oxid (P-HEO) entwickelt, in das bis zu 10 verschiedene Elemente in eine einphasigen, orthorhombische Struktur eingebaut

werden. Zusätzlich wurden die grundliegenden Mechanismen, welche die Bildung von einphasige Mischkristallen in HEOs gewährleisten, für Kochsalz-, Fluorit- und Perowskitstrukturen untersucht. Hierbei konnten unterschiedliche Prinzipien für die unterschiedlichen Strukturen festgestellt werden. Während in HEOs mit Kochsalzstruktur (engl. Rocksalt, R-HEOs) eine entropiegesteuerte Phasenumwandlung beobachtet werden konnte, spielten Parameter wie Toleranzfaktoren, Oxidationszustände und die damit zusammenhängende Ladungskompensation bei der Bildung der Fluorit- und Perowskitstrukturen die entscheidende Rolle.

Neben der Synthese und den strukturellen Untersuchungen der HEO Materialien handelt ein wesentlicher Teil dieser Doktorarbeit von der Erforschung ihrer funktionellen Eigenschaften. Oxidmaterialien im Allgemeinen zeigen ausgeprägte Struktur-Eigenschaftsbeziehungen, daher wurden die funktionellen Eigenschaften der HEOs in Bezug auf ihre Struktur und Zusammensetzung untersucht. Es wurden drei verschiedene Klassen von Materialeigenschaften untersucht: elektrochemisch, optisch und magnetisch. Übergangsmetall-basierte R-HEOs konnten dabei als Elektrodenmaterial für Li-Ionen Sekundärbatterien (LIBs) erfolgreich getestet werden. Hoch reversible Kapazitäten (über 600 mAh/g während mehr als 900 Zyklen) wurden hierbei beobachtet. Der Großteil der Kapazität entstammt elektrochemischen Reaktionen, die unterhalb von 1 V (vs Li^+/Li) ablaufen, dementsprechend konnte das Material als Anode für LIBs genutzt werden. Einzigartige elektrochemische Reaktionsmechanismen, welche direkt aus der hohen Entropie des Systems resultieren, prägen hierbei die Elektrochemie. Lanthanoid-basierte Fluorit-HEOs (F-HEOs) dagegen, zeigten interessante optische Eigenschaften wie zum Beispiel eine Bandlücke von 2 eV, welche durch eine Wärmebehandlung in unterschiedlicher Gasatmosphäre reversibel durchgestimmt werden kann (zwischen 2 – 3.2 eV). Durch die Nutzung elementspezifischer Charakterisierungstechniken, z.B. Röntgenabsorptionsspektroskopie (XAS) und Elektronenenergieverlustspektroskopie (EELS), konnten die individuellen Effekte der verschiedenen Kationen in den F-HEOs identifiziert werden. Die dabei beobachteten Merkmale der elektronischen Struktur konnten als Erklärung für die veränderlichen optischen Eigenschaften herangezogen werden. Das zugrundeliegende Prinzip dieser reversiblen Bandänderung steht im Zusammenhang mit der Anwesenheit redoxaktiver, multivalenter Kationen, wie zum Beispiel $Pr^{3+,4+}$, welche unbesetzte tiefliegende Energiezustände ausbilden können. Abschließend wurden P-HEOs, welche aus verschiedenen Seltenerdkationen auf den A-Plätzen und/oder verschiedenen Übergangsmetallkationen auf den B-Plätzen bestehen, auf ihre magnetischen Eigenschaften untersucht. Die chemische Unordnung in der Struktur führt hier zu einer zusätzlichen ferromagnetischen Wechselwirkung in der ansonsten überwiegend antiferromagnetisch wechselwirkenden Matrix. Die ferromagnetisch wechselwirkenden Anteile sind entweder das Resultat von kleinen ferromagnetischen Bereichen oder verkanteten Spins.

Diese Doktorarbeit illustriert und unterstreicht die Vielseitigkeit und die Anwendbarkeit des Konzepts der Hochentropie-Oxide. Die Struktur-Eigenschaftsbeziehungen wurden dazu in drei verschiedenen Oxidklassen untersucht und vorgestellt. Da die HEO Materialien erst wenige Jahre bekannt sind und die Forschung dementsprechend am Anfang steht, müssen noch viele grundlegende Aspekte untersucht werden, damit sich ihr volles Potential für praktische Anwendungen offenbart.

Contents

1. Introduction

1.1. Motivation

Discovery of new materials, followed by the study of their structure and properties, is one of the key aspects of materials science and engineering [1, 2]. In 2004, Cantor *et al.* [3] pioneered a new design approach for materials discovery, with an aim "to investigate the unexplored central regions" of multicomponent (metallic) phase diagrams. Unlike in conventional alloys, typically consisting of one principal element, several multicomponent systems containing five or more metallic elements in equiatomic proportions have been studied [3]. The presence of the elements in (nearly) equal proportion helps to investigate the central compositions of the respective phase diagrams. It was observed that, despite the chemical complexity, most of the systems resulted in significantly lower number of phases compared to the maximum allowed by the Gibbs phase rule [3]. For instance, $Co_{20}Cr_{20}Fe_{20}Mn_{20}Ni_{20}$ crystallized in a single phase face centered cubic (fcc) structure [3]. This finding is rather intriguing, given the fact that formation of secondary phases, intermetallics or amorphous structure is a common scenario in complex systems like superalloys or bulk metallic glasses [4, 5]. Subsequently in 2004, Yeh *et al.* [6] proposed that the tendency to form a single phase solid solution in multicomponent (near) equiatomic alloys can be related to an enhanced configurational entropy of mixing in these systems, stemming from the increased number of constituent elements and their equiatomic proportions.[1] Based on this hypothesis, Yeh *et al.* [6] coined the term "high entropy alloys (HEAs)" to classify multicomponent (near) equiatomic alloys. Hence, the discovery of HEAs can be credited to two new ideas [3, 6]: (a) one is the approach to investigate unexplored compositions close to the central regions of multicomponent phase diagrams, where unexpected synergies can be anticipated; (b) while the other is the control of the configurational entropy (by altering the number of elements or their proportions) to influence the phase composition of a complex multicomponent system. Following these two primary concepts, HEAs have gained significant interest, which has resulted in unique alloy compositions, crystal structures, microstructures, and most importantly tailorable properties. Several HEA compositions are now known to exhibit exceptional properties, exceeding those of commercial alloys [7–9]. These features of HEAs have helped the field to grow as an independent research topic in materials science, which is evident from the numerous[2] reports published over the last 15 years. Furthermore, the approach to design HEAs (following the two aforementioned concepts) is now extended to other kind of materials, i.e., going beyond metallic alloys.

---

[1] The entropy of mixing is calculated from the Boltzmann equation, see in chapter 2, Eqn. 2.1.

[2] Currently, there are over two thousand papers related to HEAs.

Starting as early as 2004, attempts have been made to investigate non-metallic high entropy materials (HEMs)[3] like nitrides and carbides [10–13]. However, a major leap in the research interest on non-metallic HEMs has been observed since 2015, following the first report on high entropy oxides (HEOs) [14]. Rost *et al.* [14] demonstrated the possibility to incorporate five different elements into the cation sub-lattice of a single phase rock-salt structure, leading to the first HEO composition $(Co_{0.2}Cu_{0.2}Mg_{0.2}Ni_{0.2}Zn_{0.2})O$. A subsequent study [15] from our group in 2016 supported this initial investigation [14] and extended the "high entropy" based design approach to other type of oxide systems. A single phase HEO with fluorite structure containing five different rare-earth cations, $(Ce_{0.2}La_{0.2}Pr_{0.2}Sm_{0.2}Y_{0.2})O_{2\text{-}\delta}$, was synthesized. The tendency of multicomponent equiatomic HEOs to crystallize in a phase pure solid solution [14, 15] is in congruence with HEAs, hence, justifying the use of the term "high entropy oxides". It should be noted that before HEOs, oxide systems of such chemical complexities, i.e. containing five or more cations in equiatomic proportions, were neither experimentally explored nor theoretically predicted. This depicts the importance of the initial studies on HEOs [14, 15] and motivates this doctoral work to investigate other possible HEOs with different compositions and crystal structures.

Besides the commonality of the terminology, "high entropy", the underlying features of HEAs and HEOs are very different. One main reason is the fact that HEAs comprise metallic bonding while in HEOs bonds are typically ionic, implying additional oxidation state related restrictions for phase stability. This makes the formation of a single-phase solid solution in HEOs rather unique, as phase separation is a common scenario observed in heavily doped oxides. For instance, the NiO-CuO system [16] lacks extended miscibility, such that NiO doped with higher amount of CuO or vice versa would result in multiple phases. The same is true for the MgO-ZnO system. However, HEOs, like $(Co_{0.2}Cu_{0.2}Mg_{0.2}Ni_{0.2}Zn_{0.2})O$, are phase-pure despite the presence of many such immiscible pairs in comparable proportions. This makes the reasons behind the phase stability in HEOs interesting. More importantly, different types of HEOs exhibit different phase stability mechanisms. For instance, some show the dominant effect of (configurational) entropy influencing their phase stability like $(Co_{0.2}Cu_{0.2}Mg_{0.2}Ni_{0.2}Zn_{0.2})O$, whereas in other HEOs like $(Ce_{0.2}La_{0.2}Pr_{0.2}Sm_{0.2}Y_{0.2})O_{2\text{-}\delta}$, the presence of certain cations and their related oxidation states are the dominant factors. Thus, understanding the phase stability mechanisms in different types of HEOs is an important goal of this thesis.

The reports by Bérardan *et al.* [17, 18] in early 2016 depicted that HEOs not only attract fundamental physico-chemical interests but also possess appealing functional properties. Rocksalt-HEOs (R-HEOs) exhibit colossal dielectric constants on the order of 10^5 at 440 K with bulk resistance of 30 $M\Omega$, which is three orders of magnitude higher compared to the constituent parent oxides [17]. It was also observed that Li doped $(Co_{0.2}Cu_{0.2}Mg_{0.2}Ni_{0.2}Zn_{0.2})O$, crystallizing in a rocksalt structure, shows extremely high room temperature Li-ion conductivity on the order of 10^{-3} S cm^{-1} [18], which is better than many of the conventional solid electrolytes, like LiPON [18–20]. The underlying principle of the high Li-ion conduction in a closed packed R-HEO lattice, containing Li^+ and transition metal cations of comparable sizes, is very unique. One of the reasons

---

[3] HEMs now include a variety of high entropy systems like the metallic alloys, oxides, nitrides, carbides, diborides, etc.

behind the unexpected properties observed in HEOs can be related to high entropy based design concept and the resulting synergies due to the presence of multiple elements. The compositional flexibility of HEOs offers numerous possibilities to tailor their functional properties. This is a major motivation for pursuing research work on HEOs.

1.2. Objectives

At the beginning of this doctoral work, literature on HEOs was limited to four of the aforementioned reports [14, 15, 17, 18]. Hence, the primary goal of this doctoral work has been rather diverse and fundamental, with the main aim being the exploration of a broad area of structure and properties of HEOs. The objectives of the research performed within the framework of this dissertation are as follows:

1. Exploring HEOs with different compositions and crystal structures.
2. Identifying the underlying principles for phase purity and related phase transformations in different types of HEOs.
3. Investigating different functional properties specific to different types of HEOs.
4. Deducing the mechanisms governing the observed structure-property relationships in HEOs.

1.3. Outline of the thesis

In this doctoral work, the implementation of the high entropy based design approach on oxides of three different crystal structure types has been explored, followed by the investigation of their electrochemical, optical and magnetic properties. The findings are presented in the form of a cumulative dissertation, which includes 8 published articles. Although the articles are connected by a common string, i.e., “high entropy oxide”, they are fundamentally very different. Hence, each article is preceded by a brief introduction. It should be noted that a crystal structure based classification for HEOs has been adopted here. The outline of the thesis is as follows[4]:

Chapter 2 provides the scientific background of high entropy materials (HEMs). The basic concepts of HEMs, such as entropy based materials classification, typical phase composition and related thermodynamic parameters, are highlighted. This is followed by HEOs-specific fundamental details, like cation selection criteria, phase composition, the entropy-driven phase transformation and other factors influencing phase composition. Finally, a brief highlight of the different types of HEMs is provided.

---

[4] There is no chapter in the main text dedicated to materials and methods, as the specific techniques and related modifications used are already discussed in the respective published articles. Nevertheless, a brief description of the experimental techniques is provided in the Appendix A.

Chapter 3 focuses on transition metal based rocksalt type HEOs (R-HEOs). **Section 3.1** explores the possible synthesis routes of R-HEOs and helps in the selection of the most suited one for the studies to follow. In **Section 3.2**, the electrochemical properties of transition metal based R-HEOs are investigated, wherein R-HEO is probed as an electrode material for lithium ion battery.

Chapter 4 pertains to rare-earth based fluorite type HEOs (F-HEOs). **Sections 4.1** is a comprehensive study on several types of F-HEOs, where their fundamental structural characteristics and optical properties are investigated. **Section 4.2** is a continuation which depicts the possibility to reversibly tune the optical properties of F-HEOs and provides a comprehensive picture of their dynamic band structure.

Chapter 5 deals with perovskite type HEOs (P-HEOs). The possibility to form HEOs with crystal structures possessing two different cation sites and complex compositions is surveyed in **Section 5.1**. In addition, the governing principles for the phase purity and temperature dependent phase transitions in P-HEOs are identified. **Section 5.2** explores the magnetic properties of P-HEOs along with elucidation of their structure-property relationship.

Chapter 6 presents the conclusion to all the results and findings demonstrated in this thesis. **Section 6.2**, the outlook, is divided into two subsections. **Section 6.2.1** briefly highlights the current status of research in the field of HEOs,[5] which is succeeded by a mini-review (research news) and a viewpoint article present at the end of the chapter. Finally, based on the already existing studies, directions for future research related to this dissertation are proposed in **Section 6.2.2**.

---

[5] As the results presented in this thesis have initiated several of the current research works on HEOs, so this section is presented after the conclusions.

2. Scientific background

2.1. Fundamental aspects of high entropy materials (HEMs)

The study of HEMs, like oxides, nitrides, carbides, borides, etc., [14, 21–23] has thrived by building on the foundation laid by the HEAs [3, 6]. Although each of these systems is different, still the definitions, classifications and hypotheses pertaining to HEAs are often extended to other HEMs. These fundamentals common to all HEMs are provided in the following sections, before focusing on the HEOs.

2.1.1. Definition and classification

1. **Composition-based definition**. In the first report by Cantor *et al.* [3], the term "equiatomic multicomponent alloys" was used instead of "high entropy alloys". No specific definition was provided for "equiatomic multicomponent alloys" as the nomenclature was self-explanatory [3], i.e., any alloy system consisting of several elements in equiatomic proportions. In contrast, the entropy-based definition (as discussed later) often comes with a clause regarding the magnitude of entropy. However, the composition-based classification is rather universal and can be used to define any system where the constituent elements are present in equiatomic proportions [24]. Following this composition-based definition there are other terms which are now used instead of HEAs. These terminologies, such as multi-principal element alloys, compositionally complex alloys and baseless alloys[1], highlight the immensity of the composition space independent of the magnitude of entropy.
2. **Entropy-based definition**. Yeh *et al.* [6] coined the term high entropy, relating multicomponent solid solutions with the magnitude of entropy. Succeeding reports adhered to this entropy-based classification and perhaps, this is the most commonly used nomenclature. The basis of this classification is associated with the Boltzmann equation (Eqn. 2.1).

$$S_{config} = -R(\sum_{i=1}^{N} x_i ln x_i) \tag{2.1}$$

---

[1] Baseless alloy is not only a composition-based definition but also indicates that in HEA there is no base or host component.

In Eqn. 2.1, S_{config} is the molar configurational entropy of mixing, x_i represents the mole fraction of constituent elements, N is the number of elements, and R is the universal gas constant.[2] The S_{config} in a solid solution with N-components (where $N = 2$, 3, 4, or 5) as a function of the mole fraction of the N^{th} component is plotted in Fig. 2.1. It can be observed that S_{config} increases with the addition of more elements to a system. Furthermore, S_{config} reaches a maximum when all elements are present in equiatomic fractions, bridging the composition-based definition with the entropy-based one. In a five component system, the maximum S_{config} value that can be achieved is 1.61 R. Earlier, 1.61 R was proposed as the critical value for defining a high entropy system. This criterion was rather stringent and would even exclude the 'near-equiatomic' systems with 5 components. So, the following entropy-based classification is now widely accepted [24, 25] in literature.

High entropy: $S_{config} \geq 1.5$ R

Medium entropy: 1 R $\leq S_{config} \leq 1.5$ R

Low entropy: $S_{config} < 1$ R

---

[2] It should be noted that the Eqn. 2.1 holds true for purely ideal conditions, which is seldom the case. Nevertheless, Eqn. 2.1 provides a reasonable estimate for S_{config} in realistic cases where the random elemental distribution can be confirmed experimentally.

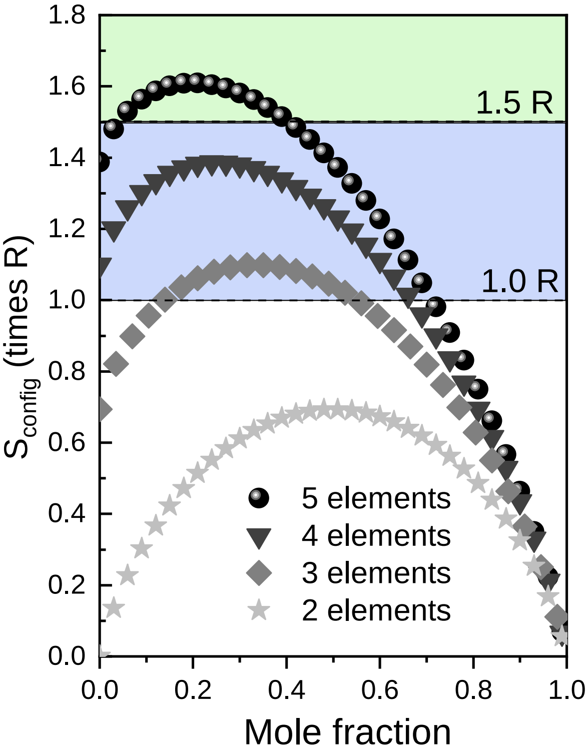

Figure 2.1.: Dependence of configurational entropy on the number of elements and their mole fractions.

In addition a definition based on both the composition- and entropy-based approaches has now been established. HEMs can be defined as systems containing five or more principal elements with the concentration of each element being between 35 and 5 at.-%, so that S_{config} is higher than 1.5 R [24, 25]. Therefore, this definition preserves the initial motivation of probing the central regions of the respective multicomponent phase diagrams. Simultaneously, this classification also broadens the composition space of HEMs, as systems in which minor elements (not in equiatomic amounts) are often added can also be classified as HEMs. The entropy-based classification is used in this thesis.

2.1.2. Phase compositions in HEMs

HEMs show distinctive features compared to conventional systems. The most appealing one is the tendency to form single phase solid solutions despite the presence of several components in comparable amounts. At thermodynamic equilibrium, the maximum number of phases (*P*) that can be formed is related to the number of components (*C*) as dictated by Gibbs phase rule [1, 2]. At a constant pressure, which is mostly the case, Gibbs phase rule is denoted as follows (Eqn. 2.2) [1, 2], where *F* represents the degrees of freedom or the number of independent variables:

$$P = C - F + 1 \tag{2.2}$$

The minimum value of *F* is 0, which indicates a discrete equilibrium point in a phase diagram (such as an eutecoid point in a binary phase diagram), where both the composition and temperature are fixed. For a 5 components HEA, like $Co_{20}Cr_{20}Fe_{20}Mn_{20}Ni_{20}$, the maximum number of phases (*P*) expected at thermodynamic equilibrium is 6. For a non-equilibrium scenario the maximum number of phases can be even higher. But this five component HEA is phase pure, i.e., $P = 1$ [3]. The X-ray diffraction (XRD) pattern shown in Fig. 2.2a confirms the phase purity of face centered cubic (*fcc*) $Co_{20}Cr_{20}Fe_{20}Mn_{20}Ni_{20}$ [3, 26]. In addition, atom probe tomography (APT) results shown in Fig. 2.2b support the chemical homogeneity of the system, ruling out any possible local clustering of the constituent elements. Local clustering signifies a lowering of the random atomic distribution, which consequently means lowering of the S_{config}. Thus, the absence of clustering is in agreement with high S_{config} anticipated from Eqn. 2.1. The anomalous behavior that HEAs (or HEMs) show much fewer phases than expected from Gibbs phase rule is another criterion, which is often used to characterize them [24, 25]. Even multicomponent systems, which are not phase pure but rather crystallize into fewer phases than the maximum predicted by the Gibbs phase rule are also categorized as “high entropy” based on this anomaly. For instance, $Al_{16.7}Co_{16.7}Cr_{16.7}Cu_{16.7}Fe_{6.7}Ni_{16.7}$-HEA crystallizes into two phases in contrary to the maximum of 5 phases predicted by Eqn. 2.2.

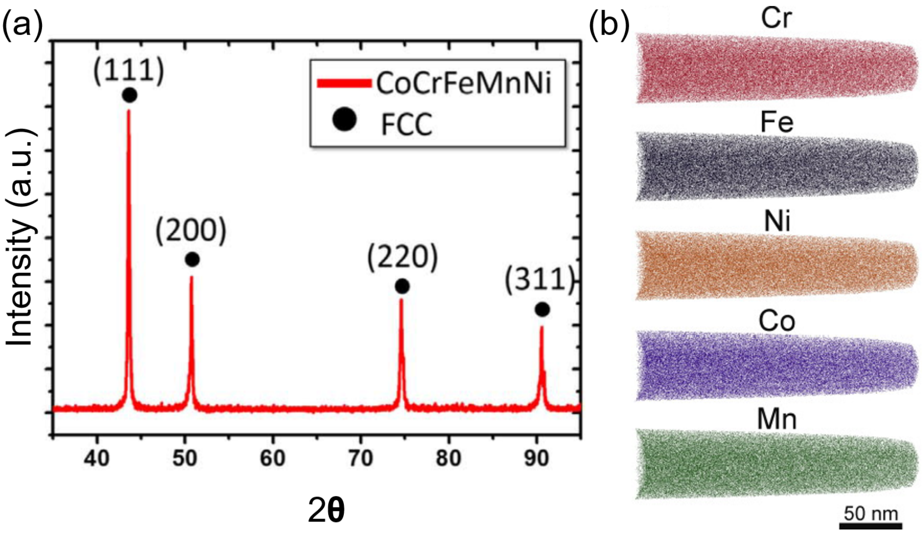

Figure 2.2.: (a) XRD patterns showing the phase purity and (b) 3D-reconstruction of elemental distribution maps obtained from APT depicting the chemical homogeneity in *fcc*-$Co_{20}Cr_{20}Fe_{20}Mn_{20}Ni_{20}$-HEA. ((a) Reproduced with permission from [26] ©2018, ELSEVIER. (b) Reproduced with permission from [27] ©2015, ELSEVIER.)

2.1.3. Four core effects

Four core effects [24, 25] have been recognized for HEMs, which largely explain their distinctive characteristics, for instance, the formation of fewer phases than expected from the Gibbs phase rule.[3] These core effects are as follows:

1. **High entropy effect.** HEMs are basically classified on the basis of this hypothesis. It is believed that the preference to crystallize as a single phase solid solution (or fewer phases) is promoted by the enhanced S_{config} of HEMs (as per Eqn. 2.1). The increase in S_{config} affects the overall entropic term in the Gibbs free equation (Eqn. 2.3).

$$\Delta G_{mix} = \Delta H_{mix} - T\Delta S_{mix} \tag{2.3}$$

The Gibbs free energy (ΔG_{mix}) is an interplay between the enthalpy of mixing (ΔH_{mix}) and the entropy of mixing (ΔS_{mix}), which governs the phase composition of a system at a given temperature (T). ΔG_{mix} should be negative for a particular phase to form. The dependency of ΔH_{mix} on the mole fraction X_A and X_B in a binary (regular) solution is shown in Eqn. 2.4.

$$\Delta H_{mix} = \beta X_A X_B \tag{2.4}$$

---

[3] It should be noted that these “core effects” were hypothesized during the early years of HEAs. The current studies indicate that these core effects are not always relevant to every HEA/HEM. Nevertheless, as mentioned above, these effects are still considered as important, as they can support several features of the HEMs.

ΔH_{mix} can be either positive or negative depending on the constant β, while the term ΔS_{mix} is always positive. Hence, the term $-T\Delta S_{mix}$ is always negative. The relationship between ΔH_{mix}, ΔS_{mix} and ΔG_{mix} for a binary solid solution is pictorially depicted in Fig. 2.3. Three simple cases of ideal or regular solutions have been considered in this context, however, it should be noted that ideal or regular solutions are rather rare in reality.

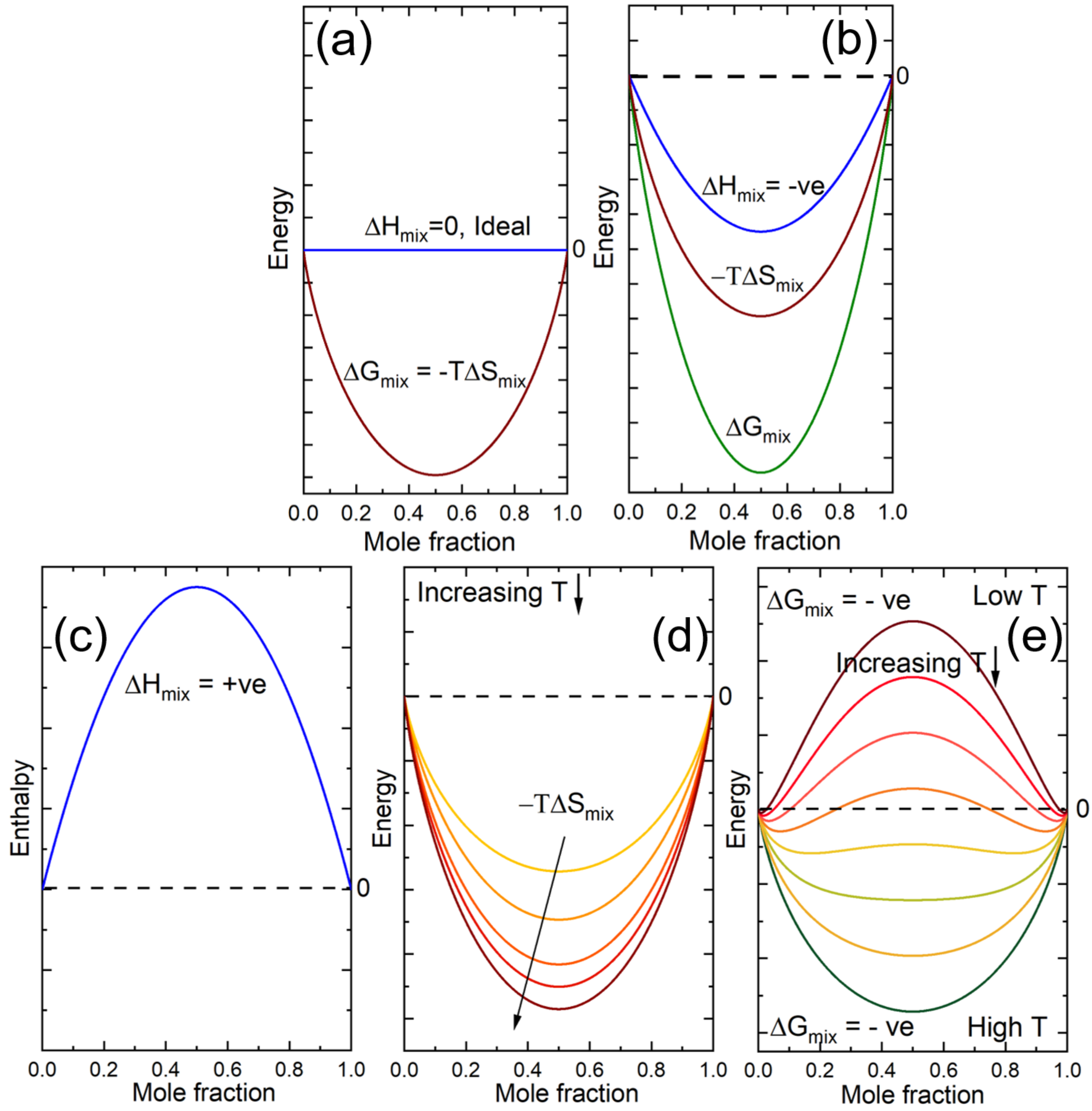

Figure 2.3.: The relationship between ΔH_{mix} and ΔS_{mix}, governing the ΔG_{mix} as a function of composition, where in (a) $\Delta H_{mix} = 0$, (b) $\Delta H_{mix} < 0$ and (c) $\Delta H_{mix} > 0$. An ideal scenario with increasing temperature (T) lowering the free energy is shown in (d), while a simple regular solid solution with positive ΔH_{mix} at different T is shown in (e).

Ideal scenario: It is the most simple case, where ΔH_{mix} is zero. Thus, ΔG_{mix} is negative and equals to $-T\Delta S_{mix}$, as shown in Fig. 2.3a.

Enthalpically favorable scenario: In many systems ΔH_{mix} can be negative, which indicates that the formation of a solid solution is preferred, as depicted in Fig. 2.3b. In this case the magnitude of ΔS_{mix} is less relevant.

Enthalpically unfavorable scenario: ΔH_{mix} can be positive in systems where the constituent elements do not prefer to be directly coordinated with each other, as shown in Fig. 2.3c. In such a scenario the $-T\Delta S_{mix}$ becomes crucial, and the phase stability of the solution is governed by the relative magnitude of $-T\Delta S_{mix}$. With increasing temperature, the absolute value of $T\Delta S_{mix}$ increases. Thus, $-T\Delta S_{mix}$ becomes more negative (Fig. 2.3d). Now, depending upon the magnitude ΔH_{mix}, different temperatures will be needed to compensate the enthalpy penalty and make the ΔG_{mix} negative, or in other words stabilizing the binary solution (as shown in Fig. 2.3e).

In HEMs, it is believed that the $-T\Delta S_{mix}$ becomes sufficiently large to overwhelm any enthalpy related penalties (ΔH_{mix}), thus, minimizing the ΔG_{mix} for formation of a single phase. Concurrently, in most of the HEMs high temperatures are needed to compensate the ΔH_{mix}. Hence, at room temperature single phase HEMs are metastable. Furthermore, it is also believed that S_{config} is the major contributor to ΔS_{mix} in HEMs, thus the other entropy contributions (like vibrational, electronic and magnetic) [24, 25] are often not accounted for.[4] It is important to note that a high S_{config} does not always ensure the formation of single phase HEM and in actuality the ΔH_{mix} and T do play critical roles in determining the phase composition of HEMs.

2. **Sluggish-diffusion effect.** It has been proposed that diffusion processes in HEMs are slower than in conventional systems [28, 29]. The main reason related to this is their chemical complexity. For instance, in HEAs the local atomic neighborhood varies enormously compared to binary alloys or alloys with low solute contents. This considerable difference in local atomic configuration in HEAs can lead to different local bonds. This means that the local energy for each site is different, i.e., some are lower energy sites while other have higher energies. Both these cases will lead to slower diffusion. In the case of the lower energy sites the chances of an atom getting trapped in that particular site is enhanced, whereas, for the higher energy ones the atom will most likely hop back and forth to the original lattice site instead of diffusing through. Tsai *et al.* [28] confirmed this, where they observed that the rate of diffusion of Ni atoms diffusion in $Co_{20}Cr_{20}Fe_{20}Mn_{20}Ni_{20}$ is slower (under certain circumstances) compared to other lesser complex alloys. However, in a recent report, Divinski *et al.* [30] critically evaluated the diffusion kinetics in different HEAs and concluded that the use of the term “sluggish diffusion” is rather ambiguous. Nevertheless, “sluggish diffusion” is still considered as one of the core effects in HEAs/HEMs, which is not only used to explain their metastable phase compositions at room temperature (i.e., inhibition of possible phase segregation), but also considered as a pivotal factor in determining their properties, like superior creep resistance of some HEAs [31].

---

[4] Nonetheless, the effect of the vibrational, electronic and magnetic entropy should not be neglected [24].

3. **Lattice-distortion effect.** A typical HEM lattice is populated by 5 (or more) different elements. Although the elements are chosen based on parity of their atomic sizes, it is inevitable to have size differences among the constituent atoms. Especially, the difference between the largest and the smallest one is often substantial. These differences lead to distortions of the HEMs lattices, thus, affecting many of their structure dependent properties. For instance, lattice distortion can hinder dislocation movement resulting in pronounced solid solution strengthening in HEAs [32].

4. **Cocktail effect.** Prior to the discovery of HEAs in 2003, Ranganathan published an article entitled 'Alloyed pleasures: Multimetallic cocktails' [33]. The main message of this report is that the characteristics of a system are the result of the synergies amongst the constituent elements. This is true for any system but is enhanced in case of HEMs, as there are multiple interactions possible. Hence, this collective effect has been considered as one of the key parameter in HEMs that can explain many of their properties, which cannot be deduced using simple rule of mixtures. For instance, by addition of soft (*fcc*)-Al to *fcc*-$Co_{20}Cr_{20}Cu_{20}Fe_{20}Ni_{20}$-HEA, softening of the material can be expected with the resulting solid solution being *fcc*. However, the addition of Al actually favours body centered cubic (*bcc*) structure [29] and subsequently hardens the aforementioned HEA.

These four core effects are fundamental and can be applied to all systems in general. The coexistence of all these four core effects makes the HEMs unique. Each of the core effects govern specific features. For instance, the high entropy effect is critical from the thermodynamic point as it can affect the phase composition, while sluggish diffusion being a kinetic aspect can impede phase transition and help to retain the "metastable" phases (at lower temperatures where the entropy effect decreases). On the other hand, the lattice distortion and the cocktail effect govern various structure dependent functional properties. Hence, unprecedented properties are often encountered in different HEMs.

2.2. High entropy oxides (HEOs)

2.2.1. Definition

Based on the publications on high entropy oxides (HEOs) [14, 17, 34, 35] and the descriptions therein, here, HEOs are classified as single phase oxide systems containing 5 or more cations in near-equiatomic proportions, which are statistically distributed on the respective cationic lattice site(s). This classification ensures a high value of S_{config}, which can be calculated for a $A_xB_yO_z$ type oxide as per Eqn. 2.5:

$$S_{config} = -R[x(\sum_{a=1}^{N} x_a ln x_a)_{A-site} + y(\sum_{b=1}^{M} y_b ln y_b)_{B-site} + z(\sum_{c=1}^{P} z_c ln z_c)_{O-site}] \tag{2.5}$$

The values x_a, y_b and z_o are the mole fractions of the ions present in the A-site, B-site and O^{2-}-site (or anion site), respectively. M and N represent the number of cations present in A-site and B-site, respectively. While P is the number of elements present on the O^{2-}-site, this can be either vacancies or other anions, like in oxyfluorides or oxynitrides. The S_{config} contribution from O^{2-}-site is ideally zero ($\ln 1 = 0$), if there are no oxygen vacancies or other anions present. Moreover, several oxides have only a single cation sub-lattice such as, rocksalt, fluorite, etc., leading to a modified Eqn. 2.5 (if oxygen vacancies are ignored). As a result, it can be observed that Eqn. 2.6 is identical as Eqn. 2.1.

$$S_{config} = -R[(\sum_{a=1}^{N} x_a ln x_a)] \tag{2.6}$$

Hence, the dependency of S_{config} in HEOs (as per Eqn. 2.6) on the cation mole fraction is identical to Fig. 2.1. Similar to HEAs, when the $S_{config} \geq 1.5$ R then an oxide system is classified as HEO.[5] Likewise if S_{config} is between 1 R to 1.5 R, then the oxide is classified as a medium entropy oxide (MEO).

2.2.2. Pauling's rules and guidelines for cations selection in HEOs

There are five general statements proposed by Linus Pauling, which can predict the structure in which an ionic compound can possibly crystallize [36, 37]. Like any other ionic compounds, HEOs are expected to follow Pauling's rules. These rules are listed in the decending order of their influence [36, 37].

1. Pauling's first rule states that each cation is coordinated by a polyhedron of anions. The number of anions forming this polyhedron, which is also the coordination number (CN) of the cation, depend upon ratio of cation to anion radii (r_c/r_a). The equilibrium inter-ionic distance between the cation and anion is determined from the sum of their radii ($r_c + r_a$). Table 2.1 highlights the dependency of CN on critical radius ratios. As an example, in $CaTiO_3$ perovskite, CaO forms a *fcc* sublattice with CN of Ca^{2+} being 12 as the $r_{Ca}/r_O \sim 1$, whereas the CN of Ti^{4+} is 6 as $r_{Ti}/r_O \geq 0.43$.

2. The second rule ensures the local charge neutrality of the coordination polyhedra. Charge neutrality is achieved when the total sum of the bond strength reaching a specific ion equals its valency. The bond strength is defined as the valency of an ion divided by its CN. For example, CeO_2 crystallizes in fluorite structure with CN of Ce^{4+} being 8. Therefore, bond strength of Ce^{4+} is 4/8, i.e., 1/2. Consequently, this implies that the anion, i.e., O^{2-} should have CN of 4, which is true.

---

[5] Here is it important to note that S_{config} (per formula unit) used for classification of HEOs is calculated only based on the cation mole fraction, which means that the overall cation mole fraction is considered as 1.

Table 2.1.: Critical radius ratios (r_c/r_a) for different coordination number (CN) and polyhedron type around the central ion.

r_c/r_a	CN	Polyhedron type
≥ 1	12	Cuboctahedron
≥ 0.732	8	Cubic
≥ 0.414	6	Octahedron
≥ 0.225	4	Tetrahedron
≥ 0.155	3	Triangular
≥ 0	2	Linear

3. The third rule determines how the different elements (like corners, edges or faces) of the coordination polyhedra are shared. This is mostly governed by the fact that a cation prefers to maximize its distance from another cation, in order to minimize repulsion. Ideally, corner sharing leads to the smallest repulsion. Hence, polyhedra prefer sharing corners over edges and edges over faces.
4. The fourth rule also deals with the sharing of the polyhedra elements. However, it is a more stringent version of rule 3 and is ideal for compounds containing different cations with large valency and small CN. In order to increase the distance between highly charged cations so that the electrostatic repulsion between them is smaller, these kind of compounds do not tend to share polyhedral elements at all, or at most share corners, like the SiO_4^{4-} tetrahedra in SiO_2.
5. The fifth rule is often called the rule of parity, which suggests that simple structures (with less crystallographic sites) are often preferred over more complicated arrangements. In fact this rule has a close correlation with HEOs. It indicates that if several cations of similar size and identical valency are incorporated into a lattice then there is a high probability that the cations are distributed randomly on a single lattice site. Upon increasing the dissimilarity of the cations, the tendency to form ordered arrangements becomes prominent and ultimately leads to completely different coordination for each cation.

Most of the structural features of a known ionic compound can be understood using the Pauling's rules. Consequently, structural features of an unknown composition can also be anticipated using the same. Thus, the cation selection criteria for HEOs (in order to achieve single phase) are mainly influenced by Pauling's rules. However, there are some additional conditions (2 and 3 in the following list) which need to be followed in order to distinguish HEOs from conventional oxides. These criteria are as follows:

1. Cations should have similar ionic radii at a specific oxidation state and co-ordination number. The different lattice sites that the cations can occupy should be considered during the selection.
2. At least one of the constituent mono-cationic oxide systems should have a crystal structure different from others.

3. At least one pair among the constituent oxides should not be completely miscible.

2.2.3. Structure and phase composition in HEOs

$(Co_{0.2}Cu_{0.2}Mg_{0.2}Ni_{0.2}Zn_{0.2})O$ was the first HEO system to be investigated [14]. The constituent cations were chosen based on the fact that they have similar ionic radii (in a 2+ oxidation state with CN being 6). In agreement with Pauling's rules[6], the system crystallizes in a single phase rocksalt structure as can be observed from the room temperature XRD pattern in Fig. 2.4a. Hence, in this thesis, $(Co_{0.2}Cu_{0.2}Mg_{0.2}Ni_{0.2}Zn_{0.2})O$ based HEOs are termed as rocksalt type HEOs (R-HEOs). One important factor affecting the S_{config} is the local structure of HEOs, as any type of clustering or segregation of elements will decrease the number of possible microstates, thereby lowering the overall entropy. Homogeneous distribution of the constituent cations at the atomic scale was confirmed from the APT studies (Fig. 2.4b). Furthermore, the extended X-ray absorption fine structure (EXAFS) studies showed that the local chemical environments for all cations were nearly identical (Fig. 2.4c), hence, confirming the random distribution of cations.

The formation of a single-phase R-HEO with random and homogeneous distribution of the cations is rather intriguing given the fact that many of the binary oxide pairs present in R-HEO do not prefer formation of a single phase. A simple example of such a pair is CuO-NiO, in which despite the cations being isovalent and of similar sizes the system lacks extensive solubility [16]. A similar

---

[6] The r_c/r_a in $(Co_{0.2}Cu_{0.2}Mg_{0.2}Ni_{0.2}Zn_{0.2})O$ is 0.58.

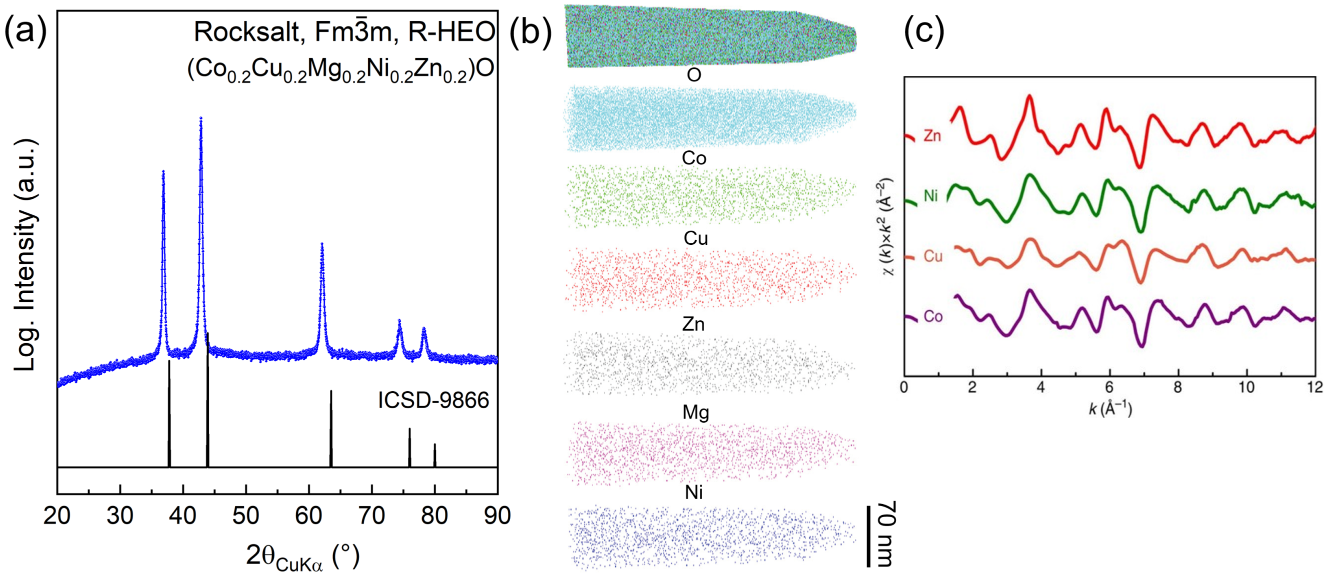

Figure 2.4.: (a) XRD pattern showing the phase purity of rocksalt type HEO, (b) 3D atomic distribution maps obtained from APT depicting it chemical homogeneity, and (c) EXAFS further confirming the random cationic distribution in the rocksalt lattice. (Reproduced with permission from (a) [34] ©2019, JOHN WILEY AND SONS (b) [38] ©2019, ELSEVIER and (c) [14] ©2019, SPRINGER NATURE.)

situation is true for the ZnO-MgO pair where extensive solubility is only observed in terminal positions of the phase diagram [39] and not when the cations present are in comparable amount. Importantly, all these pairs are present in the R-HEO and in equal amounts, but still a single phase is obtained. These facts indicate interesting thermodynamic features of HEOs, which are addressed in the following section.

2.2.4. Thermodynamic aspects of HEOs

The lattice energy (or enthalpy) of ionic compounds (like oxides) primarily depends on two fundamental competing interactions, which lead to the formation of ionic bonds [36]. One is the Coulombic attraction between cation and anion, which is the basis of an ionic bond. The other is the repulsion between the cation and the anion, which becomes prominent at very close separation, as dictated by Pauli exclusion principle. Hence, depending upon these two competing electrostatic interactions an equilibrium distance (R_0) between the ions is established. Taking all factors into account, the lattice energy (E_c) of a crystalline ionic compound can be defined by Born–Landé equation (Eqn. 2.7).

$$E_c = -N_A \alpha \frac{Z_c Z_a e^2}{4\pi\varepsilon_o R_0}[1 - \frac{1}{n}] \tag{2.7}$$

In Eqn. 2.7, N_A is the Avogadro constant, Z_c and Z_a are the cationic and anionic charge, respectively, ε_0 is the permittivity of free space and $n \sim 10$ is the Born exponent. The sum of the cationic and anionic radii determines the equilibrium separation between the ions, which is denoted by the term R_0. One of the important parameters in Eqn. 2.7 is the Madelung constant (α), which corresponds to the magnitude of electrostatic stabilization of a particular crystal structure. For instance, α for wurzite and rocksalt are different. In fact this difference drives the stabilization of ZnO as wurtzite rather than as rocksalt. Naturally, it also implies that the stabilization of ZnO in a rocksalt lattice is energetically costly and ~25 kJ mol^{-1} is needed to transform wurzite ZnO to rocksalt [40]. Likewise, for a transformation of tenorite (CuO) to rocksalt ~22 kJ mol^{-1} is required [41].

HEOs combine several mono-cationic oxides, which have different crystal structures, such as both Cu and Zn are present in R-HEO, $(Co_{0.2}Cu_{0.2}Mg_{0.2}Ni_{0.2}Zn_{0.2})O$. Hence, an enthalpy penalty stemming from this kind of structural (or lattice energy) differences is the primary contributor to ΔH_{mix} (in the Gibbs free energy Eqn. 2.3) for the formation of phase pure HEOs. For instance, in R-HEOs, the enthalpy penalty arising from structural differences is expected to be ~10 kJ mol^{-1}, i.e., $0.2(22 + 25)$ kJ mol^{-1} [14]. Naturally, the enthalpy penalty is expected to be lower if cations like Cu or Zn are eliminated from R-HEO. For instance, the enthalpy penalties[7] in $(Co_{0.25}Cu_{0.25}Mg_{0.25}Ni_{0.25})O$ and $(Co_{0.25}Mg_{0.25}Ni_{0.25}Zn_{0.25})O$ are ~5.5 kJ mol^{-1} and ~6.2 kJ mol^{-1}, respectively. This trend has been confirmed from the molecular dynamics (MD) simulations, where it can be observed that the 4-cation systems without Zn or Cu have lower ΔH_{mix} than R-HEO [42],

---

[7] The calculations are purely based on the lattice energy differences, hence, are just estimates.

see Fig. 2.5a. It should be noted that a 4-cation system (with cations in equal amount) falls under the category of medium entropy oxides (MEOs), as S_{config} is 1.39 R. Furthermore, it can also be observed that exclusion of cations, like Ni, Mg or Co, which prefer rocksalt configurations, leads to an increase in ΔH_{mix} compared to R-HEO (Fig. 2.5a) [42]. However, like in all materials, the thermodynamics of HEOs is not purely governed by ΔH_{mix}. It has been experimentally observed that all the MEOs are difficult to crystallize in single phase rocksalt structure (irrespective of their composition and calculated ΔH_{mix}) compared to the R-HEO. Fig 2.5b compares the phase composition of R-HEO with the different MEO variants.[8] Multiple phases were observed in all the MEOs systems, even in the systems without Zn or Cu [14] where the enthalpy penalty is expected to be lower compared to R-HEO (Fig 2.5b) [14]. This finding indicates a possible role of entropy in determining the phase composition of R-HEO, as the R-HEO has a higher S_{config} compared to the MEOs.

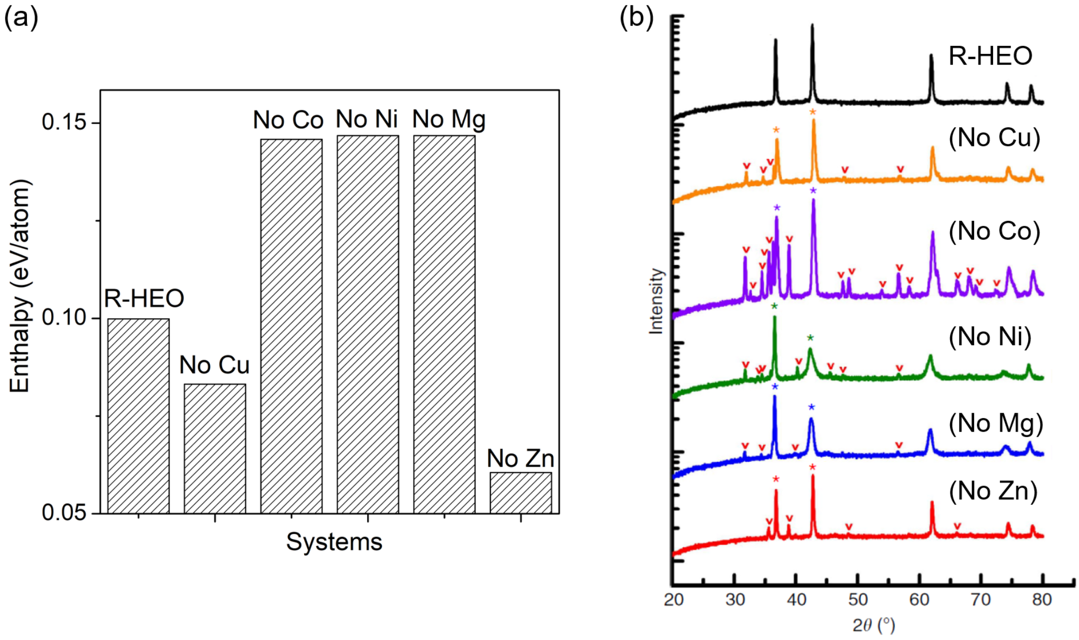

Figure 2.5.: Comparison between 5-cationic HEO and 4-cationic medium entropy oxides (MEOs): (a) variation in enthalpy, (b) XRD patterns showing phase purity in HEO and mutliple phases in MEOs. Reproduced with permission from (a)[42] ©2018, ELSEVIER. [14] ©2015, SPRINGER NATURE.)

2.2.5. Entropy-stabilized HEOs

The role of entropy in the phase stability of R-HEOs was studied via heat treatments at different temperatures. A reversible phase transformation from a single phase solid solution to multiple

---

[8] It should be noted that all the systems were synthesized under similar conditions, hence, additional effects can be neglected.

phases was observed, when R-HEOs were cyclically heat treated at different temperatures (Fig. 2.6a) [14]. Phase separation occurred at temperatures lower than 900 °C and was most prominent at $\sim$750 °C . However, upon subsequent heating at higher temperatures (above 900 °C) the single phase R-HEO could be regained. This phase transformation supports the entropy driven phase stabilization effect. As can be seen in Fig. 2.3e at lower temperatures the overall $-T\Delta S_{mix}$ term might not be large enough to compensate for the enthalpy-driven phase separation. Upon increasing the temperature, the $-T\Delta S_{mix}$ becomes large enough to neutralize the enthalpy penalty and stabilize a single phase solid solution (Fig. 2.3e). This phase transformation is further supported by the calorimetry data for R-HEOs. As observed in Fig. 2.6b, the transformation from the multiphase (below 900 °C) mixture to the single phase material is endothermic in nature. This endothermicity is rather intuitive, as additional energy of $\sim$10 kJ mol^{-1} (as mentioned earlier) is needed to overcome the ΔH_{mix} for the formation of the single phase rocksalt structure [14]. Thus, an interesting interplay between entropy and enthalpy can be observed, where the enthalpy term favors the multi-phase mixture whereas the entropy term (at high temperatures) stabilizes the single phase R-HEO structure. Hence, R-HEO can be considered as metastable at room temperature or in temperature range where $-T\Delta S_{mix}$ is smaller than ΔH_{mix}. It is assumed that the "sluggish diffusion" aspect (See Sec. 2.1.3) considered in HEMs supports the retention of entropy-stabilized single phase at lower temperatures and the impedance of enthalpy driven phase separation [14, 34].

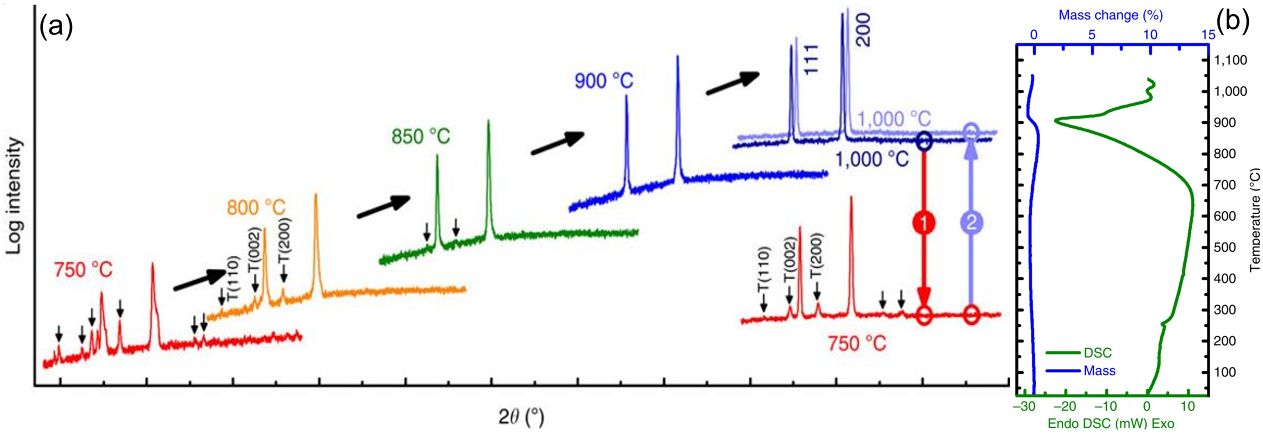

Figure 2.6.: Reversible phase transformation upon cyclic heat-treatment, evidenced from (a) XRD and (b) calorimetry, as an indication of entropy driven phase stabilization effect in R-HEOs. (Reproduced with permission from [14] ©2019, SPRINGER NATURE.)

Based on this entropy driven phase stabilization effect, HEOs can be categorized into two groups. One is the entropy-stabilized HEOs, such as the R-HEOs, which exhibit reversible phase transformation (from single to multiple phases) upon cyclic heat-treatment. The other group, which do not show this signature, are classified as the non-entropy-stabilized HEOs [34]. The following section elaborates on a group of non-entropy stabilized HEOs [15].

2.2.6. Non entropy-stabilized HEOs

The scope of HEOs was broadened by the discovery of fluorite type high entropy oxides (F-HEOs), in which 5 or more different rare-earth cations in equiatomic amounts can be incorporated into the cation sub-lattice [15]. A representative XRD pattern of $(Ce_{0.2}La_{0.2}Pr_{0.2}Sm_{0.2}Y_{0.2})O_{2-\delta}$ portrays the possibility to form a single phase F-HEOs (Fig. 2.7). The constituent cations of F-HEOs were selected based on the rules mentioned in Sec. 2.2.2., which ensure the fact that all the constituent oxides are not isostructural or completely miscible [15, 43, 44]. Hence, formation of the single phase F-HEOs is interesting. Furthermore, the chemical homogeneity of the cations on an atomic length scale was identified from the APT studies (Fig. 2.7).

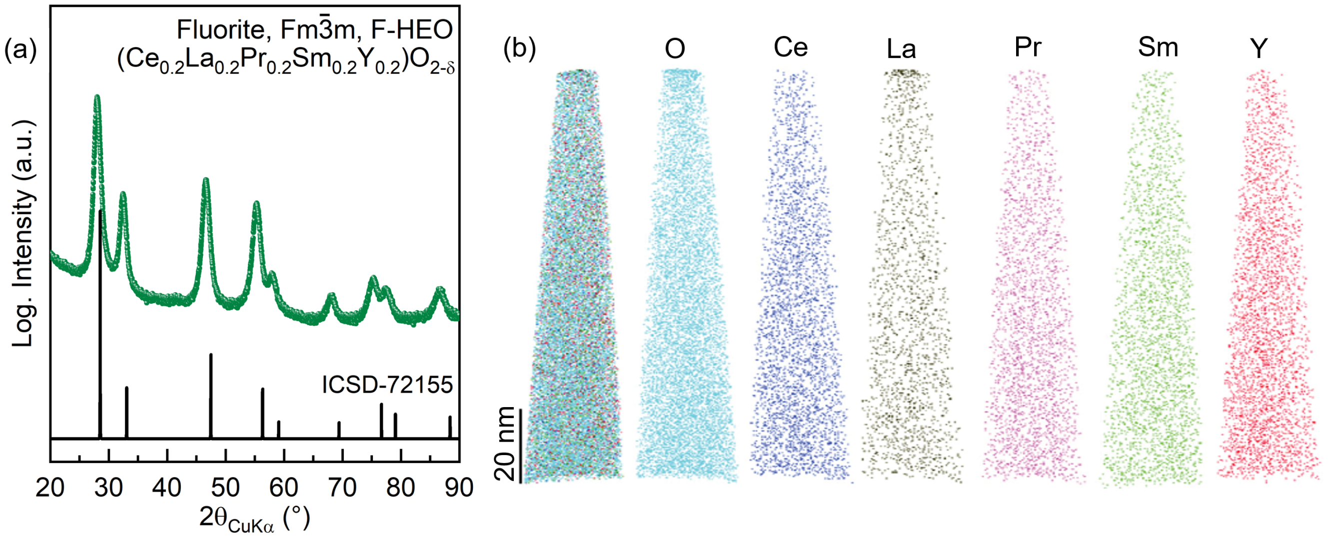

Figure 2.7.: (a) XRD patterns and (b) 3D atomic distribution maps obtained from APT depicting the phase purity and homogeneity, respectively, in F-HEOs. ((a) Reproduced with permission from [34] ©2019, JOHN WILEY AND SONS. (b) Reproduced with permission from [38] ©2019, ELSEVIER.)

Unlike R-HEOs, F-HEOs did not show a typical entropy driven phase stability effect [15], i.e., the phase purity in F-HEOs could be maintained even upon heating at temperatures lower than the synthesis temperature. This behavior can have two explanations.

(i) The formation of a single phase in F-HEOs is thermodynamically favorable, i.e., ΔH_{mix} is already negative (as shown in Fig. 2.3b). Hence, ΔG_{mix} will be negative independent of the magnitude of $-T\Delta S_{mix}$ (2.3b). However, this situation is rather unlikely, as not all the constituent monocationic rare earth oxides are fluorite, nor do all of them exhibit extensive miscibility in each other [43, 44].

(ii) Although the enthalpy penalty is positive, it is possible that $-T\Delta S_{mix}$ (even at low temperatures) is large enough to compensate the small (positive) ΔH_{mix}. In this case the ΔG_{mix} will be mostly negative over a wide temperature range. Thus, the critical temperature for the enthalpy dominated phase separation can be really low. Most likely, at those low temperatures the kinetics prevent the phase segregation.

Although both the aforementioned thermodynamic scenarios are possible for the phase purity of F-HEO, the exact reason still remains unclear. Hence, experiments were conducted in order to investigate the various possibilities. Surprisingly, it was observed that the F-HEOs without Ce resulted in multiphase mixtures, as displayed in Fig. 2.8a. Furthemore, the phase compostions obtained were invariant to any kind of heat treatment or the number of cations (i.e., the S_{config}) present in the systems. Hence, a dominant role of Ce over any other effect (such as configurational entropy) can be identified. Thus, comparisons between F-HEOs and CeO_2 were drawn, since the later is a well known [45, 46] fluorite type oxide. Identical to CeO_2, Ce in F-HEOs was found to be present in 4+ oxidation state, as can be observed from X-Ray photoelectron spectroscopy spectra (see 2.8b) [15]. The presence of a stable 4+ cation is essential for the stability of fluorite structure (as is discussed in Chapter 4). Furthermore, it has been observed that other than Ce, only Pr exhibits a 4+ state (more precisely a mixed 3+ and 4+ state), whereas all the other cations are present in 3+ state (details in Chapter 4). However, the systems containing Pr and not Ce are not phase pure (see Fig. 2.8a). Thus, it can be concluded that the absence of Ce^{4+} in F-HEOs leads to a huge enthalpic penalty, which is larger than the configurational entropy gain.

In summary, the important role of a single cation (like Ce^{4+})[9] is identified, where even its presence in minimal amounts (~0.2 of the overall cation mole fraction for the five cation system) is sufficient to overcome all other thermodynamic effects, and almost solely govern the phase stability of a highly complex system like F-HEO.

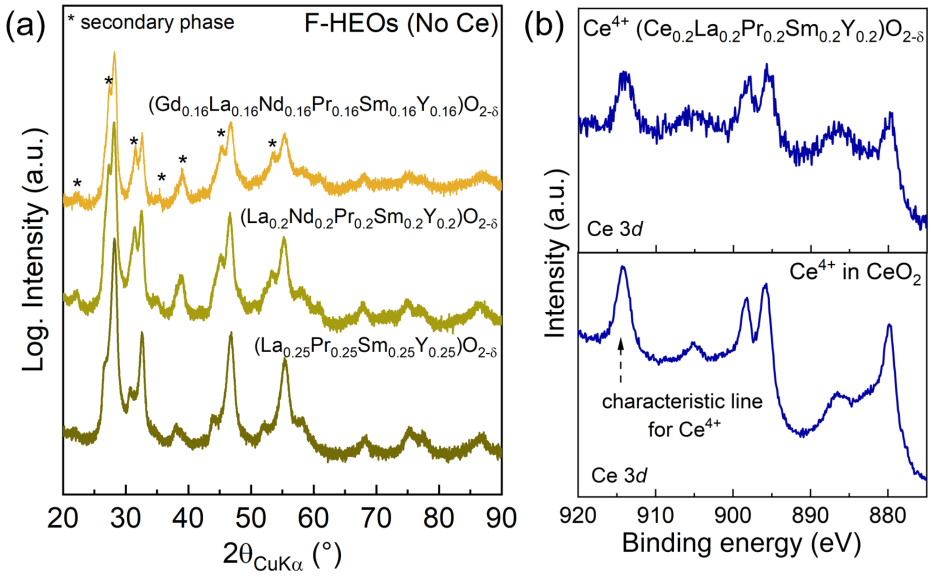

Figure 2.8.: XRD patterns of F-HEOs without Ce displaying the presence of multiple phases and implying importance of Ce in phase purity of F-HEOs. (c) XPS showing the presence of Ce^{4+} in F-HEOs. (Reproduced with permission from [15] ©2017, TAYLOR AND FRANCIS.)

---

[9] Perhaps this can be true for any stable 4+ cation, which can afford 8-fold coordination.

2.3. Highlights of HEMs

In general, HEMs are characterized by their phase-purity despite the high chemical complexity. The presence of 5 or more elements in comparable proportions increases the configurational entropy ($\geq$ 1.5 R) of these systems, and is the reason behind the “high entropy” based nomenclature [3, 6, 9, 24, 25]. Following is a list, portraying the multifunctional properties of few major subgroups of HEMs.

High entropy alloys (HEAs.) Most of the research on HEAs addresses their remarkable mechanical performance. For instance, HEAs are known for their excellent fracture toughness (above 200 $\mathrm{MPa{\cdot}m^{1/2}}$) with high yield strengths ($\sim$1 GPa), which place them on the top of Ashby plots for engineering materials [7]. Furthermore, superior fracture toughness even at low temperatures ($\sim$77 K) make HEAs potential materials for cryogenic applications [7]. On the other hand, several HEAs are known for high strength retention capability at elevated temperatures, which along with their slower diffusion aspect makes them a promising replacement for Ni based superalloys [47]. Apart from these, there are other properties, like lower thermal and electrical conductivity, high corrosion resistance, tailorable magnetism, etc., which make HEAs an important member of the multifunctional materials class [25, 48, 49].

High entropy nitrides (HENs). Soon after the discovery of HEAs, studies focusing on the deposition of HEN films were reported in 2004 [10]. HENs exhibit high hardness and good oxidation resistance properties, posing them as potential candidates for high temperature coatings [12, 50]. Most of the HENs are synthesized using physical vapor deposition techniques. Recently, HENs (comprising of V, Cr, Nb, Mo, Zr) were synthesized using a mechanochemical-assisted soft urea method resulting in mesoporous structures with extremely high surface area [21]. This flexibility in the synthesis technique motivates future research on the functional properties of HENs.

High entropy oxides (HEOs.) As discussed above, HEOs are a new class of oxides characterized by the presence of several equiatomic cations on a given lattice site. Classifications of HEOs can be done based on their crystal structure, composition and phase stability mechanism. In this dissertation a crystal structure based classification for HEOs is adopted, given the fact that several of the functional properties of oxides are structure dependent (see Chapter 3, 4 and 5), such as, transport properties, magnetic behavior, catalytic activity and electrochemical features [17, 18, 51–54]. Section 6.2 further highlights the recent developments in HEOs.

High entropy carbides (HECs.) Most of the investigations pertaining to HECs have been rather recent [11, 22, 55, 56]. Out of the HECs reported, some of them crystallize into a single phase solid solution, such as $(\mathrm{Hf_{0.2}Nb_{0.2}Ta_{0.2}Ti_{0.2}Zr_{0.2}})\mathrm{C}$ [22, 55]. HECs exhibit superior hardness of $\sim$40GPa, exceeding the hardness of the parent carbides. Thus, HECs can find applications as ultra-high temperature ceramics (UHTCs).[10]

---

[10] UTHCs are often classified as systems with melting temperatures above 3300 K.

High entropy borides (HEBs). Gild *et al.* [23] reported the possibility to form HEBs with hexagonal structure, e.g., $(Hf_{0.2}Zr_{0.2}Ta_{0.2}Mo_{0.2}Ti_{0.2})B_2$. Hardness and the oxidation resistance of the HEBs are found to be better than the parent borides, which present HEBs as viable alternatives for UTHCs [23, 57].

High entropy oxyfluoride (HEOFs). Very recently, the possibility to co-populate both the cation and anion sites of an ionic system by multiple elements was explored, resulting in a single phase rocksalt type HEOF, $Li_{0.5}(Co_{0.1}Ni_{0.1}Zn_{0.1}Mg_{0.1}Cu_{0.1})O_{0.5}F_{0.5}$ [58]. HEOF exhibits a reversible capacity of $\sim$130 mAhg^{-1} for 300 cycles with a working potential of 3.4 V vs. Li/Li$^+$, making it a suitable cathode material for lithium ion batteries (LIBs) [58].

Apart from the aforementioned systems, there are also reports on high entropy sulfides [53], intermetallics [59] and silicides [60], which are the youngest members of the HEM family.

3. Rocksalt type high entropy oxides

In the rocksalt crystal structure, the anions form a *fcc* lattice with all the octahedral sites occupied by the cations (Fig. 3.1). Thus, a rocksalt lattice can be represented as two inter-penetrating *fcc* sub-lattices, one of the anions and other of the cations, which are displaced by ½<100> or ½<111>, as shown in Fig. 3.1. The coordination number is 6 for both anions and cations. A schematic of a rocksalt lattice is shown in Fig. 3.1. Several divalent mono-cationic oxides, such as, MgO, CoO, NiO, CaO, etc., with cation to anion radius ratio (r_c/r_a) between 0.414 to 0.732 crystallize in the rocksalt structure (see Table. 2.1). The r_c/r_a in case of $(Co_{0.2}Cu_{0.2}Mg_{0.2}Ni_{0.2}Zn_{0.2})O$ is 0.58[1]. Thus, this HEO composition crystallizes in a rocksalt structure (R-HEO). In general, rocksalt type mono-cationic transition metal oxides (TMOs) like, NiO, CoO, FeO, etc., show interesting features, among which semiconducting, magnetic, catalytic and electrochemical properties are the most investigated ones [61–65]. Many of these properties have a direct correlation with the crystal structure. For instance, several rocksalt TMOs, especially NiO, CoO are well-known anodes for secondary lithium ion batteries (LIBs). The mechanism of Li reactivity in rocksalt type oxides

---

[1] r_c is the average radii of constituent cations at 2+ oxidation state in 6-fold coordination.

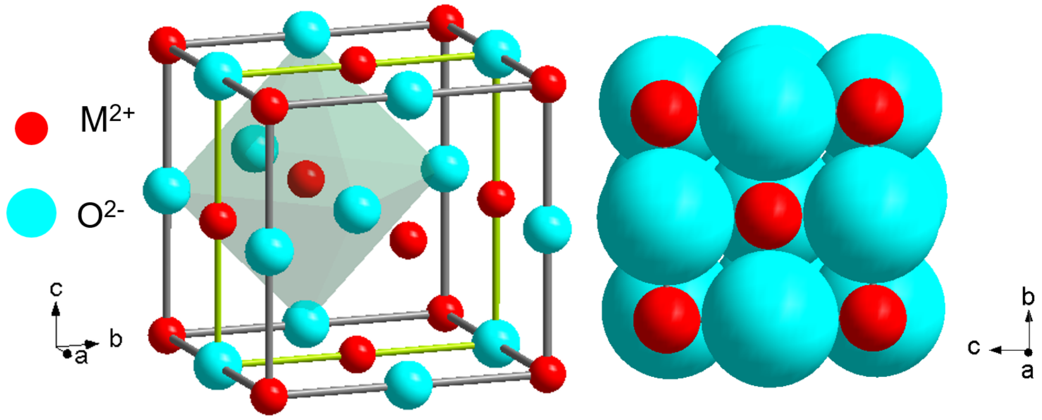

Figure 3.1.: Ball stick and space-filling model of an oxide with rocksalt structure, where the cations occupy the $4a$ (0,0,0) sites and anions occupy the $4b$ (½, ½,½) sites. Plane outlined with green sticks in (a) shows the other possible face centered cubic arrangement with oxygen on (0,0,0) sites.

differs from the classical Li insertion/de-insertion process[2] due to the closed packed nature of the lattice as depicted in Fig. 3.1b. Hence, a conversion type reaction mechanism is observed in these oxides, which involves the formation and decomposition of Li_2O, coupled with the reduction and oxidation of the constituent metals. Owing to this mechanism, high Li storage capacities (often above 700 mAh/g) can be achieved, as the overall redox reaction is a two-electron transfer process [65, 67, 68]. These interesting features of rocksalt TMOs motivate the investigation of R-HEOs, which is comprised of several transition metal cations.

In the initial studies [14, 17, 18] a solid-state technique was employed for the synthesis of microcrystalline R-HEOs. Particle size and morphology often affect the structure and properties of oxides. Hence, it was worthwhile to explore other routes for R-HEOs synthesis. The results presented in Section 3.1. deal with three different synthesis techniques for HEOs, each resulting in unique particle size and morphology.

Several studies have focused on the influence of crystallographic structures and microstructures on the functional features of R-HEOs, some of which are discussed below. Bérardan *et al.* [18] reported that R-HEOs exhibit colossal dielectric constants, which can be tailored by changing the fraction of the constituent elements, especially Cu. Cu in R-HEO is present in 2+ oxidation state, resulting in Jahn-Teller distortion [69, 70]. Thus, changing the concentration of Cu alters the local environment of Cu^{2+} ions from an octahedral to rhombic geometry [69], affecting the dielectric properties of R-HEOs. Chen *et al.* [71, 72] showed that R-HEOs can act as stable high temperature CO oxidation catalysts, which can be further improved by decreasing the particle size. Lower thermal conductivity compared to the constituent parent oxides was observed in R-HEOs [51]. This lowering of conductivity could be linked to the high disorder (entropy) in the R-HEOs, as the multiple constituent cations act as phonon scatterers [51]. Magnetic order can be observed in R-HEOs at temperatures below 120 K, where the Néel temperatures and magnetic ground states can be effectively tailored by changing the composition [73, 74]. Bérardan *et al.* reported high Li^+ (on the order of 10^{-3} S cm^{-1}) and Na^+ (on the order of 10^{-6} S cm^{-1}) conductivities in alkali doped R-HEOs. High Li^+ conductivity in rocksalt type TMOs is rather rare. Nonetheless in R-HEOs, it is hypothesized that ionic conduction occurs through the oxygen vacancies that are created as a result of charge compensation when monovalent elements (like Li^+ or Na^+) are doped in R-HEOs. It is known that high Li^+ diffusivity in the electrodes can also help to achieve higher energy density and better cyclability. Hence, this initial report on Li^+ conduction (which is linked to Li^+ diffusivity) in R-HEOs, along with the fact that the rocksalt type TMOs are promising anodes, provided the motivation to investigate R-HEOs as potential electrode materials for LIBs. This electrochemical aspect of R-HEOs is elucidated in Section 3.2.

---

[2] In systems like $LiMO_2$ (M=Co, Ni, Cr, Mn, etc.), the Li^+ and M^{3+} ions occupy alternate (111) planes of a rocksalt structure forming a rhombohedral structure with layered sequence of –O–Li–O–M–O– along the *c* axis. This kind of atomic arrangement allows stable insertion/extraction of Li^+ into/from the Li planes happening at potentials above 3.5 V (vs Li^+/Li). In addition, fast 2-D Li-ion diffusion through the MO_2 layer and good electronic conductivity makes these layered structures highly efficient cathodes for lithium ion batteries. Nevertheless, the capacities delivered are below 300 mAh/g (theoretically) because the effective number of electron transfer is always below 1. [66, 67]

3.1. Overview of publication I: Nanocrystalline multicomponent entropy stabilized transition metal oxides

The first publication of this dissertation is a comprehensive study focusing on the synthesis of HEOs by three different techniques: flame spray pyrolysis (FSP), nebulized spray pyrolysis (NSP) and reverse co-precipitation (RCP).[3] An identical precursor preparation technique, i.e., dissolution of the nitrate salts of the constituent metals in aqueous solution, was used for comparing these three synthesis methods. FSP is an aerosol based synthesis technique, where the mist of the precursor solution is carried on to a flame ($T > 1500\,^{\circ}C$). The decomposition reaction happens in the flame. All the reactions occur in the course of 0.01 s and the products so formed undergo a rapid quenching on the order of 10^4 °C s^{-1}. As a result of the short residence time and rapid quenching, the average particle size of the resulting powder was in the range of 10 nm. However, due to the short reaction time, single phase R-HEO could not be obtained directly after FSP. Subsequent heat treatment at 1000 °C for an hour was required to achieve a single phase. Akin to FSP, NSP is also an aerosol based synthesis process. However, the mist of the precursor solution is carried through a hot wall reactor (maintained at a specific temperature) instead of the flame. The precursor residence time in NSP is $\sim$0.15 s. Hence, a single phase R-HEO could be directly synthesized during the pyrolysis in the hot wall reactor at 1150 °C. The particles obtained from NSP had hollow spherical morphology consisting of nanocrystallites. Unlike FSP and NSP, RCP is a wet chemistry based approach in which the mildly acidic precursor solution is precipitated by adding it into basic NH_4OH solution. The pH of 10 was strictly maintained throughout the reaction.[4] The precipitates so formed were initially dried at 120 °C and then calcined at 1000 °C for 1 hour. Single phase R-HEO with highly agglomerated particles were synthesized. Among the aforementioned techniques, NSP was found to be the most suitable one for lab scale synthesis of HEOs, given the fact that it's a quick single step process, which can yield particles comprised of nanocrystallites.

Entropy-mediated phase stabilization effects were also studied by (i) comparing R-HEOs with 4 cationic rocksalt medium-entropy oxides (R-MEOs) and (ii) conducting cyclic heat treatments at lower and higher temperatures. Cu was eliminated from $(Co_{0.2}Cu_{0.2}Mg_{0.2}Ni_{0.2}Zn_{0.2})O$ in order to make a 4 cation MEO. Removal of the Cu leads to two opposing effects. On one hand it decreases the configurational entropy of the system, thus decreasing the tendency to form single-phase rocksalt structure. On the other hand, Cu is one of those elements which induces an additional enthalpy penalty arising from the Jahn-Teller effect of Cu^{2+}. Consequently, its elimination will favor the formation of phase-pure R-HEO. In reality, a higher temperature, compared to R-HEO, was required for the synthesis of phase pure R-MEO without Cu, which implies a dominating role of entropy over enthalpy. In addition for R-HEOs, a reversible transformation from single phase to multiple phases upon cyclic heat treatments was observed independent of the synthesis technique

---

[3] Refer to Experimental techniques, A.1. for detail.

[4] Further studies have shown that maintaining the pH is very critical to obtain R-HEOs in proper stoichiometry, as higher pH often leads to dissolution of the precipitate back into the solution. Now, pH of 9 has been found as an optimum providing more consistent results.

used.[5] This further strengthens the entropy-mediated phase stabilization hypothesis in R-HEOs.

3.2. Overview of publication II: High entropy oxides for reversible energy storage

This article explores the potential of R-HEOs as electrode materials for lithium ion batteries (LIBs). Half cells with R-HEO, $(Co_{0.2}Cu_{0.2}Mg_{0.2}Ni_{0.2}Zn_{0.2})O$, as the working electrode and Li-metal as the counter electrode were prepared. The cells were galvanostatically cycled in a potential window of 0.01 V − 3 V. R-HEOs exhibited long-term cycling stability (over 500 cycles) with specific capacity above 600 mAh/g and Coulombic efficiency >99.5% when cycled at a specific current of 200 mA/g. Furthermore, good rate capability behavior with (almost) complete capacity recovery even after cycling at high specific currents (3000 mA/g) was observed. These results are indeed promising given the fact that the average particle size of the R-HEOs used was in the micrometer range. Cyclic voltammetry (CV) depicted that most of the electrochemical reactions in R-HEOs take place at potentials below 1 V (vs Li^+/Li) posing their possible use as anodes in a full cell.

Although the R-HEOs show specific capacities similar to binary TMOs (like CoO, NiO, etc.), the cyclic stability is substantially enhanced. One possible reason for this cyclic stability can be the synergistic effect arising from the presence of several cations in R-HEOs. Hence, to investigate the role of specific elements, several 4 cationic rocksalt type medium entropy oxides (R-MEOs) were studied. R-MEOs exhibited very different electrochemical behavior compared to R-HEOs. For instance, in R-MEO without Cu the initial discharge potential is significantly lower, while R-MEO without Zn results in a very different redox behavior (as can be observed from cyclic voltammetry). However, none of the R-MEOs exhibited a stable cyclic performance like R-HEOs and started degrading even before 50 cycles. This finding hints towards a dominant effect of entropy (or synergy) on the electrochemical characteristics of R-HEO.

Furthermore, what makes the R-HEOs unique is the unconventional redox reaction mechanism. In a typical conversion type oxide electrode (like CoO, NiO, etc.), lithiation steps involve the disruption of the oxide structure to the form Li_2O and corresponding metals (nanoparticles). Hence, by the end of a lithiation step the initial oxide structure is fully disintegrated. However in case of R-HEO, the presence of a R-HEO type structure even after the lithiation step was observed, and in fact could be identified even after several cycles. This means that a complete conversion of R-HEOs into the respective metals never happened during the lithiation steps. Hence, it is hypothesized that only a part of the cations present in R-HEOs participate in the redox reaction while the unreacted cations form a R-HEO type "host" structure which is preserved during the complete cycling process. The retention of the host structure facilitates a stable cycling behavior, as those metal cations which react during lithiation can be reintegrated into this host structure upon delithiation. The stability of the "host" structure can be related to the fact that the initial R-HEO structure is entropy-stabilized and is consistent with the observation that R-HEOs show

---

[5] See Section 2.2.5. for further information on entropy driven phase transformation.

better cyclic stability than R-MEOs. Hence, it can be concluded that entropy-mediated structural stabilization possibly plays an important role in achieving a stable cyclic performance of R-HEOs.

These aforementioned results[54], i.e, the high capacity retention capability and entropy-mediated partial conversion based reaction mechanism, provided the motivation for further investigation of HEOs as a battery material. Recently, it was reported [75] that the electrochemical performance of R-HEOs can be further enhanced to specific capacities above 1000 mAh/g for over 300 cycles by decreasing the particle size. In addition, the report [75] also supported the partial conversion based reaction mechanism and the retention of the rocksalt type host structure upon cycling. Subsequently, we reported on the practical application of R-HEO as an anode in a full cell LIB using $LiNi_{1/3}Co_{1/3}Mn_{1/3}O_2$ as cathode. Coin type full cells were found to deliver an initial specific discharge capacity of 446 mAh/g, while specific capacity around 250 mAh/g could be maintained even after 100 cycles [76]. Finally, a pouch type full cell with a total capacity of 2.5 mAh was assembled and used as a power source for lighting up 32 LEDs (Fig. 3.2).

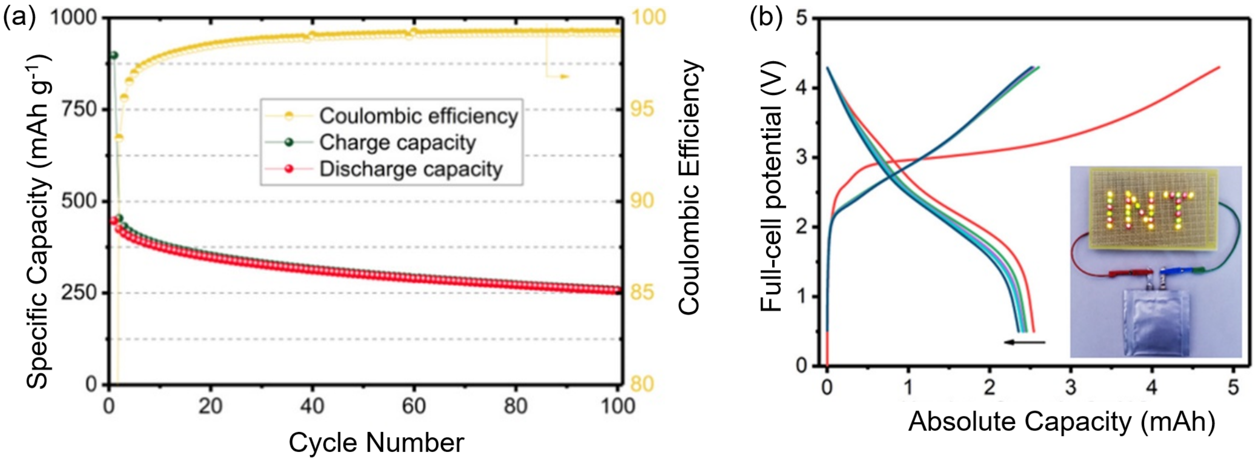

Figure 3.2.: (a) Capacity retention capability of NCM//R-HEO full-cells in the voltage range of 0.5–4.5V at a specific current of 120 mA g^{-1}. (b) Charge/discharge profiles of a pouch type full cell. The inset shows an array of LEDs powered by the pouch cell. [76] ©2019, ELSEVIER

Statement of personal contribution

1. **Nanocrystalline multicomponent entropy stabilised transition metal oxides**
   A. Sarkar, R. Djenadic, N.J. Usharani, K.P. Sanghvi, V.S.K. Chakravadhanula, A.S. Gandhi, H. Hahn, S.S. Bhattacharya, *Journal of the European Ceramic Society*, 37, 747 (2017)
   Reprinted with permission from *Journal of the European Ceramic Society*, ©2017, ELSEVIER.

   The experiments were planned by myself under the guidance of Prof. S.S. Bhattacharya, Prof. A.S. Gandhi and Prof. H. Hahn. The synthesis, characterization (except for TEM) and related analysis were performed by myself. Dr. R. Djenadic, N.J. Usharani and K.P. Sanghvi supported the synthesis effort. Dr. V.S.K. Chakravadhanula performed the TEM measurements and analysis. The manuscript was written by myself with feedback from Dr. R. Djenadic, Prof. A.S. Gandhi, Prof. H. Hahn and Prof. S.S. Bhattacharya.

2. **High entropy oxides for reversible energy storage**,
   A. Sarkar, L. Velasco, D. Wang, Q. Wang, G. Talasila, L. de Biasi, C. Kübel, T. Brezesinski, S. S. Bhattacharya, H. Hahn and B. Breitung, *Nature Communications*, 9, 3400 (2018)
   Reprinted under the terms of the CC BY 4.0 license.

   Dr. B. Breitung and Prof. H. Hahn supervised the project. The experiments were planned by myself under the guidance of Dr. B. Breitung and Prof. H. Hahn. The synthesis of the materials, fabrication of the electrodes, characterization (except for TEM and *operando* XRD) and the data analysis were performed by myself. Dr. D. Wang performed the TEM measurements and analysis, with assistance from Dr. L. Velasco and Prof. C. Kübel. Dr. Q. Wang supported the fabrication of the electrodes with higher loading. Prof. S.S. Bhattacharya and G. Talasila supported the synthesis efforts and were involved in several scientific discussions. Dr. L. de Biasi performed and analyzed *operando* XRD measurements under the supervision of Dr. T. Brezesinski. The manuscript was written by myself with corrections from Dr. B. Breitung, Dr. T. Brezesinski and Prof. H. Hahn. All the co-authors commented on the manuscript.

Journal of the European Ceramic Society 37 (2017) 747–754

Contents lists available at www.sciencedirect.com

Journal of the European Ceramic Society

journal homepage: www.elsevier.com/locate/jeurceramsoc

Nanocrystalline multicomponent entropy stabilised transition metal oxides

Abhishek Sarkar[a,b,*], Ruzica Djenadic[c,d], Nandhini J. Usharani[b], Kevin P. Sanghvi[b], Venkata S.K. Chakravadhanula[a,c,e], Ashutosh S. Gandhi[f], Horst Hahn[a,c,d], Subramshu S. Bhattacharya[b,**]

[a] Institute of Nanotechnology, Karlsruhe Institute of Technology, Hermann-von-Helmholtz-Platz 1, 76344 Eggenstein-Leopoldshafen, Germany
[b] Indian Institute of Technology Madras, Chennai-600036, India
[c] Electrochemical Energy Storage, Helmholtz Institute Ulm, Helmholtzstraße 11, 89081 Ulm, Germany
[d] Joint Research Laboratory Nanomaterials — Technische Universität Darmstadt & Karlsruhe Institute of Technology, Alarich-Weiss-Str. 2, 64287 Darmstadt, Germany
[e] Karlsruhe Nano Micro Facility, Karlsruhe Institute of Technology, 76344 Eggenstein-Leopoldshafen, Germany
[f] Indian Institute of Technology Bombay, Powai, Mumbai-400076, India

ARTICLE INFO

Article history:
Received 3 August 2016
Received in revised form
14 September 2016
Accepted 19 September 2016
Available online 21 September 2016

Keywords:
Spray pyrolysis
Reverse co-precipitation
Structural properties
Entropy stabilisation
Nanocrystalline

ABSTRACT

Multicomponent entropy stabilised oxides containing four and five metal elements in equiatomic amounts were successfully synthesised in nanocrystalline form by nebulised spray pyrolysis (NSP), flame spray pyrolysis (FSP) and reverse co-precipitation (RCP) techniques, demonstrating that entropy stabilisation of these recently discovered materials is independent of the synthesis method. Both 4- and 5-cationic systems, (Co,Mg,Ni,Zn)O and (Co,Cu,Mg,Ni,Zn)O, can be stabilised into a single rocksalt structure directly only using NSP, while in FSP and RCP, stabilisation can be achieved after thermal treatment. This result indicates, that in 5-cationic NSP system configurational entropy is high enough to directly stabilise single rocksalt phase at lower temperature, while higher synthesis temperature is required to compensate the lower configurational entropy in 4-cationic system. Retention of single-phase at room temperature indicates sluggish diffusion kinetics, making entropy stabilised phases quenchable.

1. Introduction

In the era of material development, there is a constant and interminable quest for new materials. Several doped oxides and binary/ternary oxide ceramic compounds have been thoroughly studied, and as a result, a large potential for applications in the field of electronics as transistors, transparent conductors and sensors has been identified [1–5]. However, till date only a few studies have been reported on oxide ceramics having multiple transition metal (TM) elements in equimolar or near-equimolar ratios [6–8], the so called entropy stabilised oxides (ESOs). On the other hand, the near-equimolar metallic alloy systems commonly called high entropy alloys (HEAs) [9], are well-known, where the primary basis is the stabilisation of the crystalline phase by high configurational entropy. The HEAs have been a sought-after topic for research in the recent years owing to their augmented properties [10,11] when compared to conventional alloys with one or two principal elements. These systems also open the prospects not only for improved properties but also for studying the mid-range of the multicomponent phase diagrams [9], which in the earlier cases were limited to the apex of the diagrams as only one or two principal elemental alloys were studied. While high entropy carbide and nitride systems have been investigated [12–14], high-entropy oxide (HEO) based ceramic systems were not synthesised until recently. Rost et al. [6] successfully synthesised a multicomponent oxide system consisting of five elements (Co, Cu, Mg, Ni, and Zn). The authors demonstrated that an oxide system can be entropy stabilised into a single-phase structure (rocksalt, in this case). High entropy oxides can be very well considered to be equivalent to HEAs in terms of the configurational entropy calculations [9]. An oxide phase has two different kinds of sublattices: the oxygen sublattice and the cation sublattice(s). In case of HEO it is anticipated that only the cation

---

* Corresponding author at: Institute of Nanotechnology, Karlsruhe Intitute of Technology, 76344 Eggenstein-Leopoldshafen, Germany.
** Corresponding author at: Indian Institute of Technology Madras, Chennai-600036, India.
E-mail addresses: abhishek.sarkar@kit.edu (A. Sarkar), ssb@iitm.ac.in (S.S. Bhattacharya).

http://dx.doi.org/10.1016/j.jeurceramsoc.2016.09.018
0955-2219/© 2016 Elsevier Ltd. All rights reserved.

sublattice is altered and the oxygen sublattice is still only occupied by oxygen. Hence, the configurational entropy contribution of oxygen sublattice would remain zero and the entire configurational entropy of the system can be considered to be solely dependent on the cation sublattice. If a large number of cation species are randomly distributed in the cation sublattice, the configuration entropy would be significant. Due to the similarities with HEA, it is anticipated that HEOs would be enriched with novel properties like their metallic analogues owing to the synergising effect of the multiple elements present in equivalent amounts. Two recent studies by Bérardan et al. [7,8] showed that these new group of materials have interesting properties which can make them a strong contender in the field of energy. Besides "colossal dielectric constant" found in the (Co,Cu,Mg,Ni,Zn)O system [7], the study [8] also showed that the room temperature Li ion conductivity in Li-doped (Co,Cu,Mg,Ni,Zn)O is several orders of magnitude higher than the contemporary solid electrolyte (LiPON [15]) and are comparable to those attained in liquid electrolytes [16].

The present study deals with the possibility to synthesise the transition metal high entropy oxides (TM-HEOs) in the nanocrystalline form by several methods other than solid state techniques reported earlier [6,7]. The effects of different synthesis techniques on the crystal structure, elemental composition and particle morphology are analysed. Emphasis was placed on obtaining nanocrystalline transition metal HEOs as it is well-known that nanocrystalline materials can exhibit novel properties considerably different from their micron-sized counterparts. Based on the premise of wide range of functional properties (like magnetic, electronic, catalytic and mechanical) [4] related to the *d*-electron effect, two multicomponent oxide combinations containing transition metal ions were chosen for this study: (Co,Mg,Ni,Zn)O and (Co,Cu,Mg,Ni,Zn)O. The TM-HEO nanopowders were synthesised by two spray pyrolysis techniques – flame spray pyrolysis (FSP) and nebulised spray pyrolysis (NSP), and a wet-chemical technique – reverse co-precipitation (RCP). The approaches used here are known for their potential in the successful production of homogenous nanocrystalline oxides [17–19]. The techniques were selected such that FSP and NSP are rapid processes with short precursor/particle residence times, while RCP is a slower process with enough time for diffusion, which would additionally help in understanding the effect of reaction time on the phase composition, structure and morphology of the synthesised powders. Further, FSP and NSP being relatively faster processes not only reduce the synthesis time significantly but also enable stabilisation of metastable phases [20,21] due to their rapid quenching effect (fast cooling rates). Additionally, these processes have higher potential for industrial application compared to solid-state reaction technique in terms of production rate [6]. Reverse co-precipitation, on the other hand, was chosen over classical co-precipitation [22,23] because it has a greater potential in the production of homogeneous single-phase multicomponent systems as the pH is maintained constant throughout the process, and all the cations can be precipitated simultaneously into a mixed hydroxide.

Certain criteria were applied for the choice of the cations following Rost et al. [6]: (i) similar cationic radii at a specific oxidation state and co-ordination number; this approach is complementary to the Hume-Rothery rules [24,25] for metallic systems, which was followed in order to minimise distortion and strain effects that ensure complete miscibility in a single-phase, (ii) all the selected oxide systems should not have the same crystal structure; if all the oxides would have similar crystal structures then there would be a high probability that the multicomponent system will end up in a single-phase structure same as that of the individual oxides, and (iii) at least one binary oxide pair should not be miscible at 0.5 mol fraction. This information was obtained from available oxide pseudo-binary phase diagrams [26,27]. The last criterion uses the same analogy as the second mentioned earlier as otherwise it is quite natural for systems with complete miscibility in their binary phase diagrams to end-up as single-phase structures in multicomponent combinations. Table 1 gives an overview of the crystal structures, space groups, oxidation states, co-ordination numbers and corresponding cationic radii of the individual oxides used in this study.

Table 1
Crystal structures, space group (SG) [28], oxidation state, co-ordination number (CN) and corresponding cationic radii (r_c) [29].

Oxide	Structure	Space group (number)	Oxidation	CN	r_c [nm]
CoO	Rocksalt	$Fm\bar{3}m$ (225)	2+	VI	0.65[a]
CuO	Tenorite	$C12/c1$ (15)	2+	VI	0.73
MgO	Rocksalt	$Fm\bar{3}m$ (225)	2+	VI	0.72
NiO	Rocksalt	$Fm\bar{3}m$ (225)	2+	VI	0.69
ZnO	Wurtzite	$P6_3mc$ (186)	2+	IV	0.60
ZnO[b]	Rocksalt	$Fm\bar{3}m$ (225)	2+	VI	0.74

[a] Low spin.
[b] The rocksalt structure is only observed at high pressures (>9 GPa, [30]).

2. Experimental

2.1. Material synthesis

Two HEO systems (Co,Cu,Mg,Ni,Zn)O and (Co,Mg,Ni,Zn)O, where the elements are listed alphabetically for easy nomenclature, were synthesised using nitrates of the individual metals ($Co(NO_3)_2{\cdot}6H_2O$ (Sigma Aldrich, 99.9%), $Cu(NO_3)_2{\cdot}2.5H_2O$ (Sigma Aldrich, 99.9%), $Mg(NO_3)_2{\cdot}6H_2O$ (Sigma Aldrich, 99.9%), $Ni(NO_3)_2{\cdot}6H_2O$ (Sigma Aldrich, 99.9%), and $Zn(NO_3)_2{\cdot}6H_2O$ (Alfa Aesar, 99.9%)) in the stoichiometric amounts in all three synthesis methods due to their high aqueous solubility. The total concentration of the aqueous solution was a synthesis/process dependent parameter used to enhance the rate of powder production. It will be specified in each synthesis procedure that was adopted.

2.1.1. Flame spray pyrolysis process

The total concentration of the precursor solution was 1 mol l^{-1} and was higher compared to NSP and RCP owing to its lower production rate (80–100 mg h^{-1} in the laboratory type reactor used). The FSP experimental setup is described in detail elsewhere [18,31]. The precursor solution was nebulised within a compressed air nebuliser and the mist formed was carried to the flame by oxygen as the carrier gas (5 standard l min^{-1}). Liquefied petroleum gas (0.04 standard l min^{-1}) and oxygen (20 standard l min^{-1}) were used as fuel and oxidiser for the flame, respectively. The gas flow rates were controlled by means of mass flow controllers. Thermal decomposition/pyrolysis reactions took place in the flame. The residence time of the particles formed in the flame was very short (typically, around 0.01 s [32]), leading to rapid heating as well as quenching. As a result, powders with very fine crystallite sizes were obtained. The formed particles were collected in a filter-based collection unit connected to a vacuum pump.

2.1.2. Nebulised spray pyrolysis process

The total concentration of the aqueous precursor solutions for NSP synthesis was 0.1 mol l^{-1}. The experimental setup is described in detail elsewhere [33]. The precursor solution was continuously delivered into the nebuliser at a rate of ~120 ml h^{-1}. The mist containing fine droplets of the precursor solution was formed by an ultrasonic nebuliser, which was transported by flowing oxygen (5 standard l min^{-1}) into the hot-wall reactor, where nanoparticles were formed at a temperature of 1150 °C and a total pressure of 900 mbar. One of the systems, (Co,Mg,Ni,Zn)O, was also synthesised at 1250 °C in order to study influence of temperature on phase composition. The (Co,Mg,Ni,Zn)O powders synthesised at 1150 °C and 1250 °C are designated as NSP1150 and NSP1250, respectively. The powders were collected using a filter-based collector maintained at 100 °C in order to prevent water vapour condensation on the deposited powders. This well-established method facilitated direct synthesis of nanocrystalline powders with a high production rate of 1–2 g h^{-1} in the laboratory type reactor with homogeneous distribution of the elements in the nanoparticles. The residence time of the particles in the NSP hot-wall reactor was calculated to be around 0.15 s, which is slightly longer than in FSP (0.01 s) but much shorter than in RCP (residence time at least $3.6 \cdot 10^3$ s). Additionally, NSP method is a very flexible technique in terms of precursors that can be used as well particle morphologies that can be formed [34].

2.1.3. *Reverse co-precipitation process*

The concentration of the precursor solution in the RCP process was same as that in the NSP, 0.1 mol l^{-1}. A base solution with initial pH 10 was prepared by adding 25 ml of ammonia (NH_3, Merck, 25%) in 200 ml of deionised water. The precursor solution was added to the ammonia solution in a controlled fashion along with continuous stirring of the mixture at ambient conditions. Ammonia solution was added externally to the mixture at regular intervals in order to maintain the pH level at 10. After filtering, the precipitate was dried at 120 °C for 4 h and lightly ground in an agate mortar and finally calcined at 1000 °C for 1 h to obtain desired crystalline oxide phase. The pH, rate of addition of precursors' solution into the base and temperature of calcination were the factors affecting the crystal structure, morphology and crystallite size of the powder synthesised by RCP.

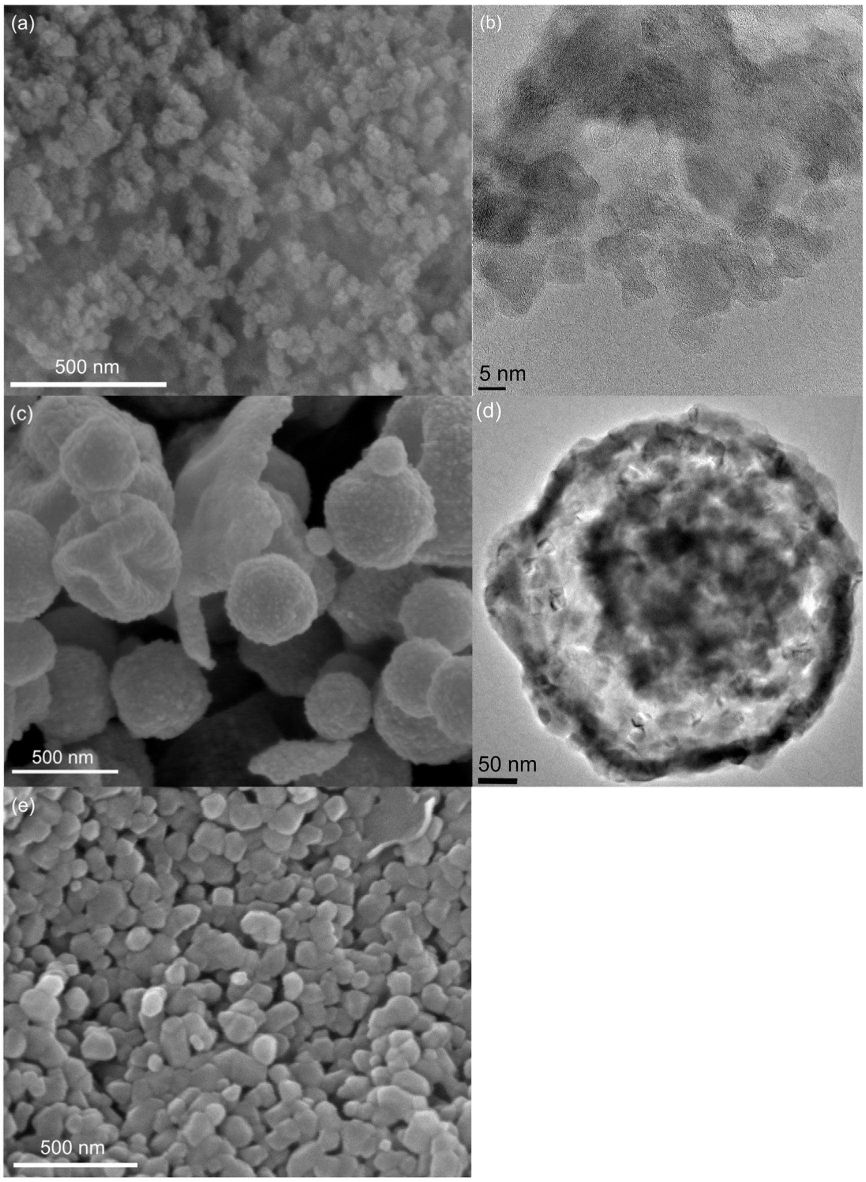

Fig. 1. SEM (left) and TEM (right) micrographs of (Co,Cu,Mg,Ni,Zn)O powder synthesised via FSP (a, b), NSP (c, d), and RCP (e).

2.2. Characterization

Room temperature X-ray diffraction (XRD) patterns of the as-synthesised powders were recorded using a Bruker D8 diffractometer with Bragg-Brentano geometry using Cu-Kα radiation with a Ni filter and a LYNEXE detector having a fixed divergence slit (0.3°). A step size of 0.02° and a collection time of 4 s at 30 kV and 40 mA over the diffraction angle (2θ) range between 10° and 90° were used. Rietveld analysis (TOPAS 3, Bruker [35]) of the XRD patterns was performed to determine the structure and phase composition of the as-synthesised and thermally treated powders using the structural file of NiO ($Fm\bar{3}m$, ICSD 9866) that was modified according to the number and the type of elements present in the refined system. The instrumental intensity distribution for the XRD data was determined using a reference scan of LaB_6 (NIST 660a). Thermal displacement parameters were constrained to be the same for all atoms.

The microstructure of the FSP and NSP powders was studied using a high-resolution scanning electron microscope, SEM (Philips XL30 FEG) and high resolution aberration (image) corrected Titan 80–300 transmission electron microscope, TEM (FEI, Eindhoven, the Netherlands) equipped with a Gatan US4000 slow scan CCD camera (Gatan Inc., Pleasanton, CA).

The elemental composition was determined using energy dispersive spectroscopy (EDS) with an accelerating voltage of 20 keV on a scanning electron microscope, SEM (ZEISS Gemini Leo 1530) equipped with INCA EDS X-Ray spectrometer.

3. Results and discussions

3.1. Microstructure and elemental composition of the synthesised powders

Fig. 1 shows the SEM and TEM images of (Co,Cu,Mg,Ni,Zn)O system synthesised using different techniques. This composition was selected for comparing powder morphology obtained from different synthesis techniques. The FSP powder had very fine particles (Fig. 1a) hence were not clearly resolved in SEM images. Further TEM analysis (Fig. 1b) confirmed the presence of spherical as well as cuboidal particles of around 10 nm in size. Spherical morphology wherein the fine nanoparticles were aggregated in shape of hollow spheres (Fig. 1c and d) with a broad particle size distribution (from few nanometres to few micrometres) was observed for the powder synthesised by the NSP process. The RCP method produced larger dense agglomerated particles with (Fig. 1e) with particle size ranging from 50 nm to 150 nm. As the particles were distinctly identified by SEM imaging, TEM imaging was not performed on the powders synthesised by this technique.

Elemental analysis by EDS of the synthesised (Co,Cu,Mg,Ni,Zn)O powders, Table 2, confirmed that in all samples the elements were present in near equiatomic amounts.

Table 2
Cationic composition (at.%) of the synthesised (Co,Mg,Ni,Zn)O (Co,Cu,Mg,Ni,Zn)O powders based on EDS analysis.

System	Synthesis	Co	Cu	Mg	Ni	Zn
(Co,Mg,Ni,Zn)O	FSP	11.6	–	11.2	11.2	11.0
	NSP1150	11.0	–	11.5	10.6	12.5
	NSP1250	11.0	–	12.0	10.7	11.3
	RCP	10.1	–	11.2	10.0	9.7
(Co,Cu,Mg,Ni,Zn)O	FSP	10.1	11.4	11.1	10.7	9.2
	NSP	10.9	10.9	11.3	11.3	11.0
	RCP	12.5	11.5	12.3	12.3	11.3

3.2. Structure and phase composition of the synthesised powders

Fig. 2 displays the XRD patterns of (Co,Cu,Mg,Ni,Zn)O and (Co,Mg,Ni,Zn)O synthesised by the NSP, FSP and RCP techniques. The results obtained for both systems are similar. Asymmetric XRD peaks were observed in case of both powders synthesised by the FSP method. The reason for the asymmetry was the convolution of peaks from two rocksalt ($Fm\bar{3}m$) phases with lattice parameters close to each other and similar compositions, which was confirmed by Rietveld analysis of the XRD patterns (Fig. 3a). The observed distribution of lattice parameters was most likely related to the presence of a temperature gradient in the flame that led to the formation of two rocksalt phases with similar lattice parameters: one within the higher temperature zone (inner core of the flame) and the other from the lower temperature zone (outer shell of the flame). Besides distribution of lattice parameter, the distribution of crystallite sizes was present as well (10±2–73±32 nm). Additionally, the XRD pattern of FSP powders showed a peak at about 33° which could not be unambiguously identified or assigned to any of the known compounds that could be formed by the elements used in the synthesis and available in the Inorganic Crystal Structure Database (ICSD).

The XRD patterns of the 5-cationic (Co,Cu,Mg,Ni,Zn)O powder synthesised via NSP showed symmetric and broad peaks (Fig. 2a). Rietveld analysis revealed that the powder crystallised into a single rocksalt structure (Fig. 3b). As the NSP process had a longer particle residence time (around 0.1 s [36]) in the reactor (longer reaction zone, lower oxygen flow) than FSP, the ions had more time for diffusion and thus, the obtained powder was homogeneous in structure unlike in the case of FSP. However, it is noteworthy that even though the NSP process had a longer residence time compared to FSP it was still short enough for avoiding excessive growth, leading to the formation of nanocrystalline HEO powders with crystallite sizes of around 40 nm. While the 5-cationic (Co,Cu,Mg,Ni,Zn)O system, crystallised into a single-phase structure, the 4-cationic (Co,Mg,Ni,Zn)O (NSP1150) system additionally showed the presence of wurtzite ($P6_3mc$) phase (2.51 wt.%), Fig. 2b.

Rietveld refinement of the powder synthesised at higher temperature (NSP1250) (Fig. 3c) showed that the increase in the synthesis temperature from 1150 °C to 1250 °C led to the formation of single-phase rocksalt structure even in the 4-cationic (Co,Mg,Ni,Zn)O (NSP1250) system. The indication is that higher temperature is required for the 4-component material to become single phase as the configurational entropy is less than 5-component system. Therefore, our observation is in agreement with the results published by Rost et al. [6] as the entropy factor dominates over the enthalpy factor at higher temperatures. It should also be noted that the absence of Cu^{2+}, which in oxide form has tenorite structure (see Table 1), from the (Co,Mg,Ni,Zn)O system did not aid the stabilisation of the rocksalt structure. Crystallisation of the system containing Cu^{2+} into a rocksalt structure is probably an endothermic process due to the strong Jahn-Teller effect associated with Cu^{2+} [37,38]. It should therefore be easier for a system without Cu to crystallise in rocksalt structure. However, we observed that higher temperature was required for (Co,Mg,Ni,Zn)O system to crystallise in a phase-pure rocksalt structure than the Cu-containing 5-cationic system. The dominant role of configurational entropy is highlighted by these considerations. In case of the 5-cationic (Co,Cu,Mg,Ni,Zn)O system the configurational entropy is $1.61 \cdot R$ and in case of the 4-cationic (Co,Mg,Ni,Zn)O system the configurational entropy is $\sim 1.39 \cdot R$ (where R is the universal gas constant) [9]. Hence, higher temperature was required so that the overall $T\Delta S$ factor in Gibb's free energy relation ($\Delta G = \Delta H - T\Delta S$) increased in order to compensate for the decrease in the configurational entropy of the 4-component system. This confirms that

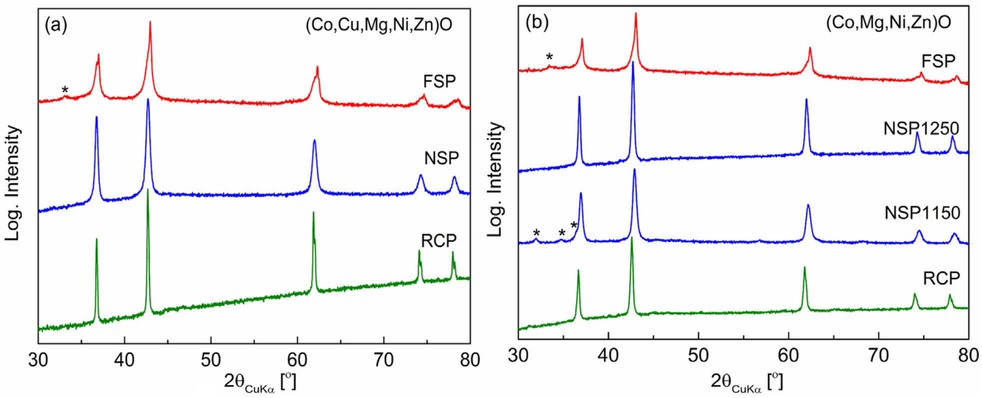

Fig. 2. XRD patterns of (a) (Co,Cu,Mg,Ni,Zn)O and (b) (Co,Mg,Ni,Zn)O powders synthesised using FSP, NSP and RCP (* secondary phase: FSP – unknown; NSP1150 – wurtzite).

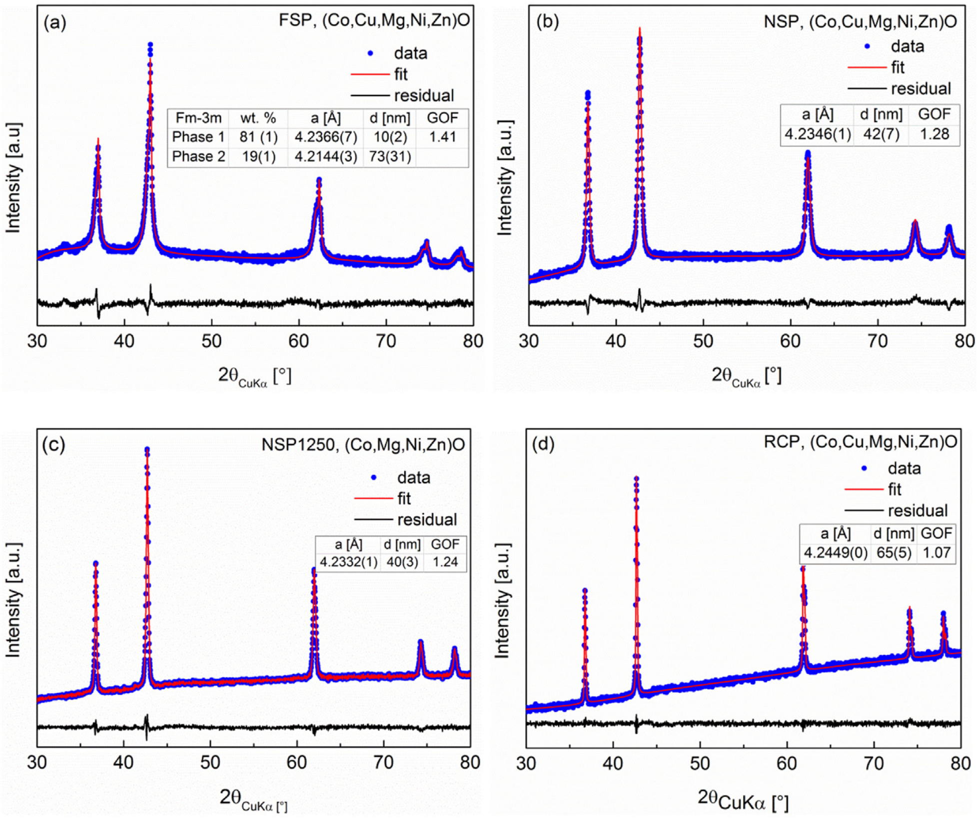

Fm-3m	wt. %	a [Å]	d [nm]	GOF
Phase 1	81 (1)	4.2366(7)	10(2)	1.41
Phase 2	19(1)	4.2144(3)	73(31)	

a [Å]	d [nm]	GOF
4.2346(1)	42(7)	1.28

a [Å]	d [nm]	GOF
4.2332(1)	40(3)	1.24

a [Å]	d [nm]	GOF
4.2449(0)	65(5)	1.07

Fig. 3. XRD patterns together with Rietveld fits of selected multicomponent oxide powders relevant for discussion: (a) FSP (Co,Cu,Mg,Ni,Zn)O powder showing presence of two rocksalt phases with similar lattice parameters, (b) NSP (Co,Cu,Mg,Ni,Zn)O powder showing presence of a single rocksalt phase, (c) NSP1250 (Co,Mg,Ni,Zn)O powder showing temperature effect on stabilisation of rocksalt structure, and (d) RCP (Co,Cu,Mg,Ni,Zn)O powder showing single-phase rocksalt structure indicating presence of additional factor besides configurational entropy (here thermal treatment, i.e., temperature and time) responsible for the structural stabilisation. The tables inside of the images give an overview of lattice parameters (*a*), crystallite size (*d*) and goodness of fit (GOF) for studied samples. The values in the parentheses represent errors in *a* and *d*.

even 4-component systems can be stabilised as a single-phase by configuration entropy but at higher temperatures.

Rietveld analysis of the XRD patterns of the RCP powders (Fig. 3d, only 5-cationic system shown) revealed that the both 5- and 4-cationic systems crystallised into a single rocksalt phase with an average crystallite size of 65 nm. The RCP technique required a calcination step to obtain the desired crystalline phase (see Section 2.1) and hence, the system got sufficient time for the diffusion of cations to desired positions in the rocksalt lattice. Therefore, formation of single-phase in both 5- and 4-cationic systems was achieved via RCP owing to its longer time for diffusion and homogenisation, although from the configurational entropy point of view, the 4-cationic system should not have formed a single-phase (see above discussion for NSP1250 system). This confirmed that not only configurational entropy but also temperature and time for diffusion played a role in single-phase formation. It is also to be noted that

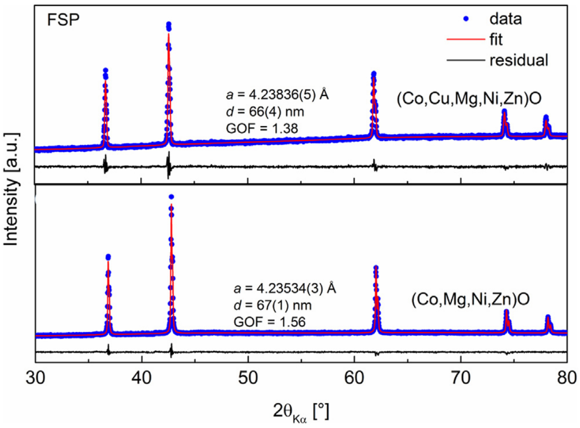

Fig. 4. XRD pattern along with Rietveld refinement for FSP powders annealed at 1000 °C/1 h. The values inside of the images give an overview of lattice parameters (*a*), crystallite size (*d*) and goodness of fit (GOF) for studied samples. The values in the parentheses represent errors in *a* and *d*.

irrespective of the synthesis technique the actual lattice parameter, *a* (see data given in Fig. 3d) for both systems were in good agreement with the theoretical lattice parameter, a_t calculated by Vegard's law [39] based on the data [40] available for the studied systems (a_t = 4.235 Å for (Co,Cu,Mg,Ni,Zn)O and a_t = 4.233 Å for (Co,Mg,Ni,Zn)O). This indicated that the system followed the ideal rule of mixing, similar to random solid solutions wherein all the cations are randomly distributed in the rocksalt lattice positions. This was additionally supported by the observation that the FSP powders (4- and 5-cationic) which had two rocksalt phases in the as-synthesised form (Fig. 3) crystallised into a single-phase after annealing at 1000 °C for 1 h (Fig. 4). The asymmetries in the peaks that had been observed in the as-synthesised powders were no longer present, and Rietveld refinement (Fig. 4) yielded a good fit confirming presence of nanocrystalline single rocksalt phase. The obtained crystallite sizes were 67±1 nm and 66±4 nm for the (Co,Mg,Ni,Zn)O and (Co,Cu,Mg,Ni,Zn)O systems, respectively.

The confirmation of configurational entropy effect on phase stabilisation was studied on the (Co,Cu,Mg,Ni,Zn) composition. Phase pure powders were selected as starting material for this study, i.e. the calcined FSP and RCP powders and the as-synthesised NSP powder. The powders were heat treated at 750 °C for 1 h and air quenched, and the same powder (750 °C) further heat-treated at 1000 °C for 1 h and air quenched. The obtained results were similar, independent of the synthesis technique, and are summarised in Fig. 5. After heat treatment at 750 °C several diffraction peaks other than from rocksalt appeared, indicating phase separation in the material. This observation is consistent with the expectation that the enthalpy of mixing is positive due to the presence Zn^{2+} and Cu^{2+} that have higher tendency to form non-rocksalt phases,

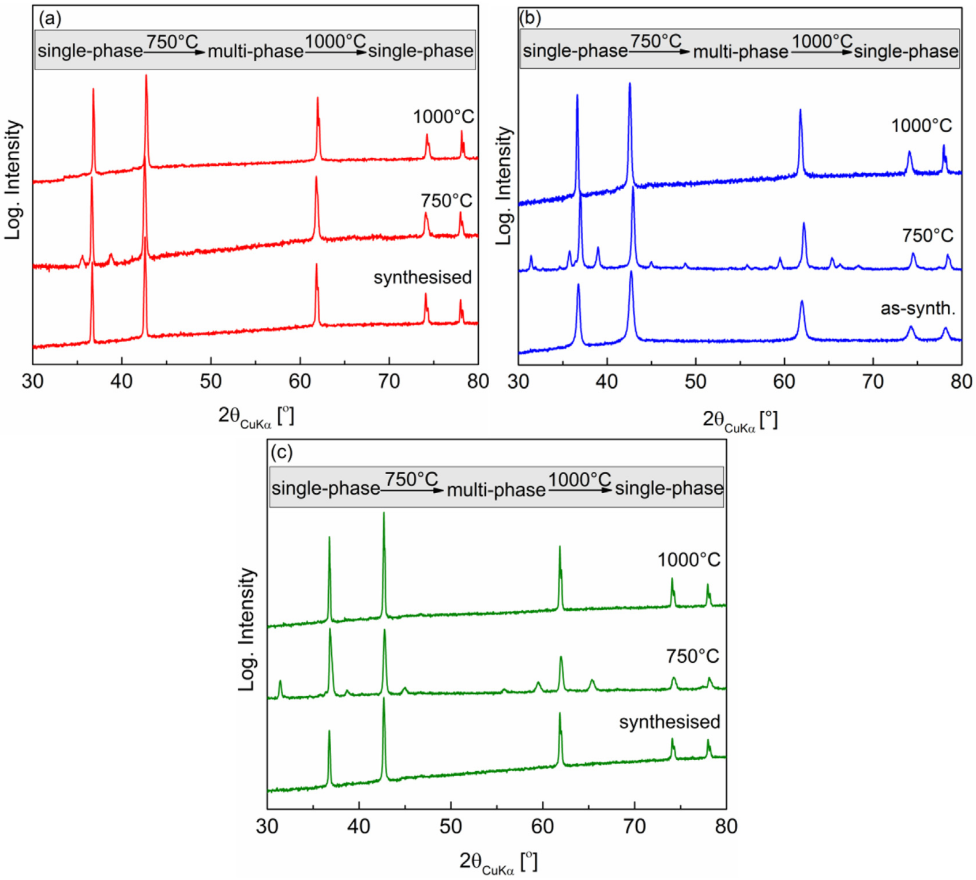

Fig. 5. XRD pattern of the (Co,Cu,Mg,Ni,Zn)O powders showing the reversibility of phase transformations upon heat treatment and confirming effect of configurational entropy on the phase stabilisation in case of (a) FSP, (b) NSP and (c) RCP powders.

large ionic radii difference when Zn^{2+} is in tetrahedral coordination (the most stable co-ordination state for Zn in oxide form, see Table 1.) and Jahn-Teller distortion for Cu^{2+}. Thus reversion from single-phase to multi-phase state at lower temperature is an indication of the dominant effect of entropy in the material. The second heat treatment performed at 1000 °C resulted in a reversion into a phase-pure rocksalt. This reversion from single-phase to multiple phases and then back again to a single-phase upon heat treatment were in correspondence with the similar observation reported by Rost et al. [6] for the same (microcrystalline) system synthesised via solid state reaction route. The retention of single-phase even at room temperature indicates that the diffusion kinetics is sluggish due to the presence of large number of elements, making entropy stabilised phases quenchable. This is in full agreement with the "sluggish diffusion effect" observed in HEA [9,41]. Similar to the systems obtained by solid state synthesis [6–8], the entropy effect is thought to govern the single-phase formation, which dissociates into multiple phases when held at lower temperature as the positive enthalpy of mixing (ΔH) becomes dominant over the entropy factor ($T\Delta S$), making the rocksalt solid solution unstable. The system again reverts back to a single-phase solid solution when treated at higher temperature as the entropy factor stabilises it. These observations demonstrate the effects of "sluggish diffusion" and entropy, irrespective of the synthesis method.

4. Conclusions

Single-phase nanocrystalline high entropy oxides (HEOs) comprised of transitional metals in equiatomic amounts were successfully synthesised using three different synthesis techniques. The nebulised spray pyrolysis (NSP) process resulted in the direct synthesis of nanocrystalline single-phase rocksalt structure and structural analysis showed the reversibility of phase transformations confirming the effect of entropy on phase stabilisation. The reverse co-precipitation (RCP) process, which required an annealing step, yielded as well nanocrystalline single-phase powders. On the other hand, during flame spray pyrolysis (FSP), due to the temperature gradient in the flame and the extremely short residence time, ultrafine nanocrystalline powders with two (or more) rocksalt phases having very close lattice parameters were synthesised. However, upon thermal treatment, the powder transformed to a single rocksalt phase retaining the particle size in nanometre range. The enthalpy of single-phase formation for ESOs is positive due to the large variation in cationic radii of Zn^{2+} (in wurtzite) and Cu^{2+} (in tenorite), difference in the preferred coordination number for Zn^{2+} (in wurtzite) and non-bonding electron effects like Jahn-Teller distortion for Cu^{2+}. This increase in positive enthalpy is compensated by increase in configurational entropy or temperature. The NSP process provided a critical insight to this study as it had a residence time (0.15 s) lying between that in FSP (0.01 s) and RCP ($3.6 \cdot 10^3$ s). The residence time in synthesis by NSP was sufficient for the 5-cationic system to crystallise into a single-phase at slightly lower temperatures (1150 °C) when compared to the 4-cationic system. The 4-cationic system required higher synthesis temperature (1250 °C) due to its lower configurational entropy in order to overcome the positive enthalpy ΔH by increasing $T\Delta S$ term. Heat treatments at several temperatures revealed that the entropy dependent phase selection of the nanocrystalline materials were similar to that of microcrystalline ESO reported in the literature.

Acknowledgements

The authors would like to thank the Helmholtz Association (Germany) for financial support through the Helmholtz Portfolio Project "Electrochemical Storage in System – Reliability and Integration", Karlsruhe Nano Micro Facility (KNMF, Germany). We thank Dr. Christian Kübel for providing access to the electron microscopy unit at KIT, the Sophisticated Analytical Instrument Facility (SAIF, IIT Madras) for the access to the scanning electron microscopy unit, and Dr. Oliver Clemens (Technische Universität Darmstadt, Germany) for helpful discussion related to Rietveld refinement. A. Sarkar acknowledges support of DAAD IIT/Master sandwich program 2015-16.

References

[1] F.H. Aragón, I. Gonzalez, J.A.H. Coaquira, P. Hidalgo, H.F. Brito, J.D. Ardisson, W.A.A. Macedo, P.C. Morais, Structural and surface study of praseodymium-doped SnO_2 nanoparticles prepared by the polymeric precursor method, J. Phys. Chem. C 119 (2015) 8711–8717.

[2] R. Djenadic, M. Botros, H. Hahn, Is Li-doped $MgAl_2O_4$ a potential solid electrolyte for an all-spinel Li-ion battery? Solid State Ionics 287 (2016) 71–76.

[3] A. Salehi, Selectivity enhancement of indium-doped SnO_2 gas sensors, Thin Solid Films 416 (2002) 260–263.

[4] B. Raveau, Transition metal oxides: Promising functional materials, J. Eur. Ceram. Soc. 25 (2005) 1965–1969.

[5] S. Sato, R. Takahashi, M. Kobune, H. Gotoh, Basic properties of rare earth oxides, Appl. Catal. A Genet. 356 (2009) 57–63.

[6] C.M. Rost, E. Sachet, T. Borman, A. Moballegh, E.C. Dickey, D. Hou, J.L. Jones, S. Curtarolo, J.-P. Maria, Entropy-stabilized oxides, Nat. Commun. 6 (2015) 8485.

[7] D. Bérardan, S. Franger, D. Dragoe, A.K. Meena, N. Dragoe, Colossal dielectric constant in high entropy oxides, Phys. Status Solidi – Rapid Res. Lett. 10 (2016) 328–333.

[8] D. Bérardan, S. Franger, A.K. Meena, N. Dragoe, Room temperature lithium superionic conductivity in high entropy oxides, J. Mater. Chem. A 4 (2016) 9536–9541.

[9] B.S. Murty, J.W. Yeh, S. Ranganathan, High-entropy alloys, Butterworth-Heinemann, London, 2014.

[10] Y. Zhang, T.T. Zuo, Z. Tang, M.C. Gao, K.A. Dahmen, P.K. Liaw, Z.P. Lu, Microstructures and properties of high-entropy alloys, Prog. Mater. Sci. 61 (2014) 1–93.

[11] M.-H. Tsai, J.-W. Yeh, High-entropy alloys: A critical review, Mater. Res. Lett. 2 (2014) 107–123.

[12] M.-H. Hsieh, M.-H. Tsai, W.-J. Shen, J.-W. Yeh, Structure and properties of two Al–Cr–Nb–Si–Ti high-entropy nitride coatings, Surf. Coat. Technol. 221 (2013) 118–123.

[13] W.J. Shen, M.H. Tsai, K.Y. Tsai, C.C. Juan, C.W. Tsai, J.W. Yeh, Y.S. Chang, Superior oxidation resistance of $(Al_{0.34}Cr_{0.22}Nb_{0.11}Si_{0.11}Ti_{0.22})_{50}N_{50}$ high-entropy nitride, J. Electrochem. Soc. 160 (2013) C531–C535.

[14] V. Braic, A. Vladescu, M. Balaceanu, C.R. Luculescu, M. Braic, Nanostructured multi-element (TiZrNbHfTa)N and (TiZrNbHfTa)C hard coatings, Surf. Coat. Technol. 211 (2012) 117–121.

[15] K. Senevirathne, C.S. Day, M.D. Gross, A. Lachgar, N.A.W. Holzwarth, A new crystalline LiPON electrolyte: Synthesis, properties, and electronic structure, Solid State Ionics 233 (2013) 95–101.

[16] W. Xu, X. Chen, F. Ding, J. Xiao, D. Wang, A. Pan, J. Zheng, X.S. Li, A.B. Padmaperuma, J.G. Zhang, Reinvestigation on the state-of-the-art nonaqueous carbonate electrolytes for 5 V Li-ion battery applications, J. Power Source 213 (2012) 304–316.

[17] G.L. Messing, S.-C. Zhang, G.V. Jayanthi, Ceramic powder synthesis by spray pyrolysis, J. Am. Ceram. Soc. 76 (1993) 2707–2726.

[18] M. Kumar, S. Bhattacharya, Flame synthesis and characterization of nanocrystalline titania powders, Process. Appl. Ceram. 6 (2012) 165–171.

[19] N. Mahmed, O. Heczko, O. Söderberg, S.-P. Hannula, Room temperature synthesis of magnetite (Fe_3O_4) nanoparticles by a simple reverse co-precipitation method, IOP Conf. Ser. Mater. Sci. Eng. 18 (2011) 32020.

[20] J. Suffner, D. Wang, C. Kübel, H. Hahn, Metastable phase formation during flame spray pyrolysis of $ZrO_2(Y_2O_3)$–Al_2O_3 nanoparticles, Scr. Mater. 64 (2011) 781–784.

[21] O.B. Milosevic, L.T. Mancic, M.E. Rabanal, L. Gomez, J.M. Torralba, Nanoscale particle processing through aerosol routes, in: K. Ewsuk, R. Nogi, Y. Waesche, T. Umakoshi, K. Hinklin (Eds.), Characterization and Control of Interfaces for High Quality Advanced Materials II, Vol. 198, John Wiley & Sons Inc., Hoboken, New Jersey, 2007, pp. 347–352.

[22] M. Houshiar, F. Zebhi, Z.J. Razi, A. Alidoust, Z. Askari, Synthesis of cobalt ferrite ($CoFe_2O_4$) nanoparticles using combustion, coprecipitation, and precipitation methods: A comparison study of size, structural, and magnetic properties, J. Magn. Magn. Mater. 371 (2014) 43–48.

[23] H. Chen, Y. Gao, Y. Liu, H. Luo, Coprecipitation synthesis and thermal conductivity of $La_2Zr_2O_7$, J. Alloys Compd. 480 (2009) 843–848.

[24] L. Kaufman, Hume-Rothery and CALPHAD thermodynamics, in: P.E.A. Turchi, A. Gonis, R.D. Shull (Eds.), CALPHAD Alloy Thermodyn, TMS, Warrendale, 2002, pp. 3–19.

[25] Z. Wang, Y. Huang, Y. Yang, J. Wang, C.T. Liu, Atomic-size effect and solid solubility of multicomponent alloys, Scr. Mater. 94 (2015) 28–31.

[26] D.S. Kenny, A. Navrotsky, Approximate activity-composition relations in the system MgO-ZnO at 1205 ± 5 °C, J. Inorg. Nucl. Chem. 34 (1972) 2115–2119.

[27] C.H. Bates, W.B. White, R. Roy, The solubility of transition metal oxides in zinc oxide and the reflectance spectra of Mn^{2+} and Fe^{2+} in tetrahedral fields, J. Inorg. Nucl. Chem. 28 (1966) 397–405.

[28] Y.-M. Chiang, D.P. Birnie, W.D. Kingery, Physical Ceramics, Wiley, 1997.

[29] R.D. Shannon, Revised effective ionic radii and systematic studies of interatomic distances in halides and chalcogenides, Acta Crystallogr. A 32 (1976) 751–767.

[30] H. Liu, J.S. Tse, H. Mao, Stability of rocksalt phase of zinc oxide under strong compression: Synchrotron x-ray diffraction experiments and first-principles calculation studies, J. Appl. Phys. 100 (2006) 93509.

[31] B. Thiébaut, Flame spray pyrolysis: A unique facility for the production of nanopowders, Platinum Met. Rev. 55 (2011) 149–151.

[32] A.J. Gröhn, S.E. Pratsinis, A. Sánchez-Ferrer, R. Mezzenga, K. Wegner, Scale-up of nanoparticle synthesis by flame spray pyrolysis: The high-temperature particle residence time, Ind. Eng. Chem. Res. 53 (2014) 10734–10742.

[33] R. Djenadic, M. Botros, C. Benel, O. Clemens, S. Indris, A. Choudhary, B. Thomas, H. Horst, Nebulized spray pyrolysis of Al-doped $Li_7La_3Zr_2O_{12}$ solid electrolyte for battery applications, Solid State Ionics 263 (2014) 49–56.

[34] D.S. Jung, S. Bin Park, Y.C. Kang, Design of particles by spray pyrolysis and recent progress in its application, Korean J. Chem. Eng. 27 (2010) 1621–1645.

[35] Topas V5, General profile and structure analysis software for powder diffraction data, User's Manual, Bruker AXS, Karlsruhe, 2015.

[36] K. Okuyama, W.W. Lenggoro, Preparation of nanoparticles via spray route, Chem. Eng. Sci. 58 (2003) 537–547.

[37] H.A. Jahn, E. Teller, Stability of polyatomic molecules in degenerate electronic states. I. Orbital degeneracy, Proc. R. Soc. A Math. Phys. Eng. Sci. 161 (1937) 220–235.

[38] G. Peralta, D. Puggioni, A. Filippetti, V. Fiorentini, Jahn-Teller stabilization of magnetic and orbital ordering in rocksalt CuO, Phys. Rev. B 80 (2009) 140408(R).

[39] A.R. Denton, N.W. Ashcroft, Vegards law, Phys. Rev. A 43 (1991) 3161–3164.

[40] G. Bergerhoff, R. Hundt, R. Sievers, I.D. Brown, The inorganic crystal structure data base, J. Chem. Inf. Comput. Sci. 23 (1983) 66–69.

[41] J.-W. Yeh, Recent progress in high-entropy alloys, Ann. Chim. Sci. Des. Mat. 31 (2006) 633–648.

nature COMMUNICATIONS

ARTICLE

DOI: 10.1038/s41467-018-05774-5 OPEN

High entropy oxides for reversible energy storage

Abhishek Sarkar [1], Leonardo Velasco[1], Di Wang[1,2], Qingsong Wang[1], Gopichand Talasila[1], Lea de Biasi[1], Christian Kübel [1,2,3], Torsten Brezesinski [1], Subramshu S. Bhattacharya[4], Horst Hahn[1,3] & Ben Breitung [1,2]

In recent years, the concept of entropy stabilization of crystal structures in oxide systems has led to an increased research activity in the field of "high entropy oxides". These compounds comprise the incorporation of multiple metal cations into single-phase crystal structures and interactions among the various metal cations leading to interesting novel and unexpected properties. Here, we report on the reversible lithium storage properties of the high entropy oxides, the underlying mechanisms governing these properties, and the influence of entropy stabilization on the electrochemical behavior. It is found that the stabilization effect of entropy brings significant benefits for the storage capacity retention of high entropy oxides and greatly improves the cycling stability. Additionally, it is observed that the electrochemical behavior of the high entropy oxides depends on each of the metal cations present, thus providing the opportunity to tailor the electrochemical properties by simply changing the elemental composition.

---

[1] Institute of Nanotechnology, Karlsruhe Institute of Technology, Hermann-von-Helmholtz-Platz 1, 76344 Eggenstein-Leopoldshafen, Germany. [2] Karlsruhe Nano Micro Facility, Karlsruhe Institute of Technology, Hermann-von-Helmholtz-Platz 1, 76344 Eggenstein-Leopoldshafen, Germany. [3] Helmholtz Institute Ulm for Electrochemical Energy Storage, Helmholtzstraße 11, 89081 Ulm, Germany. [4] Department of Metallurgical and Materials Engineering, Nano Functional Materials Technology Centre (NFMTC), Indian Institute of Technology Madras, Chennai 600036, India. Correspondence and requests for materials should be addressed to H.H. (email: horst.hahn@kit.edu) or to B.B. (email: ben.breitung@kit.edu)

The demand for energy storage devices (batteries) for both stationary and mobile applications has increased rapidly during the past years and it is expected to continue to grow in the future. The most commonly used electrochemical energy storage devices are intercalation based Li-ion batteries, which exhibit very high efficiency and reversibility[1,2]. Nonetheless, other Li-storage schemes are being presently pursued especially conversion or alloying modification approaches since they hold the promise for achieving very high capacity storage systems. Unfortunately, many of these systems have been found to lack both good reversibility and efficiency[3,4].

Recently, a new class of oxide systems, also known as high entropy oxides (HEO), was formulated and reported with first demonstrations for transition-metal-based HEO (TM-HEO)[5–7], rare-earth-based HEO (RE-HEO)[8] and mixed HEO (TM-RE-HEO)[9]. HEO are based on a new, quite revolutionary concept of entropy stabilization, that is, to stabilize a certain crystal structure that can differ from the typical crystal structures of the constituent elements, thereby increasing the configurational entropy of the resulting compounds. This concept was first reported for metallic high entropy alloys (HEA). In recent years, the study of HEA has grown into an independent field of materials research, as evidenced by numerous publications[10].

Several reports on TM-HEO[5,6], RE-HEO[8], and mixed TM-RE-HEO[9] have demonstrated that high entropy stabilization in oxides with 5 or more cations in equiatomic concentrations leads to the formation of single-phase rock-salt, fluorite, or perovskite structures. These compounds often show interesting and unexpected properties, such as extraordinarily high room temperature Li-ion conductivities for solid state electrolytes in TM-HEO[5], very narrow and tailored band gaps in RE-HEO[8] and colossal dielectric constants in TM-HEO[11]. The main driver for the growing interest in HEO is the potential to obtain novel properties by exploiting the enormous number of possible elemental combinations[5,12]. The fast growth of the field of HEO is being facilitated by the availability of many synthesis and processing routes, which were shown to provide highly reproducible material systems[6,7].

As previously mentioned, one of the unexpected properties of the TM-HEO is the high Li-ion conductivity ($>10^{-3}\,\mathrm{S\,cm^{-1}}$), as reported by Bérardan et al.[5]. The possible insertion of Li-ions into a rock-salt structure opens several diffusion pathways for Li-ions through the crystal lattice, giving rise to the increased conductivity.

Here we present new results on the electrochemical properties of several TM-HEO, such as storage capacity and the cycling stability of HEO structures. The concept of high entropy crystal structure stabilization enables us to build conversion-based electrodes, which can be cycled over 500 times without significant capacity degradation. It is shown that the reduction of the entropy by removal of a single element leads to a completely different electrochemical behavior and cycling degradation. Additionally, unique possibilities to fine-tune the electrochemical performance of high-entropy materials is demonstrated, by making use of the different effects of each individual element on the electrochemical characteristics. Moreover, based on TEM investigations a possible reaction mechanism is proposed, which considers the entropy stabilization and the supporting rock-salt matrix structure during the entire conversion process.

Results

As-prepared TM-HEO characterization. The morphology of the various TM-HEO powders, as reported in an earlier publication[6], comprises both hollow and filled spheres with sizes in the nano-to-micrometer range. The overview scanning electron microscopy (SEM) image in Figure 1a shows the variety of particle morphologies and sizes. A higher magnification view of the individual particles, both hollow and filled, can be seen in the inset. The crystallinity and the phase purity (rock-salt structure) of the TM-HEO (($(Co_{0.2}Cu_{0.2}Mg_{0.2}Ni_{0.2}Zn_{0.2})O$) were examined by means of powder X-ray diffraction (XRD), followed by Rietveld refinement analysis. More details about Rietveld refinement can be found in the supporting information (Supplementary Figure 1). The prepared TM-HEO was subsequently used as active material for application in Li-cells without any further heat treatment step.

The $(Co_{0.2}Cu_{0.2}Mg_{0.2}Ni_{0.2}Zn_{0.2})O$ electrodes were tested in secondary Li-based battery cells, using 63 wt% of the TM-HEO as active material and evaluated at different specific currents during cycling. Figure 1b, c depict representative data for this TM-HEO system. Galvanostatic cycling experiments were performed in the voltage range from 0.01 to 3 V with respect to Li^+/Li. The most probable reaction mechanisms are insertion of Li into the rock-salt HEO crystal structure, or a conversion reaction forming metals and Li_2O[3,13]. The most prominent materials for Li-insertion (intercalation)[2] are represented by layered structures like graphite, lithium cobalt oxide (LCO)[1], or lithium nickel cobalt manganese oxide (NCM) which are frequently used as electrode materials in Li-ion batteries, whereas insertion processes in rock-salt structures have been rarely reported[14]. The precondition for insertion in the TM-HEO would be that the Li-ion fits into the rock-salt lattice, where all octahedral positions are occupied by cations. As per Pauling's rule, the possibility of accommodating Li^+ in the tetrahedral position is energetically costly considering that the ratio of ionic radii (Li^+ to O^{2-}) is greater than 0.414 (the upper limit for accommodating an ion in the tetrahedral position)[15]. Additionally, this would lead to strong repulsive interactions between the cations in the lattice[15]. As known from the literature, transition metal oxides are prone to conversion reactions, i.e., during the charging-discharging cycle complete phase transformations may occur[14,16]. Consequently, it is reasonable to assume that reversible conversion reactions take place in TM-HEO, which either completely or partially reduce the metal ions upon lithiation.

The measured capacities at various specific currents of the TM-HEO are presented in Fig. 1b. Conversion electrodes often show substantial capacity degradation at high currents due to kinetic limitations of diffusion driven processes during de-/lithiation. For conversion type materials, the theoretical capacity is directly related to the amount of electrons transferred per formula unit (Supplementary Equation 1). The basic reaction for a binary metal oxide can be represented as $MO_x + 2xLi \rightarrow M + xLi_2O$. Because it is not known what reactions are occurring during the redox processes in the case of TM-HEO (additional processes might be alloying of Zn with Li, formation of intermetallic phases etc.), we cannot predict with high accuracy the theoretical capacity of our compounds. However, we believe that it is in the range of capacities reported for divalent oxide conversion materials ($700\text{–}1000\,\mathrm{mAh\,g^{-1}}$).

Although some conversion materials have been reported to show high specific capacities and high degrees of reversibility, most of them are tediously modified, e.g., regarding morphology and structure or they are coated with additional functional materials to enhance their electrochemical performance[17–19]. Usually, the particle size in conversion materials has a considerable influence on the electrochemical properties, since large size particles usually lead to low capacity as well as low rate capability and reversibility. Nevertheless, despite the large size particles present in the TM-HEO, the material shows high specific capacities even when applying high specific currents. Furthermore, it is able to fully recover and even increase the initial capacity after raising the current to $3\,\mathrm{A\,g^{-1}}$ for 5 cycles,

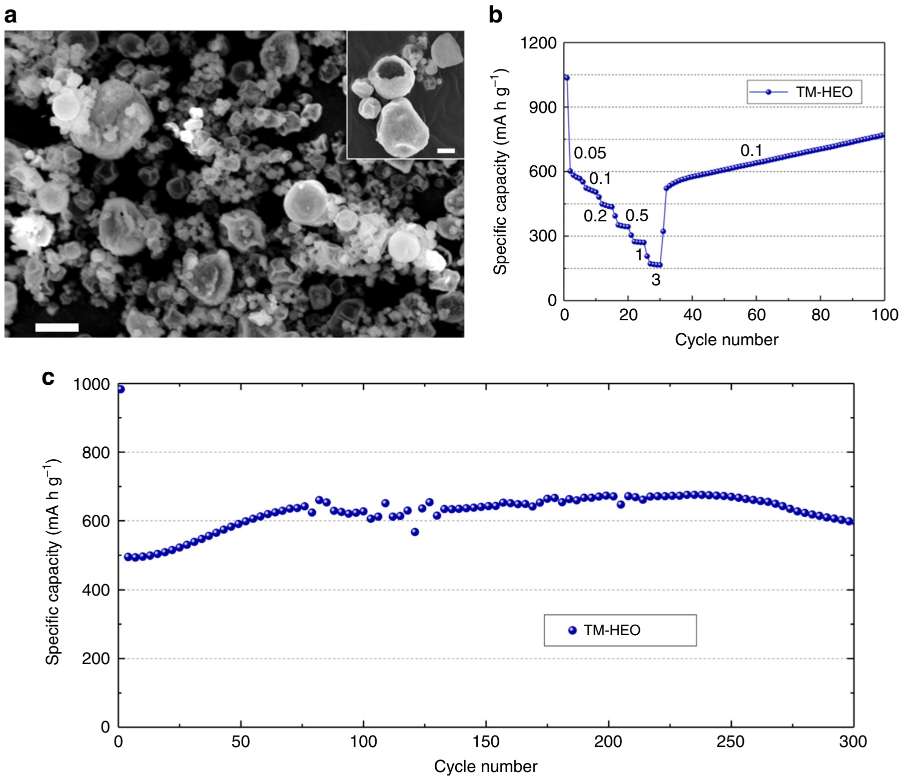

Fig. 1 TM-HEO particles and their specific capacities. **a** SEM micrograph of the as-synthesized TM-HEO powder with typical particle sizes from the nano-to-micrometer range. The inset shows that the powder contains both hollow and filled spheres. The scalebars shown in **a** and the inset correspond to 2 μm and 1 μm, respectively. **b** Galvanostatic rate capability test (current values given in units of A g^{-1}). The capacity decreases as the specific current is increased stepwise up to 3 A g^{-1}, but it recovers at 0.1 A g^{-1} and even increases after 100 cycles to 770 mAh g^{-1}. **c** Long-term cycling performance at 0.2 A g^{-1}

so that after 100 cycles a specific capacity of 770 mAh g^{-1} is reached. Capacity increase over prolonged cycling is typical of conversion type materials and can be attributed to activation processes, occurring in electrodes with large particle sizes[14,17]. Figure 1c shows the cycling performance of the TM-HEO over 300 cycles at 200 mA g^{-1} with two initial formation cycles at 50 mA g^{-1}. Even with the micrometer-sized particles, as shown in Fig. 1a, and without any optimization of the other components in the electrochemical cell (i.e., electrolyte, binder and electrode composition), the cells display good stability at high capacity values, especially when considering the conversion type of reaction involved. The aforementioned increase in capacity is also observed during the first 75 cycles. The initial discharge capacity amounts to 980 mAh g^{-1}, and after stabilization at the third cycle, the cell reaches a capacity of ~600 mAh g^{-1}, which even increases to around 650 mAh g^{-1} after 70 cycles; the voltage profiles can be found in the supporting information (Supplementary Figure 2). The fluctuations in capacity seen between the 75th and 150th cycles were observed for several different cells. However, after around 150 cycles, the capacity was found to stabilize, therefore we attribute this behavior to structural changes associated with the active material. The conversion reactions of individual transition metal oxides (CuO, NiO, CoO etc.) with similar particle sizes and shapes show comparable initial specific capacities (500–700 mAh g^{-1}) [14,20,21], but they fall short when it comes to capacity retention and efficiency[22,23].

Comparison between high entropy and medium entropy compounds. The substantial number of cation metals in the TM-HEO makes it possible to remove specific elements and to then investigate the resulting change of the electrochemical behavior, thus allowing to assign certain electrochemical characteristics to specific elements. Additionally, the exclusion of one of the elements from a 5-cation system results in a significant decrease of the configurational entropy from ~1.61 R to ~1.39 R, which necessitates a post annealing treatment to obtain a single-phase oxide, as explained in the experimental section of the paper. To compare the 4-cation systems with the 5-cation system, the latter was subjected to the identical additional heat treatment as that used for the 4-cation oxides to facilitate comparison. In fact, in a long-term experiment (Fig. 2a), it was shown that, at a specific current of 200 mA g^{-1}, the 5-cation sintered system can be cycled over hundreds of cycles with specific capacities of up to 590 mAh g^{-1}. The typical electrochemical behavior of conversion materials discussed above (decaying/increasing capacity with cycling) is also apparent in this experiment. As anticipated, the first drop in capacity is more prominent since the calcined TM-HEO sample comprises even bigger particle sizes and agglomerates than the as-prepared TM-HEO (Supplementary Figure 3). The Coulombic efficiency in the stable region (cycle no. 60–400) stabilizes between 99.4 and 99.95%. Because of the heat treatment, slightly different capacity values for the 5-cation system were expected, as shown in Fig. 2a. According to the established nomenclature, 4-cation systems belong to the “medium entropy”

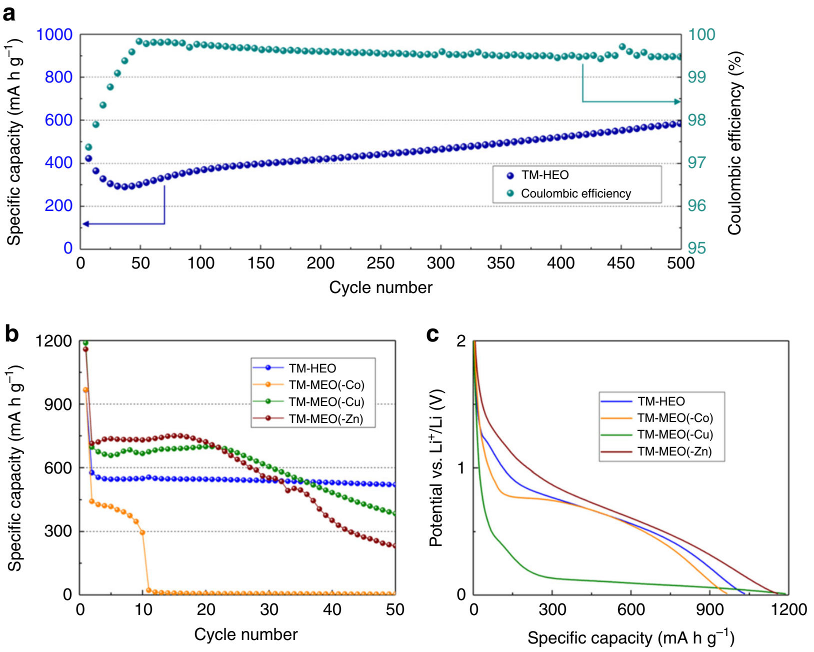

Fig. 2 Specific capacities and lithiation profiles of TM-HEO and TM-MEO. Comparison of the different medium and high entropy oxides under investigation. **a** Long-term cycling stability of the calcined TM-HEO at 200 mA g^{-1} together with the corresponding Coulombic efficiency. **b** It can be seen that the TM-HEO shows stable capacity retention at 50 mA g^{-1}, while the materials without Zn and Cu reveal severe capacity degradation. The material without Co fails completely after 10 cycles. **c** Discharge (lithiation) profiles of the first cycle for the different compounds. The material without Cu shows a significantly lower discharge potential and it might be interesting as anode material for primary batteries

Table 1 Synthesized single-phase compounds used for electrochemical testing

	Entropy	Removed element	Abbreviation
$(Co_{0.2}Cu_{0.2}Mg_{0.2}Ni_{0.2}Zn_{0.2})O$	1.61 R	-	TM-HEO
$(Co_{0.25}Cu_{0.25}Mg_{0.25}Ni_{0.25})O$	1.39 R	Zn	TM-MEO(-Zn)
$(Co_{0.25}Mg_{0.25}Ni_{0.25}Zn_{0.25})O$	1.39 R	Cu	TM-MEO(-Cu)
$(Cu_{0.25}Mg_{0.25}Ni_{0.25}Zn_{0.25})O$	1.39 R	Co	TM-MEO(-Co)

group, while 5-cation systems belong to the “high entropy” group[24]. It should be noted that all “medium entropy” oxides (MEO) showed a completely different and rather unstable electrochemical behavior when compared to the “high entropy” oxides (Fig. 2b). The electrochemical behavior of the “medium entropy” oxides, initially displaying high specific capacities, but then showing varying degrees of degradation with increasing numbers of cycles, compares well with that of established conversion materials with large particle sizes. By contrast, the 5-cation high entropy oxide displays a high capacity value that does not degrade with increasing cycle number. The capacity comparison between the 5-cation TM-HEO and the 4-cation oxides leads us to conclude that the “high entropy” material exhibits a novel and interesting electrochemical behavior, probably related to the entropy stabilization. Such an observation has not been previously reported. Figure 2b shows a comparison of the electrochemical performance of the 5-cation TM-HEO and three of the 4-cation systems, without Zn, Cu, or Co, respectively (see Table 1). Despite efforts to synthesize every possible MEO structure, both TM-MEO(-Mg) and TM-MEO(-Ni) (i.e., $(Co_{0.25}Cu_{0.25}Zn_{0.25}Ni_{0.25})O$ and $(Co_{0.25}Cu_{0.25}Mg_{0.25}Zn_{0.25})O$, respectively) could not be stabilized as single-phase compounds, even at much higher temperatures. Therefore, we refrain from including them in the comparison of the entropy-stabilized oxides, since we believe that simple mixtures of different compounds are not comparable to the single-phase materials. Nevertheless, the electrochemical and XRD characterization results of the multiphase compounds are depicted separately in Supplementary Figure 4.

The configurational entropy was calculated using the following formula:[24]

$$S_{\mathrm{config}} = -R\left[\left(\sum_{i=1}^{N} x_i \ln x_i\right)_{\mathrm{cation-site}} + \left(\sum_{j=1}^{N} x_j \ln x_j\right)_{\mathrm{anion-site}}\right] \qquad (1)$$

where x_i and x_j represent the mole fractions of ions present in the cation- and anion-site, respectively. The contribution of the anion-site is expected to have a minor influence on S_{config}, given that only one anion is present. More details about the entropy calculation for the TM-HEO and one of the TM-MEO materials are given in Supplementary Equation 2.

Although every composition was synthesized as single-phase rock-salt structure (the XRD patterns of all the compounds can be found in Supplementary Figure 5), significant differences in the electrochemical behavior between the TM-HEO and the “medium entropy” materials are clearly evident. The individual compounds are cycled at 50 mA g^{-1} in a potential range between 0.01 and 3 V with respect to Li$^+$/Li. Figure 2b shows the TM-HEO with a specific capacity of 555 mAh g^{-1} after the initial formation cycles, which decreases to 520 mAh g^{-1} after 50 cycles. The removal of Co (TM-MEO(-Co)) leads to a complete failure of the cell after approx. 10 cycles, with no signs of recovery during the subsequent cycles (Fig. 2b). This seems to imply that Co can be considered as a critical and necessary element for TM-HEO to have high specific capacity and good cycling stability, whereas the removal of Zn (TM-MEO(-Zn)) and Cu (TM-MEO(-Cu)) does not impede the overall reversibility. Nevertheless, the cells deliver lower capacities after 30–35 cycles, even though the initial capacity of both oxides is higher than that of the 5-cation system, but with a rapid drop after only a few cycles. Similar electrochemical behavior has been reported for large particle size conversion materials and has often been explained by side reactions, which occur during the redox processes, such as particle fracture/pulverization and increased solid-electrolyte interphase formation[2]. Another aspect discussed in the literature is the potential improvement in conductivity when metallic species like Cu dendrites are present[25], which might lead to better cycling stability, too. To examine whether Cu dendrites are formed during the conversion process, energy-dispersive X-ray spectroscopy (EDX) measurements were conducted on electrodes after 100 cycles. However, the data show no indication of any Cu aggregation in the materials (Supplementary Figure 6)[26].

Therefore, the 4-cation systems can serve as reference materials when the entropy stabilization is not as large as in the HEO. Such effects were not observed during TM-HEO cycling. SEM examination of the cycled materials revealed fully intact spheres, embedded in the carbon/polymer matrix of the electrode (Supplementary Figure 7).

The above results demonstrate that an increase in concentration (25 at% in 4-cation systems vs. 20 at% in 5-cation systems) of constituent elements, which are known for their electrochemical activity (e.g., Co), leads to the expected increase in capacity, but the 4-cation systems do not exhibit the stability of the 5-cation system. Another interesting effect due to removal of Cu from the TM-HEO has been noted. As seen in Fig. 2c, the initial (average) discharge potential is significantly decreased. The large capacity of this compound at the low potential could be an interesting option for primary anode applications (around 800 mAh g^{-1} in the 0.03–0.13 V range).

The cyclic voltammograms (CVs) are depicted for all the systems in Supplementary Figure 8. The CV curves look very different for the different materials, which is another clear indication that the reaction mechanism and the electrochemical behavior can be tailored by changing the elemental composition. Removal of Zn from the TM-HEO causes a completely different electrochemical behavior during the oxidation of the compound. The CVs and differential capacity plots establish that the absence of Zn leads to a two-step oxidation process, rather than a single one as for all the other samples (Supplementary Figure 9). These two oxidation peaks, centered around 1.7 V and 2.2 V, resemble the formation of individual NiO and CoO[17,27]. This suggest that, in the case of TM-MEO(-Zn), the parent rock-salt structure is apparently not regained upon Li extraction, but instead separates into different phases.

Despite potential alloying of elemental Zn with Li[28], we did not find any signs of this reaction. Usually, the formation of ZnLi occurs at a low potential of around 0.2 V[28] and would lead to an additional gain in capacity of ~40 mAh g^{-1} for the TM-HEO[29]. Although the CV curves (Supplementary Figure 8) for TM-MEO (-Zn) and the Zn-containing materials do not show significant differences, alloying of Zn with Li cannot be ruled out completely, especially for TM-MEO(-Cu), where the vast majority of Li uptake occurs at low potential. However, even if this reaction takes place in the TM-HEO, the capacity gain will only account for ~6.7% of the total capacity.

These examples for TM-MEO(-Cu), TM-MEO(-Zn), and TM-MEO(-Co) demonstrate that even the removal of a single element leads to significant changes in the electrochemical properties. However, the changes are different for each element removed. On the other hand, the addition of other cations into the single-phase structure (e.g., Fe, Mn, Cr, V) could open new possibilities for developing a modular method to tailor electrodes suited to particular needs. The opportunities to tailor the electrochemical properties in such a flexible way (countless cation combinations are possible), as offered by HEO, are unique compared to conventional conversion or intercalation electrodes. In the following sections of the paper, a possible interpretation, related to the entropy stabilization of the crystal structure, is presented.

Structural investigations and influence on the reaction mechanism. To better understand the reactions and the underlying mechanism of reversible lithium storage, a comprehensive characterization using XRD and transmission electron microscopy (TEM) was performed. Two possible pathways exist for a reversible conversion reaction: (1) the initial TM-HEO phase/structure is being (re)transformed with each lithiation/delithiation cycle or (2) only a few distinct elements are participating in the phase transformation, while the others are keeping the rock-salt structure intact. A full transformation of the stable single-phase TM-HEO with a rock-salt structure is not expected, considering the high synthesis temperature of above 1000 °C in an oxygen atmosphere.

To gather more information on the lithiation mechanisms, operando XRD was conducted during the first two cycles of the cell. These measurements were correlated with high-resolution (HR) TEM and selected area electron diffraction (SAED) studies. The operando XRD measurements were performed on a TM-HEO electrode in transmission geometry. Figure 3 depicts the initial discharge/charge cycle. The intense reflections appearing over the whole cycle originate from the Cu current collector. This is clearly inferred, since the reflections of the initial rock-salt structure vanish during the lithiation and do not reappear after delithiation. This behavior is typical of conversion materials and it is a result of the formation of small crystallites, which have sizes below the detection threshold of XRD[13,14]. Nevertheless, SAED measurements conducted on the as-prepared, lithiated and delithiated particles show that the reflections, originating from the rock-salt structure, corresponding to the (111) and (200) plane do not disappear, even when the sample is fully lithiated. The preservation of the rock-salt structure (if only partially) over the entire redox process, is identified as a likely reason for the observed stable cycling behavior. No reflections of other crystal structures were detected based on the XRD patterns. The presence of completely unreacted TM-HEO regions, which would appear as spots or sharper diffraction rings in the SAED in the lithiated and cycled state, can be ruled out. From the combined structural characterization, it becomes evident that the entire volume of the TM-HEO is modified, giving rise to a reduction of the size of the coherently scattering regions and their chemical composition initiated by the exchange of Li ions. As will be described in the model below, the diffuse SAED rings, observed after the first cycle, thus belong to the material, which participated in the conversion reaction as host matrix.

TEM micrographs of the as-prepared TM-HEO (Fig. 4a) show a high degree of crystallinity and reveal the long-range order, as also evident from the XRD pattern in Supplementary Figure 1. TEM investigations of cycled TM-HEO confirm the presence of small crystalline regions, which still exhibit a long-range order that is visible in the diffraction rings. However, grain boundaries and defects reduce the size of the uniform structures below the coherence length for the XRD and, thus, these structures are not visible in the operando XRD patterns[14,18].

In a typical conversion reaction, metal oxides are being reduced to zero-valent metals and lithium oxide with lithiation. Since,

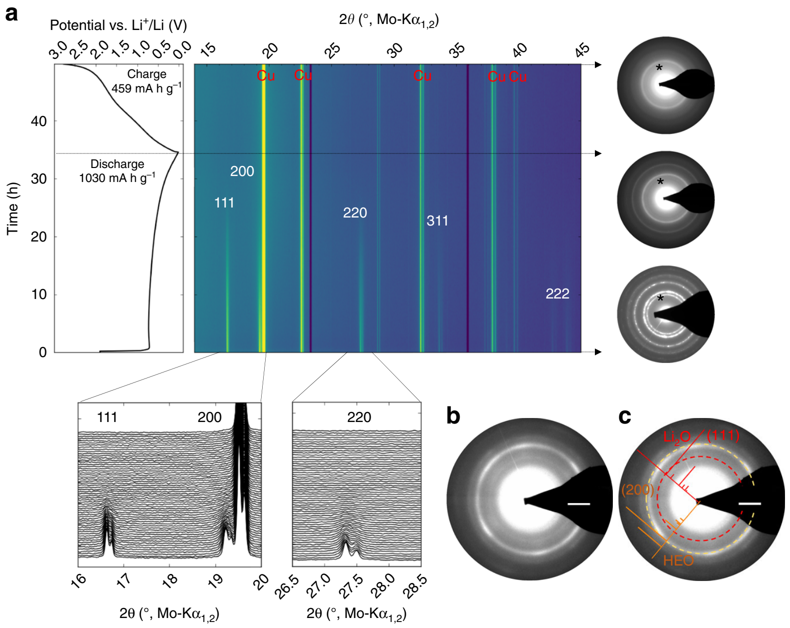

Fig. 3 Operando XRD on TM-HEO. **a** XRD results obtained during the first full lithiation/delithiation cycle. The black lines with arrows indicate the as-prepared, fully lithiated and fully delithiated states as a function of time, with the corresponding potential curve shown on the left side. The XRD reflections fade with lithiation over the first few hours and, after the first full cycle, the reflections are not visible anymore. In the SAED patterns on the right side, crystallites, much smaller than the starting size, are still visible due to the shorter wavelength of the electrons. The asterisk indicates the (200) lattice plane of the rock-salt structure, which is maintained during the entire process. The presence of a very faint SAED ring in the lithiated samples in **b** and **c** (d-spacing 2.68 Å, scalebars 2 1/nm) could be attributed to the (111) diffraction of Li_2O. From the combined XRD and TEM results, it can be concluded that the rock-salt structure is preserved during cycling and serves as a host matrix for the redox processes. Unreacted TM-HEO can be ruled out since otherwise, the corresponding diffraction spots should be visible in the SAED and the XRD reflections should not disappear completely. Supplementary Figure 10 shows an SAED pattern obtained on an electrode after 10 full cycles, still showing the rock-salt structure. The voltage profile seen for the operando XRD measurement is plotted versus the dis/charge time. The first cycle discharge capacity amounts to around 1030 mAh g^{-1}, which corresponds to an uptake of roughly 2 Li per formula unit. The initial charge capacity is lower, being 459 mAh g^{-1}

these compounds are likely to have different crystal structures, compared to the as-prepared rock-salt structure of TM-HEO, a completely disordered structure after the delithiation cycle or separation into distinct elements could be expected. However, a pseudo long-range "ordered" structure, containing many defects, is observed (Fig. 4b, c).The lattice spacings, corresponding to the (111) and (200) planes of the rock-salt structure, are still clearly visible in the high-resolution image (Fig. 4b) and in its fast Fourier transform (FFT) (Fig. 4c). The experimental observations indicate that, even in the lithiated state, the rock-salt lattice is preserved and serves as a host structure for the conversion reactions. The cations involved in the conversion reactions can diffuse back during the lithiation and delithiation cycles. For the conversion reactions to occur, it is necessary that, during the lithiation process, some of the cations are reduced to the metallic state. However, it appears that these reduced cations remain "trapped" inside the crystal structure of the TM-HEO. It is suggested that the rock-salt structure is preserved by the remaining unreduced cations, which facilitates the re-occupation of the previously reduced cations to the original sites of the HEO lattice during the subsequent oxidation reaction. The observed defect structure is most likely the result of stresses in the crystal lattice (due to the conversion reactions of the participating metal elements), which leads to the size reduction of the crystallites and their disappearance in the diffraction signals.

To support the above hypothesis, the products of the conversion reaction (Li_2O and metallic species) were analyzed via TEM. Interestingly, no metallic phases were found, which seems to be the consequence of the aforementioned reaction mechanism (i.e., reduction inside the rock-salt matrix). Although Li_2O is known to be highly sensitive to the electron beam, the presence of Li_2O could be rationalized from the samples after the first and second lithiation cycles (see SAED patterns in Fig. 3a, b). The d-spacing of 2.68 Å could be attributed to the (111) reflection of Li_2O. Because Li_2O is only forming due to the conversion reaction, this can be seen as an indirect support of the proposed reaction scheme.

Additionally, to support the hypothesis of a fully recovered TM-HEO rock-salt structure, spatially resolved EDX spectroscopy measurements were performed to rule out any segregation of elements and/or possible changes in the elemental composition of the materials during cycling. Figure 4d depicts scanning TEM (STEM)-EDX maps of the TM-HEO after the initial cycle. As shown in Supplementary Figure 11, EDX of the as-prepared material does not show any qualitative differences compared to the cycled TM-HEO.

The stability of the "high entropy" materials, when compared to the "medium entropy" compounds, can be explained in terms of the higher absolute value of configurational entropy, which decreases the Gibbs free energy in the TM-HEO structure. While the conversion of the lithiated TM-HEO back to the original rock-salt structure will be favored by the reduced Gibbs free energy, the TM-MEO with one element removed are not sufficiently entropy stabilized to ensure full transformation. The

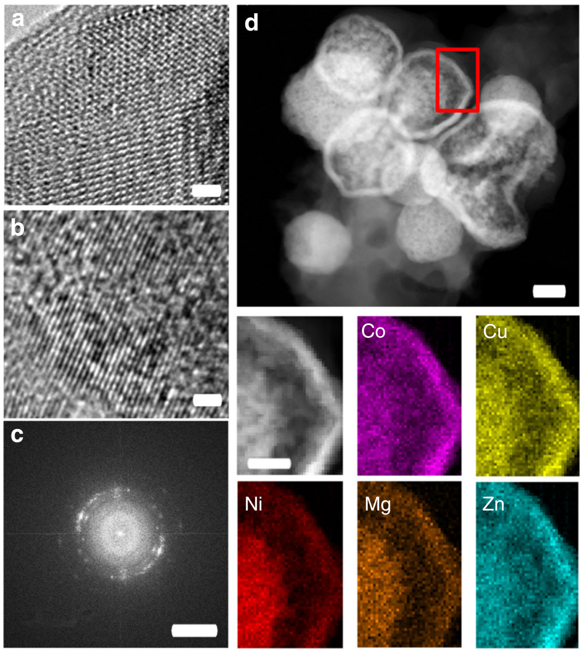

Fig. 4 HRTEM and EDX analysis of the active material. **a**, **b** HRTEM images of the as-prepared and cycled TM-HEO, respectively. The crystallites in **b** are substantially smaller and do not show order over longer distances. The lattice fringes in **b** are not completely straight, but show a small divergence from the original axis. Nevertheless, the small regions with dimensions on the order of a few nanometers exhibit lattice fringes oriented in a specific direction, likely due to the former long-range order, which is partially lost during the conversion reaction. **c** FFT of a HRTEM image of a few crystallites. The arcs in the FFT correspond to the cubic rock-salt structure, but they indicate a certain texture. The lattice fringes are discontinuous between different crystallites; however, the misorientation is small, caused probably by large amounts of defects or low angle boundaries. **d** STEM image showing the spheres consist of small particles and the respective elemental maps of the area indicated by the red rectangle. No apparent segregation occurs at the length scale of aggregates of nanoparticles. The scalebars in **a** and **b** correspond to 1 nm, in **c** to 5 1/nm, in **d** to 200 nm and for the compared EDX analysis to 60 nm

argument of higher stability is also evident from the fact that significantly longer heating times during or after synthesis are required for stable medium entropy oxides compared to the high entropy oxides. Supporting this assumption is the altered oxidation process presented in Supplementary Figure 9 for TM-MEO(-Zn). This material undergoes similar conversion reactions, exhibiting the well-known drawbacks of limited capacity retention and low cycling stability. By contrast, the TM-HEO shows a much more stable electrochemical performance, likely associated with entropy stabilization. Additional support for this hypothesis is also provided by the details of the Coulombic efficiency during cycling. While the TM-HEO provides values in the range between 98.5 and 99.5%, the TM-MEO(-Zn) exhibits Coulombic efficiencies substantially lower (85–95%) over the first 50 cycles (Fig. 5a). This difference alone is already indicative of important side reactions, reducing the efficiency when the entropy stabilization of the active material is not sufficient. For comparison of the “high entropy materials”, “medium entropy materials” and “multiphase materials”, the Coulombic efficiencies over the first 50 cycles are depicted in Fig. 5a. As is seen, only the “high entropy material” shows stable behavior and can be cycled for hundreds of times. Even higher loading of TM-HEO cells reveals Coulombic efficiencies of >98.5% (Fig. 5b). In addition, Fig. 5b shows results from the respective rate performance test, where the areal capacity after 30 cycles amounts to 1.3 mAh cm^{-2}. Despite the fact that the loading was increased by a factor of ~5 (0.5 vs. 2.3 mg cm^{-2}), the specific capacity decreased only slightly (see also electrochemical performance of an electrode containing 80 wt% of TM-HEO in Supplementary Figure 12).

Proposed conversion-based mechanism. A schematic of the proposed reaction mechanism is illustrated in Fig. 6. Within the large as-prepared TM-HEO particles, which are poly-/nanocrystalline, lithiation induces conversion reactions of some of the cations (e.g., Co^{2+}, Cu^{2+}) while the other cations stabilize the rock-salt structure, thereby acting as a kind of matrix. We believe that the instance that single-phase compounds without Mg^{2+} or Ni^{2+} apparently cannot be synthesized is an indication of the stabilizing role of those ions to keep the structure intact during the redox processes. The pivotal role of Mg^{2+} in keeping the HEO structure intact can be explained by the fact that Mg is inactive in the given potential range. The conversion reactions occur on much smaller length scales, on the order of several nm, while the crystallite sizes in the as-prepared powder are much larger. A phase separation of the elements, forming known conversion materials such as $ZnCo_2O_4$, can be ruled out, since the corresponding crystal structures could not be identified, even in the SAED measurements.

The preservation of the rock-salt structure even during lithiation is completely new and is unexpected from the traditional conversion reaction point of view. The fact that the TEM and SAED results reveal highly disordered defect-rich rock-salt regions, without any second phase being present, is in good agreement with the proposed mechanism (Fig. 6). The re-incorporation of the metal ions into the TM-HEO rock-salt structure at room temperature upon electrochemical cycling, facilitated by high entropy stabilization, is expected to add a new dimension to the traditional conversion based lithiation mechanism.

Discussion

In this study, to our knowledge for the first time, it is shown that high entropy oxides are very promising materials for reversible electrochemical energy storage. The variation of the composition of the oxides allows tailoring the Li-storage properties of the active material. The incorporation of different elements into HEO offers a modular approach for the systematic design of the electrode material. Additionally, it is shown that entropy-stabilized oxides have high capacity retention and exhibit a de-/lithiation behavior, which is drastically different from classical conversion materials. The new effect is attributed to configurational entropy stabilization of the lattice, which conserves the original rock-salt structure while serving as a permanent host matrix for the conversion cycles. Based on these—necessarily limited—first, but promising results, further investigations toward high entropy oxide electrode materials should be pursued to explore their full potential for energy storage applications.

Methods

Synthesis. A versatile synthesis technique proven to yield highly crystalline HEO is the Nebulized Spray Pyrolysis (NSP) method, the details of which have been reported elsewhere[6]. In the NSP method, a solution, containing metal salts, is sprayed as a mist and then transported by means of a carrier gas (typically containing oxygen) into the hot zone of a tubular furnace. At the elevated temperature, the precursor solution transforms into the desired crystalline oxide. As the composition of the final product, a nanocrystalline oxide powder, is determined by the composition of the precursor solution, the process is highly reproducible and

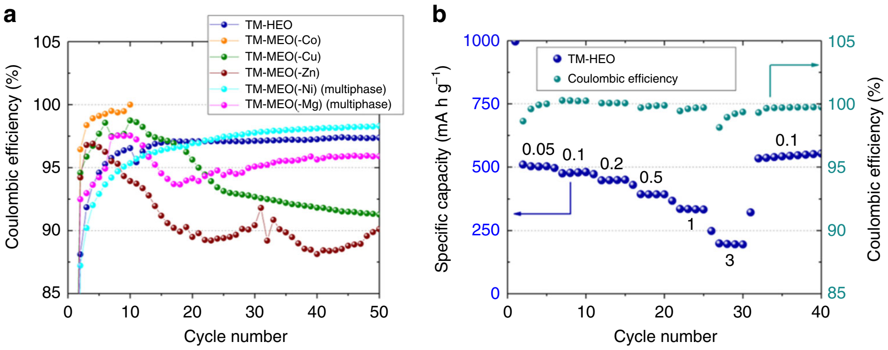

Fig. 5 Coulombic efficiencies of the TM-MEO and TM-HEO compounds and rate test of a higher-loaded TM-HEO electrode. **a** Coulombic efficiency vs. cycle number for all the tested electrode materials at 50 mA g^{-1}. Only TM-HEO reveals stable cycling behavior. The multiphase material without Ni exhibits comparable efficiencies, but with much lower specific capacities (below 250 mAh g^{-1} after 40 cycles) (Supplementary Figure 4). **b** Rate performance test performed on a TM-HEO cell with an overall higher loading (2.3 mg$_{\text{TM-HEO}}$ cm^{-2}). The current values in **b** are given in units of A g^{-1}

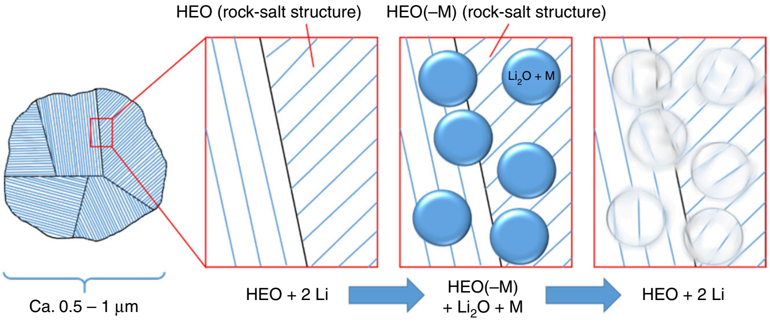

Fig. 6 Schematics of the proposed de-/lithiation mechanism during the conversion reaction of TM-HEO. M in the figure stands only for the cations Co, Cu, Zn, and Ni, since Mg is electrochemically inactive in the potential range applied here. The as-prepared TM-HEO is made of poly-/nanocrystallites, exhibiting an ordered structure, as evidenced by SAED, TEM, and XRD. During the lithiation, some of the divalent metals of the TM-HEO react with Li to form nano-Li$_2$O and nano-M nuclei via a conversion reaction. The SAED measurements clearly show that the rock-salt structure is preserved in this state. The nanosized nuclei grow inside the rock-salt host structure, causing stresses to build up, thus resulting in the introduction of defects. Consequently, the reflections in the XRD pattern disappear—the nuclei “destroy” the long-range order; nevertheless, the participating ions remain “trapped” inside the host matrix and can easily diffuse back into the crystal structure in the subsequent oxidation process. Hence, the parent HEO structure is restored after delithiation

provides quantities on the scale of 1–2 g h^{-1} for a laboratory reactor. In the present study, the respective transition metal ions were dissolved in an aqueous-based solvent using the corresponding nitrates ((Co(NO$_3$)$_2$·6H$_2$O (Sigma Aldrich, 99.9%), Cu(NO$_3$)$_2$·2.5H$_2$O (Sigma Aldrich, 99.9%), Mg(NO$_3$)$_2$·6H$_2$O (Sigma Aldrich, 99.9%), Ni(NO$_3$)$_2$·6H$_2$O (Sigma Aldrich, 99.9%), and Zn(NO$_3$)$_2$·6H$_2$O (Alfa Aesar, 99.9%)). The particles are formed in the gas phase of the hot-wall reactor, operated at 1150 °C. For the 5-cation system, a single-phase structure was obtained directly during the synthesis process. By contrast, the 4-cation systems (see Table 1) required a post annealing treatment (1 h at 1000 °C under ambient atmosphere) to form a single-phase compound. This annealing step was also applied to the 5-cation system, to make sure that all the compounds had the same synthesis/heat treatment history to facilitate comparison of the electrochemical properties among the different systems.

Electrode processing. TM-HEO electrodes were prepared by casting a water slurry containing 63 wt% TM-HEO, 22 wt% Super C65 carbon black additive (Timcal) and 15 wt% Selvol 425 poly(vinyl alcohol) (Sekisui)[30] onto Cu foil (Gould Electronics). The resulting electrode tapes were dried in vacuum at 80 °C for 6 h. The typical areal loading of active material was 0.5–1 mg cm^{-2} unless mentioned otherwise (2.3 mg cm^{-2} for high-loading electrodes). Coin-type cells with 600 µm-thick Li metal foil (Albemarle Germany GmbH) and glass microfiber separator (Whatman, GF/A; GE Healthcare Life Sciences) were assembled inside an argon-filled glovebox ([O$_2$] < 0.5 ppm, [H$_2$O] < 0.5 ppm). The electrolyte used was 1 M LiPF$_6$ in a 3:7 weight mixture of ethylene carbonate and either dimethyl carbonate or ethyl methyl carbonate (BASF SE). All capacities given are related to the mass of the active material.

Characterization. Operando XRD was performed using a high-intensity laboratory Mo-K$\alpha_{1,2}$ diffractometer, optimized for battery research. Details of the setup as well as a description of calibration procedures can be found elsewhere[31–33]. Powder XRD patterns were recorded using a Bruker D8 Advance diffractometer with a Cu-Kα radiation source and a LYNXEYE detector having a fixed divergence slit (0.3°). For operando XRD, coin cells, equipped with polyimide windows, were assembled inside a glovebox by stacking electrode (Ø 12 mm), glass fiber separator (Ø 17 mm) and Li metal foil anode (Ø 16 mm) and using 150 µl of electrolyte[33]. During the operando XRD experiment, the cell was cycled at 100 mA g^{-1} in the voltage range between 0.01 and 3 V. 2D diffraction patterns were collected in transmission geometry with an exposure time of 300 s. The intensities of two consecutive patterns were added up and then integrated to obtain 1D data, resulting in a total time resolution of 600 s. Transmission electron microscopy (TEM) experiments were conducted on powder samples dispersed onto a carbon-coated gold grid. The samples were loaded onto a Gatan TEM vacuum transfer holder inside a glovebox and transferred to the TEM without exposure to air. The TEM samples were examined using a Titan 80–300 electron microscope (FEI), equipped with a CEOS image spherical aberration corrector, high angle annular dark field (HAADF) scanning transmission electron microscopy (STEM) detector (Fischione model 3000) and a Tridiem Gatan image filter (GIF). The microscope was operated at an accelerating voltage of 300 kV. SEM was performed on a ZEISS Gemini Leo 1530. Galvanostatic charge/discharge measurements were performed at room temperature and at various specific currents of 50–3000 mA g^{-1} in the voltage range between 0.01 and 3.0 V vs. Li^+/Li using a MACCOR battery cycler.

Data availability. The data used for this study are available from the corresponding authors upon request.

Received: 8 March 2018 Accepted: 25 July 2018

References

1. Mizushima, K., Jones, P. C., Wiseman, P. J. & Goodenough, J. B. Li_xCoO_2 $(0<x<-1)$: a new cathode material for batteries of high energy density. *Mater. Res. Bull.* **15**, 783–789 (1980).
2. Nitta, N., Wu, F., Lee, J. T. & Yushin, G. Li-ion battery materials: present and future. *Mater. Today* **18**, 252–264 (2015).
3. Reddy, M. A. et al. CF_x derived carbon-FeF_2 nanocomposites for reversible lithium storage. *Adv. Energy Mater.* **3**, 308–313 (2013).
4. Breitung, B., Baumann, P., Sommer, H., Janek, J. & Brezesinski, T. In situ and operando atomic force microscopy of high-capacity nano-silicon based electrodes for lithium-ion batteries. *Nanoscale* **8**, 14048–14056 (2016).
5. Bérardan, D., Franger, S., Meena, A. K. & Dragoe, N. Room temperature lithium superionic conductivity in high entropy oxides. *J. Mater. Chem. A* **4**, 9536–9541 (2016).
6. Sarkar, A. et al. Nanocrystalline multicomponent entropy stabilised transition metal oxides. *J. Eur. Ceram. Soc.* **37**, 747–754 (2017).
7. Rost, C. M. et al. Entropy-stabilized oxides. *Nat. Commun.* **6**, 8485 (2015).
8. Sarkar, A. et al. Multicomponent equiatomic rare earth oxides with a narrow band gap and associated praseodymium multivalency. *Dalton Trans.* **46**, 12167–12176 (2017).
9. Sarkar, A. et al. Rare earth and transition metal based entropy stabilised perovskite type oxides. *J. Eur. Ceram. Soc.* **38**, 2318–2327 (2018).
10. Miracle, D. B. & Senkov, O. N. A critical review of high entropy alloys and related concepts. *Acta Mater.* **122**, 448–511 (2017).
11. Bérardan, D., Franger, S., Dragoe, D., Meena, A. K. & Dragoe, N. Colossal dielectric constant in high entropy oxides. *Phys. Status Solidi Res. Lett.* **10**, 328–333 (2016).
12. Dąbrowa, J. et al. Synthesis and microstructure of the $(Co,Cr,Fe,Mn,Ni)_3O_4$ high entropy oxide characterized by spinel structure. *Mater. Lett.* **216**, 32–36 (2018).
13. Wang, F. et al. Conversion reaction mechanisms in lithium ion batteries: study of the binary metal fluoride electrodes. *J. Am. Chem. Soc.* **133**, 18828–18836 (2011).
14. Poizot, P., Laruelle, S., Grugeon, S., Dupont, L. & Tarascon, J. M. Nano-sized transition-metal oxides as negative-electrode materials for lithium-ion batteries. *Nature* **407**, 496–499 (2000).
15. Chiang, Y.-M., Birnie, D. P. & Kingery, W. D. *Physical Ceramics: Principles for Ceramic Science and Engineering* (John Wiley & Sons, Inc., New York, 1997).
16. Helen, M. et al. Single step transformation of sulphur to Li_2S_2/Li_2S in Li-S batteries. *Sci. Rep.* **5**, 12146 (2015).
17. Ding, C. et al. A bubble-template approach for assembling Ni–Co oxide hollow microspheres with an enhanced electrochemical performance as an anode for lithium ion batteries. *Phys. Chem. Chem. Phys.* **18**, 25879–25886 (2016).
18. Sun, Y., Hu, X., Luo, W. & Huang, Y. Ultrathin CoO/graphene hybrid nanosheets: a highly stable anode material for lithium-ion batteries. *J. Phys. Chem. C* **116**, 20794–20799 (2012).
19. Suchomski, C. et al. Microwave synthesis of high-quality and uniform 4 nm $ZnFe_2O_4$ nanocrystals for application in energy storage and nanomagnetics. *Beilstein J. Nanotechnol.* **7**, 1350–1360 (2016).
20. Liu, H., Wang, G., Liu, J., Qiao, S. & Ahn, H. Highly ordered mesoporous NiO anode material for lithium ion batteries with an excellent electrochemical performance. *J. Mater. Chem.* **21**, 3046 (2011).
21. Wang, C. et al. Morphology-dependent performance of CuO anodes via facile and controllable synthesis for lithium-ion batteries. *ACS Appl. Mater. Interfaces* **6**, 1243–1250 (2014).
22. Goriparti, S. et al. Review on recent progress of nanostructured anode materials for Li-ion batteries. *J. Power Sources* **257**, 421–443 (2014).
23. Ji, L., Lin, Z., Alcoutlabi, M. & Zhang, X. Recent developments in nanostructured anode materials for rechargeable lithium-ion batteries. *Energy Environ. Sci.* **4**, 2682 (2011).
24. Murty, B. S., Yeh, J. W. & Ranganathan, S. *High-Entropy Alloys* (Butterworth-Heinemann, London, 2014)
25. Morcrette, M. et al. A reversible copper extrusion-insertion electrode for rechargeable Li batteries. *Nat. Mater.* **2**, 755–761 (2003).
26. Débart, A., Dupont, L., Patrice, R. & Tarascon, J. M. Reactivity of transition metal (Co, Ni, Cu) sulphides versus lithium: the intriguing case of the copper sulphide. *Solid State Sci.* **8**, 640–651 (2006).
27. Wang, Y. F. & Zhang, L. J. Simple synthesis of CoO-NiO-C anode materials for lithium-ion batteries and investigation on its electrochemical performance. *J. Power Sources* **209**, 20–29 (2012).
28. Mueller, F. et al. Iron-doped ZnO for lithium-ion anodes: impact of the dopant ratio and carbon coating content. *J. Electrochem. Soc.* **164**, A6123–A6130 (2017).
29. Bresser, D. et al. Transition-metal-doped zinc oxide nanoparticles as a new lithium-ion anode material. *Chem. Mater.* **25**, 4977–4985 (2013).
30. Reitz, C. et al. Hierarchical carbon with high nitrogen doping level: a versatile anode and cathode host material for long-life lithium-ion and lithium-sulfur batteries. *ACS Appl. Mater. Interfaces* **8**, 10274–10282 (2016).
31. de Biasi, L. et al. Between Scylla and Charybdis: balancing among structural stability and energy density of layered NCM cathode materials for advanced lithium-ion batteries. *J. Phys. Chem. C.* **121**, 26163–26171 (2017).
32. Kondrakov, A. O. et al. Anisotropic lattice strain and mechanical degradation of high- and low-nickel NCM cathode materials for Li-ion batteries. *J. Phys. Chem. C.* **121**, 3286–3294 (2017).
33. de Biasi, L. et al. Unravelling the mechanism of lithium insertion into and extraction from trirutile-type $LiNiFeF_6$ cathode material for Li-ion batteries. *CrystEngComm* **17**, 6163–6174 (2015).

Acknowledgements

One of the authors (Q.W.) acknowledges financial support by EnABLES. This project has received funding from the European Union's Horizon 2020 research and innovation program under Grant Agreement No 730957. H.H. and A.S. acknowledge financial support from the Helmholtz Association and the Deutsche Forschungsgemeinschaft (DFG) project HA/1344/43-1. We acknowledge support by Deutsche Forschungsgemeinschaft and Open Access Publishing Fund of Karlsruhe Institute of Technology.

Author contributions

A.S. synthesized the materials, fabricated the electrodes and performed the electrochemical experiments and analysis. L.V. synthesized the materials and analyzed HRTEM micrographs. D.W. and C.K. conducted and analyzed HRTEM and EDX measurements. G.T. supported the synthetic efforts. L.d.B. performed and analyzed operando XRD measurements. Q.W. prepared the electrodes with higher loading and helped with CV analysis. T.B. supervised the XRD measurements and co-wrote the manuscript. S.B. developed the material synthesis and supported the synthesis efforts. H.H. and B.B. supervised the synthesis and experiments, directed the project and co-wrote the manuscript.

Additional information

Supplementary Information accompanies this paper at https://doi.org/10.1038/s41467-018-05774-5.

Competing interests: The authors declare no competing interests.

Reprints and permission information is available online at http://npg.nature.com/reprintsandpermissions/

Publisher's note: Springer Nature remains neutral with regard to jurisdictional claims in published maps and institutional affiliations.

4. Fluorite type high entropy oxides

The fluorite structure is based on a *fcc* packing of the cations with all the tetrahedral interstices filled by the anions, as shown in Fig. 4.1. As per Paulings rule [36], fluorite structure can ideally form when the ratio of the cation to anion radii (r_c/r_a) is between 0.732 to 1, see Table 2.1. Hence, oxide systems like CeO_2, UO_2, etc., crystallize in fluorite structure where the cations in their 4+ oxidation states are large enough to accommodate the 8-fold coordination (CN). Yttria-stabilized-zirconia (YSZ) is another classic example of fluorite type oxide. However, ZrO_2 is monoclinic at room-temperature as the Zr^{4+} is too small to accommodate the 8-fold CN. Hence, doping with the larger Y^{3+} makes fluorite structure more favorable. The substitution of Zr^{4+} by Y^{3+} leads to the formation of oxygen vacancies (V_o) in order to maintain the charge neutrality of the system. The oxygen defects in fluorite type oxides lead to interesting properties, such as the enhancement in the O^{2-}-conductivity, change in the band gap, etc. [77–79]. Thus, fluorite type oxides (due to their inherent structural features and related doping) are of high technological importance and have several practical applications, e.g., as solid state electrolytes, thermal barrier coatings, catalysts, etc. [37, 78, 80]. The chemical diversity present in high entropy oxides can affect each of these properties, motivating the studies on fluorite type HEOs (F-HEOs).

F-HEOs are mostly comprised of bigger cations, lanthanides or the 5*d*/4*d* transition metals, which can accommodate 8-fold CN of oxygen. For instance, the r_c/r_a for $(Ce_{0.2}La_{0.2}Pr_{0.2}Sm_{0.2}Y_{0.2})O_{2-\delta}$ is

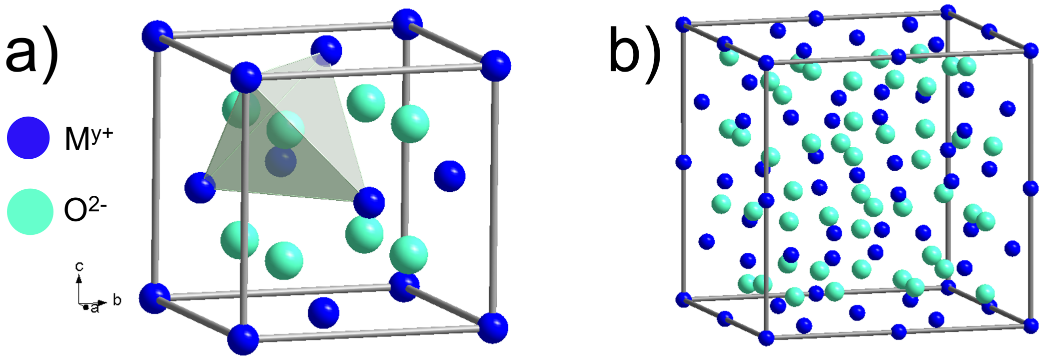

Figure 4.1.: Ball stick model of a) fluorite oxide, where the cations occupy the 4a (0,0,0) sites and anions occupy the 8c (¼,¼,¼) sites, and b) bixbyite oxides possessing two Wyckoff sites for the cations and the lattice volume is eight times that of fluorite.

0.76[1]. Currently, there are four published reports, which show the possibility to obtain single-phase F-HEOs with different compositions [15, 71, 81, 82]. In one of these reports the studied F-HEO, $(Ce_{0.2}Hf_{0.2}Sn_{0.2}Ti_{0.2}Zr_{0.2})O_2$, exhibits a typical entropy-driven phase transformation (see Section 2.2.5.), hence, falls under the group of entropy stabilized HEOs [71]. However, the majority of the F-HEOs systems [15, 81, 82] falls under the category of non-entropy stabilized HEOs. As discussed in Section 2.2.6., it is observed that Ce, due to its stable 4+ state, plays an important role in determining the (single) phase stability in these non-entropy stabilized F-HEOs. In fact, the entropy-stabilized F-HEO also contains Ce [71]. Although there are no base system as such in HEOs, due to the importance of cerium, CeO_2 can be considered as the host lattice for F-HEOs. However, the large fraction of 3+ cations in F-HEOs makes it unique, and the resulting concentration of V_o are expected to be much higher compared to conventional doped CeO_2 systems. This defect chemistry of F-HEOs is demonstrated below in Section 4.1. and 4.2., where a combination of spectroscopic approaches is adapted to understand the structural and chemical features of F-HEOs.

In terms of properties, F-HEOs exhibit lower thermal conductivity compared to YSZ [82].[2] The reduction in thermal conductivity in F-HEOs is consistent with reports on high entropy alloys (HEAs) and the reason for this behavior can be linked with the high chemical disorder, resulting in multiple phonon scattering [9, 25]. Simultaneously, the electrical conductivity in F-HEOs is also found to be an order magnitude lower than YSZ [82]. The reason for this finding can be related to structural distortion, resulting from the presence of several cations with different sizes. The hardness of F-HEOs is also found to be comparable (even in some cases slightly higher) to YSZ [82]. The combination of structural stability along with low thermal conductivity and high hardness make F-HEOs suitable candidates for thermal barrier coatings. Exploring the optical property of F-HEOs is another topic of interest, as oxides of the rare earth elements (which are also present in F-HEOs) exhibit interesting optical characteristics. In this context, a major part of Sections 4.1. and 4.2. deals with the effect of composition and atmosphere of heat-treatment on the optical properties of F-HEOs.

---

[1] r_c is the average radii of the constituent cations in 8-fold coordination, with the oxidation state of the cations are experimentally confirmed.

[2] The F-HEOs in this context contain Y and Zr [82], thus, the comparison with YSZ is valid.

4.1. Overview of publication III: Multicomponent equiatomic rare earth oxides with a narrow band gap and associated praseodymium multivalency

This article is a comprehensive study focusing on the influence of defect chemistry on the fundamental aspects of F-HEOs.[3] Several equiatomic compositions, starting from CeO_2 to $(Ce_{1/7}Gd_{1/7}Nd_{1/7}La_{1/7}Pr_{1/7}Sm_{1/7}Y_{1/7})O_{2-\delta}$, were investigated. It was observed that F-HEOs containing up to 6 different rare earth cations crystallized in a single phase fluorite structure directly upon synthesis, while a small amount of secondary phase was observed in the 7 cation system.

X-ray photoelectron spectroscopy (XPS) performed on the F-HEOs confirmed that most of the constituent rare earth elements were present in 3+ oxidation state, except for Ce and Pr, which were present in a 4+ and a 3+/4+ mixed state, respectively. Hence, a large concentration of oxygen vacancies (V_o) were formed as a result of the internal charge compensation. An intense broad band at ~570 cm^{-1} in the Raman spectra of F-HEOs confirmed the presence of V_o. Furthermore, an irreversible phase transition from fluorite to bixbyite was observed when F-HEOs were above 1000 °C in air. Bixbyite structure (see Fig. 4.1b) is a low symmetry oxygen deficient body centered cubic variant of the fluorite family, where one out of every four oxygen ions is missing. In case of F-HEOs, the large concentration of V_o gets ordered at higher temperatures leading to the irreversible transformation to bixbyite structure.

F-HEOs possess a characteristics dark brownish color, indicating lower optical band gap. Ultraviolet-visible-near infrared diffuse reflectance spectroscopy was performed and direct band gap values of ~2 eV were obtained for F-HEOs. These values are lower than the band gap values of the constituent parent oxides as depicted in Fig. 4.2. Typically, in metal oxides there is a direct correlation between the optical properties and V_o. However, in F-HEOs such a dependency was not evidenced and the band gap values were relatively invariant to the concentration of V_o. Upon further investigation, we observed that F-HEOs without Pr were pale whitish in color, and as a result the band gap values of those systems were close to 3 eV. Hence, an immediate relation between the presence of Pr and lowering of the band gap can be observed. It is deduced that the multivalent state $Pr^{3+,4+}$ leads to the formation of an intermediate energy state, which can furnish electronic excitation ~2 eV (see Fig. 4.2).

Hence, the present study highlights the cation-specific behavior in F-HEOs: Ce^{4+} stabilizes the single-phase fluorite structure, 3+ cations (like La, Sm and Y) result in oxygen vacancies (which drive the fluorite to bixbyite phase transition) and finally, the multivalent $Pr^{3+,4+}$ lowers the band gap.

---

[3] As discussed in Section 2.2.5, this group of F-HEOs does not exhibit a typical entropy-driven phase transformation. Hence, during the publication of this article a more general terminology, i.e., 'multicomponent equiatomic oxides', was used. Nevertheless, now the term HEOs is widely used in literature even to classify multicomponent equiatomic oxides, which do not show the typical entropy stabilization effect.

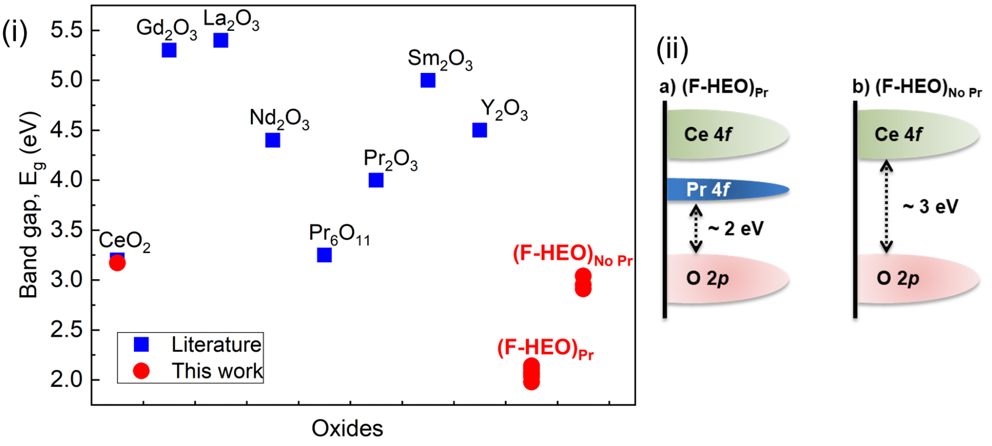

Figure 4.2.: (a) Comparison of the direct band gap values of the F-HEOs with binary rare earth oxides [45, 83–85], showing significant lowering of band gap in F-HEOs containing Pr. (b) Schematic of the energy band diagram of F-HEOs, with and without Pr.

4.2. Overview of publication IV: Role of intermediate $4f$ states in tuning the band structure of high entropy oxides

In this work, we attempt to reversibly tune the optical properties of a F-HEO composition, $(Ce_{0.2}La_{0.2}Pr_{0.2}Sm_{0.2}Y_{0.2})O_{2-\delta}$, and provide a comprehensive understanding of its dynamic electronic band structure. To alter the optical properties, heat-treatments at 750 °C were conducted under two different atmospheres, vacuum (VHT) and H_2 (H_2-HT), followed by re-heat treatment in air (RHT).

A fully reversible change of the band gap from 1.9 eV to 2.5 eV was observed upon VHT followed by RHT. The reversible change in the band gap was also reflected in terms of change in the powder color, from brownish to deep yellowish (upon VHT). The phase-purity of F-HEO was retained under all heat treatment conditions. *In-situ* and *ex-situ* electron energy loss spectroscopy (EELS) studies were conducted to study the effect of VHT. Shifting of the $M_{4,5}$ edges of Pr toward lower energy losses was observed upon VHT, indicating a lowering of its oxidation state. Likewise, reversal to the initial mixed oxidation state of Pr was observed upon RHT under air. A similar reversible trend in oxygen vacancies (V_o) concentration was evidenced from Raman spectroscopy.

Stronger reduction of F-HEO, achieved via H_2-HT, allowed for larger change of the band gap energy from 1.9 eV to 3.2 eV that could be reverted back to the initial state upon subsequent RHT in air. In addition, a reversible structural transition from fluorite to a single phase oxygen vacancy ordered C-type bixbyite structure was observed. Raman spectroscopy further strengthened this reversible behavior, as local chemical features before H_2-HT and after RHT were identical. However, the H_2-HT (unlike VHT) sample resulted in two additional Raman bands, which could not be assigned to any features known for the isostructural variants of the constituent rare earth oxides. X-ray absorption near edge spectra (XANES), using soft and hard X-rays, indicated that the crystal structure transition from fluorite to bixbyite could be correlated to the mild reduction of Ce^{4+} to mixed $Ce^{4+,3+}$ state, which further highlighted the importance of Ce^{4+} in stabilizing the fluorite structure in this group of F-HEOs. On the other hand, the tuning of the band gap energy was related to the reduction of Pr. The changes in the Pr L_3 and $M_{3,4}$ edges upon H_2-HT were rather prominent, signifying a transition from $Pr^{4+,3+}$ to a pure Pr^{3+} state. However, the complete picture of the band structure could be drawn from the changes observed in the O K-edge XANES. In case of the oxidized F-HEOs, i.e., as-synthesized or RHT, two distinct pre-edge features could be observed in the O K-edge XANES. The lowest energy feature originated from the Pr $4f$-O $2p$ hybridization, while other pre-edge was related to the Ce $4f$-O $2p$ hybridization. In fact, these features are the antibonding/conduction bands arising from the respective hybridization and are often regarded simply as the Pr $4f$ and Ce $4f$ bands. Thus, in the oxidized F-HEO the band gap correlates to the electronic transition from the bonding/valence bands (V.B.) to the Pr $4f$ band, laying around 2 eV from the V.B. However, in case of the H_2-HT sample the feature related to the Pr $4f$ band completely disappeared, which indicated that the Pr $4f$ states got occupied. Hence, the lowest energy electronic transition possible was only to the Ce $4f$ band, positioned around 3.2 eV from the V.B. Irrespective of the heat treatment, strong absorption in the O K-edge XANES occurred only above 2 eV from the Ce $4f$ feature, which indicated that the antibonding states arising from the hybridization of majority of the RE $5d$-O $2p$ orbitals are located around 5 eV from the V.B. Hence, it can be summarized that in F-HEO Ce and Pr lead to the formation of intermediate energy states resulting in a narrow band gaps, while the unoccupied state arising hybridization of the other constituent 3+ cations with oxygen is above 5 eV from the V.B.

Apart from this high temperature thermal based tuning approach, a pressure based tuning of the optical features of F-HEO was also attempted in collaboration with Center for High Pressure Science and Technology Advanced Research, Pudong, China. A reversible tuning of the band gap could be obtained but the extent of the tuning ($\Delta \sim 0.3$ eV) was found to be rather small compared to the thermal (atmosphere) based tuning [86].

Statement of personal contribution

1. **Multicomponent equiatomic rare earth oxides with a narrow band gap and associated praseodymium multivalency**
   A. Sarkar, C. Loho, L. Velasco, T. Thomas, S. S. Bhattacharya, H. Hahn and R. Djenadic, *Dalton Transactions* 46, 12167 (2017)
   Reprinted with permission from *Dalton Transactions*, ©2017, THE ROYAL SOCIETY OF CHEMISTRY.

   The experiments were planned by myself under the supervision of Dr. R. Djenadic and Prof. H. Hahn. The synthesis, characterization (except for XPS and TEM) and data analysis was performed by myself. Dr. C. Loho conducted XPS measurements and Dr. L. Velasco performed the TEM measurements, while the analysis of the data was performed by myself. Prof. S.S. Bhattacharya and Prof. T. Thomas were involved in several scientific discussions related to the project. The manuscript was written by myself with feedback from all co-authors.

2. **Role of intermediate 4f states in tuning the band structure of high entropy oxides**
   A. Sarkar, B. Eggert, L. Velasco, X. Mu, J. Lill, K. Ollefs, S. S. Bhattacharya, H. Wende, R. Kruk, R. A. Brand, H. Hahn, *APL Materials* 8, 051111 (2020)
   Reprinted under the terms of the CC BY 4.0 license.

   The experiments were planned by myself under the supervision of Prof. H. Hahn. The synthesis, characterization (except for TEM/EELS) and data analysis was performed by myself. Dr. L. Velasco and Dr. X. Mu performed the TEM/EELS measurements, while the data analysis was done by myself. Beamtime at DESY, Hamburg and BESSY, Berlin were attended by B. Eggert, Dr. L. Velasco, J. Lill and myself. Analysis of the XANES spectra was done by B. Eggert, J. Lill and myself in discussion with Dr. R.A. Brand and Dr. R. Kruk. Prof. S.S. Bhattacharya, Prof. H. Wende and Dr. K. Ollefs were involved in scientific discussions which benefited the project. The manuscript was written by myself with comments from all co-authors.

Dalton Transactions

PAPER

View Article Online
View Journal | View Issue

Cite this: *Dalton Trans.*, 2017, **46**, 12167

Multicomponent equiatomic rare earth oxides with a narrow band gap and associated praseodymium multivalency†

Abhishek Sarkar, *[a,b] Christoph Loho,[b] Leonardo Velasco,[a] Tiju Thomas,[c] Subramshu S. Bhattacharya,[c] Horst Hahn*[a,b,d] and Ruzica Djenadic‡[b,d]

Received 7th June 2017,
Accepted 18th August 2017

DOI: 10.1039/c7dt02077e

rsc.li/dalton

New multicomponent equiatomic rare earth oxides (ME-REOs) containing 3–7 rare earth elements (Ce, Gd, La, Nd, Pr, Sm and Y) in equiatomic proportions are synthesized using nebulized spray pyrolysis. All the systems crystallized as a phase pure fluorite type ($Fm\bar{3}m$) structure in spite of the high chemical complexity. A nominal increase in the lattice parameter compared to CeO_2 is observed in all ME-REOs. X-ray photoelectron spectroscopy performed on the ME-REOs confirmed that all the constituent rare earth elements are present in the 3+ oxidation state, except for Ce and Pr which are present in 4+ and in a mixed (3+/4+) oxidation state, respectively. The presence of Ce^{4+} contributes substantially to the observed stability of the single phase structure. These new oxide systems have narrow direct band gaps in the range of 1.95–2.14 eV and indirect band gaps in the range of 1.40–1.64 eV, enabling light absorption over the entire visible spectral range. Furthermore, the oxygen vacancy concentration rapidly increases and then saturates with the number of rare earth elements that are incorporated into the ME-REOs. The lowering of the band gap is found to be closely related to the presence of multivalent Pr. Interestingly, the band gap values are relatively invariant with respect to the composition or thermal treatments. Considering the high level of oxygen vacancies present and the observed low band gap values, these new material systems can be of importance where the presence of oxygen vacancies is essential or in applications where a narrow band gap is desirable.

1. Introduction

Materials shape our world and discoveries of new ones create novel opportunities and challenges. Recently, a group of researchers[1] decided to deviate from the conventional binary or doped oxides and pioneered the field of multicomponent equiatomic oxides (MEOs). This new class of materials is also known as entropy stabilized oxides due to the high configurational entropy of the systems, caused by the presence of multiple cations in equiatomic amounts. These oxides show interesting transport properties[2,3] and can be obtained by using different synthesis methods.[4,5] Until the discovery of MEOs, the idea of multicomponent equiatomic systems had more or less been limited to random solid solutions in metals known as high entropy alloys (HEAs).[6] It has been recently shown that the concept of MEOs is not only limited to transition metal-based oxides,[1] but can be extended to rare earth-based oxides also.[7] In these new multicomponent equiatomic rare earth oxides (ME-REOs), up to seven different rare earth cations (predominantly in the 3+ oxidation state) can be mixed in equiatomic amounts (unlike doping) and successfully accommodated into a single-phase fluorite ($Fm\bar{3}m$) type structure. This result is fascinating considering the fact that except for CeO_2 and PrO_2, all the binary oxides of the remaining constituent rare earth elements have crystal structures other than fluorite. Furthermore, the oxides of the constituent rare earth elements are not completely miscible (at an equiatomic ratio) according to their binary phase diagrams.[8] It has also been found that unlike the entropy dominated structure stabilization, as

---

[a] Institute of Nanotechnology, Karlsruhe Institute of Technology, Hermann-von-Helmholtz-Platz 1, 76344 Eggenstein-Leopoldshafen, Germany. E-mail: abhishek.sarkar@kit.edu, horst.hahn@kit.edu

[b] Joint Research Laboratory Nanomaterials – Technische Universität Darmstadt and Karlsruhe Institute of Technology, Alarich-Weiss-Str. 2, 64287 Darmstadt, Germany

[c] Department of Metallurgical and Materials Engineering, Indian Institute of Technology Madras, Chennai-600036, India

[d] Helmholtz Institute Ulm – Electrochemical Energy Storage, Helmholtzstr. 11, 89081 Ulm, Germany

† Electronic supplementary information (ESI) available: Table containing the details of Rietveld refinements, table and graphs showing variation of lattice parameters with respect to cationic radii, XRD patterns and Tauc plots for ME-REO systems without Pr. See DOI: 10.1039/c7dt02077e

‡ Present address: Heraeus Deutschland GmbH & Co. KG, Heraeusstr. 12–14, 63450 Hanau, Germany.

observed in the case of transition metal-based MEOs,[1] the presence of Ce in the 4+ oxidation state determines the stability of the single phase in the ME-REOs. This has been confirmed by the fact that all the ME-REO systems without Ce are not phase pure, regardless of the thermal treatment performed.[7] The study[7] has not only extended the broad spectrum of research on multicomponent oxide systems but also added a fresh insight by demonstrating that factors other than entropy can be used to stabilize simple structures and design new multicomponent material systems.

For several decades, rare earth oxides have been known for their interesting optical, electronic and chemical properties. They have been deployed in a wide range of applications such as phosphors, sunscreen cosmetics, magneto-optical devices, catalysts, biomarkers, colorants for special glasses, solid electrolytes, *etc*.[9] Each of these fields, in principle, may be influenced by ME-REOs owing to the cumulative effect of multiple RE cations. Out of the many rare earth oxides, ceria (CeO_2) has been widely studied due to its wide band gap and non-stoichiometry. The observed non-stoichiometry arises from the presence of oxygen vacancies making ceria an excellent material for UV light blockers, gas sensors, oxygen storage capacitors, catalysts and solid oxide fuel cells.[9–11] Several studies[12,13] have also focused on engineering the band gap of ceria in order to make it active in the visible light range. Making a material photoactive in the visible region leads to possibilities such as its use in photocatalytic applications.[14,15]

In this investigation, we follow-up on our previous article on ME-REOs,[7] introducing high resolution transmission electron microscopy (HR-TEM) and spectroscopic studies like X-ray photoelectron spectroscopy (XPS), UV-Vis spectroscopy and Raman spectroscopy in order to gain a deeper understanding of the structure and properties of these newly discovered materials. Information about the defect structure of these materials and its effect on their band gap is extracted from the combined spectroscopic studies.

2. Experimental section

2.1. Powder synthesis

ME-REOs containing 3–7 rare earth cations (Ce, Gd, La, Nd, Pr, Sm, and Y) in equiatomic amounts are synthesized from water-based solutions of rare earth nitrates using nebulized spray pyrolysis (NSP). CeO_2 and a binary cation system, $(Ce_{0.5}Pr_{0.5})O_2$, which are the reference systems, are synthesized using the same technique. The powders are further calcined at 1000 °C for 1 hour in air to study the effect of thermal treatment on the crystal structure and the optical properties. The detailed description of the experimental setup and synthesis procedure has been reported in our previous study.[7]

2.2. Powder characterization

The room temperature X-ray diffraction (XRD) patterns are recorded using a Bruker D8 Advance diffractometer with Bragg–Brentano geometry equipped with an X-ray tube with a Cu anode and a Ni filter. The Rietveld refinements are carried out using TOPAS 5[16] to gain information about the lattice parameters, phase compositions, crystallite sizes and lattice strains. The detailed description of the refinement parameters has been previously reported.[7]

Specimens for transmission electron microscopy (TEM), from the as-synthesized and calcined powders, are prepared by directly dispersing the finely ground powders onto a standard carbon coated copper grid. A Philips Technai F20 ST electron microscope (operating at 200 kV) is used to examine the specimens.

The oxidation states of all the elements in the representative samples of the as-synthesized and calcined system, $(Ce_{0.2}La_{0.2}Pr_{0.2}Sm_{0.2}Y_{0.2})O_{2-\delta}$, are determined using XPS, which is performed using a PHI 5000 spectrometer equipped with a monochromatic Al Kα excitation source. A charge neutralizer with low-energy electrons is used to compensate and minimize charging effects in the investigated oxides.

The UV-Vis spectra are recorded in the range from 200 nm to 1200 nm using a PerkinElmer Lambda 900 spectrophotometer. From the obtained spectra, optical band gaps are determined by applying the Tauc relation:[17]

$$[F(R_\infty)\cdot h\nu]^{1/n} = A\cdot(h\nu - E_g) \tag{1}$$

where $F(R_\infty)$ is the Kubelka–Munk function, h is the Planck's constant, ν is the vibrational frequency, A is a constant, and E_g is the band gap energy. The exponent n denotes the nature of the optical transitions. The values of $n = \frac{1}{2}$ and $n = 2$ are used for direct and indirect allowed transitions, respectively. The band gap (direct and indirect) energy values are calculated from linear regression at the inflection point of the $[F(R_\infty)\cdot h\nu]^{1/n}$ *vs.* $h\nu$ (Tauc) plots. The obtained $h\nu$-intercept values are taken as the band gap values.

The Raman spectra are recorded with a confocal micro-Raman spectrometer, Horiba Jobin Yvon HR 800, using a 633 nm He–Ne laser in the range of 300–1000 cm^{-1}. All the spectra are the result of 40 accumulations, each lasting for 20 s.

3. Results and discussion

3.1. XRD and TEM studies

Fig. 1 shows the X-ray diffraction (XRD) patterns for the as-synthesized (Fig. 1a) and calcined (Fig. 1b) powders. In our previous study,[7] the detailed structural analyses confirmed that the as-synthesized systems with 3 to 6 rare earth cations crystallize into a single phase fluorite ($Fm\bar{3}m$) type structure. The volume-weighted mean crystallite sizes of the ME-REOs (ranging from 7 nm to 10 nm) are obtained from the Rietveld analysis of the XRD patterns using TOPAS 5.[16] A small amount (~3 wt%) of secondary phase (La_2O_3 prototype), alongside the main fluorite type phase, is formed in the case of the 7 component system. The possible reason for the formation of the secondary phase can be the sluggish diffusion due to the

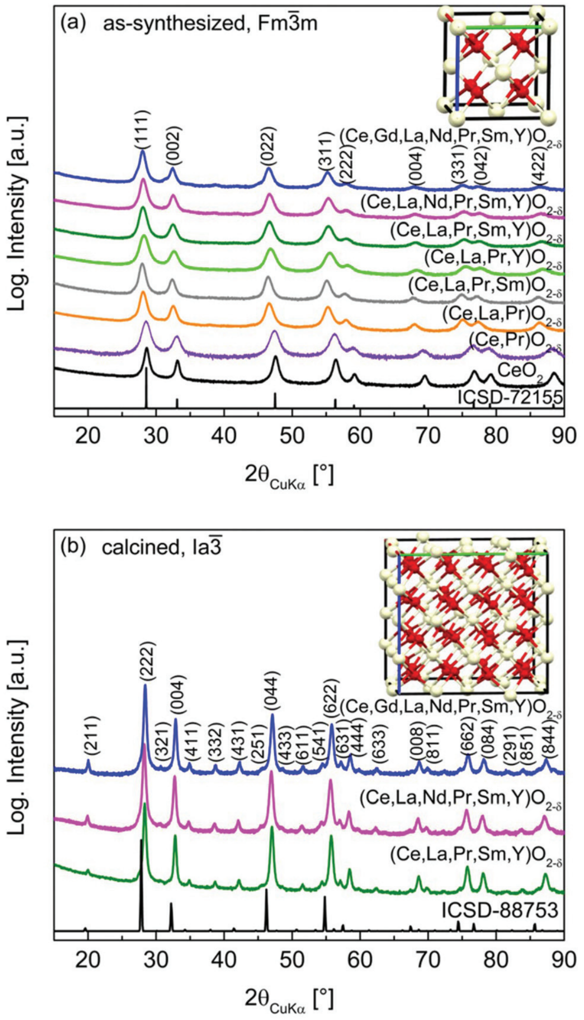

Fig. 1 XRD patterns of (a) the as-synthesized, *Fm*$\bar{3}$*m* and (b) calcined, *Ia*$\bar{3}$ ME-REO powders confirming their phase purity. The ICSD patterns are the simulated patterns of *Fm*$\bar{3}$*m* (ICSD 72155) and *Ia*$\bar{3}$ (ICSD 88753) structures.

increased number of cations, which are competing for the same position in the crystal lattice.[7] An increase in the lattice parameter compared to that of CeO_2 (see ESI, Table S1†) is observed for all the ME-REOs. The reason for lattice expansion is closely related to the oxidation state of the constituent cations and is explained in section 3.3.

Based on the structure, the general formula for ME-REOs is chosen to be $(RE)O_{2-\delta}$, where RE depends on the type and the number of elements (in equiatomic amounts) present in their alphabetical order. For instance, the sample containing five RE elements, *e.g.*, Ce, La, Pr, Sm, and Y, is labeled as $(Ce,La,Pr,Sm,Y)O_{2-\delta}$ indicating that all five cations are present in equiatomic amounts, *i.e.*, $(Ce_{0.2}La_{0.2}Pr_{0.2}Sm_{0.2}Y_{0.2})O_{2-\delta}$. The reason for the oxygen non-stoichiometry is discussed in detail in section 3.2. Upon calcination at 1000 °C, the as-synthesized powders undergo a lowering of the crystal symmetry from the fluorite (*Fm*$\bar{3}$*m*) to a bixbyite (*Ia*$\bar{3}$) type structure (a body centered subgroup of *Fm*$\bar{3}$*m*). This is evident from the additional superstructure reflections (like (211), (321), (431), *etc.*) observed in the XRD patterns (Fig. 1b) of the calcined powders. No signature of a secondary/impurity phase is observed in any of the calcined systems (see ESI, Table S1†). The mean crystallite sizes in the calcined powders are larger than that of the as-synthesized ones, but still remain in the nanometer range (29–34 nm).

HR-TEM imaging is performed on the as-synthesized and calcined $(Ce,La,Pr,Sm,Y)O_{2-\delta}$ powders, which are considered as representatives for all the systems. Both the as-synthesized and calcined samples are highly crystalline with well-defined lattice fringes that are observed for most of the particles (Fig. 2(a) and (b)). The lattice parameters of both the as-synthesized and calcined powders obtained from the selected area diffraction (SAED) patterns (Fig. 2(c) and (d)) are in good agreement with the results obtained from the Rietveld refinements (see ESI, Table S1†). In the case of the calcined samples, additional weak diffraction rings corresponding to the less intense superstructure reflections ((211), (431), *etc.*) for the lower symmetry (*Ia*$\bar{3}$) structure are observed in the SAED pattern (Fig. 2d). These weak diffraction rings are absent in the SAED pattern for the as-synthesized powder (Fig. 2c), having the higher symmetry fluorite (*Fm*$\bar{3}$*m*) type structure. These results are in good agreement with the previously discussed XRD results.

3.2. XPS studies

The oxidation states of the elements present in the as-synthesized as well as in the calcined $(Ce,La,Pr,Sm,Y)O_{2-\delta}$ powders are determined using XPS analysis. The XPS spectra of the calcined $(Ce,La,Pr,Sm,Y)O_{2-\delta}$ powder (Fig. 3) are identical to those obtained from the as-synthesized sample, ruling out any change in oxidation states during calcination. In the La 3d spectra, two doublets, at around 834 and 850 eV, are observed, which indicate the presence of La^{3+}, and is in good agreement with the reported literature results.[18] Two bands corresponding to $3d_{5/2}$ and $3d_{3/2}$ are observed in the 3d spectra of Sm at around 1080 eV and 1110 eV, respectively. These bands indicate the presence of Sm in the 3+ oxidation state.[19]

The 3d spectra of Y are in agreement with those reported in the literature[20] confirming that Y is present in the 3+ oxidation state. Unlike other lanthanide atoms (present in ME-REOs), Ce and Pr are often associated with multiple oxidation states (*i.e.*, 3+ and 4+). The reason for this is their electronic configuration and the related *in situ* redox reaction between their 3+ and 4+ oxidation states.[21] In the case of Ce, the 4+ ($4f^0$) state is more stable than Ce^{3+} ($4f^1$). In ME-REOs, Ce is found to be present in the 4+ oxidation state. This is because its 3d spectra show three distinct doublets similar to the ones observed for Ce^{4+} in CeO_2.[22] Ce^{4+} is found to contribute substantially to the stabilization of the single phase in ME-REOs. This is evidenced by the fact that the ME-REO systems without Ce are not phase pure, regardless of the number of RE elements present or the

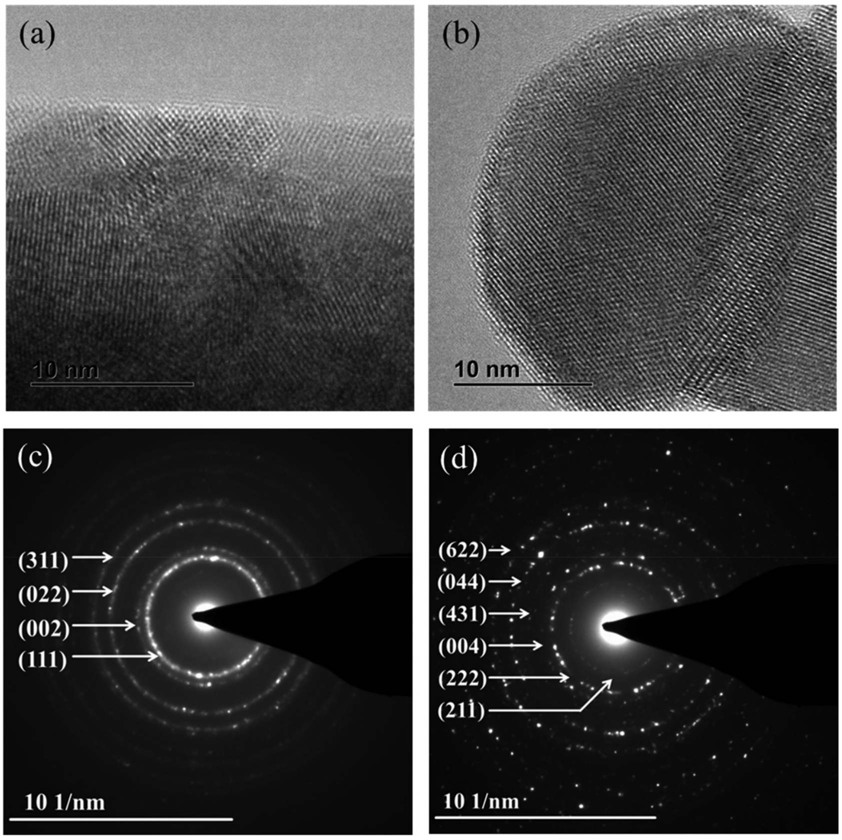

Fig. 2 HR-TEM micrographs (a and b) and SAED patterns (c and d) for the as-synthesized and calcined (Ce,La,Pr,Sm,Y)$O_{2-\delta}$ powders, respectively. The TEM results are in good agreement with the XRD results.

thermal treatment performed.[7] However, the presence of a minor amount of Ce^{3+} cannot be excluded. In the case of Pr ($4f^3$ $6s^2$), the possibility of a mixed (3+ and 4+) oxidation state is higher than that in Ce.[21] The 3d spectra of Pr in ME-REOs indicate the multivalent state of Pr owing to its close resemblance to that of Pr_6O_{11}.[23,24] Also the XRD pattern of the pure Pr-oxide (synthesized using the same method under similar conditions) matched the one of Pr_6O_{11} closely rather than PrO_2 or Pr_2O_3.[7] Additionally, the linear fitting of the variation in the lattice parameters with respect to the average cationic radii (see ESI, Fig. S1† and the related discussion), for different ME-REOs, indicates the presence of a mixed valence state of Pr (with the ratio of Pr^{3+} to Pr^{4+} close to that in Pr_6O_{11}). The presence of a higher amount of Pr^{4+} is also in good agreement with the literature[25] where it is observed that the existence of Pr^{4+} is often favored by the presence of Ce^{4+} and other RE^{3+} cations in the system. The oxidation states of the RE elements in the other ME-REOs (reported here) are the same as in (Ce,La,Pr,Sm,Y)$O_{2-\delta}$, as similar experimental (synthesis/calcination) conditions are used for all the systems. The presence of the elements in both 3+ and 4+ oxidation states justifies the selection of the general non-stoichiometric formula, (RE)$O_{2-\delta}$, for ME-REOs.

3.3. UV-Vis spectroscopy

The ultraviolet-visible (UV-Vis) absorption spectra of all the as-synthesized (RE)$O_{2-\delta}$ systems (Fig. 4a) are similar, exhibiting strong absorption below 650 nm, which is consistent with the dark brown color of the powders (see the inset in Fig. 4a). On the other hand, pure CeO_2, synthesized under similar conditions as a reference for (RE)$O_{2-\delta}$, is pale yellow and exhibits strong absorption only below 450 nm. The absorption spectra of the calcined systems (Fig. 4b) are very similar to those of the as-synthesized ones, indicating that symmetry lowering has a minimal effect on the optical properties of these systems. In both the as-synthesized and calcined systems containing Sm and Nd, several distinct absorption bands in the region from 750 nm to 1100 nm are observed. The prominent absorption bands found at 750 nm, 815 nm and 885 nm are related to the transition from the $4f^N$ ground state to the excited-state of the Nd^{3+} ion ($^4I_{9/2} \rightarrow {}^4F_{7/2}, {}^4S_{3/2}$), ($^4I_{9/2} \rightarrow {}^4F_{5/2}, {}^2H_{9/2}$), and ($^4I_{9/2} \rightarrow {}^4F_{3/2}$),[26] respectively. The absorption band in the infrared region (at 1080 nm) is related to the $^6H_{5/2} \rightarrow {}^6F_{9/2}$ transition of the Sm^{3+} ion.[27] Based on these findings and XPS results, the following conclusion regarding the oxidation states of the RE atoms in the ME-REOs can be drawn: Ce^{4+}, Gd^{3+}, La^{3+}, Nd^{3+},

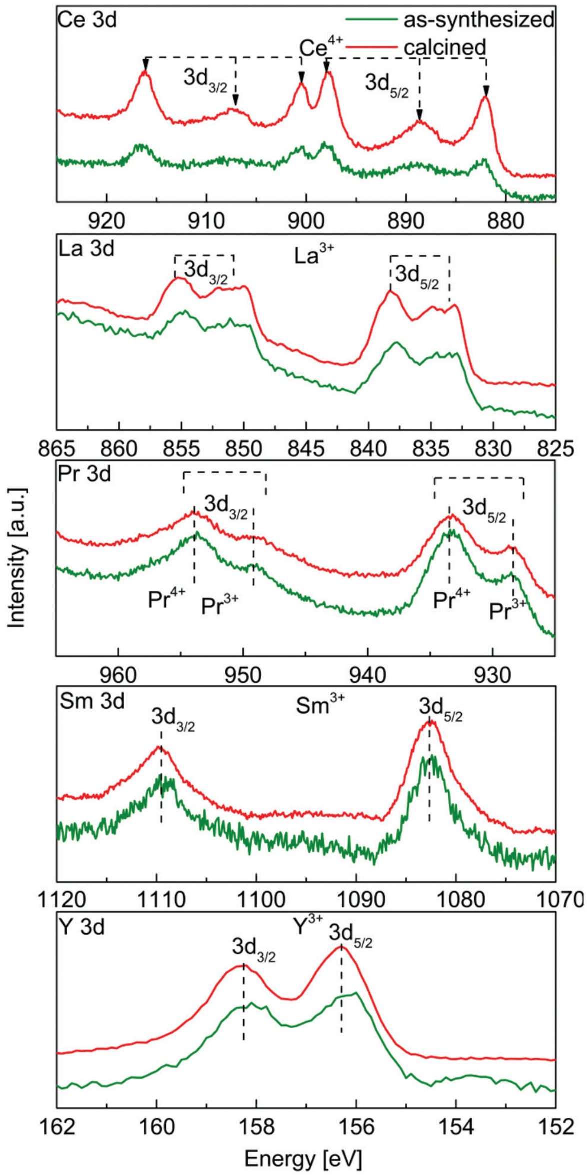

Fig. 3 XPS spectra of the as-synthesized and calcined (Ce,La,Pr,Sm,Y) $O_{2-\delta}$ powders as the representatives of $(RE)O_{2-\delta}$ systems showing no effect of calcination on the oxidation states of RE elements.

Sm^{3+}, Y^{3+} and Pr in mixed 3+ and 4+ states. The observed oxidation states can explain the expansion of the crystal lattice of ME-REOs compared to that of ceria as mentioned in section 3.1., *i.e.*, the substitution of smaller Ce^{4+} (0.94 Å) by other larger rare earth cations like Gd^{3+} (1.05 Å), La^{3+} (1.16 Å), Nd^{3+} (1.10 Å), *etc.*, in ME-REOs. The linear variation of the lattice parameters as a function of average cationic radii (see ESI, Fig. S1b† and the related discussion), for different ME-REOs, follows the Vegard's law.[28]

The band gap values of the ME-REO systems are determined from Tauc plots, $[F(R_\infty)\cdot h\nu]^{1/n}$ *vs.* $h\nu$, using the procedure described in the Experimental section. Fig. 4c and d display the Tauc plots only for the as-synthesized and calcined $(Ce,La,Pr,Sm,Y)O_{2-\delta}$ systems (which are the representative samples).

The direct band gap values (Fig. 4c) are found to be 2.06 eV and 2.03 eV for the as-synthesized and calcined $(Ce,La,Pr,Sm,Y)O_{2-\delta}$ samples, respectively. The indirect band gap values (Fig. 4d) are even lower: 1.52 eV for the as-synthesized and 1.60 eV for the calcined powders. As the electronic structure of ME-REOs is unknown, both direct and indirect band gap values for all the ME-REO systems (as-synthesized and calcined) are calculated and reported in Table 1. However, for further discussion, only the direct band gap values are considered. This decision is made based on the reports pertaining to CeO_2, which can be considered as the parent structure of ME-REOs (owing to their structural similarities). Even though the electronic structure of CeO_2 is still being debated and both direct as well as indirect band gap values are often reported,[29,30] it is believed[31,32] that direct rather than indirect transitions take place in ceria.

It can be observed from Table 1 that the band gap values are similar for both the as-synthesized and the calcined ME-REO systems (in the range of 1.98–2.14 eV) and are also relatively independent of the number of RE elements. Clearly, the change in the structure during calcination, *i.e.*, the lowering of the symmetry from $Fm\bar{3}m$ to $Ia\bar{3}$ has no significant influence on the optical response of the $(RE)O_{2-\delta}$ systems. This offers substantial compositional as well as structural flexibility without compromising their visible light absorption capabilities, which could be of importance for their practical applications. The most interesting result is that the band gap values (both direct and indirect) of ME-REOs are significantly lower when compared to the band gap values of any of the binary rare earth oxides or even many of the doped rare earth oxides.[30,33–37]

3.4. Raman spectroscopy

Oxygen vacancies are frequently associated with band gap narrowing in many oxides, including CeO_2.[32] Therefore, considering a perfect fluorite structure, like CeO_2, the presence of oxygen defects could be the possible reasons for the observed band gap narrowing in $(RE)O_{2-\delta}$. The formation of oxygen vacancies in ME-REOs can be attributed to the fact that except for Ce^{4+} and $Pr^{3+/4+}$, all other rare earth cations are present in the 3+ oxidation state. In order to maintain the charge balance, oxygen vacancies ($V_O^{\bullet\bullet}$) are created according to the following defect formation reaction written in the Kröger–Vink notation (M'_{RE} – RE^{3+} on the RE^{4+} site; $O_O^{\times}$ – oxygen on the oxygen site, no charge):

$$M_2O_3 \xrightarrow{(RE)O_2} 2M'_{RE} + 3O_O^{\times} + V_O^{\bullet\bullet} \qquad (2)$$

As all the cations are in equiatomic proportions, the concentration of oxygen vacancies is much higher than in any of the doped or non-stoichiometric binary rare oxides. In order to understand if the oxygen vacancies could be responsible for

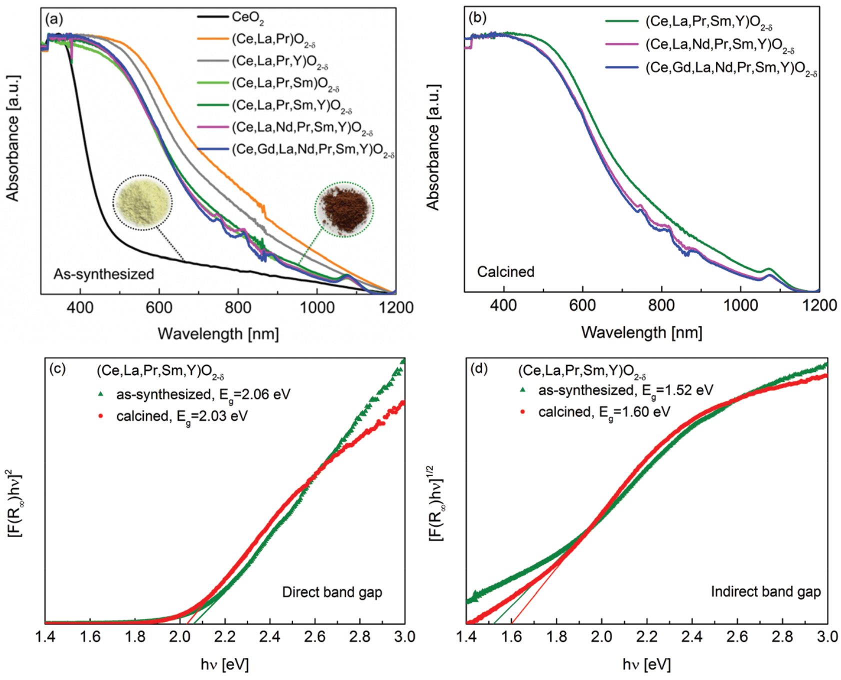

Fig. 4 UV-Vis absorption spectra of (a) the as-synthesized and (b) calcined (RE)$O_{2-\delta}$ powders showing strong absorption in the visible light region unlike CeO_2 powder. The insets in (a) show the colors of the as-synthesized powders. Tauc plots, $[F(R_\infty)\cdot h\nu]^{1/n}$ *vs.* $h\nu$, of the as-synthesized and calcined (Ce,La,Pr,Sm,Y)$O_{2-\delta}$ systems with $n = \frac{1}{2}$ for direct band gap (c) and $n = 2$ for indirect band gap (d) determination.

Table 1 Summary of the direct and indirect band gap energy (E_g) values (in eV) of the as-synthesized ($Fm\bar{3}m$) and calcined ($Ia\bar{3}$) (RE)$O_{2-\delta}$ powders

Systems	Direct E_g	Indirect E_g
As-synthesized, $Fm\bar{3}m$		
CeO_2	3.17	2.76
(Ce,La,Pr)$O_{2-\delta}$	1.95	1.42
(Ce,La,Pr,Y)$O_{2-\delta}$	1.98	1.50
(Ce,La,Pr,Sm)$O_{2-\delta}$	2.14	1.56
(Ce,La,Pr,Sm,Y)$O_{2-\delta}$	2.06	1.52
(Ce,La,Nd,Pr,Sm,Y)$O_{2-\delta}$	2.12	1.62
(Ce,Gd,La,Nd,Pr,Sm,Y)$O_{2-\delta}$	2.11	1.64
Calcined, $Ia\bar{3}$		
(Ce,La,Pr,Sm,Y)$O_{2-\delta}$	2.03	1.60
(Ce,La,Nd,Pr,Sm,Y)$O_{2-\delta}$	2.06	1.56
(Ce,Gd,La,Nd,Pr,Sm,Y)$O_{2-\delta}$	2.08	1.58

this significant band gap lowering, the amounts of oxygen vacancies are estimated using the following considerations: (i) RE^{3+} and RE^{4+} exclusively form $(RE)_2O_3$ and $(RE)O_2$, respectively, where the oxygen stoichiometry (x) in $(RE)_2O_3$ is 1.5 and in $(RE)O_2$ is 2 and (ii) $(RE)O_{2-\delta}$ systems contain RE elements in both 3+ and 4+ oxidation states (Ce^{4+}, Gd^{3+}, La^{3+}, Nd^{3+}, $Pr^{4+/3+}$, Sm^{3+}, and Y^{3+}). Thus, the oxygen stoichiometry in $(RE)O_{2-\delta}$ can then be expressed as:

$$x = 1.5\cdot[RE^{3+}] + 2\cdot[RE^{4+}] \tag{3}$$

where $[RE^{3+}]$ and $[RE^{4+}]$ are the molar fractions of RE cations in 3+ and 4+ oxidation states, respectively. Therefore, the deviation from stoichiometry, *i.e.*, the amount of oxygen vacancies (δ) can be estimated from:

$$\delta = 2 - x \tag{4}$$

Table 2 gives an overview of the level of oxygen vacancies calculated based on the XPS/UV-Vis results according to eqn (3) and (4). From Table 2 it is clear that the oxygen defect concentration increases as the number of RE cations in the 3+ oxidation state increases. Therefore, Raman spectroscopy is performed on the systems for further investigation of the oxygen vacancies due to its high sensitivity towards lattice defects.

Table 2 Overview of the estimated level of oxygen vacancies (δ) in the as-synthesized powders based on eqn (3) and (4). $[RE^{3+}]$ and $[RE^{4+}]$ represent the molar fractions of RE in 3+ and 4+ oxidation states, respectively, and x represents oxygen stoichiometry

Systems, $Fm\bar{3}m$	$[RE^{3+}]$	$[RE^{4+}]$	x	δ
CeO_2	0.00	1.00	2	0
(Ce,Pr)$O_{2-\delta}$	0.17	0.83	1.92	0.08
(Ce,La,Pr)$O_{2-\delta}$	0.45	0.55	1.78	0.22
(Ce,La,Pr,Y)$O_{2-\delta}$	0.50	0.50	1.71	0.29
(Ce,La,Pr,Sm)$O_{2-\delta}$	0.50	0.50	1.71	0.29
(Ce,La,Pr,Sm,Y)$O_{2-\delta}$	0.60	0.40	1.67	0.33
(Ce,La,Nd,Pr,Sm,Y)$O_{2-\delta}$	0.67	0.33	1.64	0.36
(Ce,Gd,La,Nd,Pr,Sm,Y)$O_{2-\delta}$	0.72	0.28	1.62	0.38

The Raman spectra, obtained using a He–Ne laser source (λ = 633 nm), for different ME-REOs are shown in Fig. 5. For CeO_2, a single sharp band at 464 cm^{-1} is observed. This band is attributed to the F_{2g} symmetric vibration mode of the 8-fold Ce–O bond in the fluorite type structure. This vibrational mode is often used for the comparison of various ceria based or related systems.[38] As mentioned earlier, CeO_2 can be considered as the parent structure of ME-REOs ($(RE)O_{2-\delta}$), wherein all the different RE elements substitute Ce. Thus, the F_{2g} band is also observed in the Raman spectra of the ME-REOs (Fig. 5). The frequency of this signal is expected to be independent of the metal identity and hence, the cation mass.[38] However, the position of the band shows a strong red shift (~15 cm^{-1}) for the ME-REOs with respect to CeO_2. Shifting of this F_{2g} band along with broadening is a common feature often related[39,40] to chemical substitutions, which lead to the expansion of the crystal lattices, variation in the M–O bond lengths and formation of oxygen defects. These reasons are valid for ME-REOs as well. The lattice parameter for the as-synthesized CeO_2 is 5.42 Å, while for all ME-REOs, a relative expansion of the crystal lattice is observed, as mentioned in section 3.3. Furthermore, it is observed that the intensity of the F_{2g} band is the strongest for pure CeO_2 and gradually decreases with the addition of more elements, for all ME-REOs, which is in good agreement with the results reported in the literature.[39,41] The intensity lowering of the band is mainly related to the formation of a multicomponent solid solution (consisting of various rare earth elements) in ME-REOs, which leads to symmetry breaking of the ceria lattice and hence, affects the F_{2g} symmetric vibration mode. Except for CeO_2, an additional broad band centered at ~570 cm^{-1} is observed for all the other systems. This band (V_o in Fig. 5) is related to the oxygen vacancies present in the systems.[19,32,39] The ratio of the integral intensity of the band corresponding to the oxygen vacancies (II_{V_o}) to the integral intensity corresponding to the F_{2g} band ($II_{F_{2g}}$) portrays the relative oxygen vacancy concentration. In some cases,[19,32] instead of a single broad band at ~570 cm^{-1}, two separate bands (at ~550 cm^{-1} and ~600 cm^{-1}) are observed which are also related to the defect states. In that case, the summation of the integral intensities of both defect bands are used instead of the single II_{V_o} to calculate the relative oxygen vacancy concentration.[19] Although this ratio, $II_{V_o}/II_{F_{2g}}$, does not provide quantitative information about the amount of oxygen vacancies, it is often used as a reliable tool to compare the amount of oxygen defects present in different systems.[19,39,42]

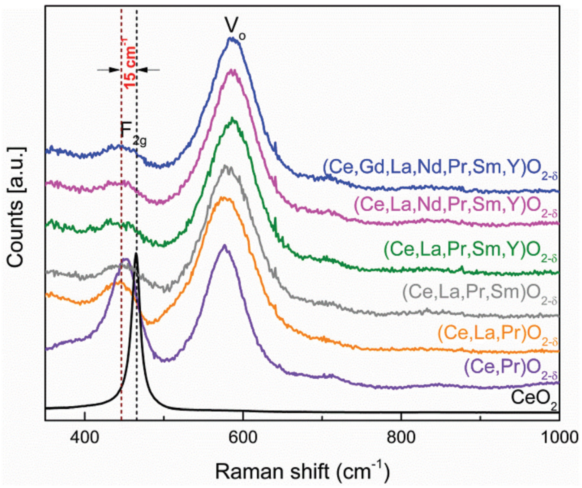

Fig. 5 Raman spectra of pure CeO_2 and different ME-REOs obtained using a He–Ne laser (λ = 633 nm). The F_{2g} vibration mode for ceria lies at 465 cm^{-1} whereas for the ME-REOs a red shift (~15 cm^{-1}) is observed. An additional broad band (~570 cm^{-1}) is observed for all the ME-REOs, which is related to the oxygen vacancies (V_o) present in the structure.

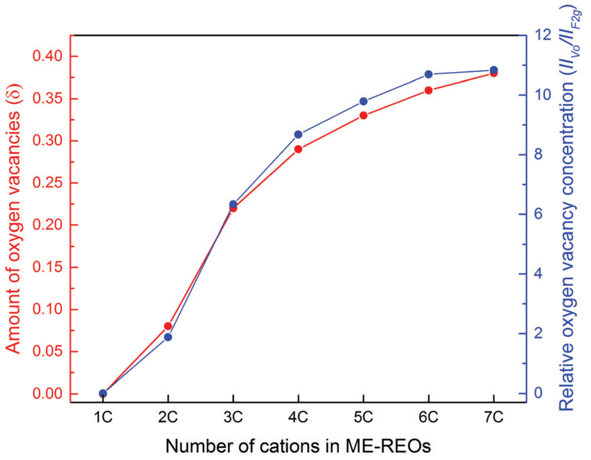

Fig. 6 Comparison of the amount of oxygen vacancies (δ) calculated from the charge balance equation (see eqn (4)) and the relative oxygen vacancy concentration estimated from the Raman spectra ($II_{V_o}/II_{F_{2g}}$), as a function of the number of cations in ME-REOs, where 1C = CeO_2, 2C = $(Ce,Pr)O_{2-\delta}$, 3C = $(Ce,La,Pr)O_{2-\delta}$, 4C = $(Ce,La,Pr,Sm)O_{2-\delta}$, 5C = $(Ce,La,Pr,Sm,Y)O_{2-\delta}$, 6C = $(Ce,La,Nd,Pr,Sm,Y)O_{2-\delta}$ and 7C = $(Ce,Gd,La,Nd,Pr,Sm,Y)O_{2-\delta}$.

Fig. 6 displays the amount of oxygen vacancies (δ) calculated from the charge balance approach (see Table 2 and eqn (4)) as well as the relative oxygen vacancy concentration ($II_{V_o}/II_{F_{2g}}$) obtained from the Raman spectra of different ME-REOs. The relative oxygen vacancy concentration obtained from Raman spectroscopy shows a rapid increase with the increase in the number of elements. It then saturates when the number of elements becomes higher than 6. This variation follows a trend similar to the variation of the amount of oxygen vacancies (δ) calculated from the charge balance equation using the XPS and UV-Vis data.

3.5. Possible reasons for the band gap narrowing

The narrowing of the band gap, in several systems,[43–45] is often related to the formation of intermediate energy states due to the presence of point defects, like oxygen vacancies. The same is likely true for ME-REOs, especially considering the high amount of oxygen vacancies present in these systems. Interestingly, the change in the band gap values in ME-REOs is not directly related to the change in the amount of oxygen vacancies (compare Tables 1 and 2). Furthermore, in oxide systems, like CeO_2 or TiO_2, where oxygen vacancies are often identified as the reason for the band gap narrowing, a decrease of band gap energy by only 0.32 eV (ref. 46) or 0.30 eV,[44] respectively, is observed. However, considering CeO_2 as the parent structure of ME-REOs, the extent of the band gap narrowing in ME-REOs is more than 1 eV, which indicates that some additional factors other than oxygen vacancies are likely involved in the band gap narrowing.

The presence of certain multivalent elements is known to have a strong impact on the band gap, and hence, the light absorption behavior, in some systems, like Cu doped ZnO[14] and Pr doped CeO_2.[21] In the case of ME-REOs, the presence of Pr in a multivalent state can be one of the reasons for the observed band gap narrowing. To ensure the validity of this reasoning, three different ME-REO systems without Pr (*i.e.*, $(Ce,La,Sm)O_{2-\delta}$, $(Ce,La,Sm,Y)O_{2-\delta}$ and $(Ce,La,Nd,SmY)O_{2-\delta}$) are synthesized. The XRD analysis (see ESI, Fig. S2-a† and the related discussion) shows that these systems are phase pure and also have a fluorite type of structure just like the ME-REOs with Pr. However, the band gap values (see ESI, Fig. S2b†) of these three ME-REO systems (without Pr) are in the range of 2.90–3.05 eV, *i.e.*, around 1 eV higher than the ME-REO systems with Pr. The band gap values of these three systems are also close to that of CeO_2 (3.2 eV) and the small difference in the values (0.30–0.15 eV) is related to the oxygen defects present in the systems. Hence, it is concluded that Pr plays a dominant role in the band gap narrowing of ME-REOs.

Based on these results, a possible schematic of the band structure of ME-REOs (Fig. 7) is discussed in the following lines. In rare earth oxides, most of the RE elements have their O 2p and RE 5d energy levels at relatively similar positions. However, the position of occupied and unoccupied RE 4f energy bands, which are located in between O 2p and RE 5d energy bands, plays a crucial role in determining the type of electronic transition and, therefore, the band gap value. In most of the RE sesquioxides, the band gap values are related to electronic transitions from O 2p to RE 5d or 5d + $4f_{\text{unoccupied}}$ energy bands (as in La_2O_3 or Sm_2O_3, respectively),[47] as shown in Fig. 7, case I. The 5d + $4f_{\text{unoccupied}}$ is relevant for those lanthanides whose unoccupied 4f bands fall into the 5d energy band.[47] The electronic transitions in the case of CeO_2 occur from the O 2p to Ce 4f energy level (see Fig. 7, case II) and these transitions are activated due to the inherent oxygen vacancies present in ceria.[47,48] In ME-REOs without Pr, the electronic transitions are possibly very similar to that in ceria, while the presence of oxygen vacancies might have narrowed down the gap between the O 2p and Ce 4f energy levels (see Fig. 7, case III). In Pr substituted CeO_2 systems, it is believed that an additional Pr 4f band, between the O 2p and Ce 4f, is present.[49] The same is likely to be true for ME-REOs with Pr. Thus, the band gap of ~2 eV in ME-REOs with Pr can be related to the electronic transition between the O 2p to Pr 4f, which lies at ~1 eV (ref. 49) below the Ce 4f energy band (see Fig. 7, case IV).

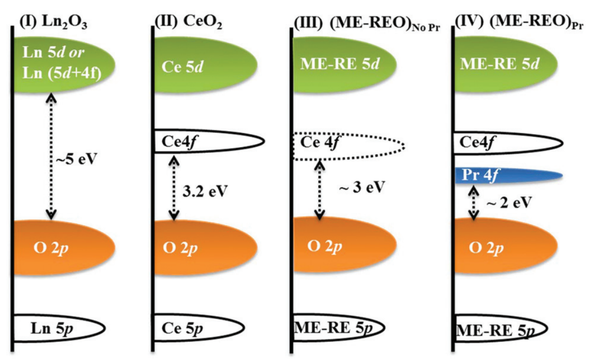

Fig. 7 Schematic of the band structures of Ln_2O_3, where Ln = Gd^{3+}, La^{3+}, Sm^{3+}, *etc*. (case I), CeO_2 (case II), ME-REOs without Pr (case III) and ME-REOs with Pr (case IV), depicting the possible mechanism for band gap narrowing.

4. Conclusions

In this work, newly discovered multicomponent equiatomic rare oxides (ME-REOs) are investigated using a combination of diffraction and spectroscopic techniques. The results show that while Ce has a strong impact on the crystal structure and phase purity of the ME-REOs, their optical properties are related to the presence of multivalent Pr. The band gap energies of ME-REOs containing Pr are in the range of 1.95–2.14 eV, enabling light absorption over the entire visible spectral range. The presence of rare earth (RE) cations in oxidation states other than 4+ results in the formation of oxygen vacancies in the ME-REOs, which is confirmed by Raman spectroscopy. A combination of Ce and Pr in the ME-REO systems helps to achieve both phase purity and a lower band gap, which are largely independent of the other RE cations present. This provides great flexibility for engineering the amount of defects (oxygen vacancies) or/and allows element-based property tuning (by adding the required cations) without compromising the phase purity or the visible light absorbing capability of ME-REOs. Further studies on ME-REOs are likely to focus on visible light absorption and oxygen vacancy related research and applications. In parallel, theoretical studies to model the electronic structure of these new oxides will be very helpful.

Conflicts of interest

The authors declare no competing financial interest.

Acknowledgements

The authors would like to thank the Helmholtz Association (Germany) for financial support through the Helmholtz

Portfolio Project "Electrochemical Storage in Systems – Reliability and Integration", Prof. Dr Heinz von Seggern and Elmar Kersting (Technische Universität Darmstadt, Germany) for providing access to the UV-Vis spectrophotometer, and Prof. Dr Oliver Clemens and Prof. Dr Christian Hess (Technische Universität Darmstadt, Germany) for fruitful discussions. Leonardo Velasco thanks the Karlsruhe Nano Micro Facility (KNMF, Germany) and Dr Christian Kübel for providing access to TEM at KIT. Tiju Thomas thanks the Department of Science and Technology, Government of India for financial support through projects (DST file no. YSS/2015/001712 and DST 11-IFA-PH-07), and the Fast Track Young Scientist Award.

References

1 C. M. Rost, E. Sachet, T. Borman, A. Moballegh, E. C. Dickey, D. Hou, J. L. Jones, S. Curtarolo and J.-P. Maria, *Nat. Commun.*, 2015, **6**, 8485.

2 D. Bérardan, S. Franger, D. Dragoe, A. K. Meena and N. Dragoe, *Phys. Status Solidi RRL*, 2016, **10**, 328–333.

3 D. Bérardan, S. Franger, A. K. Meena and N. Dragoe, *J. Mater. Chem. A*, 2016, **4**, 9536–9541.

4 Z. Rak, C. M. Rost, M. Lim, P. Sarker, C. Toher, S. Curtarolo, J.-P. Maria and D. W. Brenner, *J. Appl. Phys.*, 2016, **120**, 95105.

5 A. Sarkar, R. Djenadic, N. J. Usharani, K. P. Sanghvi, V. S. K. Chakravadhanula, A. S. Gandhi, H. Hahn and S. S. Bhattacharya, *J. Eur. Ceram. Soc.*, 2017, **37**, 747–754.

6 B. S. Murty, J. W. Yeh and S. Ranganathan, *High-Entropy Alloys*, Butterworth-Heinemann, London, 2014.

7 R. Djenadic, A. Sarkar, O. Clemens, C. Loho, M. Botros, V. S. K. Chakravadhanula, C. Kübel, S. S. Bhattacharya, A. S. Gandhi and H. Hahn, *Mater. Res. Lett.*, 2017, **5**, 102–109.

8 S. J. Schneider and R. S. Roth, *J. Res. Natl. Bur. Stand., Sect. A*, 1960, **64**, 317.

9 G. Adachi, N. Imanaka and Z. C. Kang, *Binary Rare Earth Oxides*, Kluwer Academic Publishers, Dordrecht, 2005.

10 A. M. D'Angelo, A. C. Y. Liu and A. L. Chaffee, *J. Phys. Chem. C*, 2016, **120**, 14382–14389.

11 M. Balaguer, C. Solís, S. Roitsch and J. M. Serra, *Dalton Trans.*, 2014, **43**, 4305–4312.

12 C. Mao, Y. Zhao, X. Qiu, J. Zhu and C. Burda, *Phys. Chem. Chem. Phys.*, 2008, **10**, 5633.

13 S. Kumar, A. K. Ojha, D. Patrice, B. S. Yadav and A. Materny, *Phys. Chem. Chem. Phys.*, 2016, **18**, 11157–11167.

14 N. Mary Jacob, G. Madras, N. Kottam and T. Thomas, *Ind. Eng. Chem. Res.*, 2014, **53**, 5895–5904.

15 A. Chaudhary, M. P. Nag, N. Ravishankar, T. Thomas, M. Jain and S. Raghavan, *J. Phys. Chem. C*, 2014, **118**, 29788–29795.

16 *Topas V5, General profile and structure analysis software for powder diffraction data, User's Manual*, Bruker AXS, Karlsruhe, Germany, 2015.

17 J. Tauc, R. Grigorovici and A. Vancu, *Phys. Status Solidi*, 1966, **15**, 627–637.

18 A. Machocki, T. Ioannides, B. Stasinska, W. Gac, G. Avgouropoulos, D. Delimaris, W. Grzegorczyk and S. Pasieczna, *J. Catal.*, 2004, **227**, 282–296.

19 M. Guo, J. Lu, Y. Wu, Y. Wang and M. Luo, *Langmuir*, 2011, **27**, 3872–3877.

20 P. De Rouffignac, J. Park and R. G. Gordon, *Chem. Mater.*, 2005, **17**, 4808–4814.

21 K. Ahn, D. S. Yoo, D. H. Prasad, H. W. Lee, Y. C. Chung and J. H. Lee, *Chem. Mater.*, 2012, **24**, 4261–4267.

22 J. P. Holgado, R. Alvarez and G. Munuera, *Appl. Surf. Sci.*, 2000, **161**, 301–315.

23 S. Lütkehoff, M. Neumann and A. Ślebarski, *Phys. Rev. B: Condens. Matter*, 1995, **52**, 13808–13811.

24 I. Tankov, B. Pawelec, K. Arishtirova and S. Damyanova, *Appl. Surf. Sci.*, 2011, **258**, 278–284.

25 M. Balestrieri, S. Colis, M. Gallart, G. Schmerber, M. Ziegler, P. Gilliot and A. Dinia, *J. Mater. Chem. C*, 2015, **3**, 7014–7021.

26 N. Rakov and G. S. Maciel, *J. Mater. Chem. C*, 2016, **4**, 5442–5447.

27 N. Shasmal, K. Pradeep and B. Karmakar, *RSC Adv.*, 2015, **5**, 81123–81133.

28 S. Omar, E. D. Wachsman and J. C. Nino, *Solid State Ionics*, 2008, **178**, 1890–1897.

29 T. M. Inerbaev, A. S. Karakoti, S. V. N. T. Kuchibhatla, A. Kumar, A. E. Masunov and S. Seal, *Phys. Chem. Chem. Phys.*, 2015, **17**, 6217–6221.

30 Z. C. Orel and B. Orel, *Phys. Status Solidi B*, 1994, **186**, K33–K36.

31 S. Tsunekawa, T. Fukuda and A. Kasuya, *J. Appl. Phys.*, 2000, **87**, 1318.

32 A. Filtschew, K. Hofmann and C. Hess, *J. Phys. Chem. C*, 2016, **120**, 6694–6703.

33 A. V. Prokofiev, A. I. Shelykh and B. T. Melekh, *J. Alloys Compd.*, 1996, **242**, 41–44.

34 G. Adachi and N. Imanaka, *Chem. Rev.*, 1998, **98**, 1479–1514.

35 S. Zinatloo-Ajabshir and M. Salavati-Niasari, *New J. Chem.*, 2015, **39**, 3948–3955.

36 Y.-N. Xu, Z. Gu and W. Y. Ching, *Phys. Rev. B: Condens. Matter*, 1997, **56**, 14993–15000.

37 Z. Wang, Z. Quan and J. Lin, *Inorg. Chem.*, 2007, **46**, 5237–5242.

38 C. Artini, M. Pani, M. M. Carnasciali, M. T. Buscaglia, J. R. Plaisier and G. A. Costa, *Inorg. Chem.*, 2015, **54**, 4126–4137.

39 N. Paunović, Z. Dohčević-Mitrović, R. Scurtu, S. Aškrabić, M. Prekajski, B. Matović and Z. V. Popović, *Nanoscale*, 2012, **4**, 5469.

40 B. M. Reddy, G. Thrimurthulu, L. Katta, Y. Yamada and S.-E. Park, *J. Phys. Chem. C*, 2009, **113**, 15882–15890.

41 A. Dubey, S. K. Kolekar and C. S. Gopinath, *ChemCatChem*, 2016, **8**, 3650–3656.

42 A. S. Babu, R. Bauri and G. S. Reddy, *Electrochim. Acta*, 2016, **209**, 541–550.

43 J. Wang, Z. Wang, B. Huang, Y. Ma, Y. Liu, X. Qin, X. Zhang and Y. Dai, *ACS Appl. Mater. Interfaces*, 2012, **4**, 4024–4030.

44 A. K. Rumaiz, J. C. Woicik, E. Cockayne, H. Y. Lin, G. H. Jaffari and S. I. Shah, *Appl. Phys. Lett.*, 2009, **95**, 262111.

45 B. Huang, R. Gillen and J. Robertson, *J. Phys. Chem. C*, 2014, **118**, 24248–24256.

46 S. A. Ansari, M. M. Khan, M. O. Ansari, S. Kalathil, J. Lee and M. H. Cho, *RSC Adv.*, 2014, **4**, 16782.

47 R. Gillen, S. J. Clark and J. Robertson, *Phys. Rev. B: Condens. Matter*, 2013, **87**, 125116.

48 C. W. M. Castleton, J. Kullgren and K. Hermansson, *J. Chem. Phys.*, 2007, **127**, 244704.

49 J. J. Kim, S. R. Bishop, D. Chen and H. L. Tuller, *Chem. Mater.*, 2017, **29**, 1999–2007.

APL Materials

Role of intermediate 4*f* states in tuning the band structure of high entropy oxides

Cite as: APL Mater. **8**, 051111 (2020); https://doi.org/10.1063/5.0007944
Submitted: 17 March 2020 . Accepted: 21 April 2020 . Published Online: 19 May 2020

Abhishek Sarkar, Benedikt Eggert, Leonardo Velasco, Xiaoke Mu, Johanna Lill, Katharina Ollefs, Subramshu S. Bhattacharya, Heiko Wende, Robert Kruk, Richard A. Brand, and Horst Hahn

AIP Publishing

APL Mater. **8**, 051111 (2020); https://doi.org/10.1063/5.0007944 **8**, 051111

APL Materials ARTICLE scitation.org/journal/apm

Role of intermediate 4*f* states in tuning the band structure of high entropy oxides

Cite as: APL Mater. 8, 051111 (2020); doi: 10.1063/5.0007944
Submitted: 17 March 2020 • Accepted: 21 April 2020 •
Published Online: 19 May 2020

Abhishek Sarkar,[1,2,a)] **Benedikt Eggert,**[3] **Leonardo Velasco,**[2] **Xiaoke Mu,**[2] **Johanna Lill,**[3] **Katharina Ollefs,**[3] **Subramshu S. Bhattacharya,**[4] **Heiko Wende,**[3] **Robert Kruk,**[2] **Richard A. Brand,**[2,3] **and Horst Hahn**[1,2,b)]

AFFILIATIONS

[1] Joint Research Laboratory Nanomaterials – Technische Universität Darmstadt and Karlsruhe Institute of Technology, Otto-Berndt-Str. 3, 64287 Darmstadt, Germany

[2] Institute of Nanotechnology, Karlsruhe Institute of Technology, Hermann-von-Helmholtz-Platz 1, 76344 Eggenstein-Leopoldshafen, Germany

[3] Faculty of Physics and Center for Nanointegration Duisburg-Essen (CENIDE), University of Duisburg-Essen, Lotharstr. 1, 47057 Duisburg, Germany

[4] Nano Functional Material Technology Centre (NFMTC), Department of Metallurgical and Materials Engineering, Indian Institute of Technology Madras, 600036 Chennai, India

[a)] **Author to whom correspondence should be addressed:** abhishek.sarkar@kit.edu
[b)] **Electronic mail:** horst.hahn@kit.edu

ABSTRACT

High entropy oxides (HEOs) are single-phase solid solutions consisting of 5 or more cations in approximately equiatomic proportions. In this study, we show the reversible control of optical properties in a rare-earth (RE) based HEO-$(Ce_{0.2}La_{0.2}Pr_{0.2}Sm_{0.2}Y_{0.2})O_{2-\delta}$ and subsequently utilize a combination of spectroscopic techniques to derive the features of the electronic band structure underpinning the observed optical phenomena. Heat treatment of the HEO under a vacuum atmosphere followed by reheat treatment in air results in a reversible change in the bandgap energy, from 1.9 eV to 2.5 eV. The finding is consistent with the reversible changes in the oxidation state and related *f*-orbital occupancy of Pr. However, no pertinent changes in the phase composition or crystal structure are observed upon the vacuum heat treatment. Furthermore, annealing of this HEO under a H_2 atmosphere, followed by reheat treatment in air, results in even larger but still a reversible change in the bandgap energy from 1.9 eV to 3.2 eV. This is accompanied by a disorder–order type crystal structure transition and changes in the O 2*p*–RE 5*d* hybridization evidenced from x-ray absorption near-edge spectra (XANES). The O *K* and RE $M_{4,5}/L_3$ XANES indicate that the presence of Ce and Pr (in 3+/4+ states) leads to the formation of intermediate 4*f* energy levels between the O 2*p* and the RE 5*d* gap in HEO. It is concluded that heat treatment under reducing/oxidizing atmospheres affects these intermediate levels, thus offering the possibility to tune the bandgap energy in HEOs.

I. INTRODUCTION

High entropy oxides (HEOs) were first reported in 2015,[1] and since then the topic has gained significant interest, which is evident from numerous published reports focusing on different aspects of HEOs.[2–10] HEOs can be broadly defined as single-phase solid solution oxides containing 5 or more cations in near-equiatomic compositions. The presence of multiple cations in comparable amounts leads to an enhanced configurational entropy of mixing (S_{config}), which is calculated using the Boltzmann statistical entropy equation.[1,3,11] The term "high entropy oxide" is typically used when the S_{config} of a given oxide system is above 1.5 R.[3,5,6,12] One of the most intriguing characteristics of HEOs is the phase purity despite their compositional complexity. Interestingly, the underlying principle for phase purity is distinct in different HEOs. For instance, in some systems a dominant role of entropy has been evidenced, which effectively overcomes the related enthalpic penalties and stabilizes a single-phase solid solution at high temperatures.[1,13,14]

However, in the majority of HEOs a pertinent role of configurational entropy in stabilizing the phase composition and structure has not been observed, whereas factors such as the oxidation states of specific cations and lattice strain effects govern their phase composition.[3,5,6,15,16] Irrespective of the phase stability mechanisms, the high entropy based design approach in oxides offers an extended compositional flexibility along with retention of the phase purity. Hence, compositions close to the central regions of multi-component oxide phase diagrams can be studied, where interesting synergies can be anticipated. A wide range of crystal structures and functional features exhibited by HEOs can be linked to their unique composition and related synergies.[4,6–10,17–24] Nevertheless, disentangling the role of individual elements is one of the major challenges in HEOs.

In our previous studies, we have explored the possibility to synthesize several single-phase fluorite type HEOs (F-HEOs) by populating the cationic sublattice with 5 or more rare-earth (RE) elements.[15,25] By comparing these compositions, we have observed that the presence of Pr in F-HEOs results in a lowering of the bandgap energy. Hence, we speculated that Pr due to its mixed 3+/4+ oxidation state in F-HEOs forms an intermediate unoccupied energy state, which facilitates lower energy electronic transitions of ~2 eV.[25] Understanding the electronic band structure of conventional binary rare-earth oxides is still a subject of both theoretical and practical interest.[26–28] However, the theoretical band structure calculations for complex F-HEOs are not straightforward. Hence, in this current study, we use different spectroscopic techniques to investigate the validity of our hypothesized energy band diagram in a representative F-HEO composition, $(Ce_{0.2}La_{0.2}Pr_{0.2}Sm_{0.2}Y_{0.2})O_{2-\delta}$. Initially, by means of heat treatment under reducing (vacuum/hydrogen) or oxidizing atmospheres, we have observed reversible changes in bandgap energies. The changes in the oxidation states of the RE elements and related variations in the f and d electronic shell occupancy are studied using x-ray absorption spectroscopy (XAS) and electron energy loss spectroscopy (EELS), which primarily indicates the role of internal redox reactions in determining the electronic characteristics of F-HEOs. Although this kind of redox reaction driven bandgap tuning mechanism is known for simple metal oxides,[29,30] such a possibility has not yet been explored for HEOs. Furthermore, the accompanying physico-chemical changes such as large concentrations of oxygen vacancies, reversible disorder–order transition, and Raman features upon H_2-treatment make the F-HEO different. Hence, this study not only elucidates the dynamic band structure of the F-HEO but also provides a deeper structural insight into these compositionally complex systems.

II. EXPERIMENTAL

A. Synthesis

The F-HEO, $(Ce_{0.2}La_{0.2}Pr_{0.2}Sm_{0.2}Y_{0.2})O_{2-\delta}$, was synthesized from water-based precursor solutions of the corresponding rare-earth nitrates using reverse co-precipitation (RCP) techniques. The precursor solution was added to a basic ammonia solution (pH = 10) in a controlled fashion along with continuous stirring of the mixture at ambient conditions. The formed precipitates were dried at 120 °C and further calcined at 750 °C in air to achieve the desired crystallographic phase. The temperature, 750 °C, has been determined based on the reports of the F-HEO synthesized by the nebulized spray pyrolysis method.[15] The powders obtained after this first 750 °C heat-treatment step in air are defined as the as-synthesized ("as-syn") samples. The as-synthesized samples were subsequently heat treated under different atmospheres, where the temperature, dwell time, and ramping rates (for both heating and cooling) were 750 °C, 2 h, and 10 °C/min, respectively. The heat-treatment conditions were as follows:

- Mildly reducing atmosphere: Vacuum heat treatment (VHT), corresponding to 10^{-7} mbar pressure.
- Highly reducing atmosphere: Heat treatment with flow of a 5% hydrogen–argon mixture (H_2-HT), with a gas flow rate of 50 standard liters per minute.
- Re-heat treatment under air: This was carried out after the VHT or H_2-HT, using the respective VHT/H_2-HT powder. Hence, the samples obtained are termed as RHT (meaning "re-heat treated" in air).

B. Structural and electronic characterization

All the measurements were performed at room temperature, if not stated otherwise.

1. **X-ray diffraction (XRD)**: XRD patterns were recorded using a Bruker D8 Advance diffractometer with the Bragg–Brentano geometry equipped with an x-ray tube having a Cu anode and a Ni filter. The Rietveld analysis of the XRD patterns was done using TOPAS V.5.0.[31] The instrumental intensity distributions were determined using a reference scan of LaB_6 (NIST 660a).
2. **High resolution transmission electron microscopy (HR-TEM), energy dispersive x-ray spectroscopy (EDS), and electron energy loss spectroscopy (EELS)**: Specimens for TEM were prepared by directly dispersing the finely ground powders onto a standard carbon coated copper grid. A FEI Titan 80–300 aberration (imaging Cs) corrected transmission electron microscope equipped with a Gatan Tridiem 863 image filter operated at 300 kV was used to examine the specimens. EELS spectra were collected in the TEM mode (an objective aperture of 30 μm, a convergence semi-angle of <0.5 mrad, a dispersion of 0.1 eV/channel, a collection semi-angle of 15 mrad, and an acquisition time of 5 s) and in the scanning TEM (STEM) mode (a condenser aperture of 70 μm, a convergence semi-angle of 14 mrad, a dispersion of 0.1 eV/channel, a collection semi-angle of 16 mrad, and an acquisition time of 5 s). EDS maps were collected in the STEM mode.
3. **Ultraviolet-visible (UV-Vis) spectroscopy**: The UV-Vis spectra were recorded in the diffuse reflectance mode in the range from 200 nm to 1200 nm using a PerkinElmer Lambda 900 spectrophotometer. From the obtained spectra, optical bandgaps were determined by applying the Tauc relation,[32]

$$[F(R_\infty)h\nu]^{1/n} = A(h\nu - E_g),$$

where $F(R_\infty)$ is the Kubelka–Munk function, h is Planck's constant, ν is the incident frequency, A is a constant, and E_g is the bandgap energy. The exponent n denotes the nature of the optical transitions. In this study, $n = 1/2$ has been used, which is valid for direct allowed transitions. The bandgap energy values were calculated from linear regression at the inflection point of the $[F(R_\infty)h\nu]^2$ vs hν (Tauc) plots. The obtained $h\nu$-intercept values were taken as the bandgap values.

4. **Raman spectroscopy**: Raman spectra were recorded using a Renishaw Raman microscope using the infrared (785 nm) laser and green (532 nm) laser in the range of 200–2000 cm^{-1}, with a spot size of ~1 μm and a laser power of 0.5 mW. All the spectra were the result of 10 accumulations, each lasting 20 s.
5. **X-ray absorption spectroscopy (XAS)**: XAS was utilized to study the valence states and the chemical environment of different constituents. For the investigation of the RE 4*f* and O 2*p* states, measurements were performed in the soft x-ray regime at the XUV diffractometer endstation, located at the beamline UE46_PGM-1[33] (BESSY II, Berlin), while for the investigation of the RE 5*d* states, measurements in the hard x-ray regime were performed at the beamline P65[34] (PETRA III, Hamburg). Due to the large difference of the used photon energy, different measurement procedures were used. For the (room temperature) measurements in the soft x-ray regime (O 2*p* and RE 4*f* states), the sample powder was pressed into indium foil to ensure electrical grounding, while the signal was measured in total electron yield (TEY). In the hard x-ray regime (RE-5*d* edges), the sample powder was pressed into a pellet, while the absorption measurements were performed in the transmission mode at 10 K. Because of the presence of many atomic species in these samples, careful subtraction of the background signal was necessary. More fundamentally, because of the computational difficulty in calculating the near-edge spectra from first principles in these complex mixed oxides, we have restricted our analysis here to a description of individual white line changes and comparisons with well established literature results. A recent review of the possibilities of XANES studies has been given by Henderson *et al.*[35] and in a larger context by Wende.[36]

III. RESULTS

The results obtained for heat treatment of $(Ce_{0.2}La_{0.2}Pr_{0.2}Sm_{0.2}Y_{0.2})O_{2-\delta}$-F-HEO in vacuum differ significantly to those obtained when heat-treated in a hydrogen atmosphere. Hence, two subsections specific to the heat-treating atmosphere are made.

A. Vacuum heat treatment

1. Changes in the optical properties upon VHT

The as-synthesized F-HEO powder has been subjected to vacuum heat treatment (VHT) followed by subsequent re-heat treatment (RHT) in air. An immediate indication of a reversible change can be observed by simple inspection of the powder color, as shown in Figs. 1(a)–1(c). The as-synthesized powder is dark brown in color [Fig. 1(a)], whereas VHT leads to a yellow powder [Fig. 1(b)], and upon further RHT, the initial brown color [Fig. 1(c)] is regained. Likewise, the diffuse reflectance spectra of the powders support this observation, and the corresponding changes in the bandgap energies have been estimated, as presented in Fig. 1(d). The bandgap energy of the as-synthesized powder is 1.93 eV. Upon VHT, an increase in the bandgap to 2.47 eV can be observed. The RHT of the powder in air leads to a reversal of the bandgap to 1.98 eV. This value is close to the bandgap of the as-synthesized system, and the difference (~5%) falls within the experimental error of the measurement.

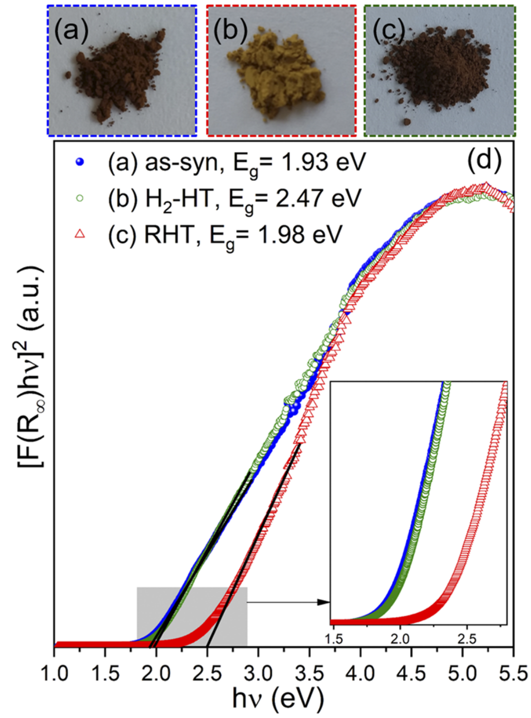

FIG. 1. Photographs of the $(Ce_{0.2}La_{0.2}Pr_{0.2}Sm_{0.2}Y_{0.2})O_{2-\delta}$ powder, where (a) is the as-synthesized powder, (b) VHT, and (c) RHT after the VHT. (d) The corresponding Tauc plot obtained from the UV-Vis spectra of these powders confirms reversible tuning of the bandgap. The bandgap values are within the 5% error bar, i.e, ±0.1 eV.

2. Structural analysis and phase composition upon VHT

One of the main characteristics of HEOs is their phase purity; hence, it is important to investigate the effect of heat treatment on the phase composition of F-HEOs. Figure 2 presents the XRD patterns, HR-TEM micrographs, and selected area electron diffraction (SAED) patterns of the as-synthesized, VHT, and RHT samples. HR-TEM micrographs along with the XRD patterns reveal the presence of nano-sized crystallites, which aggregate to form micron sized particles. Structural details obtained from Rietveld refinement of the XRD patterns are presented in supplementary material, Fig. SI1. Importantly, no change in the crystal structure, phase composition, or elemental distribution (supplementary material, Fig. SI2) can be observed upon heat treatment under varying atmospheres. A marginal increase in the lattice parameter (~0.4%, see Table I) along with broadening of the peaks due to strain effects can

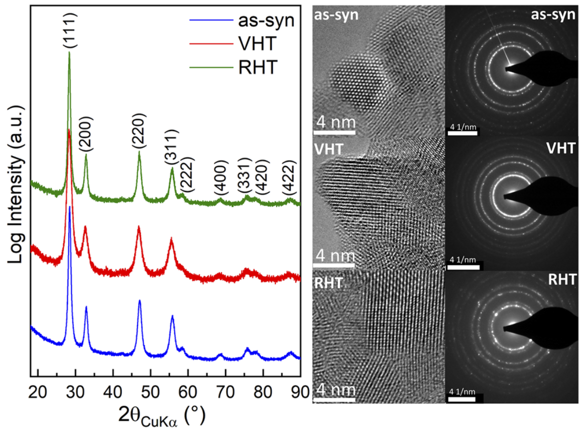

FIG. 2. XRD patterns confirming the phase purity of as-synthesized, vacuum heat treated (VHT), and air re-heat treated (RHT) F-HEOs. The TEM micrographs are in good agreement with the XRD results, confirming the nanocrystallinity and phase purity at the local level.

be observed upon VHT (Fig. 2). These observations hint toward the reduction in some of the constituent cations (resulting in larger ionic sizes) and related oxygen vacancy formation, which is the focus of Subsection III A 3.

3. Oxidation state and charge compensation upon VHT

In our previous report,[25] we inferred that the bandgap energy of ~2 eV in F-HEOs is closely associated with the presence of multivalent Pr^{3+}/Pr^{4+}. Following this speculation, it can be expected that the change/reduction in the oxidation state of Pr will affect the occupancy of the Pr 4f states. Hence, a change in the bandgap energy of F-HEOs can be expected. In order to investigate the change in the oxidation of constituent elements upon VHT, EELS measurements have been carried out.

TABLE I. Summary of the lattice parameter (a) and direct bandgap energy (E_g) values of $(Ce_{0.2}La_{0.2}Pr_{0.2}Sm_{0.2}Y_{0.2})O_{2-\delta}$ heat treated under different conditions. The a of bixbyite ($Ia\bar{3}$) should be divided by 2 to obtain the pseudosymmetric lattice parameter, which is needed for comparison purposes.

Heat treatment	Crystal structure	a (Å)	E_g (eV)[a]
As-syn (750 °C-air)	$Fm\bar{3}m$	5.4782(5)	1.93
1000 °C-air	$Ia\bar{3}$[b]	10.9632(5)	2.03
750 °C, VHT	$Fm\bar{3}m$	5.5035(4)	2.47
750 °C, VHT+RHT	$Fm\bar{3}m$	5.4832(4)	1.98
750 °C, H_2-HT	$Ia\bar{3}$	11.0035(9)	3.21
750 °C, H_2-HT+RHT	$Fm\bar{3}m$	5.4831(7)	2.04

[a] Inaccuracies of ±0.1 eV should be considered.

[b] This $Ia\bar{3}$ structure cannot be reverted back to $Fm\bar{3}m$ upon subsequent RHT at lower temperatures.[15,25]

EELS measurements have been performed on the as-synthesized, VHT, and RHT powders. The spectra for Ce and Pr $M_{4,5}$ edges are displayed in Fig. 3. The $M_{4,5}$ white lines in EELS spectra of the rare-earths (REs) result from electronic transitions between the initial state 3d and the 4f orbitals, such as $3d_{3/2} \rightarrow 4f_{5/2}$ (M_4) and $3d_{5/2} \rightarrow 4f_{7/2}$ (M_5). The relative intensity ratio (I_{M_5}/I_{M_4}) and chemical shift of the $M_{4,5}$ lines denote the change in valency (or the f-shell occupancy) of the respective RE cations.[37] The EELS spectra for Ce and Pr are of utmost importance as these two elements exhibit the highest tendency to vary between the 3+ and 4+ states, whereas La, Sm, and Y are known for their stable 3+ electronic configuration. For Ce, two white lines at 882 eV and 902 eV are observed, which are related to M_5 and M_4 transitions, respectively.[37,38] However, no noticeable chemical shifts of these lines have been observed after VHT or RHT. This finding is further supported by the fact that the I_{M_5}/I_{M_4} ratio is relatively invariant with respect to heat treatment [Fig. 3(b)]. Unlike Ce, the scenario is different for Pr. For the as-synthesized system, Pr $M_{4,5}$ white lines are observed at 931 eV and 951 eV, respectively. A significant chemical shift (of ~0.6 eV) toward low energies occurred upon VHT, which indicates a reduction in Pr from a pronounced 4+ state to 3+ dominated multivalent (3+/4+) state.[39] The formation of Pr^{3+} is supported by the pronounced shoulder at the left (or lower energies) of the Pr M_4 line. Additionally, an increase in I_{M_5}/I_{M_4} of Pr is also observed upon VHT, further confirming the decrease in Pr^{4+} [Fig. 3(b)]. Likewise, upon subsequent RHT of the VHT sample in air, a reverse behavior, i.e., an oxidation of Pr toward the initial Pr^{4+} dominated mixed valence state, could be observed.

The reduction of Pr with VHT should be compensated internally. One way of charge compensation can be via oxidation of the other constituent cations, which is not the case here. Hence, the formation of oxygen vacancies can be expected. We have utilized Raman spectroscopy to study this possibility. Two characteristic

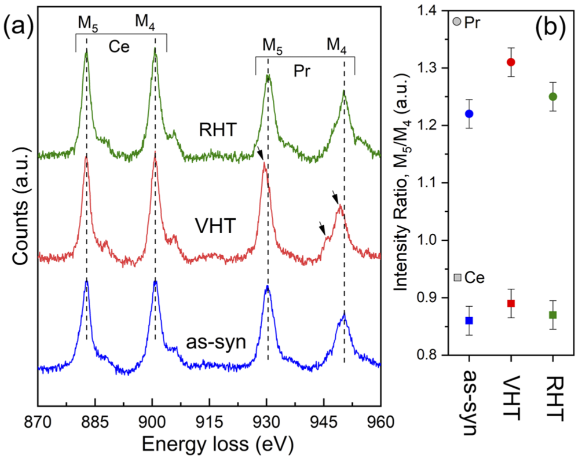

FIG. 3. (a) EELS spectra of the F-HEO showing the Ce and Pr $M_{4,5}$ edges. The chemical shift of Pr edges along with the shoulder at lower energy losses to M_4 indicates the reduction of Pr upon VHT. (b) Average Ce and Pr I_{M_5}/I_{M_4} intensity ratios calculated from (a) indicate the f-shell occupancy.

bands centered at ~452 cm^{-1} and ~580 cm^{-1} in all samples are used for the estimation of the V_O concentration (see supplementary material, Fig. SI3). The ~452 cm^{-1} band corresponds to the F_{2g} stretching mode of the fluorite structure, while the latter corresponds to the presence of V_O.[40,41] The integral intensity ratio of V_O to F_{2g} can be used for a relative estimation of the V_O concentration in different systems.[42] The inset of Fig. SI3 of the supplementary material, shows an increase in the amount of V_O concentration upon VHT, while V_O concentrations in the as-synthesized and RHT samples are nearly comparable (see the related discussion in supplementary material, Sec. 1). Although the V_O and the charge state of the elements are interlinked, it should be noted that the bandgap energy in the F-HEO is rather related to the presence of redox-active Pr and its unoccupied 4*f* intermediate band. This has been observed in our earlier report as well, where we compared various F-HEO compositions with varying amount of oxygen vacancies.[25] Nonetheless, we have probed samples using Raman spectroscopy as the change in the V_O concentration upon heat treatment supports the EELS data and indicates the reversible behavior in the F-HEO.

To summarize, we observe a reversible change in the bandgap upon VHT of the F-HEO followed by RHT. The increase in the energy gap upon VHT is expected due to the decrease in the number of unoccupied Pr 4*f* states, as evidenced from the EELS results. The reduction of Pr and resulting increase in V_O also support the increase in the lattice parameter and microstrain upon VHT. Furthermore, the fact that makes the F-HEO unique is the retention of the single-phase fluorite structure even upon VHT. The stability of a fluorite type oxide structure strongly depends on the presence of a 4+ cation, which in a VHT-F-HEO is only Ce and a minor part of Pr. Likewise, the V_O concentration (as shown from Raman spectroscopy) in VHT-$(Ce_{0.2}La_{0.2}Pr_{0.2}Sm_{0.2}Y_{0.2})O_{2-\delta}$ is rather high compared to conventional binary or doped fluorite type oxides, and δ is expected to be ~0.4. To further investigate the impact of stronger reducing atmospheres on physico-chemical features of F-HEO, heat treatment under a hydrogen atmosphere has been carried out.

B. Heat treatment under highly reducing H_2 atmosphere

$(Ce_{0.2}La_{0.2}Pr_{0.2}Sm_{0.2}Y_{0.2})O_{2-\delta}$ has been heat treated under a highly reducing 5% H_2 + Ar atmosphere (H_2-HT), followed by re-heat treatment (RHT) in air. A reversible change in the powder color can be observed after this treatment, as shown in Figs. 4(a)–4(c). Importantly, the change in the bandgap energy is larger than what was observed for VHT, i.e., increasing from 1.93 eV to 3.21 eV [Fig. 4(d)]. RHT of the H_2-HT powder in air leads to reversion of the bandgap to 2.04 eV. This bandgap tailoring of around 60% (~1.3 eV) can be considered as significant, especially given that the change is reversible.

1. Structural analysis and phase composition upon H_2-HT

Figure 5 presents the XRD patterns along with SAED micrographs for the H_2-HT and RHT samples. Rietveld refinements of the XRD patterns are provided in supplementary material, Fig. SI4. Unlike for the as-synthesized and RHT samples, we observe additional peaks in the XRD patterns for the H_2-HT sample. These additional peaks are the superstructure reflections, indicating a structural transition from a fluorite ($Fm\bar{3}m$) to C-type bixbyite ($Ia\bar{3}$) structure. Evidence of faint superstructure reflections can also be observed in the SAED pattern (Fig. 5), which further confirms the formation of the bixbyite structure. Homogeneous cationic distribution, down to the nanometer length scales, further supports the phase purity of the bixbyite formed upon H_2-HT (supplementary material, Fig. SI5).

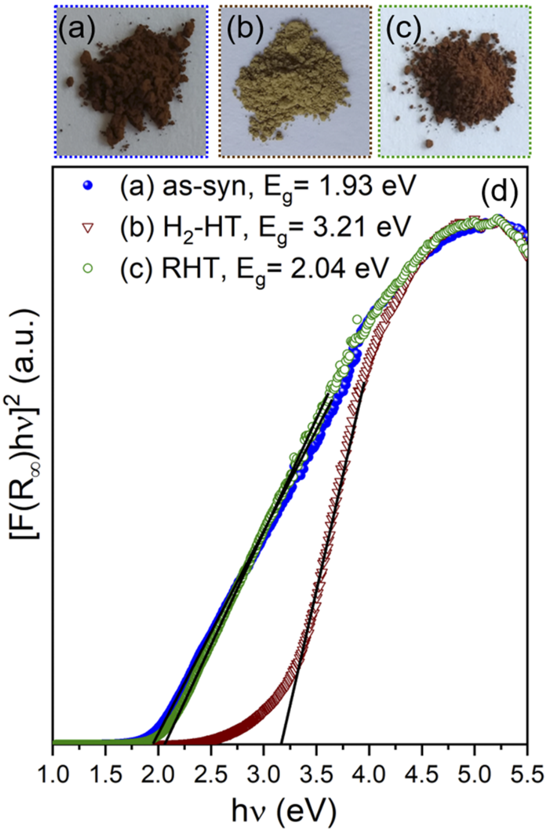

FIG. 4. Photographs (a)–(c) and Tauc plot (d) obtained from the UV-Vis spectra of the $(Ce_{0.2}La_{0.2}Pr_{0.2}Sm_{0.2}Y_{0.2})O_{2-\delta}$ powder, where (a)–(c) correspond to the as-synthesized, hydrogen heat treated (H_2-HT), and re-heat treated samples, respectively. The bandgap values are within the 5% error bar, i.e, ±0.1 eV.

Bixbyite is a well-known low symmetry oxygen deficient body centered cubic variant of the fluorite family, where one out of every four oxygen ions is missing.[43,44] The symmetry relationship between fluorite (*a*) and bixbyite (2*a*) includes a twofold increase in the lattice parameter. Thus, for direct structural comparisons, the pseudosymmetric lattice parameter of the bixbyite structure (i.e., half of the actual lattice parameter) is considered. In fact, the as-synthesized $(Ce_{0.2}La_{0.2}Pr_{0.2}Sm_{0.2}Y_{0.2})O_{2-\delta}$ sample undergoes a similar symmetry lowering when heat treated in normal atmospheric conditions (i.e., under air).[15,25] However, there are two subtle differences between the symmetry lowering happening upon normal heat

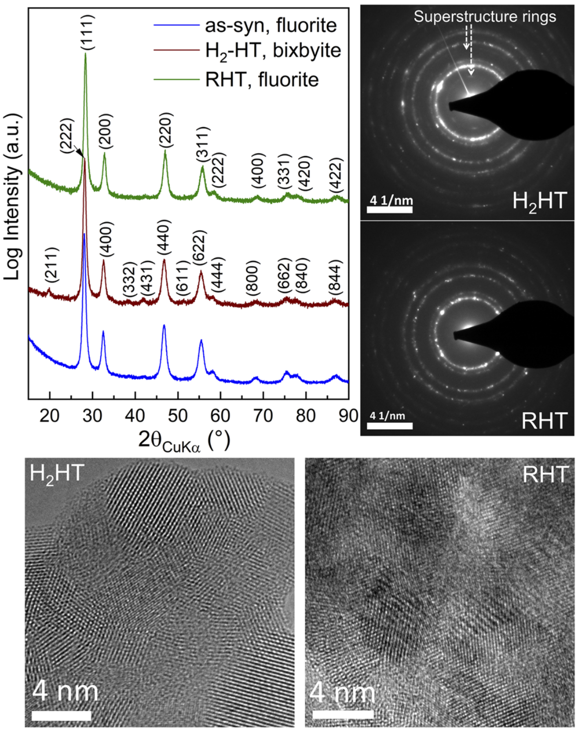

FIG. 5. A reversible transition from a fluorite to bixbyite structure is observed upon hydrogen heat treatment (H_2-HT) followed by air re-heat treatment of $(Ce_{0.2}La_{0.2}Pr_{0.2}Sm_{0.2}Y_{0.2})O_{2-\delta}$. The TEM micrographs and SAED patterns confirm the reversible disorder–order type structural transition.

treatment in air (as observed in our earlier studies) and the H_2-HT. First of all, upon H_2-HT, this phase transition happens at a much lower temperature, i.e., already at 750 °C, whereas the phase transition will happen only above 1000 °C if heat treated under a normal air atmosphere.[15,25] Second and a rather unusual phenomenon is that the phase transition to bixbyite upon H_2-HT is reversible, i.e., a single-phase fluorite structure can be regained when the H_2-heat treated sample is re-heated (RHT) in air at 750 °C (see XRD and SAED in Fig. 5). However, we observed[15,25] that the transition to a bixbyite phase is completely irreversible if the as-synthesized sample is heat treated above 1000 °C in a normal air atmosphere.[15,25] As mentioned above, the transition from fluorite to bixbyite is mostly governed by the presence of oxygen vacancies, which start to order above a certain temperature. One of the reasons for the structural transition already at 750 °C upon H_2-HT can be the formation of additional oxygen vacancies due to a stronger reducing atmosphere. This is supported by an increase (~0.5%, Table I) in the pseudosymmetric lattice parameter upon H_2-HT. In fact, 750 °C under H_2 might already be sufficient to order the oxygen vacancies. However, the temperature might still not be large enough to result in a stable ordering, making the transition back to fluorite upon RHT possible. Further discussion of this point is presented in Sec. III C.

Table I summarizes the structural and optical features obtained upon various heat treatments of F-HEOs.

We have used Raman spectroscopy to further investigate these systems due to its sensitivity to local chemical changes, especially related to light scatterers such as oxygen. It should be noted that the infrared laser, which we typically use to study the F-HEO, could not be used for the H_2-HT sample due to possible resonance effects (see supplementary material, Fig. SI6). Hence, a green laser (λ = 532 nm) has been used for comparison. It is shown in Fig. 6 that all the F-HEO systems show distinct Raman bands at ~452 cm^{-1}, ~1180 cm^{-1}, and ~580 cm^{-1}. By comparing these with the parent binary (or doped) rare-earth based oxides (containing Ce/La/Pr/Sm/Y), we can draw correlations with CeO_2 based systems.[40,42,45–47] The band at ~452 cm^{-1} can be associated with the triply degenerated F_{2g} vibration mode.[41] The band at ~1180 cm^{-1} can be related to the second order 2*LO* Raman mode, which is generally observed in ceria or its doped variants.[40,41] The strong broad band at ~580 cm^{-1} can be best fitted using a two band model, which can be attributed to the presence of oxygen vacancies (V_O) and its related bonding with the 3+ and 4+ cations.[45] Given the fact that bixbyite (as in H_2-HT) is a superstructure of fluorite, additional vibration bands or strengthening/rupturing of some existing ones can be expected. After H_2-HT, three additional bands appear. The band at ~358 cm^{-1} [Fig. 6(a)] can be attributed to a second order Raman mode arising from a combination of A_{1g}, E_g, and F_{2g} scattering tensors.[40] However, we do not find a proper match for the two

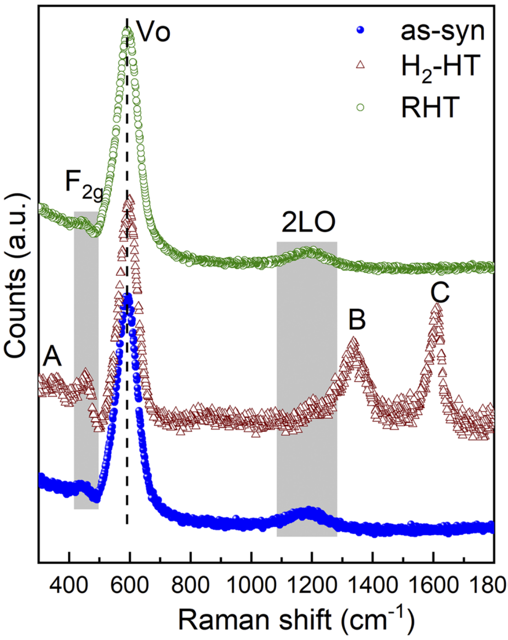

FIG. 6. Raman spectra of $(Ce_{0.2}La_{0.2}Pr_{0.2}Sm_{0.2}Y_{0.2})O_{2-\delta}$ using the 532 nm excitation laser. Three additional bands centered at 358 cm^{-1} (a), 1333 cm^{-1} (b), and 1610 cm^{-1} (c) are observed in the H_2-HT system.

prominent additional bands at ~1333 cm^{-1} and ~1610 cm^{-1}, which are observed only upon H_2-HT (see Fig. 6). Furthermore, these bands cannot be directly attributed to the crystal structural change as the bixbyite variant of $(Ce_{0.2}La_{0.2}Pr_{0.2}Sm_{0.2}Y_{0.2})O_{2-\delta}$ obtained upon normal air heat treatment does not exhibit these features (see the Raman spectra in supplementary material, Fig. SI7). Interestingly, both the bands disappear upon subsequent RHT of the H_2-HT sample in air, and a spectrum similar to the as-synthesized system is obtained. One of the plausible reasons for the appearance of the additional bands upon H_2-HT can be due to possible hydrogen incorporation in the F-HEO system. Hydrogen being a light element can lead to strong vibrational modes. Recently, it has been reported that H incorporation (even in the hydride form) is possible in the (bulk) fluorite type CeO_2 when it is heat treated above 350 °C in a H_2 atmosphere.[48] Such a H-incorporation cannot be ignored in the F-HEO as H_2-HT is done at 750 °C. Moreover, the presence of large V_O concentrations in the F-HEO might potentially facilitate H-incorporation. However, this is a speculation and finding concrete evidence of the presence of H is not simple. Hence, experiments sensitive to H, such as inelastic neutron scattering, are needed to support such a hypothesis.

In order to further understand the other physico-chemical changes happening upon H_2-HT, XAS has been performed.

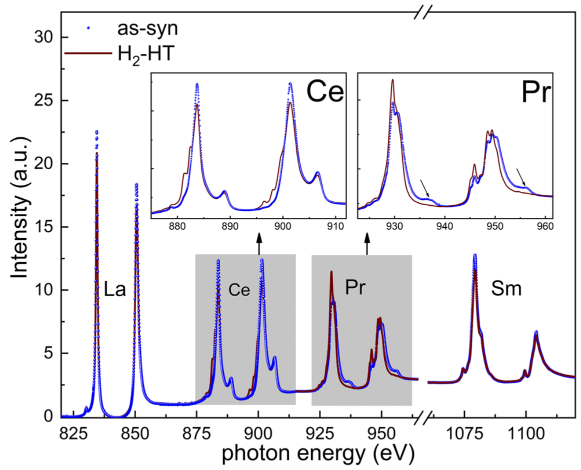

FIG. 7. XAS spectra at the different RE $M_{4,5}$ edges for the as-synthesized and H_2-heat treated sample. The respective spectrum has been normalized to the edge jump after the M_4 edge. The insets show a magnification of the Ce and Pr edges.

C. Element resolved charge state and electronic structure of F-HEO

XAS probes the (unoccupied) electronic density of states above the Fermi energy in an element specific way.[36,49] Hence, it offers the possibility to disentangle the element specific contributions in complex systems such as F-HEOs. Each of the XAS spectra has been normalized to the edge jump. In the following, the respective changes at the different absorption edges are discussed. In addition, an investigation concerning changes in the amount of unoccupied states has been performed.[50,51]

1. Rare-earth $M_{4,5}$ edges: 3d → 4f and L_3 edge: 2p → 5d

At the $M_{4,5}$ edges, the transition from the 3*d* states into the unoccupied 4*f* states occurs (in a dipole approximation). The respective absorption spectra for the as-synthesized and H_2-HT sample are shown in Fig. 7. The La $M_{4,5}$ edges indicate that both the as-synthesized and H_2-HT samples are in the 3+ valence state, while a reduction in the free states by ~3.5% can be determined by the difference of the integrated spectral area. We see a similar, intuitive behavior for Sm, which is also in a 3+ valence state in both cases, while the integrated spectral area is reduced by 3.9% upon H_2-HT. For Ce, a detailed fine structure occurs prior to both the M_5 and M_4 edges after H_2-HT (inset of Fig. 7). These additional peaks can be assigned to Ce^{3+}, while the initial peaks can be assigned to Ce^{4+}.[52,53] Therefore, it can be said that Ce is present in a 4+ dominated multivalent (3+/4+) state after H_2-HT. Due to the occurring multivalency in Ce, a change in the number of unoccupied states can only be determined from the integrated spectrum. From this analysis, an increase of 0.9% of the integrated white line intensity can be determined—such an increase can be neglected and can be explained by differences in the normalization procedure. Pr, on the other hand, is present in a multivalent 3+/4+ state (with a pronounced 4+ nature), as indicated by the prominent after edges[54] in the as-synthesized sample (see the inset of Fig. 7). It changes into a (fully) 3+ state upon H_2-HT. Furthermore, the unoccupied 4*f* states in Pr are reduced by ~15%.

Furthermore, the RE L_3 edges are also studied as the hard x rays in the transmission mode provide a better idea about the bulk nature of the sample. In the L_3 edge, the transition from the $2p_{3/2}$ states to unoccupied 5*d* states occurs. Ce and Pr L_3 spectra are shown in Fig. 8. A complete spectrum including La and Sm is provided in supplementary material, Fig. SI8. For the L_3 absorption edge, the discussion is simpler compared to the $M_{4,5}$ edges. For La and Sm, a 3+ state is evident, while no significant change in the white line intensity is visible. For Ce, a 4+ state can be observed in the as-synthesized sample, while a reduction to a mixed valent state is evident upon H_2-HT. The presence of Ce^{3+} results in shoulder A,[47] as shown in the inset of Fig. 8. Nevertheless, a pronounced Ce^{4+} state is maintained even upon H_2 with no major change in the white line intensity. For Pr, a significant change in the spectral structure is visible. The as-synthesized sample shows a distinct multiplet spectrum ($4f^2$ and $4f^1$ in the inset of Fig. 8). From the literature, it is known that such a spectrum is typically observed in multivalent $Pr^{3+/4+}$, where Pr^{4+} is ascribed to the $4f^1$ peak.[55,56] After H_2-HT, the change in the spectral near-edge fine structure indicates a complete reduction to Pr^{3+}. Accompanied with this change is a reduction in the spectral area by ~3%. This can be explained either by a change in the unoccupied 5d states or structural changes due to the EXAFS signal from the La L_2 edge ($E_{0,\mathrm{La}\,L_2}$ = 5891 eV). For this, a detailed EXAFS modeling would be necessary, which is difficult due to the relatively small available *k*-space for this complex system, as visible in supplementary material, Fig. SI8.

The mild reduction of Ce and strong reduction of Pr are in good agreement with the crystal structural transition to bixbyite observed upon H_2-HT. Ce^{4+} is known to play a pivotal role in stabilizing the

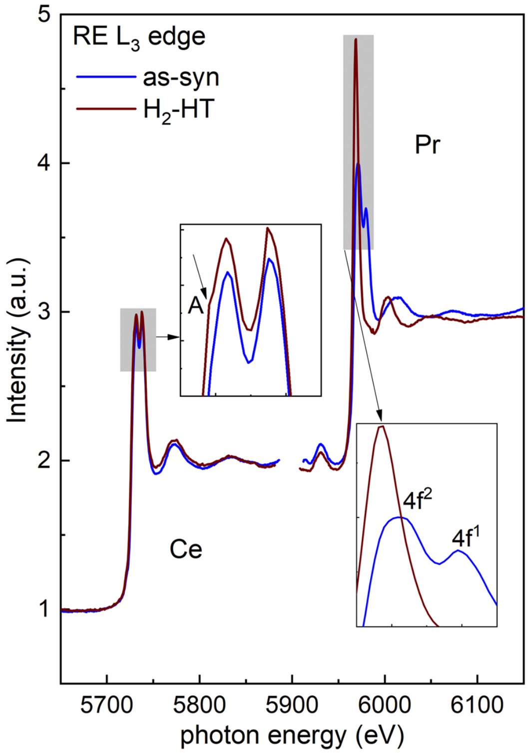

FIG. 8. XAS spectra at the Ce and Pr L_3 edges for the as-synthesized and H_2-heat treated samples. The peak for $E = 5930$ eV originates from the La L_2 edge.

fluorite lattice in F-HEOs.[15,25] Thus, even the mild reduction of Ce^{4+} most likely destabilizes the fluorite lattice. The accompanying strong reduction of Pr along with the presence of other 3+ cations leads to an enhanced V_O concentration. Hence, oxygen vacancy ordering (see Sec. III C 2) can be triggered at relatively lower temperatures (750 °C) compared to normal air heat treatment (1000 °C). As mentioned in Sec. III B 1, the ordering upon H_2-HT is most likely metastable, given the intensities of the superstructure reflections are rather weak (Fig. 5 and supplementary material, Fig. SI4) compared to XRD patterns of bixbyite obtained from air-heat treatment.[15,25] Thus, upon RHT, the fluorite structure can be regained.

2. Oxygen K-edge: 1s → 2p

Finally, we focus on the hybridization of the O 2*p* states with the RE neighbors by probing the O 1*s* → 2*p* transition at the O *K* edge. Unlike the RE cations, the XANES spectrum of the O *K* edge is rather complex as O hybridizes with all RE cations. Hence, disentangling all spectral features is not straightforward, given the fact that XANES of the F-HEO (or similar complex systems) has not been reported on before. Nevertheless, the changes happening in the RE $M_{4,5}$ and L_3 edges help us to identify the major spectral variation in O *K* edges upon heat treatment. The prominent features are observed at the photon energy $E = 528.6$ eV (A), 530 eV (B), 532 eV (C), 533 eV (D), 537 eV (E), and 539 eV (F), respectively (see Fig. 9). Feature A can be attributed to the Pr 4*f*-O 2*p* hybridization[27] (discussion pertaining to this feature is explained in Sec. IV). Features B, D, and E have been attributed to O 2*p* states, which hybridize with the 4*f*, 5d-e_g, and 5d-t_{2g} levels of Ce in stoichiometric CeO_2, respectively.[27,57] The splitting of the $5d$–e_g and $5d$–t_{2g} states occurs only if crystal field effects lift the degeneracy,[57,58] indicating that the changes in spectral features D and E are due to an alteration of the local structure (evident from Fig. 5). The relative increase in the peak intensity of feature D compared to feature E reveals a local ordering of the oxygen vacancies. This finding is in agreement with reports on doped CeO_2[38,44] and supports the formation of the C-type bixbyite structure upon H_2-HT. Feature F (539 eV) can be matched with the O 2*p* and Sm 5*d* hybridization[59,60] and hence does not change upon H_2-HT. Likewise, the presence of feature C can also be observed both in the as-synthesized and H_2-HT systems, which is possibly linked to the O 2*p*-RE 5*d* hybridization.

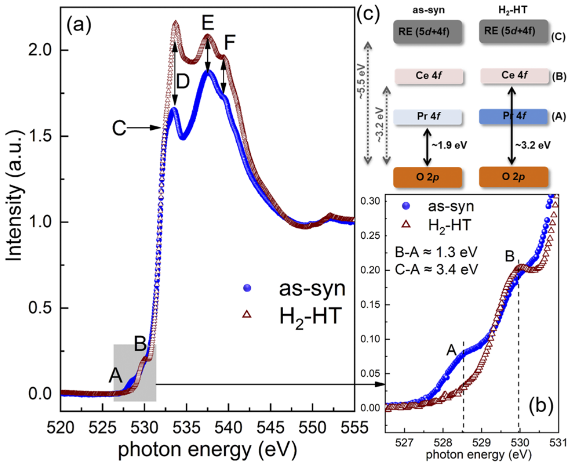

FIG. 9. (a) O *K* edge XAS spectra of the as-synthesized and H_2-heat treated sample. The spectra are normalized to the edge jump. (b) Magnification of the pre-edge region. (c) Schematic of the electronic band diagram of as-synthesized (oxidized) and H_2-heat treated (reduced) F-HEOs.

IV. DISCUSSION

In conventional rare-earth (RE) oxides, the occupied oxygen 2*p* states are hybridized with RE 5*d*/4*f* states, resulting in the formation of the bonding and anti-bonding orbitals. The O 2*p* state with the occupied RE 5*d*/4*f* state forms the valence band, which is generally classified as the O 2*p* band. However, the anti-bonding states originating from the RE-O hybridization are the conduction bands, which are generally denoted in terms of the RE state related to the specific hybridization, such as RE 5*d*/4*f*. Thus, the electronic transition from the O 2*p* state to the unoccupied RE 5*d*/4*f* states determines the bandgap energy. In fact, the changes in the electronic structure of binary rare-earth oxides can be directly correlated with the changes observed in O *K* edges.[60] Likewise, in the case of the F-HEO, the analysis of the O K XANES edge provides a comprehensive understanding of the electronic band structure and valence states (which is also supported by the other spectroscopic techniques). The most interesting features in the O K edge of F-HEOs are A and B. As mentioned above, feature B corresponds to the Ce $4f$-O $2p$ hybridization, while feature A corresponds to the Pr $4f$-O $2p$ hybridization. Feature B is present in both cases; however, the intensity of feature A decreased to almost zero after H_2-HT. This indicates distinct changes in Pr $4f$ states that are related to the reduction in Pr valency or decrease in the unoccupied states in the $4f$ level (see Pr-$M_{4,5}$ edges in Fig. 7). Here, we would like to mention that the bandgap energy difference (see Fig. 4) between the as-synthesized sample and the H_2-HT sample is ~1.3 eV. This value matches almost perfectly the energy difference between feature A (Pr $4f$-O $2p$, 528.6 eV) hybridization and feature B (Ce $4f$-O $2p$, 529.9 eV) hybridization. The weakening of feature A means an increase in the occupation of the Pr $4f$ band, thus prohibiting electronic transitions to the same. This finding validates our band energy diagram [see Fig. 9(c)], where we expect that the electronic transitions will occur from the O $2p$ state (valence bands) to Pr $4f$ (unoccupied) state in the case of the as-synthesized system. However, upon reduction of Pr, the $4f$ level will get filled; hence, the transition to unoccupied Ce $4f$ will determine the bandgap. This is exactly what we observed in the O K edge [see Fig. 9(c)] when the as-synthesized and the H_2-HT systems were compared. The fact that feature B becomes prominent upon H_2-HT, even upon the reduction of Ce^{4+}, can be explained as follows: First, the reduction of Ce^{4+} to Ce^{3+} is rather mild as the predominance of Ce^{4+} can be observed from the Ce $M_{4,5}/L_3$ edges (Figs. 7 and 8). Additionally, no major changes in the white line intensity of Ce $M_{4,5}$ indicate only negligible changes in the Ce $4f$ occupancy.

Furthermore, as shown in Fig. 9(a), both the Pr $4f$-O $2p$ and the Ce $4f$-O $2p$ hybridization are actually pre-edge features, while the main absorption corresponding to the RE $5d$-O $2p$ hybridization starts above 531 eV. This is equivalent to our hypothesized energy band diagram [Fig. 9(c)] with the two intermediate energy bands at lower energy gaps, while the gap between O $2p$ and unoccupied RE $5d$ is much larger. The energy difference between features A and C is ~3.5 eV (so is the energy difference between the onset of edge A to edge C). This means that the effective gap between O $2p$ and RE $5d$ is ~5.5 eV. In fact, this value is in good agreement with our earlier hypothesis[25] and is close to the expected energy gap in rare-earth oxides without intermediate $4f$ states.[26,60] Hence, it can be summarized that in F-HEOs, Ce and Pr lead to the formation of intermediate energy states, resulting in narrow bandgaps, whereas the other 3+ cations add to the main energy gap of ~5.5 eV. Depending upon the heat treatment condition, i.e., reducing/oxidizing atmospheres, each of these electronic structures in F-HEOs can be achieved reversibly.

V. CONCLUSIONS

This work attempts to provide a comprehensive understanding of the tunable electronic band structure in a fluorite type rare-earth based high entropy oxide (F-HEO). Owing to the element specific techniques used here, it is possible to disentangle the individual effects of the constituent cations, which can be directly correlated to the observed reversible changes in the optical features. Reversible changes (~0.5 eV) in the bandgap energies are achieved in the F-HEO upon vacuum heat treatment followed by reheating in air. Importantly, the single-phase fluorite type structure of $(Ce_{0.2}La_{0.2}Pr_{0.2}Sm_{0.2}Y_{0.2})O_{2-\delta}$ is maintained even upon vacuum heat treatment with Ce being the sole element, which is purely 4+. This shows the potential of the F-HEO to accommodate a large amount of oxygen vacancies. A stronger reduction of F-HEO, achieved via hydrogen heat treatment, allows for a larger change (~1.2 eV) in the bandgap energy, which can be reverted back to the initial state upon subsequent annealing in air. In addition, a reversible structural transition from fluorite to a single-phase oxygen vacancy ordered C-type bixbyite structure has been observed. Raman spectroscopy further strengthens this reversible behavior as local chemical features before and after reheat treatment are identical. X-ray absorption near-edge spectra (XANES), using soft and hard x rays, indicate that the crystal structure transition can be correlated to the reduction of Ce^{4+}, while tuning of the bandgap energy is related to the reduction of Pr and related changes in the Pr $4f$-O $2p$ hybridization.

Although practical applications using the F-HEO are yet to materialize, the unique combination of narrow and tunable bandgap energies along with large concentrations of oxygen vacancies in the F-HEO might be beneficial for applications related to mixed electronic–ionic conduction, catalysis, etc. In this context, understanding the exact nature of oxygen vacancy ordering and the related fluorite to bixbyite transition is important. Hence, comprehensive high temperature investigations (above 750 °C) under different atmospheres will be crucial. An electrochemical approach to tune the bandgap in the F-HEO can be another prospective research direction. In any case, further experiments and most importantly support from theoretical studies are essential to exploit the complete potential of the F-HEO.

SUPPLEMENTARY MATERIAL

The supplementary material includes the Rietveld refinements of the XRD patterns, TEM–EDS maps, Raman spectra (of vacuum heat treated F-HEO and bixbyite HEO), and XANES of La and Sm L_3 edges.

ACKNOWLEDGMENTS

A.S. and H.H. acknowledge financial support from the Deutsche Forschungsgemeinschaft (DFG) under Project No. HA 1344/43-1. B.E. and H.W. acknowledge financial support from the Deutsche Forschungsgemeinschaft (DFG) under Project No. WE 2623/14-1. X.M. and L.V. acknowledge the support of Karlsruhe Nano Micro Facility (KNMF) for the access to the TEM. A.S. thanks Soumabha Bag (INT, KIT) for fruitful discussions. We thank the Helmholtz-Zentrum Berlin for the allocation of beamtime at the beamline UE46 PGM_1 (Proposal No. 192-08578-ST/R) and Eugen Weschke for the support during the beamtime. We acknowledge DESY (Hamburg, Germany), a member of the Helmholtz Association, for the provision of experimental facilities. Parts of this research were carried out at PETRA III (Proposal No. 20190485), and we would like to thank Ruidy Nemausat for assistance in using the beamline P65. We acknowledge support by the KIT-Publication Fund of the Karlsruhe Institute of Technology.

DATA AVAILABILITY

The data that support the findings of this study are available within the article and its supplementary material.

REFERENCES

[1] C. M. Rost, E. Sachet, T. Borman, A. Moballegh, E. C. Dickey, D. Hou, J. L. Jones, S. Curtarolo, and J.-P. Maria, Nat. Commun. **6**, 8485 (2015).

[2] N. Dragoe and D. Bérardan, Science **366**, 573 (2019).

[3] A. Sarkar, Q. Wang, A. Schiele, M. R. Chellali, S. S. Bhattacharya, D. Wang, T. Brezesinski, H. Hahn, L. Velasco, and B. Breitung, Adv. Mater. **31**, 1806236 (2019).

[4] A. Sarkar, L. Velasco, D. Wang, Q. Wang, G. Talasila, L. de Biasi, C. Kübel, T. Brezesinski, S. S. Bhattacharya, H. Hahn, and B. Breitung, Nat. Commun. **9**, 3400 (2018).

[5] J. Dabrowa, M. Stygar, A. Mikuła, A. Knapik, K. Mroczka, W. Tejchman, M. Danielewski, and M. Martin, Mater. Lett. **216**, 32 (2018).

[6] J. Gild, M. Samiee, J. L. Braun, T. Harrington, H. Vega, P. E. Hopkins, K. Vecchio, and J. Luo, J. Eur. Ceram. Soc. **38**, 3578 (2018).

[7] B. Musicó, Q. Wright, T. Zac Ward, A. Grutter, E. Arenholz, D. Gilbert, D. Mandrus, and V. Keppens, Phys. Rev. Mater. **3**, 104416 (2019).

[8] N. Qiu, H. Chen, Z. Yang, S. Sun, Y. Wang, and Y. Cui, J. Alloys Compd. **777**, 767 (2019).

[9] M. P. Jimenez-Segura, T. Takayama, D. Bérardan, A. Hoser, M. Reehuis, H. Takagi, and N. Dragoe, Appl. Phys. Lett. **114**, 122401 (2019); arXiv:1902.01825.

[10] J. L. Braun, C. M. Rost, M. Lim, A. Giri, D. H. Olson, G. N. Kotsonis, G. Stan, D. W. Brenner, J.-P. Maria, and P. E. Hopkins, Adv. Mater. **30**, 1805004 (2018).

[11] Q. Wang, A. Sarkar, D. Wang, L. Velasco, R. Azmi, S. S. Bhattacharya, T. Bergfeldt, A. Düvel, P. Heitjans, T. Brezesinski, H. Hahn, and B. Breitung, Energy Environ. Sci. **12**, 2433 (2019).

[12] C. Oses, C. Toher, and S. Curtarolo, Nat. Rev. Mater. **5**, 295 (2020).

[13] K. Chen, X. Pei, L. Tang, H. Cheng, Z. Li, C. Li, X. Zhang, and L. An, J. Eur. Ceram. Soc. **38**, 4161 (2018).

[14] L. Spiridigliozzi, C. Ferone, R. Cioffi, G. Accardo, D. Frattini, and G. Dell'Agli, Materials **13**, 558 (2020).

[15] R. Djenadic, A. Sarkar, O. Clemens, C. Loho, M. Botros, V. S. K. Chakravadhanula, C. Kübel, S. S. Bhattacharya, A. S. Gandhi, and H. Hahn, Mater. Res. Lett. **5**, 102 (2017).

[16] B. Cheng, H. Lou, A. Sarkar, Z. Zeng, F. Zhang, X. Chen, L. Tan, V. Prakapenka, E. Greenberg, J. Wen *et al.*, Commun. Chem. **2**, 114 (2019).

[17] D. Bérardan, S. Franger, A. K. Meena, and N. Dragoe, J. Mater. Chem. A **4**, 9536 (2016).

[18] R. Witte, A. Sarkar, R. Kruk, B. Eggert, R. A. Brand, H. Wende, and H. Hahn, Phys. Rev. Mater. **3**, 34406 (2019).

[19] H. Chen, J. Fu, P. Zhang, H. Peng, C. W. Abney, K. Jie, X. Liu, M. Chi, and S. Dai, J. Mater. Chem. A **6**, 11129 (2018).

[20] J. Zhang, J. Yan, S. Calder, Q. Zheng, M. A. Mcguire, D. L. Abernathy, Y. Ren, S. H. Lapidus, K. Page, H. Zheng, J. W. Freeland, J. D. Budai, and R. P. Hermann, Chem. Mater. **31**, 3705 (2019).

[21] P. B. Meisenheimer, T. J. Kratofil, and J. T. Heron, Sci. Rep. **7**, 13344 (2017).

[22] D. Wang, Z. Liu, S. Du, Y. Zhang, H. Li, Z. Xiao, W. Chen, R. Chen, Y. Wang, Y. Zou, and S. Wang, J. Mater. Chem. A **7**, 24211 (2019).

[23] Y. Sharma, Q. Zheng, A. R. Mazza, E. Skoropata, T. Heitmann, Z. Gai, B. Musico, P. F. Miceli, B. C. Sales, V. Keppens, M. Brahlek, and T. Z. Ward, Phys. Rev. Mater. **4**, 014404 (2020).

[24] R. K. Patel, S. K. Ojha, S. Kumar, A. Saha, P. Mandal, J. W. Freeland, and S. Middey, Appl. Phys. Lett. **116**, 071601 (2020).

[25] A. Sarkar, C. Loho, L. Velasco, T. Thomas, S. S. Bhattacharya, H. Hahn, and R. Djenadic, Dalton Trans. **46**, 12167 (2017).

[26] R. Gillen, S. J. Clark, and J. Robertson, Phys. Rev. B **87**, 125116 (2013); arXiv:1208.0503.

[27] S. G. Minasian, E. R. Batista, C. H. Booth, D. L. Clark, J. M. Keith, S. A. Kozimor, W. W. Lukens, R. L. Martin, D. K. Shuh, S. C. E. Stieber, T. Tylisczcak, and X.-d. Wen, J. Am. Chem. Soc. **139**, 18052 (2017).

[28] L. Petit, A. Svane, Z. Szotek, and W. M. Temmerman, Phys. Rev. B **72**, 205118 (2005).

[29] K. Ahn, D. S. Yoo, D. H. Prasad, H.-W. Lee, Y.-C. Chung, and J.-H. Lee, Chem. Mater. **24**, 4261 (2012).

[30] X. Chen, L. Liu, Z. Liu, M. A. Marcus, W.-C. Wang, N. A. Oyler, M. E. Grass, B. Mao, P.-A. Glans, Y. Y. Peter *et al.*, Sci. Rep. **3**, 1510 (2013).

[31] Topas V5, General profile and structure analysis software for powder diffraction data, User's Manual (Bruker AXS, Karlsruhe).

[32] J. Tauc, R. Grigorovici, and A. Vancu, Phys. Stat. Sol. **15**, 627 (1966).

[33] E. Weschke and E. Schierle, J. Large-scale Res. Fac. JLSRF **4**, A127 (2018).

[34] E. Welter, R. Chernikov, M. Herrmann, and R. Nemausat, AIP Conf. Proc. **2054**, 040002 (2019).

[35] G. S. Henderson, F. M. F. De Groot, B. J. A. Moulton, F. M. F. D. Groot, and B. J. A. Moulton, Spectrosc. Methods Mineral. Geol. **78**, 75 (2014).

[36] H. Wende, Rep. Prog. Phys. **67**, 2105 (2004).

[37] A. M. D'Angelo, A. C. Liu, and A. L. Chaffee, J. Phys. Chem. C **120**, 14382 (2016).

[38] D. R. Ou, T. Mori, F. Ye, J. Zou, G. Auchterlonie, and J. Drennan, Phys. Rev. B **77**, 024108 (2008).

[39] W. J. Bowman, K. March, C. A. Hernandez, and P. A. Crozier, Ultramicroscopy **167**, 5 (2016).

[40] A. Filtschew, K. Hofmann, and C. Hess, J. Phys. Chem. C **120**, 6694 (2016).

[41] W. H. Weber, K. C. Hass, and J. R. McBride, Phys. Rev. B **48**, 178 (1993).

[42] M. Guo, J. Lu, Y. Wu, Y. Wang, and M. Luo, Langmuir **27**, 3872 (2011).

[43] Y.-M. Chiang, *Physical Ceramics: Principles for Ceramic Science* (John Wiley & Sons, Inc., 1997).

[44] D. R. Ou, T. Mori, F. Ye, T. Kobayashi, J. Zou, G. Auchterlonie, and J. Drennan, Appl. Phys. Lett. **89**, 171911 (2006).

[45] C. Schilling, A. Hofmann, C. Hess, and M. V. Ganduglia-Pirovano, J. Phys. Chem. C **121**, 20834 (2017).

[46] N. Dilawar, S. Mehrotra, D. Varandani, B. V. Kumaraswamy, S. K. Haldar, and A. K. Bandyopadhyay, Mater. Charact. **59**, 462 (2008).

[47] R. Schmitt, A. Nenning, O. Kraynis, R. Korobko, A. I. Frenkel, I. Lubomirsky, S. M. Haile, and J. L. M. Rupp, Chem. Soc. Rev. **49**, 554 (2020).

[48] Z. Wu, Y. Cheng, F. Tao, L. Daemen, G. S. Foo, L. Nguyen, X. Zhang, A. Beste, and A. J. Ramirez-Cuesta, J. Am. Chem. Soc. **139**, 9721 (2017).

[49] J. Stöhr, *NEXAFS Spectroscopy* (Springer, Berlin, Heidelberg, 1992).

[50] B. T. Thole, P. Carra, F. Sette, and G. Van Der Laan, Phys. Rev. Lett. **68**, 1943 (1992).

[51] P. Carra, B. T. Thole, M. Altarelli, and X. Wang, Phys. Rev. Lett. **70**, 694 (1993).

[52] S. Alayoglu, K. An, G. Melaet, S. Chen, F. Bernardi, L. W. Wang, A. E. Lindeman, N. Musselwhite, J. Guo, Z. Liu, M. A. Marcus, and G. A. Somorjai, J. Phys. Chem. C **117**, 26608 (2013).

[53] S. Heyraud, P. E. R. Blanchard, S. Liu, Q. Zhou, B. J. Kennedy, H. E. A. Brand, A. Tadich, and J. R. Hester, J. Phys.: Condens. Matter **25**, 335401 (2013).

[54] J. Herrero-Martín, J. L. García-Muñoz, S. Valencia, C. Frontera, J. Blasco, A. J. Barón-González, G. Subías, R. Abrudan, F. Radu, E. Dudzik, and R. Feyerherm, Phys. Rev. B **84**, 115131 (2011).

[55] J. L. García-Muñoz, C. Frontera, A. J. Barón-González, S. Valencia, J. Blasco, R. Feyerherm, E. Dudzik, R. Abrudan, and F. Radu, Phys. Rev. B **84**, 045104 (2011).

[56] T. Ogier, C. Prestipino, S. Figueroa, F. Mauvy, J. Mougin, J. C. Grenier, A. Demourgues, and J. M. Bassat, Chem. Phys. Lett. **727**, 116 (2019).

[57] J. A. Rodriguez, J. C. Hanson, J.-Y. Kim, G. Liu, A. Iglesias-Juez, and M. Fernández-García, J. Phys. Chem. B **107**, 3535 (2003).

[58] A. V. Soldatov, T. S. Ivanchenko, S. Della Longa, A. Kotani, Y. Iwamoto, and A. Bianconi, Phys. Rev. B **50**, 5074 (1994).

[59] S.-Y. Chen, R.-J. Chen, W. Lee, C.-L. Dong, and A. Gloter, Phys. Chem. Chem. Phys. **16**, 3274 (2014).

[60] A. B. Altman, J. I. Pacold, J. Wang, W. W. Lukens, and S. G. Minasian, Dalton Trans. **45**, 9948 (2016).

5. Perovskite type high entropy oxides

The crystal structure 'perovskite' has derived its name from the mineral perovskite, $CaTiO_3$. Perovskite type compounds have a general formula, which is close to (or derived from) the composition ABX_3, where A is usually a large cation, B is a comparatively smaller cation and X is an anion. Naturally, in case of oxides the general notation is ABO_3. The ideal perovskite structure is cubic type, where the A cations and O^{2-} form a *fcc* array with a large octahedron in the center of the cell accommodating the B cation, as shown in Fig. 5.1. The formation of a cubic perovskite structure strongly depends on the composition. Deviation from the cubic structure can be observed based on the cationic radii and corresponding oxidation states. In fact, the structural distortions are the origin of a wide-range of piezoelectric, pyroelectric and multiferroic properties of perovskites [87]. Distortions and deviations from the cubic structure in perovskites can be predicted using the Goldschmidt's tolerance factor [88], Eqn. 5.1.

$$t = \frac{(r_A + r_O)}{\sqrt{2}(r_B + r_O)} \tag{5.1}$$

In Eqn. 5.1, t is the tolerance factor, r_A is the radius of the A-cation, r_B the radius of the B-cation, and r_O is the radius of oxygen ion. Goldschmidt proposed that a cubic perovskite structure can be formed if $t \sim 1.0$. Deviation of t from the ideal value leads to structural distortion. If $t > 1$, i.e., in systems where the A cations are too big or B cations are too small, then hexagonal or

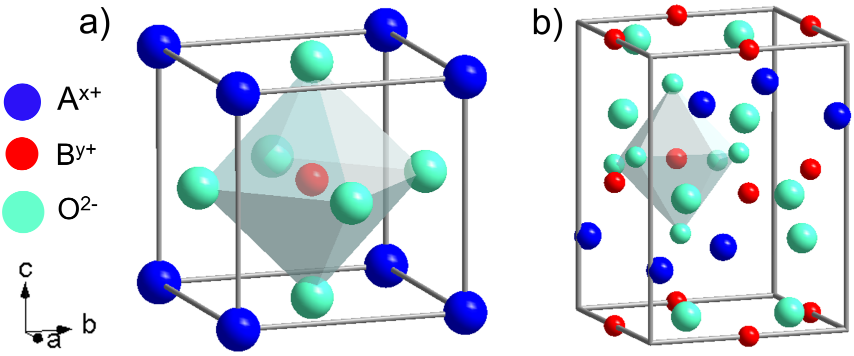

Figure 5.1.: Ball stick model of a) aristotype cubic with A-cations populated on the $1a$ (0,0,0) sites, B-cations occupying the $1b$ (½,½,½) sites and oxygen distributed on the $3c$ (½,½,0; ½,0,½; 0,½,½) sites, and b) orthorhombic distortion in perovksite type oxides.

tetragonal modifications are adapted such as in $BaNiO_3$. Conversely, if $t < 1$ then orthorhombic or rhombohedral modifications are favored.

Most of the rare-earth (RE) transition-metal (TM) based perovskites, e.g., $GdFeO_3$, $SmCoO_3$, etc., have $t < 1$, resulting in orthorhombic structure (see Fig. 5.1b), while doping of larger A-site cations (like Sr^{2+}, Ba^{2+}, etc.) results in their cubic variants. RE-TM perovskites and their doped variants are one of the most renowned class of perovskites. The interplay between the composition, the resulting structure and physical properties in these perovskites makes them suitable candidates for several engineering applications, exploiting properties such as, magneto-electric effects [89], multiferroic effects [90], catalytic activities [91], electronic [92], electrochemical and related transport properties [93, 94]. These characteristics of RE-TM perovskites motivate the exploration of high entropy based design approach in these systems, as the synergistic effect of multiple cations in the specific sub-lattices can lead to interesting features. In this regard, several perovskite type high entropy oxides (P-HEOs) were studied by either substituting the A-site by multiple RE cations and/or replacing the the B-site by several TM cations. The findings are presented in Section 5.1.

Magnetic properties of conventional RE-TM perovskite have been an area of major research interest for more than half a century [95–97]. The the presence of incompletely filled f and d shells in RE-TM perovskites leads to interesting correlations. In general, magnetic interactions between the TM ions determine the magnetism in RE-TM perovskites. The magnetic interactions mostly results from indirect coupling as there is very little direct overlap of the $3d$ wave functions of the two nearest TM cations, rather they overlap strongly with the $2p$ orbitals of the O^{2-}. Depending upon the nature of the O $2p-$ TM $3d$ hybridization, different types of magnetic behaviors are observed. The most common magnetic interaction present in these systems is the superexchange interaction [98], which involves two simultaneous and virtual electron transfers. In the first step, an electron from the completely filled O $2p$ orbital is transferred to the adjacent hybridized $3d$ orbital of the TM cation leaving a $2p$ hole. The hole is filled up by another electron transfer from the $3d$ orbital of the second TM hybridized with same O $2p$. Hence, the two TM cations are coupled via the O^{2-} with a certain superexchange interaction parameter, which depends on the geometrical characteristics of the TM-O-TM bond and the electronic configuration of the two coupled TM ions. For instance, if the cations have lobes of singly occupied $3d$ orbitals that point toward each other, then the exchange is strong and antiferromagnetic (AFM) in nature, which is the usual case with TM-O-TM bond angle of $120° – 180°$. On the other hand, the coupling between the same cations with a TM-O-TM bond angle of 90° results in superexchange interactions, which are weak and ferromagnetic (FM) in nature. Different kinds of superexchange interactions arising different kind of interionic hybridizations are summarized in the Goodenough-Kanamori-Anderson rules [97–99]. Another magnetic interaction well known in RE-TM perovskite is the double exchange interaction, which is FM and conducting in nature. TM-O-TM bonding with the TM ions having both localized and delocalized electrons typically exhibits double exchange interaction, where an electron from one TM cations can freely hop to another TM cation via O^{2-} while retaining its spin. Thus, mixed-valence configuration of the hybridized cations is important for double exchange interaction. Overall, it is evident that any kind of modification of the oxidation state or crystal structure, such as lattice distortion or tilting of the BO_6 octahedra (TM-O-TM), etc., are extremely critical for the magnetic exchange interactions. This interplay between the structure, composition, and magnetic properties in P-HEOs is the focus of Section 5.2.

5.1. Overview of publication V: Rare earth and transition metal based entropy stabilized perovskite type oxides

Prior to this article studies on HEOs were concentrated on systems where cations occupied only one Wyckoff position, such as rocksalt or fluorite. Hence, one of the main motivations of this investigation was to extend the high entropy based design concept to a complex system, i.e., perovskite (ABO_3), where cations share at least two Wyckoff positions.

Ten RE-TM based P-HEOs systems were explored, by either populating the A site with 5 RE cations in equiatomic amount while fixing the B-site to a single TM cation or vice versa. In addition one P-HEO with 10 different cations in equiatomic proportion, 5 on each A and B site, was synthesized. Six of these systems crystallized as single-phase orthorhombic perovskites at ambient temperature. Secondary phases were observed in five of the P-HEOs, each consisting of 6 cations. Interestingly, the highly complex 10-cationic $(Gd_{0.2}La_{0.2}Nd_{0.2}Sm_{0.2}Y_{0.2})(Co_{0.2}Cr_{0.2}Fe_{0.2}Mn_{0.2}Ni_{0.2})O_3$ system crystallized in a single phase orthorhombic structure. Furthermore, the local chemical homogeneity of this 10 cation system can be observed from Fig. 5.2b and c,[1] which supports the higher configurational entropy stemming from both the A- and B-sites (see Eqn. 2.5).

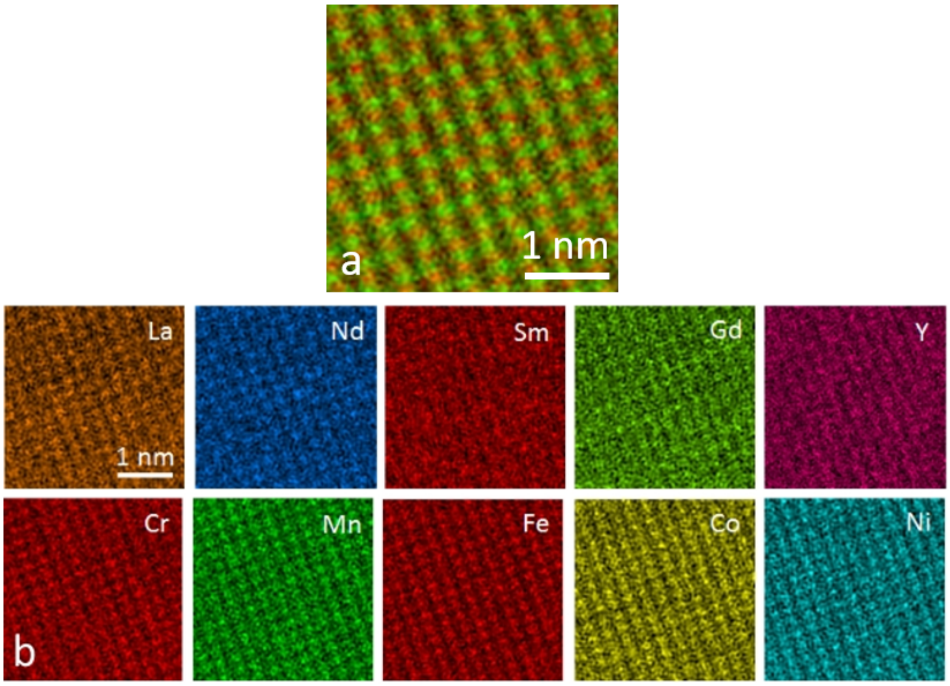

Figure 5.2.: (a) High-angle annular dark-field imaging (HAADF) scanning transmission electron microscope (STEM) micrograph along the along $[1\bar{0}1]$ zone axis, (b) STEM-Energy-dispersive X-ray spectroscopy (EDX) maps and c) color mix map obtained by summing the EDX signal from the A (green) and B (red) site of the 10 cations P-HEO.

---

[1] TEM measurements were done by Dr. Di Wang and Dr. Alexandrou Ioannis.

The 6-cationic P-HEOs have lower configurational entropy compared to the 10-cationic P-HEO. The fact that several 6-cationic P-HEOs were multiphase mixtures while the more complex 10 cation system was phase pure, hints towards a possible role of entropy affecting the phase composition of P-HEOs. It is possible that lower entropy of 6-cationic P-HEOs is not be enough to compensate the enthalpy penalties needed to form a single-phase. The enthalpy penalties in these systems possibly arises from difference in the cationic sizes, the affinity of certain elements towards a particular oxidation state and the Jahn-Teller effect. In order to further study the role of entropy, all the P-HEOs were characterized using *in-situ* high temperature X-ray diffraction (HT-XRD).[2] Two of the systems showed phase transformation. $(Gd_{0.2}La_{0.2}Nd_{0.2}Sm_{0.2}Y_{0.2})MnO_3$ exhibited a typical entropy-driven phase transformation[3], where the system reversibly transformed from multiphase to single phase (above 900 °C) upon heating. Hence, $(Gd_{0.2}La_{0.2}Nd_{0.2}Sm_{0.2}Y_{0.2})MnO_3$ can be classified as an entropy-stabilized HEO. A reversible phase transition from an orthorhombic to a rhombohedral structure was also evident in $La(Co_{0.2}Cr_{0.2}Fe_{0.2}Mn_{0.2}Ni_{0.2})O_3$. However, this transition is not entropy-mediated but rather driven by the tolerance factor.

With this paper [100], several new compositions were added to the HEO family. Importantly, each of these P-HEOs exhibit distinct structural features, which can result in unique properties. Thus, future research can focus on each of these systems separately.

5.2. Overview of publication VI: High entropy oxides: An emerging prospect for magnetic rare-earth transition metal perovskites

This article is the first investigation of the magnetic properties of P-HEOs. Five different P-HEOs, belonging to the group of 5 TM cations on B-site and a single RE cation on the A-site (such as $La(Co_{0.2}Cr_{0.2}Fe_{0.2}Mn_{0.2}Ni_{0.2})O_3$), were investigated. For comparison, the 10-cationic P-HEO was also studied. Comprehensive studies by magnetometry were combined with element specific Mössbauer spectroscopy in order to understand the interplay between the magnetic exchange interactions and the high degree of chemical disorder in P-HEOs. In agreement with Goodenough-Kanamori-Anderson rules [99], a predominant AFM superexchange behavior (at lower temperature) was observed in all the P-HEOs. It was found that the magnetic properties of P-HEO can be explained by the presence of competing magnetic exchange interactions within the TM cation sublattice. Several of the RE cations, like La^{3+} or Y^{3+} were non-magnetic, thus did not influence the magnetic response. Contributions from Gd^{3+}, Nd^{3+} or Sm^{3+} were visible only at very low temperatures. Nevertheless, the influence of A-cations was accounted in terms of size effect, as dependency between the Néel temperatures and tolerance factors (t, see Eqn. 5.1) could be observed. In addition, a vertical exchange bias (EB) of $\sim$25 % of the remanent magnetization was observed in all P-HEOs. EB is typically observed in heterogeneous structures, like multilayers or core-shell structures. The presence of EB necessitates the coexistence of the ferromagnetic

---

[2] Major part of the HT-XRD results are in Appendix A.5

[3] Details of entropy-driven phase transformation can be found in Section 2.2.5.

(FM) and AFM interactions, where the Curie temperature of the FM phase is higher than the Néel temperature of the AFM phase. Thus, such interactions in phase-pure P-HEOs are fascinating. One possibility in P-HEOs can be the canted AFM spins, which result in uncompensated magnetic moments leading to a weak FM behavior. Another possibility can be the presence of small FM clusters locked inside the AFM matrix, where the FM clusters get ordered (at higher temperatures) before the complete ordering of the AFM matrix. The presence of local FM cluster is likely and can be related to the high entropy based design approach, where the presence of several TM cations in P-HEOs can result in pairs (such as Fe^{3+}-O-Cr^{3+}) which interact ferromagnetically.

In summary, the presence of magnetic ordering despite the chemical disorder and the indication of EB despite phase purity make the P-HEOs interesting and worth studying in more detail.

Statement of personal contribution

1. **Rare earth and transition metal based entropy stabilised perovskite type oxides**
   A. Sarkar, R. Djenadic, D. Wang, C. Hein, R. Kautenburger, O. Clemens and H. Hahn, *Journal of the European Ceramic Society* 9, 2318 (2018)
   Reprinted with permission from *Journal of the European Ceramic Society*, ©2018, ELSEVIER.

   The experiments were planned by myself under the guidance of Prof. H. Hahn. The synthesis, characterization (except for TEM and ICP-MS), and data analysis was performed by myself. Dr. D. Wang performed the TEM measurements and analysis. Dr. C. Hein and Dr. R. Kautenburger performed the ICP-MS measurements. Dr. R. Djenadic and Prof. O. Clemens were involved in numerous scientific discussions during the development of the project. The manuscript was written by myself with comments from all authors.

2. **High-entropy oxides: An emerging prospect for magnetic rare-earth transition metal perovskites**
   R. Witte, A. Sarkar, R. Kruk, B. Eggert, R. Brand, H. Wende, H. Hahn, *Physical Review Materials* 3, 034406 (2019)
   Reprinted with permission from *Physical Review Materials*, ©2019, THE AMERICAN PHYSICAL SOCIETY.

   The idea of this project originated from discussion between Dr. R. Witte and myself, which was guided by Dr. R. Kruk, Dr. R. Brand and Prof. H. Hahn. The planning and execution of the magnetic measurements and analysis were carried out by Dr. R. Witte, who also provided me the training of SQUID magnetometry and Mössbauer spectroscopy during the course of this project. The synthesis and structural characterization was performed by myself. B. Eggert and Prof. H. Wende conducted the in-field Mössbauer spectroscopy. The manuscript was written by Dr. R. Witte with inputs from myself especially in the introductory and initial structural characterization part. All the authors commented on the manuscript.

Journal of the European Ceramic Society 38 (2018) 2318–2327

Contents lists available at ScienceDirect

Journal of the European Ceramic Society

journal homepage: www.elsevier.com/locate/jeurceramsoc

Rare earth and transition metal based entropy stabilised perovskite type oxides

Abhishek Sarkar[a,b,*], Ruzica Djenadic[b,c,g], Di Wang[a,d], Christina Hein[e], Ralf Kautenburger[e], Oliver Clemens[a,f,*], Horst Hahn[a,b,c,*]

[a] *Institute of Nanotechnology, Karlsruhe Institute of Technology, Hermann-von-Helmholtz-Platz 1, 76344, Eggenstein-Leopoldshafen, Germany*
[b] *Joint Research Laboratory Nanomaterials – Technische Universität Darmstadt and Karlsruhe Institute of Technology, Alarich-Weiss-Str. 2, 64287, Darmstadt, Germany*
[c] *Helmholtz Institute Ulm – Electrochemical Energy Storage, Helmholtzstr. 11, 89081, Ulm, Germany*
[d] *Karlsruhe Nano Micro Facility, Karlsruhe Institute of Technology, Hermann-von-Helmholtz-Platz 1, 76344, Eggenstein-Leopoldshafen, Germany*
[e] *WASTe Group, Inorganic Chemistry, Saarland University, Campus Dudweiler, Am Markt Zeile 5, D-66125, Saarbrücken, Germany*
[f] *Materials Design by Synthesis Group, Technische Universität Darmstadt, Alarich-Weiss-Str. 2, 64287, Darmstadt, Germany*
[g] *Heraeus Deutschland GmbH & Co. KG, Heraeusstr. 12 – 14, 63450, Hanau, Germany*

ARTICLE INFO

Keywords:
Spray pyrolysis
Multicomponent equiatomic perovskites
High entropy oxides
Structural distortion

ABSTRACT

Multicomponent oxides with perovskite type of structure containing up to 10 different cations in equiatomic amounts have been synthesised for the first time. Out of eleven systems synthesised, only six systems crystallised as single phase perovskite type compounds with random and homogenous cation distribution on the respective sites. The formation of phase pure 10-cationic system, $(Gd_{0.2}La_{0.2}Nd_{0.2}Sm_{0.2}Y_{0.2})(Co_{0.2}Cr_{0.2}Fe_{0.2}Mn_{0.2}Ni_{0.2})O_3$, in contrast to the multiphase mixtures observed in five of the lower entropy systems (containing 6 cations) indicates a possible role of entropy in the stabilisation of a single phase crystal structure. The entropy driven structural stabilisation effect is further supported by the reversible phase transformation, from single phase to multiple phase upon cyclic heat treatment, observed in the $(Gd_{0.2}La_{0.2}Nd_{0.2}Sm_{0.2}Y_{0.2})MnO_3$ system. This type of entropic signature has been observed in rocksalt based high entropy oxide systems. However, it has not been reported before for perovskite based compounds, as shown in this study.

1. Introduction

The discovery of new materials with advanced properties is one of the greatest challenges faced by the scientific community. Research work on high entropy materials was recently extended to oxide systems by Rost et al. [1], where it was observed that high configurational entropy can be effectively used to stabilise single phase rocksalt type systems containing five different cations in equiatomic amount. As per Murty et al. [2], a system can be classified as a high entropy material, if the configurational entropy (ΔS_{config}) of that system is higher than 1.5R (0.0124 $kJ \cdot mol^{-1} \cdot K^{-1}$). In case of an oxide systems with cations sharing only one Wyckoff site (like in rocksalt based systems), the ΔS_{config} can only be greater than 1.5R if 5 (or more) cations are present in near equiatomic ratios. Furthermore, ΔS_{config} attains a maximum value when all the different elements are present in equiatomic amount. Although, the chemical bonding in the oxides are very different from the metallic bonds present in high entropy alloys (HEAs) [2,3], the presence of high configurational entropy (1.61R) found in the rocksalt based multicomponent oxide system ($(Co_{0.2}Cu_{0.2}Mg_{0.2}Ni_{0.2}Zn_{0.2})O$) [1] cannot be ignored. Additionally, the fact that this system shows a reversible transformation from a multiple phases (at lower temperature) to single phase (at higher temperature) upon cyclic heat treatment confirms the claim that the single phase structure in complex oxides can indeed be stabilised by enhancing the configurational entropy of the system [1,4]. This research on high entropy oxides (HEOs) [1] has opened up a new way to design complex multicomponent oxide ceramics. The functional properties of these new oxides are yet to be fully explored, but the initial studies by Bérardan et al. [5,6] show interesting and improved properties compared to binary or doped oxide systems, providing further motivation for extensive research in this field.

The field of high entropy oxides was further broadened by the discovery of multicomponent equiatomic rare earth oxides (ME-REOs) [7,8], where it has been shown that up to seven rare earth cations could be successfully incorporated into a phase pure fluorite type crystal lattice. Recently, Jiang et al. [9] observed that entropy stabilisation in oxides can be extended to complex systems like perovskites (ABO_3), where cations share two or more Wyckoff sites. The tendency to form

---

[*] Corresponding authors at: Institute of Nanotechnology, Karlsruhe Institute of Technology, Hermann-von-Helmholtz-Platz 1, 76344 Eggenstein-Leopoldshafen, Germany.
E-mail addresses: abhishek.sarkar@kit.edu (A. Sarkar), oliver.clemens@nano.tu-darmstadt.de (O. Clemens), horst.hahn@kit.edu (H. Hahn).

https://doi.org/10.1016/j.jeurceramsoc.2017.12.058
Received 18 November 2017; Received in revised form 22 December 2017; Accepted 26 December 2017

secondary phase(s) on addition of more cations (in higher amounts than doping) could be expected to be higher for complex oxides like perovskites (ABX_3) than for oxides with simpler structure like rocksalt (AX) since the formation of other structures (e.g., ilmenite type) and/or phases of the type $A_xB_yX_z$ (e. g. Ruddlesdon-Popper type phases) are often alternatives in systems of higher chemical complexity. In the study by Jiang et al. [9] only the B-site was substituted by five different elements, whereas the A-site was fixed to one or at most two elements. Hence, in this study more complex perovskites with completely different compositions are studied, where both cation sites are populated with five different elements in equiatomic amounts, i.e., five on the A-site, or the B-site, and finally five on both the A-site and the B-site, forming a 10 equiatomic cationic system.

2. Experimental section

2.1. Cations selection

Considering ABO_3 type system, three sets of multicomponent equiatomic perovskite oxide ((ME-PO)) systems were selected: (i) systems where the A-site was substituted with 5 rare earth cations in equiatomic amounts ($5A_{0.2} = Gd_{0.2}La_{0.2}Nd_{0.2}Sm_{0.2}Y_{0.2}$), whereas the B-site was kept occupied with a single transition metal cation (Co, Cr, Fe, Mn, or Ni) forming five systems: $(5A_{0.2})CoO_3$, $(5A_{0.2})CrO_3$, $(5A_{0.2})FeO_3$, $(5A_{0.2})MnO_3$ and $(5A_{0.2})NiO_3$; (ii) systems where the B-site was substituted with 5 transition metal elements in equiatomic amounts ($5B_{0.2} = Co_{0.2}Cr_{0.2}Fe_{0.2}Mn_{0.2}Ni_{0.2}$) and keeping the A-site occupied with a single rare earth cation (Gd, La, Nd, Sm, or Y) forming five systems: $Gd(5B_{0.2})O_3$, $La(5B_{0.2})O_3$, $Sm(5B_{0.2})O_3$, $Nd(5B_{0.2})O_3$ and $Y(5B_{0.2})O_3$); and (iii) a system where both the A- and B-sites were replaced by 5 rare earth and 5 transition metal elements, respectively, in equiatomic amounts, forming 10-cationic $(Gd_{0.2}La_{0.2}Nd_{0.2}Sm_{0.2}Y_{0.2})(Co_{0.2}Cr_{0.2}Fe_{0.2}Mn_{0.2}Ni_{0.2})O_3$ system or in an abbreviated form $(5A_{0.2})(5B_{0.2})O_3$. The cations were chosen following criteria already reported for other HEOs [1,7], i.e., (i) the ionic radii of the cations (on a specific site, A or B) at a specific oxidation state and coordination number should be similar, and (ii) at least one of the perovskite systems should have different prototype structure (e.g. $YMnO_3$) [10]. An overview of the ionic radii and the space groups of various structures that could be formed using the selected elements are given in the Supplementary information, Tables S1 and S2, respectively.

2.2. Synthesis

ME-POs powders were synthesised using nebulised spray pyrolysis (NSP) [11]. The illustration of the experimental setup can be found elsewhere [12]. The nitrate salts of Gd, La, Nd, Sm, Y Co, Cr, Fe, Mn and Ni ($Gd(NO_3)_3·6H_2O$, Sigma Aldrich, 99.9%; $La(NO_3)_3·6H_2O$, Sigma Aldrich, 99.9%; $Nd(NO_3)_3·6H_2O$, Sigma Aldrich, 99.9%; $Sm(NO_3)_3·6H_2O$, ABCR, 99.9%; $Y(NO_3)_3·6H_2O$, ABCR, 99.9%; $Co(NO_3)_2·6H_2O$, Sigma Aldrich, 99.9%; $Cr(NO_3)_3·9H_2O$, Sigma Aldrich, 99.9%; $Fe(NO_3)_3·9H_2O$, Sigma Aldrich, 99.9%; $Mn(NO_3)_2·4H_2O$, ChemPure, 98.5%; $Ni(NO_3)_2·6H_2O$, Sigma Aldrich, 99.9%) were used as precursors. A water-based solution containing appropriate equiatomic cation combinations ($0.1\ mol.L^{-1}$) was continuously delivered ($\sim 0.12\ L·h^{-1}$) into the piezo-driven nebuliser. The generated mist containing fine droplets of the precursor solution was transported by flowing oxygen (5 standard $L·min^{-1}$) into the hot-wall reactor where the particles were formed at a temperature of 1050 °C and a pressure of 900 mbar. The as-synthesised particles were collected using a filter-based collector and calcined at 1200 °C for 2 h in air atmosphere with a heating/cooling rate of $10\ °C·min^{-1}$.

2.3. Characterisation

The microstructure and elemental composition of the synthesised powders were studied using a Philips XL30 FEG scanning electron microscope (SEM) equipped with an energy dispersive spectroscopy (EDS) system (Amatek, USA). Particle size distribution was obtained by measuring around 300 particles and the average particle size was obtained from a log-normal fit [13].

For the validation of the elemental composition of the powders, selected samples have been analysed in triplicate by inductively coupled plasma mass spectrometry (ICP-MS) using an Agilent 7500cx ICP-MS (Agilent, Santa Clara, USA); detailed analytical conditions are given in the Supplementary information (Table S3). For the measurements 10 mg of the synthesised powders were first dissolved in 2 ml HNO_3 (supra quality, 68%, Carl Roth, Karlsruhe, Germany) and 8 ml MilliQ deionised water (18.2 mΩ·cm). In a second step, 10 µL of the sample solution was further diluted with 9.68 mL MilliQ-water. Additionally, 10 µL of internal standard ($10\ mg\ L^{-1}$ scandium and holmium, respectively) was added to correct the time dependent sensitivity variation of the ICP-MS system followed by an addition of 300 µL of nitric acid (68%, supra quality) to prohibit metal ion sorption onto the tube surface. For quantification a calibration with 0, 5, 25, 100 and 500 $µg\ L^{-1}$ of all analysed elements were prepared under similar conditions.

Room temperature X-ray diffraction (XRD) patterns of the powders were recorded using a Bruker D8 diffractometer with Bragg-Brentano geometry using Cu-Kα radiation with a Ni filter and a VANTEC detector having a fixed divergence slit (0.3°). A step size of 0.015° and a collection time of 4 s per step at 30 kV and 40 mA over the diffraction angle (2θ) range between 10 and 90° were used. For in-situ high-temperature XRD (HT-XRD) measurements a temperature stage (Anton Paar HTK 1200, Bruker) was used to collect data in a temperature range between 30 °C and 1000 °C with a heating and cooling rate of $30\ °C·min^{-1}$. The step size and collection time were set to 0.015° and 2 s, respectively. Rietveld analysis (TOPAS 5, Bruker) [14] of the XRD patterns was performed to determine the structure and phase composition of powders. Perovskites phases could be refined using a standard orthorhombic perovskite type structure of $GdFeO_3$ (*Pbmn,* ICSD 23823). The structural files were modified according to the number and the type of elements present in the refined system. The instrumental intensity distribution for the XRD data was determined using a reference scan of LaB_6 (NIST 660a). Thermal displacement parameters were constrained to be the same for all atoms.

The TEM specimen was prepared by directly dispersing the powders onto a gold grid coated with holey carbon film. It was examined with a FEI Titan 80 – 300 electron microscope (FEI, Eindhoven, the Netherlands) equipped with CEOS image spherical aberration corrector, Fischione model 3000 high angle annular dark field (HAADF) scanning transmission electron microscopy (STEM) detector, EDAX SUTW energy dispersive X-ray spectroscopy (EDX) detector and Gatan Tridiem image filter. The microscope was operated at an accelerating voltage of 300 kV in TEM mode for HRTEM and in nanoprobe mode for STEM imaging, EDX and electron energy loss spectroscopy (EELS) spectra acquisition.

3. Results and discussion

3.1. Microstructure and chemical composition

The as-synthesised as well as the calcined multicomponent equiatomic perovskite based oxide (ME-PO) powders are mostly black in colour except for $(5A_{0.2})CrO_3$, $(5A_{0.2})FeO_3$, and $(5A_{0.2})NiO_3$, which are light green, brown and olive green, respectively (Fig. 1a). The morphology of the calcined powders studied by SEM (Fig. 1b) show spherical hollow agglomerates of particles having a mean particle size of 180 nm (inset in Fig. 1b).

The actual compositions of the systems could be the determined for 5 of the 11 compounds by ICP-MS (Supplementary information Table S4). The other 6 compounds could not be dissolved completely in a concentrated acid. The obtained overall compositions confirm that all the elements in those 5 ME-POs are present in the desired

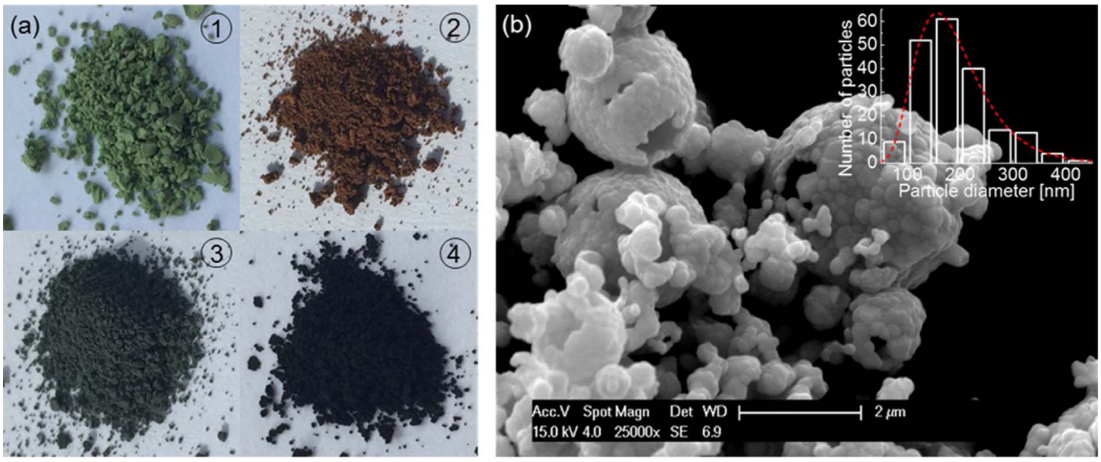

Fig. 1. (a) Photographs of several ME-PO systems showing variation in powder colour: 1. $(5A_{0.2})CrO_3$, 2. $(5A_{0.2})FeO_3$, 3. $(5A_{0.2})NiO_3$, 4. $(5A_{0.2})(5B_{0.2})O_3$. (b) SEM micrograph of $(5A_{0.2})(5AB_{0.2})O_3$ powder representing a typical morphology of ME-POs systems produced by NSP method. Inset represents log-normal particle size distribution with an average particle size of 180 nm.

stoichiometry. The EDS analysis (see Supplementary information Table S5) performed on the systems are in good agreement with the ICP-MS results, which confirm the correct overall compositions for the systems which could not be analysed using ICP-MS.

3.2. Phase composition and structural analysis

The XRD patterns of the as-synthesised powders, Supplementary information Fig. S1(a–d), show that only one of the ME-PO systems, $(5A_{0.2})CoO_3$, completely crystallises as a single phase solid solution directly under the synthesis conditions used, whereas in some of the systems ($(5A_{0.2})CrO_3$, $(5A_{0.2})FeO_3$, $La(5B_{0.2})O_3$, $Nd(5B_{0.2})O_3$) several phases are formed. In all the other systems ($(5A_{0.2})MnO_3$, $(5A_{0.2})NiO_3$, $Gd(5B_{0.2})O_3$, $Y(5B_{0.2})O_3$ and $(5A_{0.2})(5B_{0.2})O_3$) a large amount of amorphous phase is observed. One of the reasons for the presence of more than one phase in some of the systems and incomplete crystallisation in the others can be the low residence time (around 150 ms) of the particles in the NSP reactor. The residence time plays an important role in diffusion and crystallisation processes. Hence, all as-synthesised powders were subjected to a further calcination step at 1200 °C for 2 h in air and only the calcined powder are used for further characterisation and discussion. The corresponding XRD patterns are shown in Fig. 2(a–d) and the summary of their detailed structural analysis are given in Table 1.

The Rietveld analysis shows that all of the systems except $(5A_{0.2})NiO_3$ crystallise in orthorhombic perovskite type structure, but with different structural parameters and degree of secondary phases. The Rietveld refinements of all the systems (along with the Bragg peak position of the secondary phases for the multiphase mixtures) are provided in the Supplementary information (Fig. S2–S11). The average crystallite size of the perovskite phases for the different ME-POs ranges from 75–125 nm where $(5A_{0.2})CoO_3$ has the smallest and $Sm(5B_{0.2})O_3$ has the largest crystallite size. Minor amount of non-perovskite phases (up to a maximum of 5 wt.%) are observed in three of the systems: $(5A_{0.2})CrO_3$, $Sm(5B_{0.2})O_3$ and $Y(5B_{0.2})O_3$.

In the $(5A_{0.2})MnO_3$ system no additional non-perovskite type phases are found. However, strong tails at lower diffraction angles are observed for all the reflections in the XRD pattern for this system. The pattern of this phase cannot be refined using a single perovskite type phase, which is seen by the misfit (Fig. 3a) of the (020) reflection at 31.1° (2θ). This reflection shows a misfit due to its strong asymmetry, which indicates a distribution of perovskites phases with similar lattice parameters, mutually resulting from a non-isotropic composition.

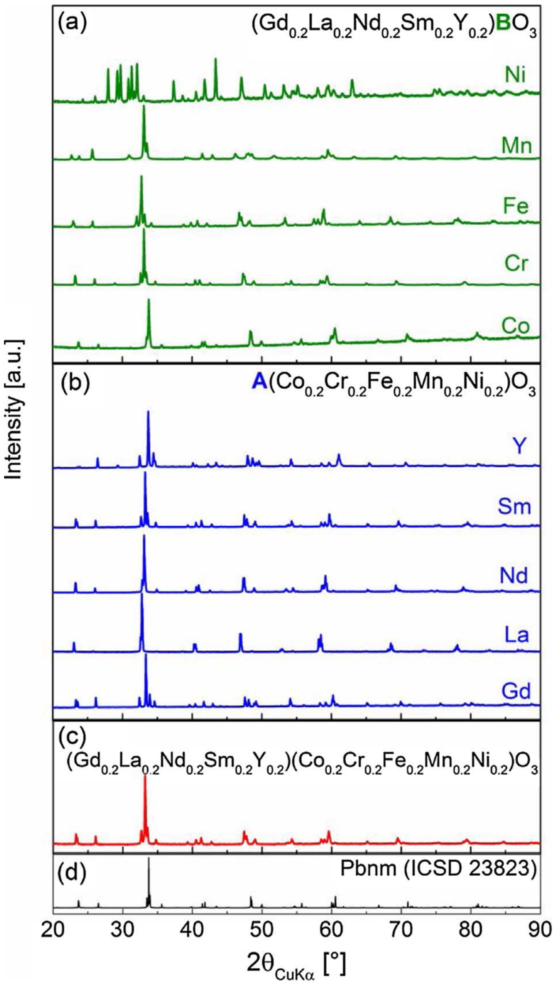

Fig. 2. XRD patterns of ME-PO powders: (a) $(5A_{0.2})BO_3$, B = Co, Cr, Fe, Mn, or Ni, (b) $A(5B_{0.2})O_3$, A = Gd, La, Nd, Sm, or Y, (c) $(5A_{0.2})(5B_{0.2})O_3$, and (d) simulated orthorhombic perovskite (*Pbnm*) pattern (ICSD 23823).

Table 1

Structural data for all (ME-PO) systems obtained from Rietveld refinement: space group (SG) along with prototype structures of secondary phases, phase fraction (*f* in wt.%), lattice parameters (*a*, *b*, *c* in Å, and *β* in °) and goodness of fit (GoF).

ME-POs	SG	*f* [wt.%]	*a* [Å]	*b* [Å]	*c* [Å]	*β* [°]	GoF
$5A_{0.2} = Gd_{0.2}La_{0.2}Nd_{0.2}Sm_{0.2}Y_{0.2}$							
$(5A_{0.2})CoO_3$	*Pbnm*	100	5.2964(2)	5.3655(2)	7.5128(3)	–	1.16
$(5A_{0.2})CrO_3$	*Pbnm*	97.7(6)	5.3799(7)	5.5035(7)	7.6614(1)	–	1.74
	$Ia\overline{3}$ (Gd_2O_3)	2.3(6)	10.729(0)				
$(5A_{0.2})FeO_3$	*Pbnm*	100	5.4094(3)	5.5936(2)	7.7259(2)	–	1.63
$(5A_{0.2})MnO_3$	*Pbnm*	42.3(1)	5.3658(4)	5.7396(4)	7.5352(5)	–	1.43
	Pbnm	40.9(1)	5.3670(4)	5.7637(5)	7.5201(7)	–	
	Pbnm	16.8(5)	5.3633(2)	5.6916(2)	7.5652(3)	–	
$(5A_{0.2})NiO_3$	*C2/m* (Sm_2O_3)[a]	60.4(3)	14.259(4)	3.6241(9)	8.8706(2)	100.6(0)	1.27
	$Fm\overline{3}m$ (NiO)	33.1(3)	4.1791(1)	–	–	–	
	I4/mmm (La_2NiO_4)	6.5(1)	3.8465(3)	–	12.5330(2)	–	
$5B_{0.2} = Co_{0.2}Cr_{0.2}Fe_{0.2}Mn_{0.2}Ni_{0.2}$							
$Gd(5B_{0.2})O_3$	*Pbnm*	100	5.2958(6)	5.5303(6)	7.5708(9)	–	1.25
$La(5B_{0.2})O_3$	*Pbnm*	100	5.4656(6)	5.5101(5)	7.7424(9)	–	1.19
$Nd(5B_{0.2})O_3$	*Pbnm*	100	5.4087(6)	5.4760(6)	7.6718(8)	–	1.47
$Sm(5B_{0.2})O_3$	*Pbnm*	98.3(3)	5.3523(6)	5.5024(6)	7.6178(9)	–	1.42
	C2/m (Sm_2O_3)[a]	1.7(3)	14.236(1)	3.6400(3)	8.7290(1)	100.4(1)	
$Y(5B_{0.2})O_3$	*Pbnm*	94.7(1)	5.2255(6)	5.5361(7)	7.4977(1)	–	1.44
	$Ia\overline{3}$ (Y_2O_3)	3.2(7)	10.597(1)	–	–	–	
	$Fm\overline{3}m$ (NiO)	2.1(1)	4.2021(1)	–	–	–	
$(5A_{0.2})(5B_{0.2})O_3$	*Pbnm*	100	5.3614(7)	5.5012(7)	7.6309(1)	–	1.45

[a] In $(5A_{0.2})NiO_3$ and $Sm(5B_{0.2})O_3$, the prototype structure used for the refinement of the *C2/m* phase is Sm_2O_3, however the composition of the phase is most likely to be $(5A_{0.2})_2O_3$.

Therefore, the flexibility of the model needs to be increased to describe the observed pattern, and it was found that a series of three orthorhombic perovskite phases with very close lattice parameters (same shape and positional parameters for all perovskite phases, see Table 1) can be used to approximately model the pattern (Fig. 3b). For this 3-phase model an increase of the *a*-axis with decrease of the *b*- and *c*-axes for the different phase fractions was found. The fit can be further improved by choosing a smoother distribution of *n* perovskite phases, by adding a constraint in such a way that the lattice parameters $(a,b,c)_i$ of phase fraction *i* are calculated according to :

$$(a,\ b,\ c)_i\ =\ (a,\ b,\ c)_{i=1} + [(a,\ b,\ c)_{i=n} - (a,\ b,\ c)_{i=1}]^* \,(i/n) \tag{1}$$

in addition to constraining the phases to the same shape and positional parameters (i.e., independent of the number of *n*, only 6 lattice parameters, $(a,b,c)_{i=1}$ and $(a,b,c)_{i=n}$, are being refined, which mimics the width of the distribution of the phases, with additional *n* scaling parameters). The phase distribution model for a fit with $n = 8$ is given in the Supplementary information, Table S6. Again, this agrees well with a segregation of rare earth cations based on their size. Fig. 3(a–c) compares Rietveld fits of the $(5A_{0.2})MnO_3$ XRD pattern by either considering a single perovskite (a) or three perovskite (b) or an $n = 8$ perovskite phases (c). In the $(5A_{0.2})NiO_3$ system, a major monoclinic phase (Gd_2O_3 type) instead of an orthorhombic perovskite phase, with higher amount of secondary rocksalt (NiO type) and tetragonal (La_2NiO_4 type) phases, are observed. The major Gd_2O_3 type phase is most likely a solid solution containing several of the rare earth cations in it.

From the XRD patterns (Fig. 2a–c), it can be clearly observed ($2\theta = 20°–30°$) that the intensities of the superstructure reflections varies in different ME-POs. This intensity variation is strongly dependent on the degree of deviation from the cubic perovskite structure, which indeed strongly depends on the lattice parameters (Table 1) of the perovskite phases. The pictorial representation of distortion from the ideal cubic lattice, based on the structural information obtained from Rietveld refinement, is shown in the Supplementary information (Figs. S12(a) and (b)). The Goldschmidt's tolerance factor (*t*) is a well-known theoretical parameter used for explaining this type of deviation from cubic symmetry and is calculated from the ionic radii [15] based on the following equation [16]:

$$t = \frac{r_A + r_O}{\sqrt{2}(r_B + r_O)} \tag{2}$$

where r_A and r_B are the ionic radii of the cation at A-site and B-site (see Table S1 in the Supplementary information), respectively, and r_o is the radius of the oxygen ion. In case of multiple cations at a specific site an average of the ionic radii is considered.

In an ideal case, for the cubic structure *t* should be equal to 1. For $t < 1$, i.e., for systems with smaller A-site cation or bigger B-site cations, orthorhombic or rhombohedral structures are preferred, whereas tetragonal or hexagonal structures are preferably formed for $t > 1$. In case of ME-POs orthorhombic perovskite phases are observed as the value of *t* is lower than 1 (Table 2) and the deviation from the cubic symmetry becomes more prominent with adding (or substituting smaller cation) on the A-site or bigger on the B-site. Another parameter which is often used to explain the deviation from the pseudo-cubic symmetry is the degree of metric distortion (ε) which can be defined as [17]:

$$\varepsilon = \left(\frac{1}{3}\right)\bullet\left[\left\{\frac{a_{norm} - a_{ps.cubic}}{a_{ps.cubic}}\right\}^2 + \left\{\frac{b_{norm} - a_{ps.cubic}}{a_{ps.cubic}}\right\}^2 + \left\{\frac{c_{norm} - a_{ps.cubic}}{a_{ps.cubic}}\right\}^2\right]^{0.5} \tag{3}$$

where $a_{ps.cubic}$ is the pseudo-cubic lattice parameter, and a_{norm}, b_{norm}, c_{norm} are the normalised values of pseudo-cubic lattice parameters taking into account the orientation of the lower symmetry cell. These values are calculated from the following equations:

$$a_{ps.cubic} = \sqrt[3]{V} \tag{4}$$

$$a_{norm} = \frac{a}{\sqrt{2}\sqrt[3]{V}},\ b_{norm} = \frac{b}{\sqrt{2}\sqrt[3]{V}},\ c_{norm} = \frac{c}{2\sqrt[3]{V}} \tag{5}$$

where *V* is the volume per ABO_3 unit, i.e.,

$$V = \frac{a * b * c}{4} \tag{6}$$

with *a, b, c* being the original lattice parameter of the orthorhombic (*Pbnm*) perovskites obtained from the Rietveld analysis (Table 1). In case of ε, the extent of deviation from the ideality follows a similar trend as the theoretical parameter *t* (Table 2). With decrease in the cationic radii at the A-site, or increase in the cationic radii at the B-site

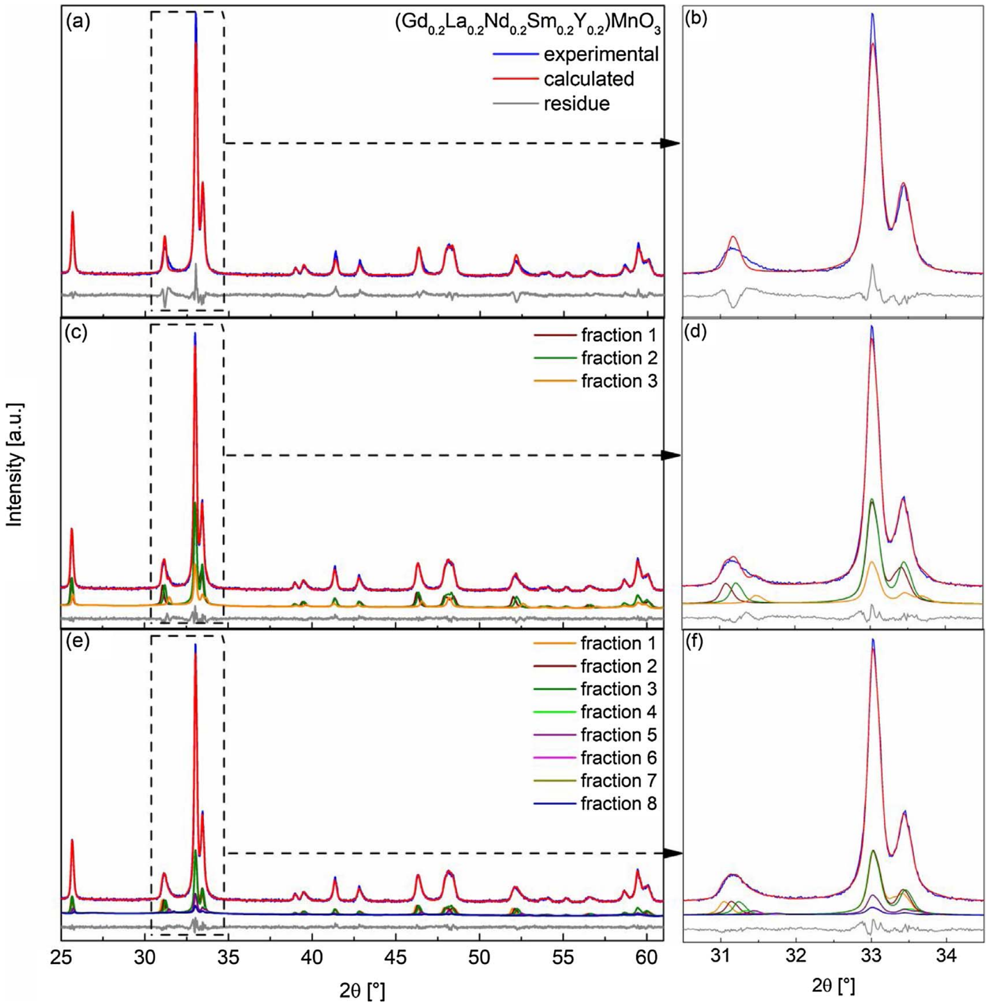

Fig. 3. XRD pattern together with Rietveld fit of $(5A_{0.2})MnO_3$, where either a single (a), 3 (b) or 8 (c) perovskite phases are used to refine the structure. The zoomed in section (b, d and f) shows that a good fit can be achieved with a strongly constrained distribution model of 8 perovskite phases.

Table 2
Overview of the Goldschmidt's factor (*t*), metric distortion (ε), and effective coordination number (ECoN) for A- and B-site elements in ME-PO systems obtained from ionic radii, lattice parameters of phase with perovskite structure and structural model, respectively.

ME-POs	*t*	ε [%]	ECoN(A)	ECoN(B)
$5A_{0.2}$ = $Gd_{0.2}La_{0.2}Nd_{0.2}Sm_{0.2}Y_{0.2}$				
$(5A_{0.2})CoO_3$	0.932	0.344	7.41	6.00
$(5A_{0.2})CrO_3$	0.927	0.547	7.24	6.00
$(5A_{0.2})FeO_3$	0.918	0.580	7.12	5.99
$(5A_{0.2})MnO_3$	0.914	2.299	6.12	5.48
$(5A_{0.2})NiO_3$[a]	0.963	–	–	–
$5B_{0.2}$ = $Co_{0.2}Cr_{0.2}Fe_{0.2}Mn_{0.2}Ni_{0.2}$				
$Gd(5B_{0.2})O_3$	0.900	1.609	7.29	5.98
$La(5B_{0.2})O_3$	0.963	0.198	10.09	5.99
$Sm(5B_{0.2})O_3$	0.921	0.685	7.59	5.99
$Nd(5B_{0.2})O_3$	0.932	0.438	7.14	5.97
$Y(5B_{0.2})O_3$	0.880	1.425	6.59	5.98
$(5A_{0.2})(5B_{0.2})O_3$	0.919	0.633	7.43	5.99

[a] Perovskite phase was not formed in this system.

(see Table S2 for the ionic radii of the cations given in the Supplementary information), ε deviates strongly from ideality ($\varepsilon > 0$) and hence, a lowering in degree of symmetry or a higher magnitude of distortion is observed. The tilting and distortion of the BO_6 octahedra in the perovskite oxides is known to be the genesis of several of their important functional properties like magnetic, ferroelectric, etc. [18]. The distortion in perovskite structure from the ideal cubic symmetry is strongly governed by the shape or relative orientation of these BO_6 polyhedra [19]. There can be three different cases: (i) cations displacement inside the octahedra mostly observed for smaller B-cations (often leading to polar structures), (ii) tilting of the octahedra mostly observed for smaller A-cations which are too small to be accommodated within a cuboctahedral cage site (often leading to orthorhombic or rhombohedral structures), and (iii) distortion of the BO_6 polyhedra often seen for compounds with Jahn-Teller active cations (e.g., Cu^{2+}, Mn^{3+}) [18,20]. Fig. S12(c–e) in the Supplementary information illustrates the increasing tilt of the BO_6 octahedra in ME-POs based on the size of the A-cations, and it shows that the tilting of the octahedra follows a similar trend as *t*.

A strong increase in the tilting is observed accompanied by the increase of ε from 0.198 in $La(5B_{0.2})O_3$ to 0.633 in $(5A_{0.2})(5B_{0.2})O_3$, followed by 1.609 in $Gd(5B_{0.2})O_3$. The lowering of symmetry due to the structural distortion is often found to be accompanied by a lowering of the coordination number of the A-site cations [17,21,22]. Hence, the effective coordination number (ECoN) for both the A- and B-site elements are calculated following the formulation proposed by Hoppe [23] and are listed in Table 2. The details of the ECoN calculation together with the refined distances of the A-O, as well as B-O are provided in the Supplementary information (see Table S7 and related discussion). From the calculated ECoN values, it can be seen that for all ME-POs the B-site cations are almost ideally octahedrally coordinated independent of the type of cations present in the A- or B-sites. However, a large deviation from the ideal 12-fold coordination of the A-site cations is observed for all systems. The ECoN(A) also follows the similar trend as t, ε and the degree of tilting of the BO_6 octahedra, i.e., a gradual decrease (from the ideal 12-fold coordination) on addition or substitution of the smaller cation at A-site or larger cation on the B-site. The origin of secondary phases observed in some of the systems can be strongly related to structural distortions in the lattices. In case of the $(5A_{0.2})MnO_3$ system, the strong Jahn-Teller distortion can be one of the plausible reasons for the high metric distortion (2.299) and the low ECoN(A) (6.12) and ECoN(B) (5.48) value. From the ε vs. t, ECoN(A) vs. t and ECoN(B) vs. t plots (Fig. 4(a), (b) and (c), respectively) it can be observed that the system which deviates most from the otherwise fairly linear behaviour is the $(5A_{0.2})MnO_3$ system. This indicates a strong enthalpic contribution due the possible Jahn-Teller distortion, which in turn can be prohibitive for the formation of a single phase perovskite structure in $(5A_{0.2})MnO_3$ at lower temperature (see Sec. 3.4 for the high temperature studies of this system). In $Y(5B_{0.2})O_3$, one possible reason for the formation of multiple phases can be the small size of Y^{3+} and its inclination towards a lower coordination state. For the other systems the following reasons can be possible for the formation of the multiphase mixtures: (i) The chemical nature of the B-site with most stable oxidation states other than 3 + is found to prohibit the formation of a single phase in the case of a multicomponent equiatomic A-site configuration, for example in case of $(5A_{0.2})NiO_3$ the difficulty to stabilise Ni^{3+} (under the synthesis conditions used) could plausibly explain the formation of high amount bunsenite (NiO) phase along with of major monoclinic type non-perovskite phase. (ii) Even for compositions which allow for the formation of perovskite type phase only, segregation of larger from smaller A-site cations along with the Jahn-Teller effect can be prohibitive for the formation of a single phase, as seen in $(5A_{0.2})MnO_3$. Therefore, these above mentioned factors can increase the enthalpy of formation of a single phase compound and hence, favour the formation of non-single phase (either with non-perovskite type impurities or multi perovskite-type phase) compositions. Thus, considering all these factors and the fact that several of the heptanary ME-POs are not phase pure makes the chemically complex single phase 10-cationic system interesting.

3.3. Chemical homogeneity

A detailed TEM study was carried out on the 10-cationic system. On all regions of the sample investigated by TEM, perfect crystallinity has been observed, evident from the sharp lattice fringes shown in the HRTEM micrographs (Fig. 5a and c). The fast Fourier transformations (FFTs) of the HRTEM micrographs are shown in Fig. 5b and d, respectively. The FTTs can be indexed to a single orthorhombic perovskite (*Pbnm*) structure, which is in agreement with XRD findings. To substantiate the local homogeneity of the element distribution in the 10-cationic system, STEM-EELS/EDX spectra imaging was conducted (Supplementary information Fig. S13). Due to the heavily overlapped signals in the EDX spectra caused by the presence of multiple cations (i.e., ten), the elemental distribution maps were mostly extracted from the EELS using the $M_{4,5}$ edges for Gd, Nd and Sm, only M_5 edge for La (since La M_4 overlaps with Ni L_3) and the $L_{2,3}$ edges for Co, Cr, Fe and Mn. The Y and Ni maps were constructed from EDX Y L and Ni K signals, respectively. These maps represent the distribution of the elements qualitatively and show that all the elements are uniformly distributed without any significant fluctuations down to nanometer scale. This confirms the local homogeneity in the studied 10 cationic system. Fig. 6 shows a HAADF-STEM image for $(5A_{0.2})(5B_{0.2})O_3$ system along the [010] zone axis. The atomic layers of A-site containing heavy rare earth cations can be easily distinguished from the light transition metal cations on the B-site by the Z-contrast (here Z is average atomic number for site A and B, respectively). The atomic columns at the A-site show similar contrast indicating a random occupancy of the rare earth cations (Gd, La, Nd, Sm and Y). Similar conclusion can be drawn for the B-site cations confirming the random distribution of Co, Cr, Fe, Mn and Ni, as well.

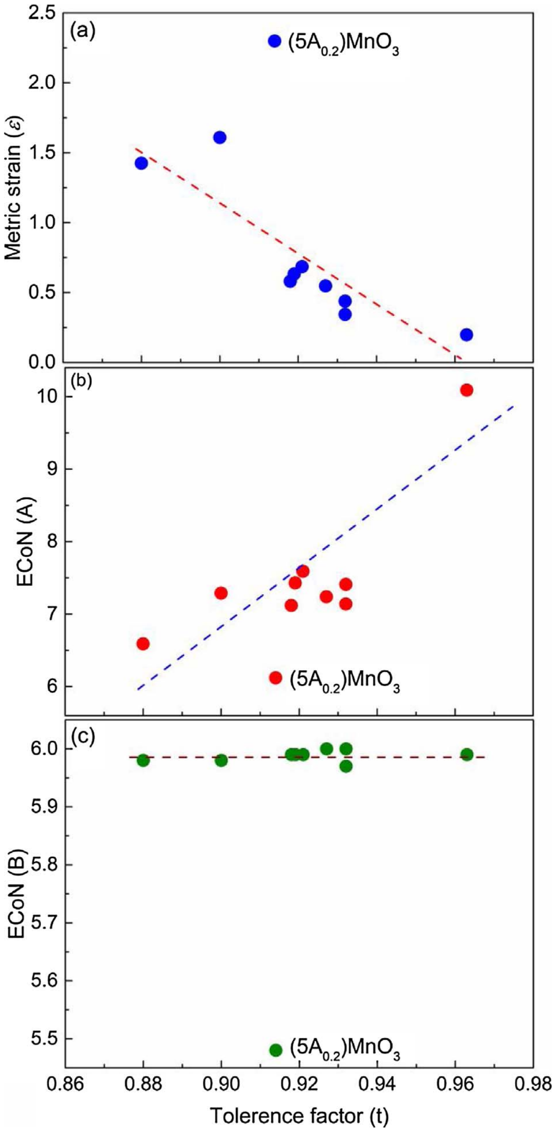

Fig. 4. Metric distortion (ε), EcoN(A) and ECoN(B) are plotted with respect to the tolerance factor (t) in diagram (a), (b) and (c) respectively. A strong deviation of the $(5A_{0.2})MnO_3$ system from the otherwise fairly linear behaviour can be observed.

3.4. Possible reasons for the stabilisation of single phase

In Section 3.2 it has been mentioned that factors like ion-size mediated segregation and affinity of an element towards particular oxidation state (and co-ordination number) can increase the enthalpy of mixing (ΔH_{mix}) for formation of the single phase. Hence, these factors

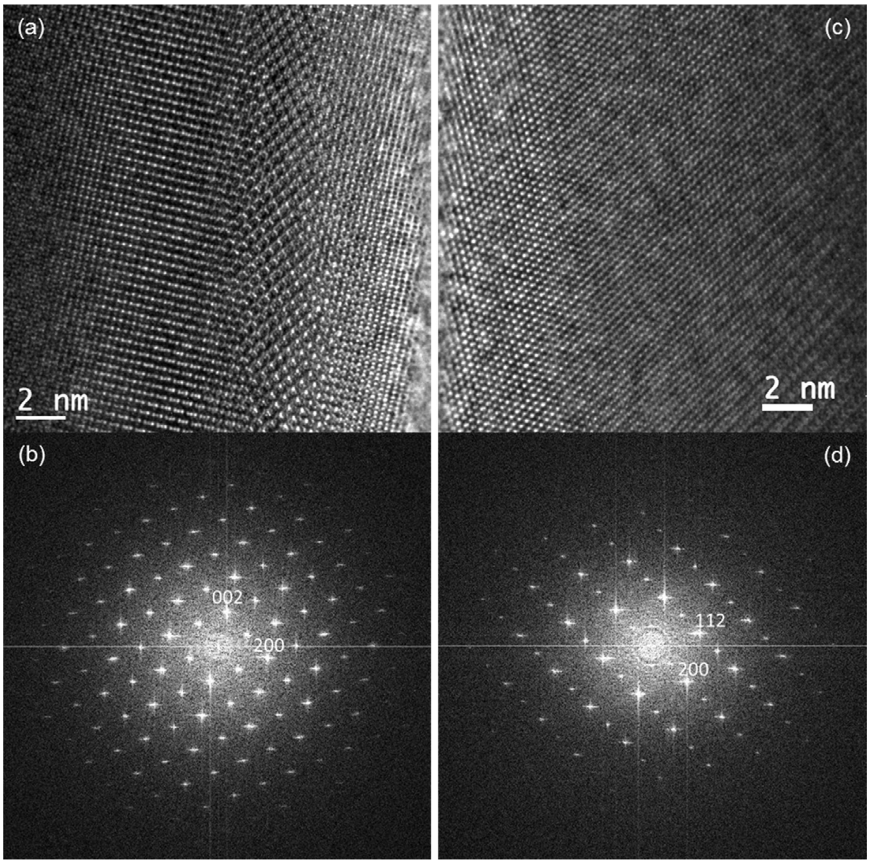

Fig. 5. HR-TEM micrographs and corresponding FFTs, respectively for $(5A_{0.2})(5B_{0.2})O_3$ system along the [010] (a, b) and [02$\bar{1}$] (c, d) zone axes.

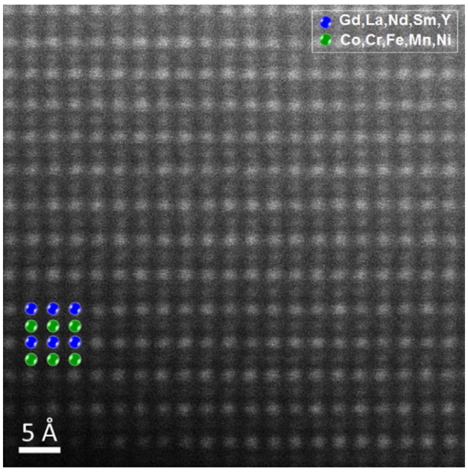

Fig. 6. HAADF-STEM image taken along [010] zone axis, where the atomic layers containing heavier atoms (Gd, La, Nd, Sm and Y) and lighter atoms (Co, Cr, Fe, Mn and Ni), respectively can be clearly distinguished.

stabilise the multiphase mixtures. Thus considering these facts, the high configurational entropy in these ME-PO systems can be one of the plausible reasons for the formation of the single phase, especially in case of the 10-cationic system. In case of multi-principal elemental alloys, better known as the high entropy alloys (HEAs), the high configurational entropy is often regarded as the reason for the formation of single phase structures in chemically complex systems. Similar entropic behaviour in stabilisation of a single phase was also observed in rock-salt based high entropy oxides (HEOs) by Rost et al. [1]. In case of the ME-POs the configurational entropy (ΔS_{config}) can be calculated using the following formula:

$$\Delta S_{config} = -R\left[\left(\sum_{a=1}^{n} x_a lnx_a\right)_{A-site} + \left(\sum_{b=1}^{n} x_b lnx_b\right)_{B-site} + 3\left(\sum_{c=1}^{n} x_c lnx_c\right)_{O-site}\right] \tag{7}$$

where x_a, x_b and x_c are the mole fraction of the ions present in the A-site, B-site and O-site (or the anion site which is oxygen in this case), respectively. For the ΔS_{config} calculations, all the ME-POs are considered to be stoichiometric, i.e., the possible oxygen defects that can be present are not taken into account. For 10-cationic system, $(5A_{0.2})(5B_{0.2})O_3$, S_{config} is 3.22R ($0.0268\,kJ\,mol^{-1}\,K^{-1}$) and is twice that of the other systems, 1.61R ($0.0134\,kJ{\cdot}mol^{-1}{\cdot}K^{-1}$) in which only one of the sites, either A- or B-sites, are substituted by 5 equiatomic cations, $(5A_{0.2})BO_3$ or $A(5B_{0.2})O_3$. The competing factors of enthalpy and entropy are generally described within the approximation of an ideal solid solution. Independent of the systems (whether it is an alloy or an oxide), whenever a non-identical species is added to an existing sub-lattice, two thermodynamically opposing factor come into existence; one is the change of ΔH_{mix} which hinders the stability of the solid solution and the other is the entropic (ΔS_{mix} /ΔS_{config}) gain from the mixing which supports the formation of the solid solution. The existence of the high ΔS_{mix} (or ΔS_{config}) (calculated from Eq. 7) due to the presence of several elements in the ME-PO systems cannot be ignored, independent of whether it actually plays a role in the structural stabilisation or not. In case of rocksalt based HEOs [1], a reversible transformation from multiphase

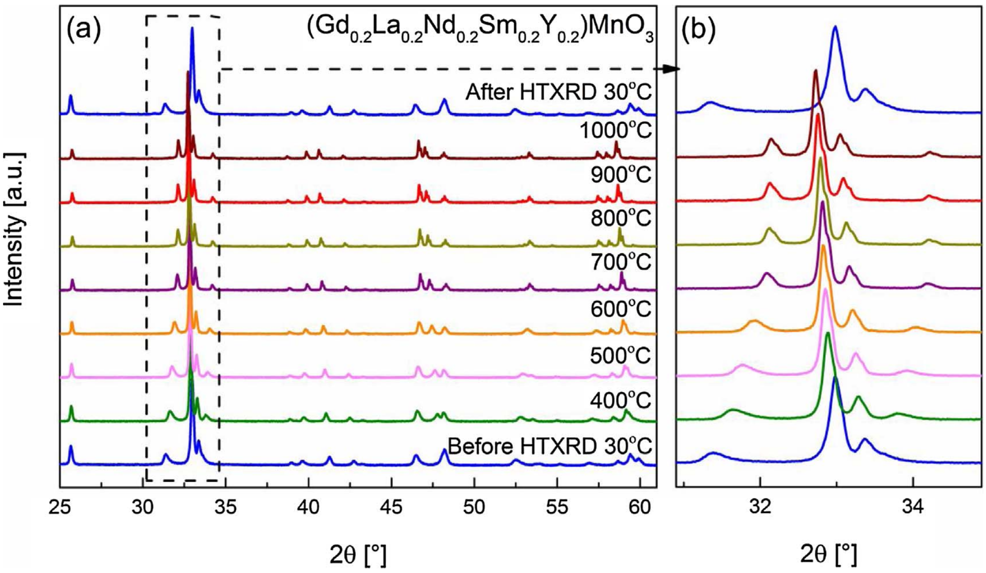

Fig. 7. Full range (a) and magnified portion (b) of the in-situ HTXRD pattern of $(5A_{0.2})MnO_3$ at different temperatures. A reversible transformation from multiple phases to a single phase perovskite occurs around 900 °C.

to single phase structure was observed upon cyclic heat treatment. At higher temperature the $T\Delta S$ term becomes dominant over the ΔH term, hence decreasing the free energy (as $\Delta G_{mix} = \Delta H_{mix} - T\Delta S_{mix}$).

Thus, in order to investigate the role of entropy in the structural stabilisation, in-situ high temperature XRD (HTXRD) measurements were performed on the ME-POs. For the $(5A_{0.2})MnO_3$ system, where a series of perovskite phases (see Fig. 3) are observed, in-situ HTXRD was performed at various temperatures (Fig. 7a). A gradual transformation from a multiphase to a single phase accompanied by distinct changes in the XRD pattern is observed with increasing temperature (Fig. 7a and b). A table with the details of the lattice parameters and phase composition of the powder at each temperature has been provided in the Supplementary information (see Table S8).

The complete transformation to single perovskite type phase in $(5A_{0.2})MnO_3$ is found to occur around 900 °C. The Rietveld refinement for the same has been shown in the Fig. 8. The single phase, thus obtained is preserved even at higher temperature 1000 °C, however, a complete reversion, i.e., a series of perovskite phases is observed while cooling back to room temperature (Fig. 7). This behaviour is very similar to the one observed in case of the rocksalt based HEOs [1], where entropic factors were found to be the reason for the stabilisation of single phase compounds at elevated temperature. Hence, a similar entropic stabilisation is likely to be true in case of the $(5A_{0.2})MnO_3$ system as well, since at higher temperature the $T\Delta S_{mix}$ term compensates the high ΔH_{mix} which is indicated to be especially high for the $(5A_{0.2})MnO_3$ system owing to the possible Jahn-Teller effect (see previous Section 3.2). HTXRD patterns of the 10-cationic system show that the single phase is preserved all along (till 1000 °C) and no phase transformation is observed at lower temperature (Supplementary information Fig. S12). This is explained as follows: (i) the entropy of mixing can be large enough compared to the enthalpy of mixing, i.e., $\Delta S_{mix} >> \Delta H_{mix}$, making ΔG_{mix} independent of ΔH_{mix}, even at lower temperatures, or (ii) even though the enthalpic penalty is larger than $T\Delta S_{mix}$ at lower temperature, the kinetics plays a limiting role (owing to the sluggish diffusion due to presence of several different cations). However, considering the facts that high configurational entropy is inherently present in these systems, one of the heptanary systems show reversible

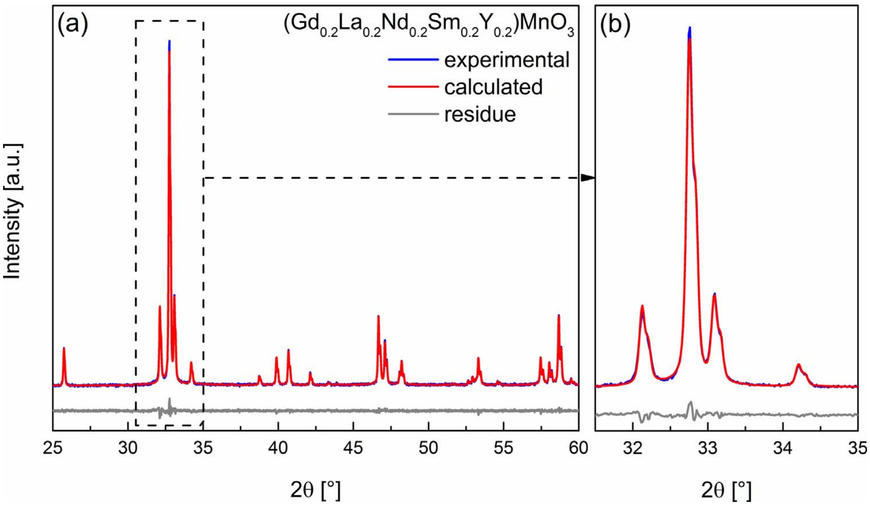

Fig. 8. In-situ HTXRD pattern together with Rietveld fit of $(5A_{0.2})MnO_3$ at 900 °C. The pattern can be well fitted using only a single perovskite phase compared to the fit at room temperature where a minimum of three perovksite phases are needed to fit the pattern and to describe the peak shape due to demixing of A-site cations adequately.

phase transformation as observed in rocksalt based HEOs [1,4], and the 10-cationic system is phase pure (in spite of its high chemical complexity) points towards the dominant role of entropy in structural stabilisation in the ME-POs. HTXRD measurements were done on all the other systems as well (see Supplementary information Figs. S15(a–d) and S16(a–d)). In case of the multiple phase systems ($(5A_{0.2})CrO_3$, $(5A_{0.2})NiO_3$, $Sm(5B_{0.2})O_3$ and $Y(5B_{0.2})O_3$) single phase could not be achieved even at higher temperatures. This further proves the fact that in these systems the enthalpic penalties needed to stabilise the single phase is very high. Hence, supports the fact that the 10-cationic system is most likely entropy stabilised.

It is also interesting that in spite of the presence of so many elements in ME-POs (especially for the 10-cationic system) the orthorhombic distortion of the perovskite phase can be maintained, even at high temperatures (see Supplementary information Fig. S12 and Table S9), instead of formation of a highly symmetric cubic aristotype structure, which is known to be formed for many multinary systems. The tendency to maintain a high symmetry is also observed in the rocksalt type entropy stabilised oxide [1] and the fluorite type multicomponent rare earth oxides [7], where distortion and ordering variants are well known for both systems [24]. Hence, the tilting of the octahedra can be assumed to have an enthalpic contribution (similar to the Jahn-Teller contribution in Cu enriched HEOs) [25] in stabilisation of the lower symmetry perovskite phase. This distortion is known to result from the lowering of the A-site coordination, and apparently this enthalpic contribution is so strong that the adoption of the cubic aristotype is energetically costly. This is further confirmed by a HT-study of the ME-POs system with the lowest deviation from the cubic symmetry (i.e. lowest value of strain ε, see Table 2), $La(5B_{0.2})O_3$. This phase can also not be transformed to a cubic structure, even at higher temperatures. However, in case of the $La(5B_{0.2})O_3$, a reversible structural transition from an orthorhombic (*Pbnm*) phase to a trigonal ($R\bar{3}ch$) phase is observed (Fig. 9). The transformation starts around 125 °C but a distinctive change in the in-situ XRD patterns of $La(5B_{0.2})O_3$ can only be observed above 140 °C. Complete transformation to a trigonal structure takes place around 300 °C, where the volume of both the phase fractions, i.e., the trigonal cell and the orthorhombic cell become equal (see Supplementary information Figs. S17 and S18 and Table S10). The trigonal structure formed is preserved even at higher temperatures 1050 °C. This explains the fact that the octahedral tilting even in this systems (where the $t = 0.963$ and $\varepsilon = 0.198$) plays a crucial role in prohibiting the system to attain a cubic structure.

4. Conclusions

Based on the results obtained from the combine XRD, ICP-MS, TEM and STEM/EDX-EELS studies, three major conclusions can be drawn:

i Out of the eleven different ME-PO systems synthesised, six of the systems can be stabilised as a single phase perovskite type compound at ambient temperature. Even the 10-cationic ($(Gd_{0.2}La_{0.2}Nd_{0.2}Sm_{0.2}Y_{0.2})(Co_{0.2}Cr_{0.2}Fe_{0.2}Mn_{0.2}Ni_{0.2})O_3$) system is phase pure along with random and homogenous cation distribution on the respective sites, in spite of its high chemical complexity for which strong stabilisation of distinct binary combinations could be expected.

ii The fact that five of the heptanary systems are multiphase mixtures whereas the 10-cationic system is phase pure indicates the possible role of unfavourable enthalpic interactions of some of the lower entropy (heptanary) systems which cannot be overcome by the entropic contribution. This indicates a possible role of entropy in the structural stabilisation.

iii The signature of entropy driven structural stabilisation effect in these perovskites systems is strongly supported by the fact that the $(Gd_{0.2}La_{0.2}Nd_{0.2}Sm_{0.2}Y_{0.2})MnO_3$ system shows a reversible transformation from a multiphase to single phase upon cyclic heat treatment. At higher temperature the single phase solid solution is favoured over the multiphase mixtures as the entropic ($T\Delta S_{mix}$) term dominates the free energy landscape. This is a typical entropy stabilisation behaviour, which has been reported only for the rocksalt based multicomponent equiatomic oxides. Hence, this study extends the concept of entropy driven structural stabilisation to multicomponent perovskite type oxides.

iv Large metric distortion from the cubic symmetry along with strong tilting of the BO_6 polyhedra and lowering of the effective coordination number of A-site cation is observed for the systems with smaller cations on the A-site and/or larger B-site cations. The enthalpic factors like cation-size-adopted metric distortion, affinity of certain elements towards a particular oxidation state and Jahn-Teller distortion which favour an ordered scenario can possibly make the formation of a cubic aristotype structure in ME-POs, energetically expensive.

Future studies will focus on the deeper understanding of the local structure of these systems along with the functional properties for their complete exploitation.

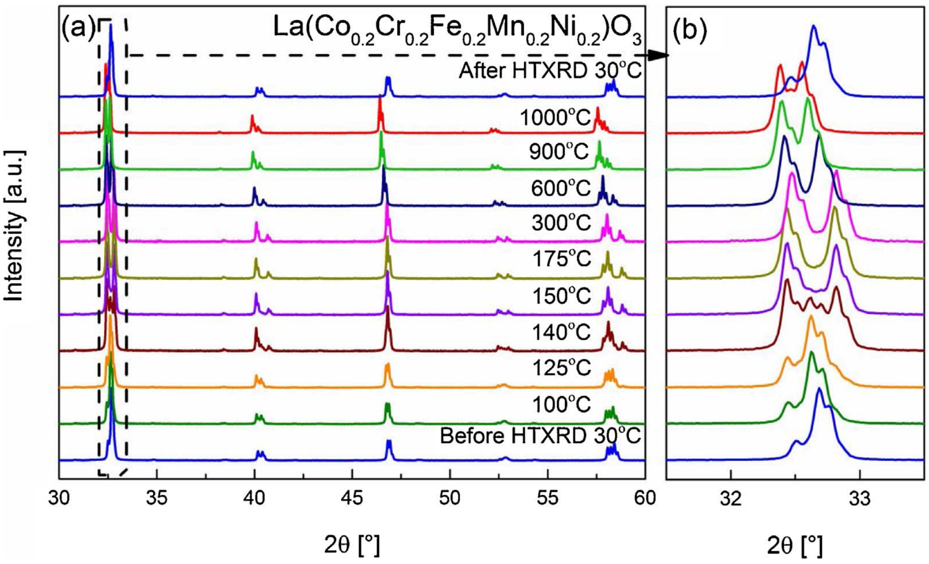

Fig. 9. Full range (a) and magnified portion (b) of the in-situ HTXRD pattern of $La(5B_{0.2})O_3$ at different temperatures. Reversible structural transition from an orthorhombic to trigonal phase starts around 125 °C and complete transition to a phase pure trigonal phase observed above 300 °C.

Conflicts of interest

There are no conflicts of interest to declare.

Acknowledgments

The authors would like to thank the Helmholtz Association (Germany) for financial support through the Helmholtz Portfolio Project “Electrochemical Storage in Systems – Reliability and Integration”. O.C. gratefully acknowledges support within an Emmy Noether Fellowship from the German Research Foundation (CL551/2-1). A.S. thanks Dr. Leonardo Velasco and Sree Harsha Nandam (Karlsruhe Institute of Technology, Germany) for fruitful discussions.

Appendix A. Supplementary data

Supplementary material related to this article can be found, in the online version, at doi:https://doi.org/10.1016/j.jeurceramsoc.2017.12.058.

Supplementary information (Electronic annex): Ionic radii of the constituent cations, space groups of the possible ternary oxide combinations, elemental compositions from EDS, operating parameters and analytical conditions of ICP-MS measurements, Rietveld refinements along with structural parameters of the different phases, the cation oxygen bond distances, description regarding the ECoN calculation, high temperature XRD patterns and related discussion are provided in the supplementary information.

References

[1] C.M. Rost, E. Sachet, T. Borman, A. Moballegh, E.C. Dickey, D. Hou, J.L. Jones, S. Curtarolo, J.-P. Maria, Entropy-stabilised oxides, Nat. Commun. 6 (2015) 8485, http://dx.doi.org/10.1038/ncomms9485.

[2] B.S. Murty, J.W. Yeh, S. Ranganathan, High-Entropy Alloys, Butterworth-Heinemann, London, 2014, http://dx.doi.org/10.1016/B978-0-12-800251-3.00010-9.

[3] J.W. Yeh, S.K. Chen, S.J. Lin, J.Y. Gan, T.S. Chin, T.T. Shun, C.H. Tsau, S.Y. Chang, Nanostructured high-entropy alloys with multiple principal elements: novel alloy design concepts and outcomes, Adv. Eng. Mater. 6 (2004), http://dx.doi.org/10.1002/adem.200300567 299–303 + 274.

[4] A. Sarkar, R. Djenadic, N.J. Usharani, K.P. Sanghvi, V.S.K. Chakravadhanula, A.S. Gandhi, H. Hahn, S.S. Bhattacharya, Nanocrystalline multicomponent entropy stabilised transition metal oxides, J. Eur. Ceram. Soc. 37 (2017) 747–754, http://dx.doi.org/10.1016/j.jeurceramsoc.2016.09.018.

[5] D. Bérardan, S. Franger, D. Dragoe, A.K. Meena, N. Dragoe, Colossal dielectric constant in high entropy oxides, Phys. Status Solidi Rapid Res. Lett. 10 (2016) 328–333, http://dx.doi.org/10.1002/pssr.201600043.

[6] D. Bérardan, S. Franger, A.K. Meena, N. Dragoe, Room temperature lithium superionic conductivity in high entropy oxides, J. Mater. Chem. A 4 (2016) 9536–9541, http://dx.doi.org/10.1039/C6TA03249D.

[7] R. Djenadic, A. Sarkar, O. Clemens, C. Loho, M. Botros, V.S.K. Chakravadhanula, C. Kübel, S.S. Bhattacharya, A.S. Gandhi, H. Hahn, Multicomponent equiatomic rare earth oxides, Mater. Res. Lett. 5 (2017) 102–109, http://dx.doi.org/10.1080/21663831.2016.1220433.

[8] A. Sarkar, C. Loho, L. Velasco, T. Thomas, S.S. Bhattacharya, H. Hahn, R. Djenadic, Multicomponent equiatomic rare earth oxides with a narrow band gap and associated praseodymium multivalency, Dalt. Trans. 46 (2017) 12167–12176, http://dx.doi.org/10.1039/C7DT02077E.

[9] S. Jiang, T. Hu, J. Gild, N. Zhou, J. Nie, M. Qin, T. Harrington, K. Vecchio, J. Luo, A new class of high-entropy perovskite oxides, Scr. Mater. 142 (2018) 116–120, http://dx.doi.org/10.1016/j.scriptamat.2017.08.040.

[10] C.J. Howard, B.J. Campbell, H.T. Stokes, M.A. Carpenter, R.I. Thomson, Crystal and magnetic structures of hexagonal YMnO 3, Acta Crystallogr. Sect. B Struct. Sci. Cryst. Eng. Mater. 69 (2013) 534–540, http://dx.doi.org/10.1107/S205251921302993X.

[11] G.L. Messing, S.-C. Zhang, G.V. Jayanthi, Ceramic powder synthesis by spray pyrolysis, J. Am. Ceram. Soc. 76 (1993) 2707–2726, http://dx.doi.org/10.1111/j.1151-2916.1993.tb04007.x.

[12] R. Djenadic, M. Botros, C. Benel, O. Clemens, S. Indris, A. Choudhary, T. Bergfeldt, H. Hahn, Nebulized spray pyrolysis of Al-doped Li7La3Zr2O12 solid electrolyte for battery applications, Solid State Ionics 263 (2014) 49–56, http://dx.doi.org/10.1016/j.ssi.2014.05.007.

[13] C.A. Schneider, W.S. Rasband, K.W. Eliceiri, NIH image to imageJ: 25 years of image analysis, Nat. Methods 9 (2012) 671–675, http://dx.doi.org/10.1038/nmeth.2089.

[14] Topas V5, general profile and structure analysis software for powder diffraction data, User’s Manual, Bruker AXS, Karlsruhe, Germany, 2015.

[15] R.D. Shannon, Revised effective ionic radii and systematic studies of interatomic distances in halides and chalcogenides, Acta Crystallogr. Sect. A 32 (1976) 751–767, http://dx.doi.org/10.1107/S0567739476001551.

[16] V.M. Goldschmidt, Die Gesetze der Krystallochemie, Naturwissenschaften 14 (1926) 477–485, http://dx.doi.org/10.1007/BF01507527.

[17] O. Clemens, M. Gröting, R. Witte, J.M. Perez-Mato, C. Loho, F.J. Berry, R. Kruk, K.S. Knight, A.J. Wright, H. Hahn, P.R. Slater, Crystallographic and magnetic structure of the perovskite-type compound BaFeO 2.5 : unrivaled complexity in oxygen vacancy ordering, Inorg. Chem. 53 (2014) 5911–5921, http://dx.doi.org/10.1021/ic402988y.

[18] R.J.D. Tilley, Perovskites: Structure-Property Relationships, John Wiley & Sons, Ltd, West Sussex, 2016.

[19] A.D. Aljaberi, J.T.S. Irvine, Crystal structure of A-site deficient La 0.2 Sr 0.7 − x Ca x TiO 3 perovskite at ambient conditions and high temperatures: a neutron powder diffraction study, Dalt. Trans. 44 (2015) 10828–10833, http://dx.doi.org/10.1039/C5DT00238A.

[20] J.A. Alonso, M.J. Martínez-Lope, M.T. Casais, M.T. Fernández-Díaz, Evolution of the Jahn − Teller distortion of MnO 6 octahedra in RMnO 3 perovskites (R = Pr, Nd, Dy, Tb, Ho, Er, Y): A neutron diffraction study, Inorg. Chem. 39 (2000) 917–923, http://dx.doi.org/10.1021/ic990921e.

[21] O. Clemens, M. Kuhn, R. Haberkorn, Synthesis and characterization of the La1 − xSrxFeO3 − δ system and the fluorinated phases La1 − xSrxFeO3 − xFx, J. Solid State Chem. 184 (2011) 2870–2876, http://dx.doi.org/10.1016/j.jssc.2011.08.037.

[22] O. Clemens, R. Haberkorn, P.R. Slater, H.P. Beck, Synthesis and characterisation of the SrxBa1 − xFeO3 − y-system and the fluorinated phases SrxBa1 − xFeO2F, Solid State Sci. 12 (2010) 1455–1463, http://dx.doi.org/10.1016/j.solidstatesciences.2010.06.002.

[23] R. Hoppe, Effective coordination numbers (ECoN) and mean fictive ionic radii (MEFIR), Zeitschrift Für Krist 150 (1979) 23–52, http://dx.doi.org/10.1524/zkri.1979.150.1-4.23.

[24] U. Mller, Inorganic Structural Chemistry, John Wiley & Sons, Ltd, Chichester, UK, 2006, http://dx.doi.org/10.1002/9780470057278.

[25] D. Berardan, A.K. Meena, S. Franger, C. Herrero, N. Dragoe, Controlled Jahn-Teller distortion in (MgCoNiCuZn)O-based high entropy oxides, J. Alloys Compd. 704 (2017) 693–700, http://dx.doi.org/10.1016/j.jallcom.2017.02.070.

PHYSICAL REVIEW MATERIALS **3**, 034406 (2019)

High-entropy oxides: An emerging prospect for magnetic rare-earth transition metal perovskites

Ralf Witte,[1,*] Abhishek Sarkar,[1,2] Robert Kruk,[1] Benedikt Eggert,[3] Richard A. Brand,[1,3] Heiko Wende,[3] and Horst Hahn[1,2]
[1]*Institute of Nanotechnology, Karlsruhe Institute of Technology, 76344 Eggenstein-Leopoldshafen, Germany*
[2]*KIT-TUD-Joint Research Laboratory Nanomaterials, Technical University Darmstadt, 64287 Darmstadt, Germany*
[3]*Faculty of Physics and Center for Nanointegration Duisburg-Essen (CENIDE), University of Duisburg-Essen,*
Lotharstraße 1, 47048 Duisburg, Germany

(Received 8 January 2019; revised manuscript received 18 February 2019; published 13 March 2019)

It has been shown that oxide ceramics containing multiple transition and/or rare-earth elements in equimolar ratios have a strong tendency to crystallize in simple single-phase structures, stabilized by the high configurational entropy. In analogy to the metallic alloy systems, these oxides are denoted high-entropy oxides (HEOs). The HEO concept allows to access hitherto uncharted areas in the multielement phase diagram. Among the already realized structures there is the highly complex class of rare-earth transition element perovskites. This fascinating class of materials generated by applying the innovative concept of high-entropy stabilization provides a new and manyfold research space with promise of discoveries of unprecedented properties and phenomena. The present study provides a first investigation of the magnetic properties of selected compounds of this novel class of materials. Comprehensive studies by DC and AC magnetometry are combined with element specific spectroscopy in order to understand the interplay between magnetic exchange and the high degree of chemical disorder in the systems. We observe a predominant antiferromagnetic behavior in the single-phase materials, combined with a small ferromagnetic contribution. The latter can be attributed to either small ferromagnetic clusters or configurations in the antiferromagnetic matrix or a possible spin canting. In the long term perspective it is proposed to screen the properties of this family of compounds with high throughput methods, including combined experimental and theoretical approaches.

DOI: 10.1103/PhysRevMaterials.3.034406

I. INTRODUCTION

High-entropy oxides (HEOs) represent a new class of oxide systems that have already attracted significant research interest since their recent discovery [1]. The key point of the high-entropy stabilization concept is the combination of a large number of cations (usually five or more) in solid solution in equiatomic proportions, which often results in the formation of a single-phase structure, overcoming the usual enthalpy driven phase separation usually encountered in heavily doped systems [2]. In this way, single-phase compounds with compositions in the center of a complex phase diagram can be produced, which are seldom studied. Such compounds, stabilized by configurational entropy, will be increasingly stable with increasing temperature. Several compositions and elemental combinations each resulting in different crystal structures, such as rocksalt, fluorite, spinels, and perovskite have been stabilized using the HEO concept [1,3–6].

In many of the studied cases (such as rocksalt [1,7], flourite [8], and perovskite type HEOs [9]) it is well understood that the large configurational entropy of the systems dominates the Gibbs free energy of formation and eventually compensates any positive enthalpic contributions. The configurational entropy of a system increases with the number of different elements distributed over the cation lattice site and it attains a maximum when all the constituent elements are present in equiatomic amounts [1]. Apart from the interesting structural ramifications, this distinct design concept may also allow for the fine adjustment of the functional properties. Some examples of already reported tailorable properties in the HEOs are high room temperature Li^+ conductivity [10], catalytic properties [11], colossal dielectric constants [7], superior capacity retention capabilities [12], and narrow and adjustable band gaps [3], to name a few. However, as the field of HEOs is at its early stage many of the material characteristics still remain to be investigated. One of such yet unexplored fields is the magnetism of HEOs, where so far only a single study exists. This study however focuses on the magnetic interaction of a rocksalt HEO with a magnetic layer in a thin film heterostructure, rather than on the intrinsic magnetic properties of the HEO compound [13].

Comparing the different HEO parent oxides structures, one can see that perovskites, with the general formula ABO_3, form one of the most complex and recognized class of oxide materials, see Fig. 1 for illustration. Amongst perovskites, rare-earth and transition metal based oxides have been by far the most extensively studied systems over the last few decades due to their unique properties, from both a fundamental as well as an application point of view. Here, A represents any number of different rare-earth (RE) ions, and B any number of different transition metal (TM) ions. Mixing REs on the A site and/or TMs on the B site allows for adjustment of structural and therefore possibly also functional properties over a wide range. The rich choice of promising characteristics and complex physics found in the parent perovskite compounds,

---

[*] ralf.witte@kit.edu

2475-9953/2019/3(3)/034406(8)

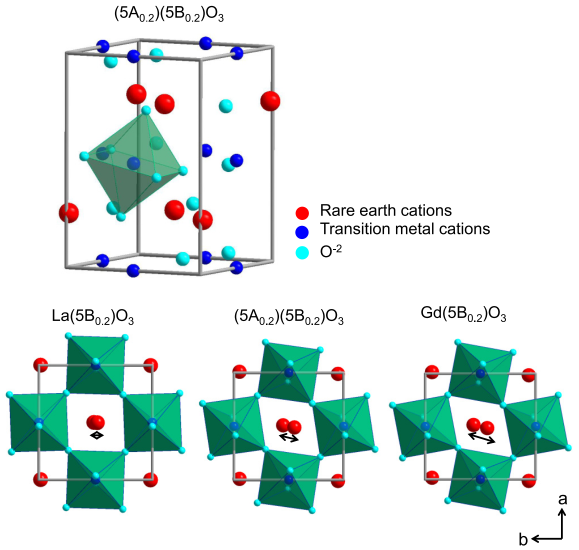

FIG. 1. Upper part: Crystal structure of a representative orthorhombic (*Pbnm*) PE-HEO, $(5A_{0.2})(5B_{0.2})O_3$. Lower part: Illustration of the increasing magnitude of tilting of the BO_6 polyhedra observed in PE-HEOs along the [001] axis with decreasing tolerance factor (larger deviation from a an ideal lattice with tolerance factor = 1) for $La(5B_{0.2})O_3$, $(5A_{0.2})(5B_{0.2})O_3$, and $Gd(5B_{0.2})O_3$.

such as multiferroic effects [14], catalytic activity [15], and electronic [16], electrochemical, and related transport properties [17,18], make them promising candidates for a broad range of engineering applications.

Many of the interesting properties in the perovskites in general are directly related to their crystal structure. Crystal structure stability in perovskites is largely governed by the Goldschmidt tolerance factor, which is a function of the constituents ionic radii [19]. Hence, tailoring the properties for desired applications often starts by altering the cationic radii, realized either by doping or substitution of specific cations. Figure 1 showcases the different degrees of octahedral tilting for three representative compounds with different tolerance factors.

However, doping or substitutional approaches very often have a limitation, in the sense that only relatively small levels of doping can be achieved, due to either the presence of phase boundaries leading to a different structure with undesired properties or phase segregation according to the equilibrium thermodynamics [20,21].

In this study, the magnetic properties of RE-TM based high-entropy perovskites are investigated. Magnetic properties of conventional RE-TM perovskites (ABO_3) have been a major research interest for almost half a century [22,23]. The interlink between their magnetic properties and crystal structure has been extremely important, as any type of structural changes, such as lattice distortion or tilting of the BO_6 octahedra (see Fig. 1), have often shown a decisive impact on material properties. In this case study, the observed unique magnetic properties of the perovskite based high-entropy oxides (PE-HEOs) mainly originate from the presence of multinary TM cations, as they govern magnetic exchange at finite temperatures. A combination of careful magnetometry and Mössbauer spectroscopy experiments has been used to unravel their complex magnetic behavior, dominated by competing antiferromagnetic (AFM) and ferromagnetic (FM) interactions in the TM sublattice. Despite the large number of constituent ions, the effect of cationic radii, as measured by changes in the Goldschmidt tolerance factor, on the magnetic ordering temperature of the compounds has also been observed.

II. EXPERIMENTAL DETAILS

A. Synthesis and structural characterization

PE-HEOs were synthesized by using the nebulized spray pyrolysis (NSP) method. This is an aerosol based synthesis technique in which the decomposition of the precursor solution at elevated temperature leads to the formation of the desired phase [24]. This phase can either be the final product or in some cases an intermediate phase which is then given further heat treatments. In this study the aqueous precursor solutions are mixtures in the appropriate concentrations of the corresponding nitrate salts of the constituent cations. The temperature of the hot wall reactor was maintained at 1050 °C during the synthesis. The as-synthesized powders were additionally heat treated at 1200 °C for 2 hours in air, in order to achieve the final single PE-HEO phase. A detailed description of the synthesis procedure is reported elsewhere [9]. Five of the systems investigated have a single RE *A*-site cation and mixed (TM) *B*-site cations, namely,

$Gd(Co_{0.2}Cr_{0.2}Fe_{0.2}Mn_{0.2}Ni_{0.2})O_3$,
$La(Co_{0.2}Cr_{0.2}Fe_{0.2}Mn_{0.2}Ni_{0.2})O_3$,
$Nd(Co_{0.2}Cr_{0.2}Fe_{0.2}Mn_{0.2}Ni_{0.2})O_3$,
$Sm(Co_{0.2}Cr_{0.2}Fe_{0.2}Mn_{0.2}Ni_{0.2})O_3$,
$Y(Co_{0.2}Cr_{0.2}Fe_{0.2}Mn_{0.2}Ni_{0.2})O_3$.

In addition, a ten equiatomic cationic system,
$(Gd_{0.2}La_{0.2}Nd_{0.2}Sm_{0.2}Y_{0.2})$
$(Co_{0.2}Cr_{0.2}Fe_{0.2}Mn_{0.2}Ni_{0.2})O_3$

which features also a mixed RE *A* site, was also studied. In the sections below, we will denote the mixed *A* site $(Gd_{0.2}La_{0.2}Nd_{0.2}Sm_{0.2}Y_{0.2})$ by $(5A_{0.2})$ and use $(5B_{0.2})$ for the mixed *B* site $(Co_{0.2}Cr_{0.2}Fe_{0.2}Mn_{0.2}Ni_{0.2})$.

Powder x-ray diffraction (XRD) patterns were recorded using a Bruker D8 diffractometer with Bragg-Brentano geometry using Cu-$K\alpha$ radiation with a Ni filter. Rietveld analysis of the XRD patterns, performed using TOPAS 5 refinement software, confirmed that four out of six systems studied crystallize into a single phase, pure orthorhombic (*Pbnm*) structure, which includes the chemically complex decanary system [9]. Transmission electron microscopy studies evidence a homogeneous distribution of the multiple elements [9]. Two systems, $Sm(5B_{0.2})O_3$ and $Y(5B_{0.2})O_3$, show in addition small amounts of nonperovskite type secondary phases (1.7 wt.% Sm_2O_3 and 3.2 wt.% Y_2O_3, 2.1 wt.% NiO respectively. See Supplemental Material [25]). Both of these minority phases have no implications for the analysis of the magnetic properties presented in the following, as they either are paramagnetic in the entire temperature regime or have an AFM transition temperature above the temperature regime investigated here. Structural details of all these systems are tabulated in the Supplemental Material [25], Table S1.

B. Magnetic and Mössbauer characterization

Magnetic characterization was performed using a Quantum Design MPMS3 superconducting quantum interference device (SQUID) vibrating sample magnetometer (VSM). After the sample mass was carefully determined the samples were mounted in the dedicated Quantum Design powder sample holders and subsequent magnetization measurements were done in VSM mode. Temperature dependent measurements were performed following a zero-field cooled (ZFC) field cooled (FC) protocol: The sample was cooled in zero magnetic field down to 2 K. Then the external field $\mu_0 H$ was applied and the magnetization then measured during warming up to 400 K (ZFC branch). Subsequently, the magnetization was measured with the magnetic field applied from 400 to 2 K (FC branch). Magnetic field dependent $M(\mu_0 H)$ measurements were also performed after cooling in zero magnetic field. In addition, some measurements were performed after deliberately cooling in a magnetic field denoted $\mu_0 H_{FC}$, which is highlighted in the respective figures and text.

^{57}Fe Mössbauer spectroscopy (MS) was carried out employing a ^{57}Co:Rh source. Samples were measured in transmission geometry using a triangular sweep of the velocity scale. In-field measurements were realized with the magnetic field parallel to the γ radiation. As is conventionally done, all center shifts are given relative to α-Fe at room temperature.

III. RESULTS AND DISCUSSION

This section is divided into two parts: Section III A presents results of detailed DC and AC magnetometry measurements as well as Mössbauer measurements of the La$(5B_{0.2})$O$_3$ compound. In this material, it is possible to study the physics of the magnetic exchange interaction in the B site sublattice independently of the RE lattice, as La^{3+} carries no magnetic moment. The magnetic exchange interactions in these oxide systems are generally governed by indirect interactions. The most common interaction present here is the superexchange interaction [26], which couples the spins of two neighboring TM ions via hybridization with the oxygen orbitals. This B-O-B coupling can be effectively AFM or FM, depending on the geometrical characteristics of the bond (90 or 180°) and the electronic configuration of the two coupled TM ions as summarized in the Kannamori-Goodenough rules [27,28].

Although AFM ordering dominates for most of the $B1^{x+}$-O^{2-}-$B2^{y+}$ couples, with x, y being their respective oxidation states, there exist also combinations where a FM interaction prevails, such as Fe^{3+}-O^{2-}-Cr^{3+} or Ni^{2+}-O^{2-}-Mn^{4+} [28]. The occurrence of the latter couple is observed for example in the ternary oxide LaNi$_{1-x}$Mn$_x$O$_3$ leading to FM long range order [29], and can be present also in the HEO compounds as a local charge compensation mechanism. We consider the compounds to be fully oxidized and stoichiometric, due to the high temperature annealing in air. Additionally, the occurrence of the double exchange mechanism, which is a delocalized kinetic exchange via the oxygen observed in multivalent manganites [30], leads to FM order. The La$(5B_{0.2})$O$_3$ PE-HEO provides thus the possibility of studying these competing exchange interactions in detail. Moreover La$(5B_{0.2})$O$_3$ has a Goldschmidt tolerance factor (see Sec. II A) which is closest to 1. Thus it is the least distorted crystal lattice and so it makes a natural starting point for the compositional sample series discussed in the next section of the paper.

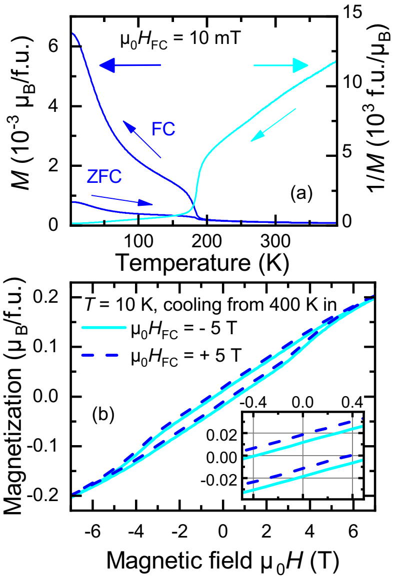

FIG. 2. (a) Temperature dependent magnetization after ZFC and in FC mode; the right-hand ordinate refers to the inverse magnetization. (b) Magnetization as function of the magnetic field $\mu_0 H$ of La$(5B_{0.2})$O$_3$ at T = 10 K, after FC in $\mu_0 H_{FC} = \pm 5$ T. The inset shows the region around the center of the coordinate system; the same axis labels apply.

Section III B presents and discusses the results of magnetization measurements of the entire series A(Co$_{0.2}$Cr$_{0.2}$Fe$_{0.2}$Mn$_{0.2}$Ni$_{0.2}$)O$_3$ (A = Gd, La, Nd, Sm, Y, $5A_{0.2}$) hence including the decenary system denoted $(5A_{0.2})(5B_{0.2})$O$_3$, and puts the findings of Sec. III A in the context of the structural series.

A. La(Co$_{0.2}$Cr$_{0.2}$Fe$_{0.2}$Mn$_{0.2}$Ni$_{0.2}$)O$_3$

Figure 2 presents (a) temperature dependent magnetization $M(T)$ (in $\mu_0 H$ = 10 mT) and its inverse as well as (b) magnetic field dependent measurements at 10 K. The $M(T)$ behavior provides clear evidence for a magnetic phase transition at T_N = 185 K, moreover the large differences between the ZFC and FC branches indicate the presence of large magnetic anisotropy. The inverse susceptibility also shows a clear magnetic transition and in addition a strong deviation from linear behavior at high temperatures above the transition. The latter is an indication of magnetic correlations existing even above the transition temperature prohibiting the extraction of the (average) effective paramagnetic moment μ_{eff} from the linear part. The presence of these correlations is reasonable, as the magnitude of the magnetic superexchange interactions of, e.g., Fe-O-Fe [23], Cr-O-Cr [31,32], or Fe-O-Cr [33] couples is quite large.

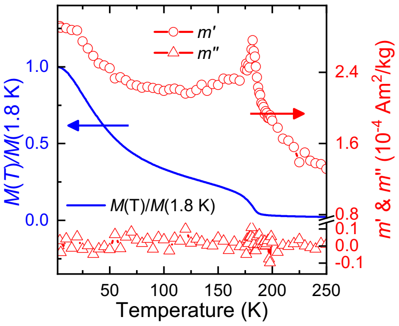

FIG. 3. In comparison to the AC magnetizations m' and m'', the normalized DC magnetization as function of temperature is shown.

Low temperature hysteresis measurements $M(\mu_0 H)$ after FC in $\mu_0 H_{FC} = \pm 5$ T [Fig. 2(b)] are nearly linear up to the highest attainable magnetic field of $\mu_0 H = 7$ T and show no sign of saturation. However, the presence of an opening of the hysteresis indicates that some magnetic moments or a projection of the magnetic moment stays aligned at zero magnetic field (remnant magnetization). Interestingly, this opening of the hysteresis curve extends even up to high magnetic field, resulting in a considerably large coercive field $\mu_0 H_C = 3.6$ T of the ferromagnetic part of the curve at 10 K, which is again a sign of strong magnetic anisotropies present in the sample. In fact, measuring the samples at $T < 10$ K results in so-called minor loops, hence the accessible magnetic field is not sufficient to reverse the magnetization completely (see additional data in the Supplemental Material [25]). This observation shows that the coercive field $\mu_0 H_C$, which is already large at 10 K, is steeply increasing with further decreasing temperature.

$M(\mu_0 H)$ curves measured after FC in ±5 T, presented in Fig. 2(b), show an obvious field offset from the center seemingly in both horizontal and vertical directions. Analyzing the derivative of the entire curve (see Supplemental Material [25]) shows that the FM part of the curve is not shifted along the field axis, as would be expected for an exchange bias effect. However the vertical exchange bias (VEB) is real and amounts to a relative size of 25% with respect to the remnant magnetization.

The VEB is known to be a possible result of uncompensated spins in AFM materials [34], which align during FC giving a net magnetic moment, but which cannot be reoriented at low temperatures by the magnetic field due to their strong coupling to the AFM lattice. However, in the PE-HEOs, we have additionally a precondition for competing FM and AFM exchange interactions because, e.g., the Fe-O-Cr or also mixed valence pairs couple ferromagnetically. Assuming a simple binomial distribution, one obtains a probability of about 10% for finding more than, e.g., three Cr^{3+} ions as nearest neighbors of one Fe^{3+} ion. These ensembles can act as small FM clusters in the AFM matrix, which get frozen and locked during FC. However the coupling to the surrounding AFM matrix results in a strong frustration and probably noncollinear arrangement of these magnetic moments at low temperatures. Moreover the exchange coupling with the AFM matrix also explains the extraordinarily large coercive fields of the FM component at low temperatures (see Supplemental Material [25], opening of the hysteresis up to nearly 7 T).

The VEB effect has been further studied as a function of temperature from which the sample was cooled in the magnetic field, here denoted T_{FC}. The VEB is largest when the magnetic field is applied above the magnetic transition, reaching a relative value of 25%. Yet when the field is applied below the transition temperature one expects that the effect will directly vanish; however, what happens instead is that the value of EB reduces gradually down to 8% when field cooling from 15 to 10 K only.

This unusual behavior reflects the fact that the strength and sign of the magnetic exchange interaction varies drastically between the parent compounds. For example, in $LaFeO_3$, T_N is 740 K [23]; $LaCrO_3$ is 290 K [31,32]. In $LaMnO_3$, antiferromagnetically coupled FM planes order below 100 K [35], while $LaNiO_3$ and $LaCoO_3$ are paramagnetic down to lowest temperatures [36,37]. Therefore the strength of the magnetic exchange and with that the magnetic correlations can be locally different, depending on the local elemental composition. This would tentatively explain a distribution of magnetic transition temperatures on a local scale.

The latter argument on mixed ionic bonds, e.g., magnetic exchange interactions, also sheds some light on the underlying mechanism leading to the VEB behavior. These competing magnetic exchange interactions will necessarily create magnetic frustration on a very local scale. But in the present case, judging from the $M(\mu_0 H)$ curves, AFM coupling still prevails. To support this conclusion, the magnetic transition was investigated with AC SQUID magnetometry (see Fig. 3 and the Supplemental Material [25]). Such a study helps to distinguish between AFM, FM, ferrimagnetic and a possible spin-glass-like frustrated configuration by comparing the frequency dependent magnetic response of the material. This investigation yields no significant effect of either the driving frequency or the amplitude of the oscillating field, which thus excludes (see Supplemental Material [25]) (i) a magnetic spin glass state as well as (ii) a purely ferrimagnetic state. Instead, the featureless appearance of m'' across the transition points towards a predominant AFM coupling [38]. This observation is not in contradiction to the postulated model of small FM clusters embedded in the matrix as they are a minor component and are exchange coupled to the AFM matrix.

The magnetometry presented above already provides valuable insights into the magnetic properties of PE-HEOs. However, a local element-specific view, as is possible with ^{57}Fe Mössbauer spectroscopy, will help to underpin the above considerations. Spectra were measured from ambient temperature across the magnetic transition down to 12 K, and selected measurements are shown in Fig. 4. At room temperature a quadrupole doublet is observed typical for octahedrally coordinated Fe^{3+} (not shown), while at 12 K a magnetic splitting is observed with an average hyperfine field B_{HF} of 49 T. The considerable value of the average B_{HF} provides evidence for a large local magnetic moment on the order of several μ_B, which is typical of Fe^{3+}. ^{57}Fe Mössbauer spectroscopy differs from magnetization in that the measured hyperfine field B_{HF} is independent of direction: the moment orientation with

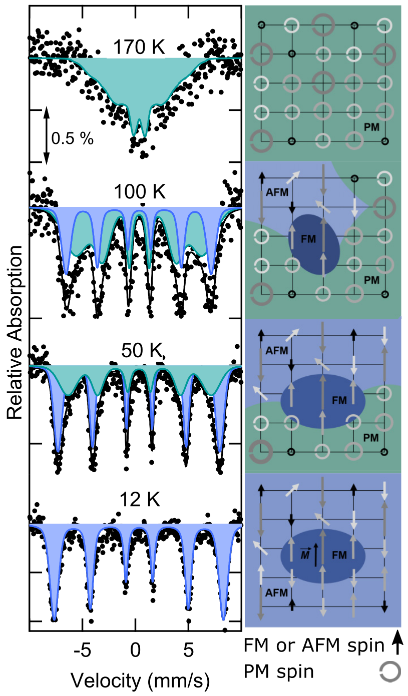

FIG. 4. Left column: Mössbauer spectra in zero magnetic field as function of temperature, represented with two sextets: one broad spectrum (green) representing dynamic fluctuating spins (on the characteristic timescale of the measurement) and one well defined subspectrum (blue) from static magnetic order. Right column: A tentative sketch of the evolution of the proposed magnetic structure. At high temperatures spins are dynamically fluctuating (PM, indicated by circles), with decreasing temperature spins start to couple FM and AFM (blue areas), followed by more and more AFM coupling areas. At low temperatures five different kinds of spins are coupled predominantly antiferromagnetically, but one pair of mixed spins couples ferromagnetically (center). This leads to a local FM cluster which is coupled to the surrounding AFM matrix. Naturally not all exchange interactions can be satisfied, resulting in magnetic frustration and spin canting.

respect to the γ-ray direction only enters into the relative line intensities and not the line separation.

The broadening of the absorption lines can be well fitted with a Gaussian distribution with a width of 2 T, representing the chemical disorder around the Fe sites. However the broadening is small compared to other (only) ternary compounds in which Fe has been substituted by, e.g., Co, Mn, and/or Cr [39–41], which show a broad distribution of hyperfine parameters or even separate individual environments. The small broadening clearly shows that the local environment of Fe is surprisingly well-defined, despite the disordered nature of the material. This comparison with ternary compounds directly shows that the HEO approach allows for the stabilization of single-phase materials in the center of complex multielement phase diagrams, which are otherwise not accessible.

Mössbauer spectra measured in a magnetic field of 5 T parallel to the γ beam at 4.3 K (see spectrum in the Supplemental Material [25]), show a partial reorientation of the hyperfine fields towards a perpendicular arrangement with respect to the magnetic field (the area ratio of absorption lines is 3:3:1). Such a behavior is typical of an AFM or canted AFM system. In conclusion the observed small magnetization originates either from a canted AFM arrangement, locally uncompensated spins or small FM clusters, or both.

A spectrum measured directly below the magnetic transition temperature at 170 K clearly shows dynamic relaxation of the magnetic moments on the timescale of the Mössbauer experiment (e.g., onset of paramagnetism, PM) and is therefore not fitted. A detailed analysis of the spectra measured at 50 and 100 K leads to the conclusion that two subspectra are required to represent the data: One spectrum has a large hyperfine splitting and well defined line width, i.e., a broadening similar to that observed at 12 K. The second subspectrum shows large broadening and a collapsing magnetic hyperfine field.[1] This latter component can be directly attributed to areas of the sample in which magnetic order is dynamic on the timescale of the Mössbauer measurement ($\tau \approx 10^{-9}$ s) at the respective temperature. Magnetic relaxation does not alter the subspectrum area, only its shape. While at 170 K the entire spectrum is dynamic, the spectral area ratio of the dynamic component decreases from 60% to 40% when cooling from 100 to 50 K, while only one well defined sextet is sufficient to represent the data at 12 K.

Summarizing the results on the purely TM based magnetism in La$(5B_{0.2})$O$_3$ one can state that below 185 K magnetic ordering sets in gradually. The complex magnetic state is also responsible for the peculiar occurrence of VEB in this structurally single-phase system. In order to observe VEB it is necessary that small ferromagnetically coupling clusters start to order at higher temperatures and are locked into the gradually ordering AFM matrix. The proposed evolution of the magnetic structure is illustrated in the sketch in Fig. 4.

This intricate magnetic behavior makes the system interesting and unique. Further studies employing wide- and small-angle neutron scattering for identifying local fluctuations of the magnetization and the magnetic structure, x-ray magnetic dichroism for the element specific temperature evolution of the magnetic moments, and possibly also local nuclear spectroscopic techniques, such as nuclear forward scattering, may help in describing in full the magnetic structure of this complex system.

B. $A(\mathrm{Co}_{0.2}\mathrm{Cr}_{0.2}\mathrm{Fe}_{0.2}\mathrm{Mn}_{0.2}\mathrm{Ni}_{0.2})\mathrm{O}_3$

Samples $A(\mathrm{Co}_{0.2}\mathrm{Cr}_{0.2}\mathrm{Fe}_{0.2}\mathrm{Mn}_{0.2}\mathrm{Ni}_{0.2})\mathrm{O}_3$ (with A = Gd, La, Nd, Sm, Y, and $5A_{0.2}$) have been characterized by magnetometry. Temperature dependent ZFC and FC curves are presented in Fig. 5. These have been grouped according to their magnitude. The magnetic transition temperatures (here denoted as Néel temperatures T_N) are plotted as a function of the Goldschmidt tolerance factor in Fig. 6. All the $M(T)$ curves clearly indicate magnetic ordering transitions, which

---

[1] For simplicity we here represent this dynamic subcomponent with Gaussian broadened Lorentzian sextets.

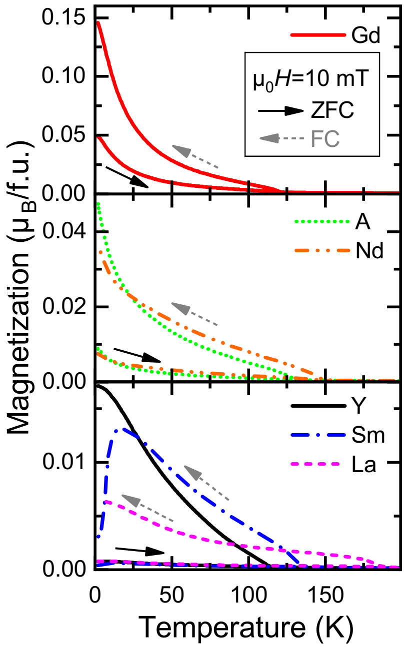

FIG. 5. Magnetization of $A(5B_{0.2})O_3$ as a function of temperature, measured after zero-field cooling and field cooling in $\mu_0 H = 10$ mT. The curves are grouped with respect to their magnitude.

are in the temperature range from 110 to 180 K. All samples, with the exception of the Sm compound, show a continuous increase in $M(T)$ with decreasing temperature. In the compounds with magnetic RE ions (Gd, Nd, $5A_{0.2}$), their large magnetic moment becomes visible at low temperatures. The $Sm(5B_{0.2})O_3$ compound, however, shows a decrease of the magnetization towards low temperatures, leading nearly to a magnetization reversal. A similar behavior has also been observed in $SmFeO_3$ [42] and has been attributed to long-range ordering of Sm^{3+} spins, which couple antiferromagnetically to the canted magnetic moment of the Fe^{3+} ion. A drop in the magnetization is also observed in orthochromites at low temperatures, which in this case has been related to a spin-reorientation transition of the antiferromagnetically coupled Cr spins [43]. What exactly is happening in case of the $Sm(5B_{0.2})O_3$ compound is not straightforwardly deducible from general principles. In order to get a more detailed physical picture, the spin structures need to be fully resolved and element-specific magnetic moments deduced.

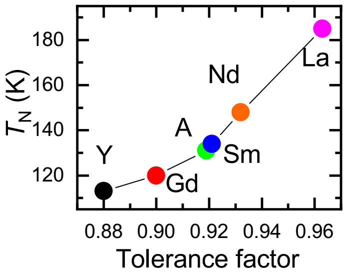

FIG. 6. Magnetic transition temperature of the samples as function of the tolerance factor of the structures and the RE element. The line serves as a guide to the eye.

What can also be noticed when comparing the two compounds with no magnetic moment on the RE site, namely, Y and La, is that the difference between FC and ZFC is much larger for the Y compound; also the magnetization reached after FC is a factor of three times larger. This is again an interesting finding as it illustrates the importance of the structural features for the magnetic properties, as the RE magnetism plays no role. The first observation can be interpreted as an indication of larger magnetic anisotropy in the structurally more distorted Y compound, which might be a reasonable explanation since locally the TM octahedra are strongly anisotropic themselves. This might in turn result in a locally large anisotropy. The underlying reason for the second observation remains unclear, as it is directly linked to the open question about the origin of the observed net magnetization, whether stemming from a frustrated system, locally uncompensated ferrimagnetic spins, or small ferromagnetic clusters.

An interesting finding is that the magnetic transition temperatures for the six compounds are directly correlated to their Goldschmidt tolerance factors (see Fig. 6). This factor is a measure of the distortion of the crystal lattice for different RE ions and is strongly related to the *B*-O-*B* bond angle, decreasing with decreasing tolerance factor. A direct correlation of magnetic transition temperatures to structural and electronic characteristics has also been found in the RE orthoferrites [44,45], RE orthochromites [46], and RE orthomanganites [47]. However, a simple geometric relation to the bond angles is only found in the ferrites, while in the chromites and maganites also other orbital overlap integrals need to be considered due to the different electron configuration of the cations [46]. Thus it is interesting that also in the chemically disordered lattice of the high-entropy oxides, in which ions with different electronic configuration magnetically interact, such a continuous structural dependency is observed.

IV. CONCLUSION

A comprehensive study of the magnetic properties of RE and TM based perovskite type high-entropy oxides is presented. Compounds with intermixed *B* site (five TM elements) and single element *A* sites (RE elements) as well as a compound with five different RE elements on the *A* sites (decenary compound) were investigated. It was found that the magnetic properties of these compounds [9] can only be explained by the presence of competing magnetic exchange interactions within the TM cation sublattice. Detailed investigations by magnetometry and element-specific Mössbauer spectroscopy evidence a complex magnetic state, which is mainly dominated by AF interactions. However, a large degree of magnetic frustration is found due to the high degree of disorder and competing FM and AF interactions. It is proposed that the sign of the magnetic exchange interactions locally alternates, leading to small FM clusters within the predominantly AF matrix. This nanoscale magnetic feature may be responsible for the vertical exchange bias of about 25% of the remnant magnetization. Considering the chemical disorder, we find it surprising that the magnetic ordering temperature of the compounds is directly controlled by the size of the RE ion (Goldschmidt tolerance factor). This correlation can be utilized to provide a method for fine adjustment of the magnetic transition temperatures in these compounds.

The concept of high-entropy multielement oxides allows for stabilization of compounds and structures beyond the doping regime which are not accessible otherwise and which can feature unprecedented novel properties. It is anticipated that also other physical properties, such as dielectric or magnetotransport properties, will be tailored with great freedom. Understanding the underlying mechanisms of the properties of these multielement materials will need joint efforts of experimental and theoretical scientists. The vast multidimensional research space will require the use of experimental and theoretical high throughput methods, such as adapted combinatoric synthesis methods [48,49] and high throughput *ab initio* calculations employing the appropriate choice of descriptors [50] in order to identify promising candidates for applications. Many other outstanding physical properties are expected, considering that the class of parent compounds is known for their spectacular properties, among them ferroelectricity and giant magnetocapacitance [51], multiferroic order [14], colossal magnetoresistance [52], and magnetocaloric [53] properties.

ACKNOWLEDGMENTS

We acknowledge financial support from the Helmholtz Association and the Deutsche Forschungsgemeinschaft (DFG), Projects No. HA 1344/43-1 and No. WE 2623/14-1. We acknowledge discussion with O. Clemens (TU Darmstadt).

[1] C. M. Rost, E. Sachet, T. Borman, A. Moballegh, E. C. Dickey, D. Hou, J. L. Jones, S. Curtarolo, and J.-P. Maria, Nat. Commun. **6**, 8485 (2015).

[2] J. Cheng, A. Navrotsky, X.-D. Zhou, and H. U. Anderson, Chem. Mater. **17**, 2197 (2005).

[3] A. Sarkar, C. Loho, L. Velasco, T. Thomas, S. S. Bhattacharya, H. Hahn, and R. Djenadic, Dalton Trans **46**, 12167 (2017).

[4] J. Dąbrowa, M. Stygar, A. Mikuła, A. Knapik, K. Mroczka, W. Tejchman, M. Danielewski, and M. Martin, Mater. Lett. **216**, 32 (2018).

[5] S. Jiang, T. Hu, J. Gild, N. Zhou, J. Nie, M. Qin, T. Harrington, K. Vecchio, and J. Luo, Scr. Mater. **142**, 116 (2018).

[6] Y. Sharma, B. L. Musico, X. Gao, C. Hua, A. F. May, A. Herklotz, A. Rastogi, D. Mandrus, J. Yan, H. N. Lee, M. F. Chisholm, V. Keppens, and T. Z. Ward, Phys. Rev. Mater. **2**, 060404(R) (2018).

[7] D. Bérardan, S. Franger, D. Dragoe, A. K. Meena, and N. Dragoe, Phys. Status Solidi RRL **10**, 328 (2016).

[8] K. Chen, X. Pei, L. Tang, H. Cheng, Z. Li, C. Li, X. Zhang, and L. An, J. Eur. Ceram. Soc. **38**, 4161 (2018).

[9] A. Sarkar, R. Djenadic, D. Wang, C. Hein, R. Kautenburger, O. Clemens, and H. Hahn, J. Eur. Ceram. Soc. **38**, 2318 (2018).

[10] D. Bérardan, S. Franger, A. K. Meena, and N. Dragoe, J. Mater. Chem. A **4**, 9536 (2016).

[11] H. Chen, J. Fu, P. Zhang, H. Peng, C. W. Abney, K. Jie, X. Liu, M. Chi, and S. Dai, J. Mater. Chem. A **6**, 11129 (2018).

[12] A. Sarkar, L. Velasco, D. Wang, Q. Wang, G. Talasila, L. de Biasi, C. Kübel, T. Brezesinski, S. S. Bhattacharya, H. Hahn, and B. Breitung, Nat. Commun. **9**, 3400 (2018).

[13] P. B. Meisenheimer, T. J. Kratofil, and J. T. Heron, Sci. Rep. **7**, 13344 (2017).

[14] S. W. Cheong and M. Mostovoy, Nat. Mater. **6**, 13 (2007).

[15] J. R. Mawdsley and T. R. Krause, Appl. Catal. A **334**, 311 (2008).

[16] *Localized to Itinerant Electronic Transition in Perovskite Oxides*, edited by J. Goodenough (Springer, Berlin, 2001).

[17] E. Koep, C. Jin, M. Haluska, R. Das, R. Narayan, K. Sandhage, R. Snyder, and M. Liu, J. Power Sources **161**, 250 (2006).

[18] S. J. Skinner and J. A. Kilner, Mater. Today **6**, 30 (2003).

[19] R. J. Tilley, *Perovskites: Structure-Property Relationships* (John Wiley & Sons, West Sussex, 2016).

[20] K. McBride, J. Cook, S. Gray, S. Felton, L. Stella, and D. Poulidi, CrystEngComm **18**, 407 (2016).

[21] S. P. Jiang, L. Liu, K. P. Ong, P. Wu, J. Li, and J. Pu, J. Power Sources **176**, 82 (2008).

[22] C. N. R. Rao, A. K. Cheetham, and R. Mahesh, Chem. Mater. **8**, 2421 (1996).

[23] M. Eibschütz, S. Shtrikman, and D. Treves, Phys. Rev. **156**, 562 (1967).

[24] R. Djenadic, M. Botros, C. Benel, O. Clemens, S. Indris, A. Choudhary, T. Bergfeldt, and H. Hahn, Solid State Ionics **263**, 49 (2014).

[25] See Supplemental Material at http://link.aps.org/supplemental/10.1103/PhysRevMaterials.3.034406 for further information on structural properties and magnetic characterization of the samples. Hyperfine parameters, as well as in-field Mössbauer spectra are also presented.

[26] P. W. Anderson, Phys. Rev. **79**, 350 (1950).

[27] J. B. Goodenough, J. Phys. Chem. Solids **6**, 287 (1958).

[28] J. Kanamori, J. Phys. Chem. Solids **10**, 87 (1959).

[29] M. C. Sánchez, J. García, J. Blasco, G. Subías, and J. Perez-Cacho, Phys. Rev. B **65**, 144409 (2002).

[30] J. B. Goodenough, Phys. Rev. **100**, 564 (1955).

[31] L. M. Daniels, M. C. Weber, M. R. Lees, M. Guennou, R. J. Kashtiban, J. Sloan, J. Kreisel, and R. I. Walton, Inorg. Chem. **52**, 12161 (2013).

[32] J. Prado-Gonjal, R. Schmidt, J.-J. Romero, D. Ávila, U. Amador, and E. Morán, Inorg. Chem. **52**, 313 (2013).

[33] K. Ueda, Science **280**, 1064 (1998).

[34] B. Henne, V. Ney, M. de Souza, and A. Ney, Phys. Rev. B **93**, 144406 (2016).

[35] E. O. Wollan and W. C. Koehler, Phys. Rev. **100**, 545 (1955).

[36] N. Y. Vasanthacharya, P. Ganguly, J. B. Goodenough, and C. N. R. Rao, J. Phys. C **17**, 2745 (1984).

[37] J.-Q. Yan, J.-S. Zhou, and J. B. Goodenough, Phys. Rev. B **69**, 134409 (2004).

[38] M. Bałanda, Acta Phys. Pol. A **124**, 964 (2013).

[39] K. Orlinski, R. Diduszko, M. Kopcewicz, and D. A. Pawlak, J. Therm. Anal. Calorim. **127**, 181 (2017).

[40] Y. Q. Jia, S. T. Liu, Y. Wu, M. Z. Jin, X. W. Liu, and M. L. Liu, Phys. Status Solidi A **143**, 15 (1994).

[41] M. V. Kuznetsov, Q. A. Pankhurst, I. P. Parkin, and Y. G. Morozov, J. Mater. Chem. **11**, 854 (2001).
[42] J. H. Lee, Y. K. Jeong, J. H. Park, M. A. Oak, H. M. Jang, J. Y. Son, and J. F. Scott, Phys. Rev. Lett. **107**, 117201 (2011).
[43] B. Rajeswaran, D. I. Khomskii, A. K. Zvezdin, C. N. R. Rao, and A. Sundaresan, Phys. Rev. B **86**, 214409 (2012).
[44] D. Treves, M. Eibschütz, and P. Coppens, Phys. Lett. **18**, 216 (1965).
[45] I. S. Lyubutin, T. V. Dmitrieva, and A. S. Stepin, J. Exp. Theor. Phys. **88**, 590 (1999).
[46] J.-S. Zhou, J. A. Alonso, V. Pomjakushin, J. B. Goodenough, Y. Ren, J.-Q. Yan, and J.-G. Cheng, Phys. Rev. B **81**, 214115 (2010).
[47] J.-S. Zhou and J. B. Goodenough, Phys. Rev. Lett. **96**, 247202 (2006).
[48] H. Koinuma and I. Takeuchi, Nat. Mater. **3**, 429 (2004).
[49] E. J. Amis, Nat. Mater. **3**, 83 (2004).
[50] S. Curtarolo, G. L. Hart, M. B. Nardelli, N. Mingo, S. Sanvito, and O. Levy, Nat. Mater. **12**, 191 (2013).
[51] T. Goto, T. Kimura, G. Lawes, A. P. Ramirez, and Y. Tokura, Phys. Rev. Lett. **92**, 257201 (2004).
[52] A. P. Ramirez, J. Phys.: Condens. Matter **9**, 8171 (1997).
[53] M. Das, S. Roy, and P. Mandal, Phys. Rev. B **96**, 174405 (2017).

6. Conclusions and outlook

6.1. Conclusions

The objective of this thesis was to explore high entropy oxides (HEOs) with different crystal structures, investigate their functional properties and propose mechanisms to explain the observed structural and functional characteristics. Three different classes of HEOs were studied for this purpose and the important findings for each of these classes are summarized below.

Rocksalt type high entropy oxides (R-HEOs). Single phase R-HEOs consisting of several transition metal (TM) cations were synthesized using three different techniques, flame spray pyrolysis (FSP), nebulized spray pyrolysis (NSP) and reverse co-precipitation (RCP). Among these, NSP is found to be the most versatile technique for synthesizing HEOs, resulting in hollow spherical micrometer sized particles composed of nanocrystallites.

Independent of the synthesis technique, the phase-purity of the R-HEOs is governed by entropy. The first indication in this context is the necessity of higher temperature or an additional heat treatment step to stabilize single phase rocksalt type medium entropy oxides (R-MEOs), which have lower configurational entropy but at the same time are compositionally less complex compared to HEOs. Furthermore, a reversible phase transition from single phase to multiple phase upon cyclic heat treatment confirms the entropy-driven structural stabilization in R-HEOs. Hence, the R-HEOs fall under the more specific sub-group of HEOs, i.e., the entropy-stabilized HEOs.

R-HEOs exhibit superior Li storage capability (above 600 mAh/g for over 500 cycles) posing potential as anodes in secondary lithium ion batteries (LIBs). The Li-storage properties can be further tailored by varying the composition or microstructure of R-HEOs. The electrodes fabricated using R-MEOs exhibited unstable electrochemical behavior, i.e., less capacity, low Coulombic efficiency and poor cyclability, compared to the R-HEOs. The stable performance of R-HEOs can be attributed to an unique electrochemical reaction mechanism. Unlike in conventional conversion electrodes [65], a complete structural conversion (from oxide to respective metals) doesn't happen in R-HEOs, instead the presence of a R-HEO type host structure throughout the cycling process is identified. The retention of the host structure along with the fact that R-HEOs show better performance than R-MEOs indicate a link between the entropy-driven structural stability and enhanced cyclic performance in R-HEOs.

Fluorite type high entropy oxides (F-HEOs). F-HEO systems containing 5-7 rare-earth (RE) cations, in equiatomic proportion, were studied. Systems containing up to 6 different RE cations crystallize in a single phase fluorite structure. The addition of the seventh element results in minor secondary phases, a primary indication of effects in addition to entropy being dominant in F-HEOs. Importantly, it is observed that the absence of Ce in F-HEOs always leads to multiphase mixtures independent of the number of cations. Furthermore, XPS studies reveal that all the cations in F-HEOs are present in a 3+ oxidation state, except for Ce^{4+} and $Pr^{3+,4+}$. Hence, it is deduced that the stable 4+ states of Ce stabilize the single fluorite phase in F-HEOs.

F-HEOs display a narrow band gap enabling light absorption in the visible spectral range. XANES studies, especially at the oxygen K-edge, provide a fundamental understanding of the electronic band structure of chemically complex F-HEOs. Some of the constituent cations, like Pr^{4+} and Ce^{4+}, form low laying intermediate antibonding energy bands, stemming from the hybridization of their $4f$ orbitals with the oxygen $2p$ orbitals. The F-HEOs consisting of Pr^{4+} exhibit band gap of $\sim$2 eV, as electronic transition from valence band (V.B.) to the unoccupied Pr $4f$ state is possible. The occupancy of the intermediate Pr $4f$ band can be manipulated by changing the oxidation state of redox active Pr. Hence, it is possible to reversibly tune the band gap via heat treatment conducted under different environments, i.e., from 2 eV to 2.5 eV in vacuum (VHT) and 2 eV to 3.2 eV in hydrogen (H_2-HT) atmospheres. Heat treatment of F-HEO under reducing atmospheres enhances the occupancy of the Pr $4f$ states. In case of H_2-HT, when Pr is completely reduced to its 3+ state, electronic transition from V.B. to Pr $4f$ is prohibited. Hence, the lowest energy electronic transition that is possible is from V.B. to the Ce $4f$ state, which is positioned at $\sim$3.2 eV from the V.B. Therefore, depending upon the heat treatment condition each of the band structure in F-HEO can be achieved reversibly and reproducibly. Importantly, the phase purity of the F-HEO is retained under all heat treating condition.

Perovskite type high entropy oxides(P-HEOs). Unlike, R-HEOs and F-HEOs, perovskites have two different cation sites. Hence, the successful synthesis of single phase P-HEOs extended the high-entropy based design concept to complex oxides. Eleven different P-HEOs with RE cations on the A-sites and TM cations on the B-sites were synthesized. From the eleven studied systems, six crystallize in single phase orthorhombic perovskite structure. The orthorhombic distortion is prominent in P-HEOs, where the amount of distortion is governed by the cationic sizes like in conventional perovskites. Interestingly, the highly disordered 10-cationic system containing 5 different RE and 5 different TM cations (all in equiatomic proportion) resulted in a single phase whereas several (compositionally less complex) 6-cationic systems showed phase separation. This hints at a possible role of entropy in stabilizing single phase in P-HEOs. The conclusion is further strengthened by the fact that the P-HEO containing only Mn on the B-site reveals a typical entropy-driven reversible phase transformation upon cyclic heat treatment.

The magnetic behavior of P-HEOs was probed. It is observed that the antiferromagnetic (AFM) ordering in P-HEOs exists at lower temperatures despite the chemical disorder. A structure-property relationship can also be deduced, as the magnetic transition temperatures are linked to the degree of orthorhombic distortion (or the tolerance factor) in different P-HEOs. The magnetic ordering in all the systems is predominantly related to the superexchange interactions among the TM cations. The effect of the RE cations is negligible, and only noticeable at very low temperatures. Interestingly, a small ferromagnetic (FM) signature resulting in vertical exchange bias, which is typical of heterogeneous systems, can be identified in single phase P-HEOs. The origin of the net

FM moment can be related to the canting of the AFM spins or presence of FM clusters, where the latter can arise from the synergy between the multiple TM cations.

To summarize, in this dissertation three different types of HEOs have been explored, among which R-HEOs and some of the P-HEOs show entropy-driven phase stabilization while the phase composition in F-HEOs is predominantly determined by the oxidation state of the constituent cations. In terms of functional properties, it is observed that R-HEOs possess interesting electrochemical characteristics, F-HEOs exhibit tunable optical features and P-HEOs depict distinctive magnetic ordering.

6.2. Outlook

Current state of research on high entropy oxides

The section briefly highlights the current status of research on HEOs, which were first reported in 2015 [14]. Currently, there is around fifty papers on HEOs, majority of which are published in the last two years and some being the follow up of works presented in this dissertation. A research highlight and a viewpoint article focusing on the recent developments on HEOs, which are written within the framework of this thesis, are presented at the end of this chapter.

One of the key parameters, which supports the increasing attention on HEOs is the ease of synthesis. Currently, there are several synthesis and processing routes known for HEOs, which are listed in Table 6.1.

Table 6.1.: Different synthesis and processing routes of high entropy oxides.

Product type	Techniques used	References
Powder	Conventional solid-state	[14, 101]
	Nebulized spray pyrolysis	[15, 102]
	Flame spray pyrolysis	[102]
	Reverse co-precipitation	[102, 103]
	Hydrothermal	[103]
	Mechanochemical	[104]
	Sonochemical	[105]
	Solution combustion	[106, 107]
	Solvothermal	[108]
	Polymeric steric entrapment	[109]
Thin film deposition	Pulsed laser deposition	[14, 110, 111]
	Magnetron sputtering	[112]
Pellet	Conventional sintering	[18, 103]
	Spark plasma sintering	[82, 113]

One of the major drawback for the synthesis of HEOs is the requirement of the high temperature, as in several HEOs single phase is obtained only at high temperatures. This often restricts the formation of nanocrystalline structures or more precisely[1] nanoparticles of HEOs. However, this limitation is now taken care off, which is evident from the reports on successful synthesis of HEOs via mechanochemistry [104], sonochemistry [105], etc.

Apart from the exploration of new synthesis techniques, several studies focus on the investigation of new HEO compositions, structure and related underlying principles for single-phase stabilization. HEOs can now be categorized into four major groups on the basis of their crystal structures, namely rocksalt, fluorite (or bixbyite), perovskite and spinel [14, 15, 54, 101]. Out of these HEOs types, only a handful of compositions have shown the typical entropy-driven phase transformation behavior. The highlight article succeeding this chapter includes a list of the different types HEOs, which categorize them based on their entropy-driven phase stabilization effect. There are also recent reports on pyrocholore [114] and magnetoplumbite [115] type HEOs, and these systems fall under the category of non-entropy stabilized HEOs.

More importantly, the factor that will decide the success of HEOs is undoubtedly their properties. Especially, the prospects that the HEOs offer in contrast to conventional materials (with simple compositions) need to be critically evaluated, to exploit their benefits for practical applications. Table 6.2 is a list of properties of HEOs that have already been investigated.

Table 6.2.: Structure and properties of high entropy oxides.

HEO type	Techniques used	References
Rocksalt HEOs	Colossal dielectric susceptibility	[17, 69]
	Room temperature Li-ion conductivity	[18]
	Anode for Li-ion batteries	[54, 58, 75]
	Cathodes for Na-ion batteries	[116]
	As chemical anchor of polysulfide for Li-S batteries	[117]
	High temperature CO catalyst	[71, 72]
	Low thermal conductivity	[51]
	Antiferromagnetic ordering	[73, 74]
Fluorite-HEOs	Narrow and tunable band gap	[102, 118]
	Low thermal and electrical conductivity	[82]
Perovskite-HEOs	Antiferromagnetic ordering	[119, 120]
	Large magnetic anisotropy	[120, 121]
Spinel-HEOs	Room temperature ferrimagnetism	[107, 122]
	Diffusion	[123]
	Oxygen evolution reaction (OER) electrocatalyst	[108]

Several of the studies include comparisons of HEOs with either the parent binary oxides, or the conventional materials that are known to exhibit the best results. The advantages of HEOs can be

---

[1] For instance, NSP is a very efficient HEOs synthesis route leading to nanocrystallites but due to the high synthesis temperature these nanocrystallites agglomerate to form micrometer sized particles with reduced surface area.

identified in two ways: (a) simply, if the achieved values (of the studied properties) are better and (b) if the underlying mechanism governing the properties are unique and can be utilized to tailor them. One such area in which HEOs exhibit potential is their use as thermal barrier coatings, where the thermophysical properties of HEOs along with good mechanical and structural stability can be utilized [51, 82]. Currently, the potential of HEOs in the field of batteries appears to be even more intriguing. For instance, the room temperature Li-ion conductivity in HEOs exceeds that of conventional electrolytes like LiPON, showing promises for their use as solid state electrolytes in LIBs [18]. Another, interesting feature is the remarkable reversible Li-ion storage capability of HEOs [58, 75, 76], showing their potential as anodes in LIBs. In addition, recently the use of HEOs in post-Li batteries like Na-ion and Li-Sulfur batteries have been explored [116, 117].

Future work

The combination of all the aforementioned reports highlights the potential of HEOs, which certainly warrants future studies. In fact the possibilities with HEOs are countless, as the synergies arising from the presence of multiple elements can practically affect all the properties associated with metal oxides. Following is a short list of few such future research directions related to this dissertation.

(i) **Role of configurational entropy in HEOs.** Configurational entropy (S_{config}) is one of the key aspects of HEOs. In some cases the role S_{config} is rather prominent (like in R-HEOs), while in most of the other HEOs it's not clear. Hence, estimating the real enthalpy-entropy (more specifically S_{config}) share in different types of HEOs is not only important from a fundamental of point view but can also be helpful for designing new HEO compositions. However, the task is rather tedious, as S_{config} is just one of the several components of the overall entropy. Although the "entropy-stabilization effect" studied via cyclic heat treatment is typically used to understand the role of entropy in HEOs, it cannot be guaranteed that the observed phase transition (at certain temperature) is solely due to S_{config}. This is because (first-order) phase transitions happening due to effects like change in oxidation states (especially of Co/Mn/Cu), Jahn-Teller distortion, etc., can also be reversible and involve heat of reaction. These effects cannot be ignored in HEOs, but at the same time are difficult to be separated from the "entropy-stabilization effect". Nevertheless, systematic experiments supported by computational thermodynamic studies are important to gain a better understanding of the real role of S_{config} in stabilization of different types of HEOs.

(ii) **HEOs based cathode.** Use of R-HEOs as anode in a full-cell Li-ion battery (LIB), with $Li(Ni_{1/3}Co_{1/3}Mn_{1/3})O_2$ (NCM 111) as the cathode has been already reported [76]. NCM 111 is a layered rocksalt, which is composed of several equiatomic cations. In fact it is believed that the presence of several cations enhances the cyclic stability and capacity of NCM 111 [67]. Hence, fabricating layered rocksalt compositions using the high entropy approach can be worthwhile, as it may even improve the cyclic performance compared to NCM. On the other hand, Li doped variants of R-HEOs depict superior Li-ion conductivity at room temperature. Thus, fabricating a HEO based cathode material would also offer the possibility to design an all-solid-state LIB, by sandwiching the HEO-cathode with the Li-doped R-HEOs (as electrolyte) and R-HEOs (as anode). Nevertheless, there are numerous parameters, such as the adhesion among components, working potentials, interfacial reactions, resistances, etc., that should be addressed before probing the possibility of HEOs based all-solid-state LIBs.

(iii) **Oxygen defects based applications for F-HEOs.** Fluorite type oxides like gadolinium doped ceria (GDC) or yttrium doped zirconia (YSZ) are known for their oxygen ion conductivity, where the ionic conductivity is linked to the oxygen vacancies. F-HEOs have large concentrations of oxygen vacancies, which can potentially promote oxygen ion conductivity at (relatively) lower temperatures. However, an optimal amount of oxygen vacancies is of utmost importance, which can be tailored for F-HEOs via composition or heat-treatments. Catalysis, which often has a direct correlation with the defect concentrations, is another application that can be investigated using F-HEOs.

(iv) **H_2-storage using F-HEOs.** The reason for the anomalous results obtained from Raman spectroscopy of the H_2-heat-treated F-HEOs is yet to be explored in detail [118]. Possible hydrogen incorporation in F-HEOs will be an interesting outcome. In this context, in-depth spectroscopic analysis along with H_2-sorption experiments will be crucial. A positive indication of H_2 incorporation should be followed by further optimization of the structure and composition of F-HEOs for enhanced H_2-storage.

(v) **Electron or hole doping in P-HEOs.** The parent RE-TM perovskites doped with aliovalent elements, exhibit multifaceted properties, like multiferroic effect, magnetoelectric effect, mixed ionic–electronic conduction, etc. A similar approach can be adapted for P-HEOs, where each of the P-HEO can be treated as an independent parent system for doping. For instance, aliovalent (2+, hole or 4+, electron) A-site dopants in $(Gd_{0.2}La_{0.2}Nd_{0.2}Sm_{0.2}Y_{0.2})MnO_3$ can strongly influence its structure and properties, as observed in $(La_{1-x}Sr_x)MnO_3$ [124].

(vi) **Alternative processing techniques.** Already a wide range of synthesis and processing techniques are known for fabrication of HEOs powder and pellets (Table. 6.1). Thin film deposition of HEOs, on the other hand, has been mostly limited to pulsed laser deposition and a sole study utilizing magnetron sputtering (Table. 6.1). In both cases, single target of the desired HEO composition was used for ablation/sputtering. Targets of HEOs are not commercially available, furthermore films with different compositions require different targets. Hence, modified physical vapor deposition techniques involving simultaneous use of multiple parent oxide targets will be of interest. Likewise, simpler, solution based deposition techniques, like spray pyrolysis, dip coating, spin coating, etc., can be advantageous.

(vii) **Combinatorial and high-throughput methods.** Given the complexity of HEOs, numerous structural and chemical combinations are possible. Hence, experimentally scavenging the "sweet-spot" for specific purposes can be rather tedious. Thus, combinatorial approaches, high-throughput methods and artificial intelligence for materials discovery followed the functional properties identification will be essential for the advancement of HEOs.

Statement of contribution

1. **High-Entropy Oxides: Fundamental Aspects and Electrochemical Properties**
   A. Sarkar, Q. Wang, A. Schiele, M. R. Chellali, S. S. Bhattacharya, D. Wang, T. Brezesinski, H. Hahn, L. Velasco, B. Breitung, *Advanced Materials* 31, 1806236 (2019)
   Reprinted under the terms of the CC BY-NC-ND 4.0 license.

   This invited article was written by myself under the guidance of Dr. B. Breitung and Prof. H. Hahn. All co-authors commented on the manuscript.

2. **High entropy oxides: The role of entropy, enthalpy and synergy**,
   A. Sarkar, B. Breitung and H. Hahn, *Scripta Materialia* 187, 43-47 (2020)
   Reprinted with permission from *Scripta Materialia*, ©2020, ELSEVIER.

   This viewpoint article, on invitation from Prof. Jeff De Hosson, was written by myself under the guidance of Dr. B. Breitung and Prof. H. Hahn.

ADVANCED MATERIALS

www.advmat.de

High-Entropy Oxides: Fundamental Aspects and Electrochemical Properties

Abhishek Sarkar, Qingsong Wang, Alexander Schiele, Mohammed Reda Chellali, Subramshu S. Bhattacharya, Di Wang, Torsten Brezesinski, Horst Hahn, Leonardo Velasco,* and Ben Breitung**

High-entropy materials, especially high-entropy alloys and oxides, have gained significant interest over the years due to their unique structural characteristics and correlated possibilities for tailoring of functional properties. The developments in the area of high-entropy oxides are highlighted here, with emphasis placed on their fundamental understanding, including entropy-dominated phase-stabilization effects and prospective applications, e.g., in the field of electrochemical energy storage. Critical comments on the different classes of high-entropy oxides are made and the underlying principles for the observed properties are summarized. The diversity of materials design, provided by the entropy-mediated phase-stabilization concept, allows engineering of new oxide candidates for practical applications, warranting further studies in this emerging field of materials science.

1. Introduction

One of the fundamental driving forces in materials science is the development of advanced materials with tailorable properties. A new concept of materials design, rendering the possibility to affect the phase stability of solid solutions through precise control of configurational entropy, has evolved with the discovery of high entropy alloys (HEAs).[1,2] More recently, the field of high entropy materials has been broadened to include different groups of nonmetallic compounds, like oxides,[3] carbides,[4] borides[5] nitrides,[6] and sulfides.[7] Rost et al. discovered the possibility to incorporate five different cations, in equiatomic ratios, into a single-phase oxide system and defined this as "entropy-stabilized oxide" due to the clear evidence of an entropy-driven structural stabilization effect.[3] In subsequent publications by Bérardan et al., a more general nomenclature, "high-entropy oxides (HEOs)" analogous to "high entropy alloys," has been established to classify multicationic equiatomic oxide systems.[8–10] The same nomenclature, HEOs, has been used here. HEOs are located at the center of a multinary phase diagram, which is often the least explored realm of materials compositions, therefore unexpected behaviors can be anticipated.[8,9,11,12] The formation of chemically complex, single-phase HEOs is noteworthy, since enthalpy-dominated phase separation is a common scenario in most of the complex multinary systems. Investigations into these new material classes have already resulted in many unexpected and interesting findings. Considering the increasing attention being paid to this promising design concept of oxides, the recent results and achievements in the field of HEOs are highlighted in this research news article.

2. Entropy Stabilization Concept and Structural Features

2.1. High-Entropy Concept and Entropy-Based Material's Classification

The general concept of entropy stabilization is based on the possibility to stabilize a single-phase crystal structure by increasing the configurational entropy (S_{config}) of the system. This can be

---

A. Sarkar, Dr. Q. Wang, A. Schiele, Dr. M. R. Chellali, Dr. D. Wang,
Dr. T. Brezesinski, Prof. H. Hahn, Dr. L. Velasco, Dr. B. Breitung
Institute of Nanotechnology
Karlsruhe Institute of Technology (KIT)
76344 Eggenstein-Leopoldshafen, Germany
E-mail: horst.hahn@kit.edu; leonardo.estrada@kit.edu;
ben.breitung@kit.edu

The ORCID identification number(s) for the author(s) of this article can be found under https://doi.org/10.1002/adma.201806236.

DOI: 10.1002/adma.201806236

A. Sarkar, Prof. H. Hahn
Joint Research Laboratory Nanomaterials – Technische Universität
Darmstadt and Karlsruhe Institute of Technology (KIT)
64287 Darmstadt, Germany

Prof. S. S. Bhattacharya
Nano Functional Material Technology Centre
Department of Metallurgical and Materials Engineering
Indian Institute of Technology Madras
Chennai 600036, India

Dr. D. Wang, Dr. B. Breitung
Karlsruhe Nano Micro Facility
Karlsruhe Institute of Technology (KIT)
76344 Eggenstein-Leopoldshafen, Germany

Prof. H. Hahn
Helmholtz Institute Ulm for Electrochemical Energy Storage (HIU)
89081 Ulm, Germany

done by increasing the number of elements, randomly distributed on the same lattice sites. The molar configurational entropy of oxide systems can be calculated according to Equation (1)[12]

$$S_{\text{config}} = -\text{R}\left[\left(\sum_{i=1}^{N} x_i \ln x_i\right)_{\text{cation-site}} + \left(\sum_{j=1}^{M} x_j \ln x_j\right)_{\text{anion-site}}\right] \tag{1}$$

where x_i and x_j represent the mole fraction of elements present in the cation and anion sites, respectively, and R is the universal gas constant. For HEOs, the contribution of the anion site is expected to only have a minor effect on S_{config}, given that only one anion is present (i.e., the effect of possible oxygen vacancies is not considered). S_{config} in an N-components solid solution (with $N = 2, 3, 4$, or 5) as a function of the mole fraction of the Nth component is plotted in **Figure 1**a.[3] It can be observed that S_{config} increases with the addition of more elements to a given system. Furthermore, S_{config} reaches a maximum when all elements are present in equiatomic fractions (Figure 1a). In an equiatomic 5-cation system, the maximum S_{config} value that can be achieved is 1.61 R. As per empirical classification, based on its configurational entropy introduced by Murty et al.,[12] materials with $S_{\text{config}} \geq 1.5$ R can be classified as "high entropy", materials with $1.5\ \text{R} > S_{\text{config}} \geq 1$ R as "medium entropy" and materials with $S_{\text{config}} < 1$ R as "low entropy" systems. The dependency of the free energy of mixing (ΔG_{mix}) on the enthalpy of mixing (ΔH_{mix}) and the entropy of mixing (ΔS_{mix}) is presented in Equation (2).

$$\Delta G_{\text{mix}} = \Delta H_{\text{mix}} - T\Delta S_{\text{mix}} \tag{2}$$

In many cases, a single phase is achieved if $S_{\text{config}} \geq 1.5$ R, as then the $T\Delta S_{\text{mix}}$ can be large enough to dominate the free energy landscape and overcome ΔH_{mix}. This emphasizes the fact that high temperatures are beneficial in the formation of high or medium entropy (single-phase) systems; at room temperature, many these systems must be considered metastable. However, several studies have already shown that this criterion ($S_{\text{config}} \geq 1.5$ R) does not guarantee the formation of a single-phase material.[11,12] In many cases, the configurational entropy gain is not enough to compensate for ΔH_{mix} and, as a result, intermediate products with more favorable formation enthalpies are produced.[11,12] Still, in most of the research on multicomponent near-equiatomic systems the term "high entropy" is commonly used, as there is an assured S_{config} gain (following Boltzmann's entropy Equation (1)) with addition of more elements.[5,6,8,9,11–14]

2.2. Structural Features of High-Entropy Oxides

Initial studies on HEOs concentrated on systems with a rock-salt structure, consisting of only one Wyckoff site for the cations.[3] The first investigated system of this materials class was $(\text{Co}_{0.2}\text{Cu}_{0.2}\text{Mg}_{0.2}\text{Ni}_{0.2}\text{Zn}_{0.2})\text{O}$[3] and, for simplicity, here it is termed rock-salt type HEO (R-HEO). X-ray diffraction (XRD) measurements on R-HEO and corresponding structural analysis confirmed the crystallization of a single-phase rock-salt structure, as shown in Figure 1b.[3,8,15] The range of HEOs has since widened to include a single-phase fluorite structure, resulting from the incorporation of five (or more) equiatomic cations, mostly rare-earth elements, here termed fluorite type HEO (F-HEO); see Figure 1c.[16–18] However, both R-HEO and F-HEO comprise only one Wyckoff site for the cations. Thus, the formation of single-phase perovskite-based HEO (PE-HEO) and spinel-based HEO (SP-HEO) materials was important in providing evidence that this design concept can be extended to structures with multiple cation sites.[13,19–21] Figure 1d shows two single-phase orthorhombic PE-HEOs with 6 and 10 cations.[20] The 6-cation PE-HEO, $(\text{Gd}_{0.2}\text{La}_{0.2}\text{Nd}_{0.2}\text{Sm}_{0.2}\text{Y}_{0.2})\text{MnO}_3$, reveals the possibility to stabilize multiple A-site cations in an orthorhombic structure upon heat-treatment above 900 °C. The 10-cation PE-HEO, $(\text{Gd}_{0.2}\text{La}_{0.2}\text{Nd}_{0.2}\text{Sm}_{0.2}\text{Y}_{0.2})(\text{Co}_{0.2}\text{Cr}_{0.2}\text{Fe}_{0.2}\text{Mn}_{0.2}\text{Ni}_{0.2})\text{O}_3$, on the other hand, illustrates the possibility to form a chemically complex HEO, wherein both the A- and B-sites are populated by multiple cations and all the constituent elements are uniformly distributed on the respective sites.[20]

One important factor affecting the configurational entropy is the local structure of HEOs, as any type of clustering or segregation of elements will decrease the number of possible microstates, thereby lowering the overall entropy.[12] Figure 1e shows a high-resolution transmission electron microscopy (HR-TEM) image along with a selected-area electron diffraction (SAED) pattern of R-HEO.[22] The well-defined lattice fringes and the SAED results indicate the absence of local clustering (of secondary phases), in agreement with the XRD findings, confirming the phase purity of material. The corresponding elemental distribution maps obtained by scanning TEM (STEM)–energy-dispersive X-ray spectroscopy (STEM–EDX, Figure 1f) demonstrate the homogeneity of R-HEO even on the nanometer length scale.[3,22] Consistent results were obtained for other HEOs, such as F-HEO and PE-HEO.[13,16,18,20] Extended X-ray absorption fine structure (EXAFS) studies on R-HEO (Figure 1g) suggest random distribution of elements in the crystal lattice, owing to the fact that the local chemical environment for all cations is found to be nearly identical.[3,23] The combination of these results confirms the single-phase nature and the statistical distribution of cations in the specific sublattice.

2.3. Entropy-Dominated Phase-Stabilization Effects

The entropy-based phase-stabilization effect in HEOs is demonstrated by a set of controlled experimental results obtained from the heat-treatment of HEOs at different temperatures.[3,15,20] In many cases, like for $(\text{Co}_{0.2}\text{Cu}_{0.2}\text{Mg}_{0.2}\text{Ni}_{0.2}\text{Zn}_{0.2})\text{O}$, $(\text{Ce}_{0.2}\text{Zr}_{0.2}\text{Hf}_{0.2}\text{Sn}_{0.2}\text{Ti}_{0.2})\text{O}_2$, or $(\text{Gd}_{0.2}\text{La}_{0.2}\text{Nd}_{0.2}\text{Sm}_{0.2}\text{Y}_{0.2})\text{MnO}_3$, the system undergoes a reversible phase transformation from single-phase solid solution to multiphase mixture when calcined at relatively lower temperatures.[3,8,18,20,24] For R-HEO (Figure 1h), demixing of the rock-salt structure is observed when the system is heat-treated at 750 °C.[3] The single-phase state is regained upon subsequent heating at 1000 °C. This reversible transformation supports the entropy-dominated phase-stabilization concept, as at lower temperatures the overall $T\Delta S_{\text{mix}}$ term might not be large enough to compensate for the enthalpy-driven phase separation. Hence, systems that show this kind of behavior, e.g., $(\text{Co}_{0.2}\text{Cu}_{0.2}\text{Mg}_{0.2}\text{Ni}_{0.2}\text{Zn}_{0.2})\text{O}$, can be classified as entropy-stabilized, which is an important subset of HEOs. This reversible phase transformation is further supported by the calorimetry data for

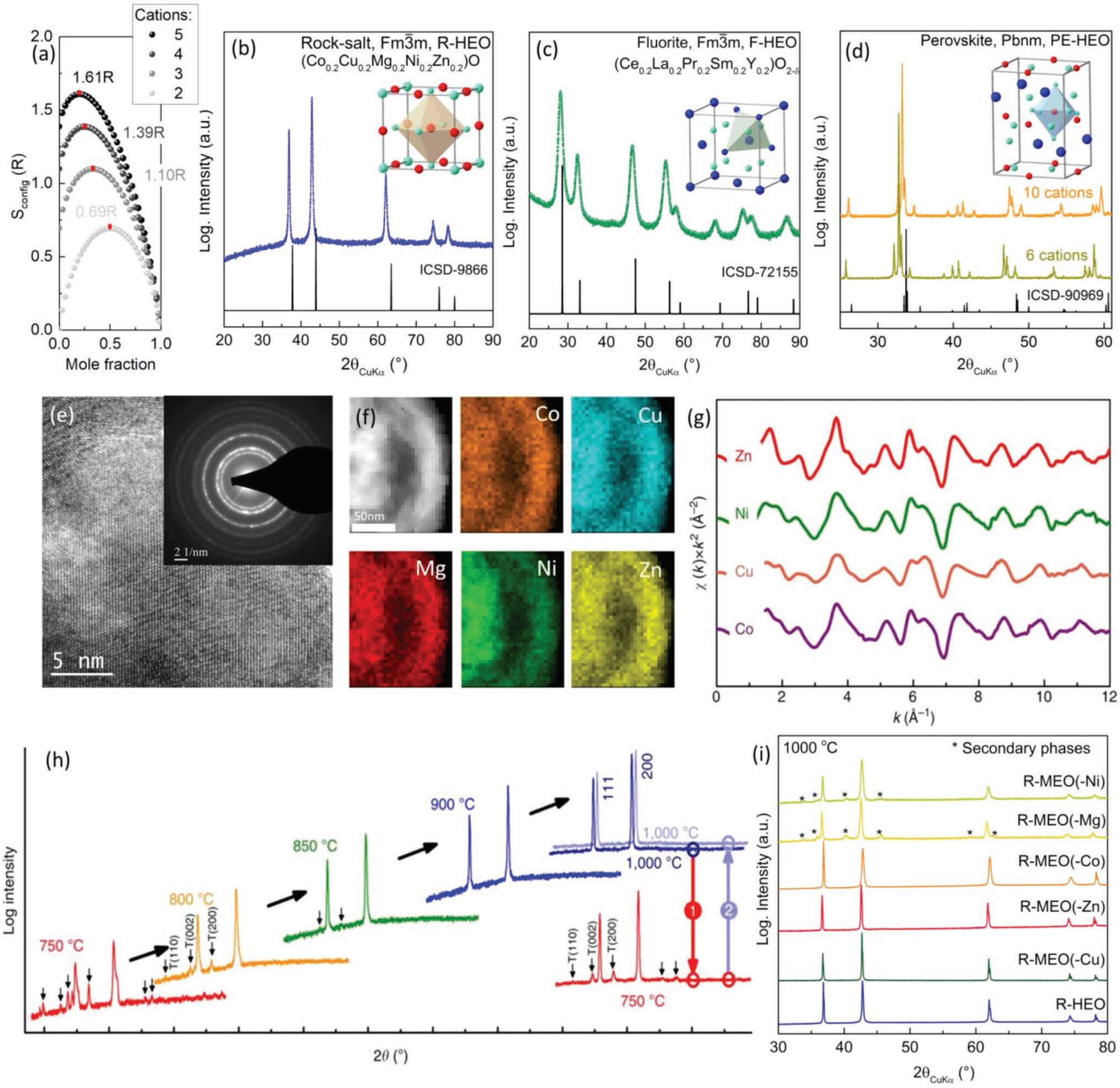

Figure 1. a) Dependence of configurational entropy on the number of elements. XRD patterns of HEO systems: b) R-HEO, c) F-HEO, and d) PE-HEOs. e) HR-TEM image and SAED pattern of R-HEO. f) STEM image and elemental distribution maps indicating chemical uniformity of R-HEO. g) Random distribution of cations from EXAFS. h) Reversible phase transformation as an indication of entropy stabilization effect. i) XRD patterns of different types of R-MEOs. a,g,h) Reproduced under the terms of the CC-BY 4.0 license (http://creativecommons.org/licenses/by/4.0/).[3] Copyright 2015, the authors, published by Springer Nature. b) Reproduced with permission.[15] Copyright 2017, Elsevier. c) Reproduced under the terms of the CC-BY 4.0 license (http://creativecommons.org/licenses/by/4.0/).[16] Copyright 2017, the authors, published by Taylor and Francis. d) Reproduced with permission.[20] Copyright 2018, Elsevier. e,f,i) Reproduced under the terms of the CC-BY 4.0 license (http://creativecommons.org/licenses/by/4.0/).[22] Copyright 2018, the authors, published by Springer Nature.

R-HEO,[3,25] which again indicate an entropy-driven structural stabilization effect, as the transformation from the multiphase (enthalpy favorable) mixture to the single-phase entropy-stabilized material is endothermic in nature.[3,25,26] This reversible phase transformation upon cyclic heat-treatment is not observed for many other classes of HEOs, for instance $(Ce_{0.2}La_{0.2}Pr_{0.2}Sm_{0.2}Y_{0.2})O_{2-\delta}$, $(Gd_{0.2}La_{0.2}Nd_{0.2}Sm_{0.2}Y_{0.2})FeO_3$, etc.[13,16,17] The preservation of the single-phase lattice in these cases can be attributed to the formation of a thermodynamically favorable structure, i.e., ΔH_{mix} is already negative. Hence, ΔG_{mix} will be low (zero or negative) and the influence of $T\Delta S_{mix}$ will be minimal.[20] Therefore, in **Table 1**, different kinds of HEOs reported to date are listed along with a distinction for the systems that show the entropy stabilization effect (cyclic heat-treatment behavior).

Table 1. List of published works on different high-entropy oxides. The table is divided into four different crystal structures along with a clear distinction between the entropy-stabilized and nonentropy-stabilized HEOs.

HEO compositions	Entropy stabilization	Literature reference
Rock-salt-type HEOs (R-HEOs)		
$(Co_{0.2}Cu_{0.2}Mg_{0.2}Ni_{0.2}Zn_{0.2})O$ (Several derivatives of this system containing additional elements like Li, Na, Ga, K, etc.)	Yes	[3,8–10,15,23–25,28–30]
Fluorite-type HEOs (F-HEOs)		
$(Ce_{0.2}La_{0.2}Sm_{0.2}Pr_{0.2}Y_{0.2})O_{2-\delta}$ $(Nd_{0.16}Ce_{0.16}La_{0.16}Sm_{0.16}Pr_{0.16}Y_{0.16})O_{2-\delta}$	No	[16,31]
$(Hf_{0.2}Zr_{0.2}Ce_{0.2})(Y_{0.2}Gd_{0.2})O_{2-\delta}$ $(Hf_{0.25}Zr_{0.25}Ce_{0.25})(Y_{0.125}Ca_{0.125})O_{2-\delta}$ (7 more derivatives of these systems)	No[a]	[17]
$(Ce_{0.2}Zr_{0.2}Hf_{0.2}Sn_{0.2}Ti_{0.2})O_2$	Yes	[18]
Perovskite-type HEOs (PE-HEOs)		
$Ba(Zr_{0.2}Sn_{0.2}Ti_{0.2}Hf_{0.2}Nb_{0.2})O_3$ $Sr(Zr_{0.2}Sn_{0.2}Ti_{0.2}Hf_{0.2}Nb_{0.2})O_3$ $(Sr_{0.5}Ba_{0.5})(Zr_{0.2}Sn_{0.2}Ti_{0.2}Hf_{0.2}Nb_{0.2})O_3$ (11 more derivatives of these systems)	No[a]	[13,21]
$(Gd_{0.2}La_{0.2}Nd_{0.2}Sm_{0.2}Y_{0.2})(Co_{0.2}Cr_{0.2}Fe_{0.2}Mn_{0.2}Ni_{0.2})O_3$ $La(Co_{0.2}Cr_{0.2}Fe_{0.2}Mn_{0.2}Ni_{0.2})O_3$ $(Gd_{0.2}La_{0.2}Nd_{0.2}Sm_{0.2}Y_{0.2})FeO_3$ (7 more derivatives of these systems)	No	[20]
$(Gd_{0.2}La_{0.2}Nd_{0.2}Sm_{0.2}Y_{0.2})MnO_3$	Yes	[20]
Spinel-type HEOs (SP-HEOs)		
$(Co_{0.2}Cr_{0.2}Fe_{0.2}Mn_{0.2}Ni_{0.2})_3O_4$	No[a]	[19]

[a] Cyclic heat-treatment has not been reported in the literature.

Another indication of the entropy-based phase-stabilization effect can be observed by intentionally changing the S_{config} of the systems. Lowering the S_{config} can be achieved by reducing the number of constituent cations (Equation (1)). Analogous to medium entropy alloys, four equiatomic cationic systems are classified as "medium entropy" oxides, MEOs, as the $S_{\text{config}} = 1.39$ R.[12,22] Rock-salt type MEOs are termed R-MEOs(-X), wherein X represents the cation removed from the parent R-HEO, i.e., $(Co_{0.2}Cu_{0.2}Mg_{0.2}Ni_{0.2}Zn_{0.2})O$. Of note, the MEO and HEO classification is only valid for isothermal material comparisons. Because the configurational entropy in MEOs is lower than in HEOs, the former often require higher synthesis temperatures than HEOs to compensate for their lower entropy to form a single phase.[3,22,27] This is illustrated in Figure 1i, in which R-MEOs(-X), synthesized at the same temperature as R-HEO, needed an additional heat-treatment step at 1000 °C to form single-phase compounds. In some cases, like R-MEO(-Ni) or R-MEO(-Mg), single-phase materials cannot be obtained, even after treatment at 1000 °C, as in these cases the ΔH_{mix} term may be significantly larger.[3,22] These experimental observations provide clear indications of an S_{config}-based phase-stabilization effect in R-HEOs and have been recently supported by theoretical (molecular dynamics) studies by Anand et al.[27]

3. Electrochemical Properties

Apart from the structural features, the driving factors for the increasing interest in HEOs are their tailorable properties, which can be utilized in many different areas of application.[8,28–31] Chen et al. showed that R-HEO can act as a CO oxidation catalyst and as a support to stabilize single atomically dispersed platinum species.[28] More recently, there have been reports regarding the thermal properties of HEOs, where an interesting correlation between the low thermal conductivity and the disorder in the systems (i.e., multiple cations acting as phonon scatters) has been observed.[17,30] Reports are also available on thin film deposition,[21,32] sintering,[24,25,29] mechanical,[17,29] magnetic,[33] and optical properties[31] of HEOs. Theoretical studies have not been extensively performed on all classes of HEOs, nevertheless, there are reports on R-HEO, which correlate: (i) the lattice distortion with the Jahn–Teller effect and (ii) the phase composition with the thermodynamic parameters.[27,34,35] The main focus of this research news article is on the electrochemical energy storage properties of R-HEOs, which will be discussed in detail below.

Bérardan et al. reported that R-HEOs exhibit colossal dielectric constants, which can further be tailored by changing the fraction of constituent elements.[8,10] This study, along with the work done on high-entropy nitrides for supercapacitors,[6] indicates that high-entropy materials are interesting for applications in modern microelectronics and for the development of new capacitance-based energy storage devices. The same group showed that a large fraction of aliovalent dopants (Li^+, Na^+, K^+, etc.) can be incorporated into a single-phase R-HEO lattice due to two reasons: (i) Internal defect formation (e.g., oxygen vacancies) and (ii) internal charge compensation within the system, which is achieved by oxidation of Co^{2+} to Co^{3+}. Doped R-HEOs, especially those containing alkali ions (Li^+ or Na^+), revealed interesting transport properties. It was found that at room temperature the Li-ion conductivity of Li-doped R-HEO was on the order of 10^{-3} S cm^{-1}.[9] Furthermore, it increased with doping

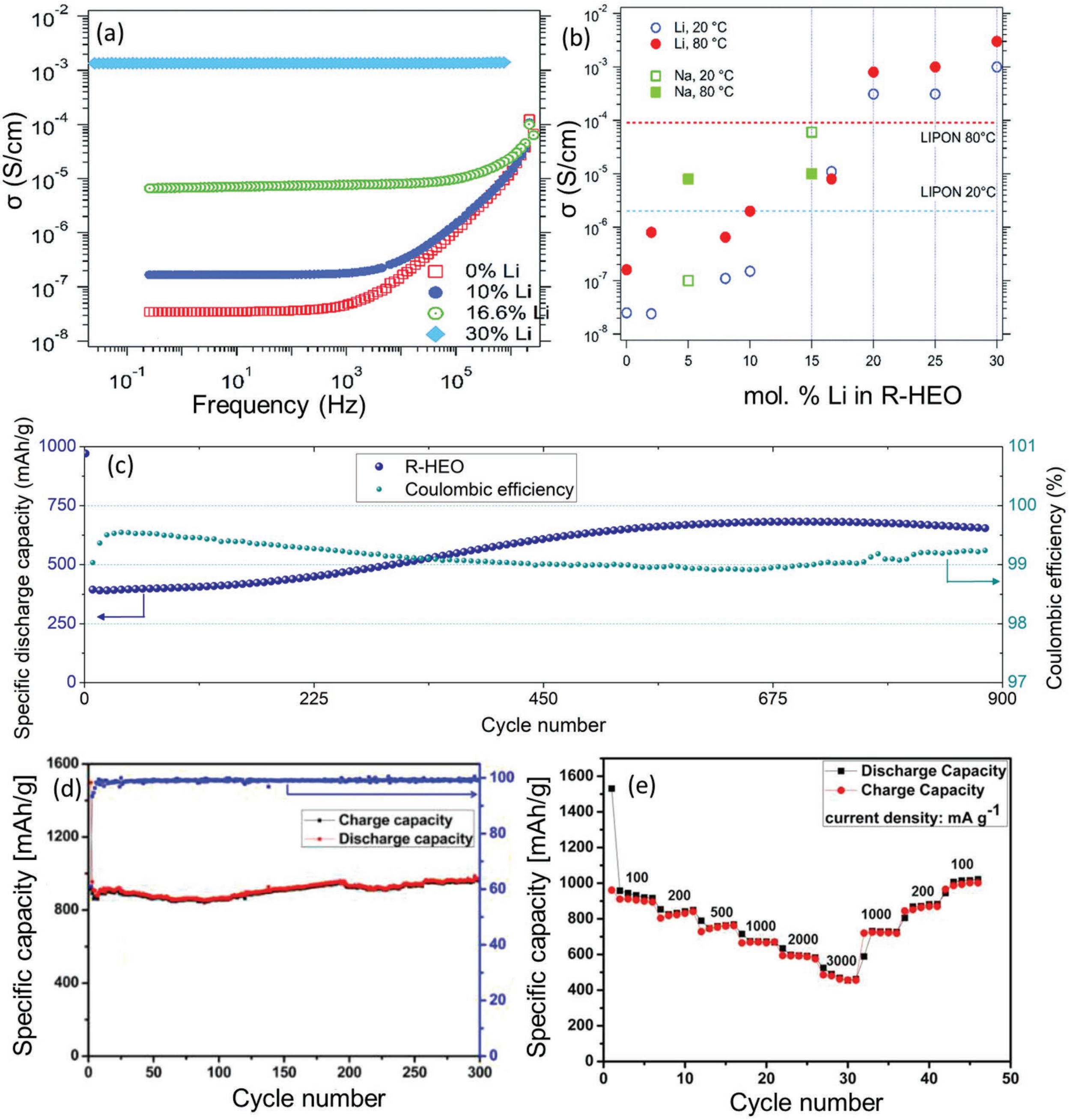

Figure 2. a) Variation in ionic conductivity with Li$^+$-doping level in R-HEO. b) Comparison of ionic conductivities of Li$^+$- and Na$^+$-doped R-HEOs. c) Long-term cycling performance and Coulombic efficiency of R-HEO cells at 200 mA g^{-1} using micrometer-sized particles. d) Long-term cycling performance and Coulombic efficiency of R-HEO with nanometer-sized particles. e) Rate performance test of nanometer-sized R-HEO with the specific current given in units of mA g^{-1}. a,b) Reproduced with permission.[9] Copyright 2016, Royal Society of Chemistry. c) Reproduced under the terms of the CC-BY 4.0 license (http://creativecommons.org/licenses/by/4.0/).[22] Copyright 2018, the authors, published by Springer Nature. d,e) Reproduced with permission.[40] Copyright 2018, Elsevier.

level, from 10^{-8} S cm^{-1} (pristine R-HEO) to 10^{-3} S cm^{-1} (30% Li-doped), as displayed in **Figure 2**a. These results indicate the large domain of composition-based tailorable properties in HEOs. Na-ion conductivities, on the order of 10^{-6} S cm^{-1}, have also been reported for this material class.[9] These ionic mobility values are rather high, especially when compared to many of the existing solid-state electrolytes (Figure 2b), and therefore, HEOs might show promise for use in all-solid-state battery cells.[36–39] From a series of controlled experiments, it has been deduced that alkali ions (Li$^+$ and Na$^+$) likely move through the oxygen vacancies that are created in the R-HEO lattice upon their incorporation.[9] These ionic conductivities are also much larger than the electronic one (≈10^{-9} S cm^{-1}), opening up the possibility to use R-HEOs as pure ionic conductors, as the leakage current will be negligible.

The aforementioned results on the Li-ion conductivity of R-HEOs motivated subsequent studies regarding their performance in Li-ion battery cells.[22,40] It can be seen that the R-HEO shows promising long-term cycling stability (over 900 cycles), with specific capacities >650 mAh g^{-1} and Coulombic efficiencies >99.5% at a specific current of 200 mA g^{-1} (Figure 2c)[22] despite the use of micrometer-sized particles. Moreover, Qiu et al. reported an increase in specific capacity to >900 mAh g^{-1} for more than 300 cycles (Figure 2d) when using R-HEO with nanometer-sized particles.[40] R-HEO with micrometer-sized particles revealed a rate capability behavior with complete capacity recovery, even after cycling at high specific currents.[22] Qiu et al. showed that decreasing the particle size clearly improves the rate performance (Figure 2e); the cells delivered large specific capacities of about 490 mAh g^{-1} at a specific current of 3000 mA g^{-1}, with capacity recovery to ≈1000 mAh g^{-1} at 100 mA g^{-1}.[40] These results demonstrate that even higher specific capacities can be achieved upon further optimization in terms of particle size, electrolyte, binder, etc. The voltage profiles of R-HEO are indicative of a conversion type reaction, with virtually linear voltage decay over the entire potential range after the first cycle.[22,40]

As mentioned in the previous section, an entropy-mediated phase-stabilization effect is known for R-HEOs.[3] A profound effect of entropy on the electrochemical characteristics of R-HEO has been observed, too.[22] By extracting one of the present cations from the R-HEO the entropy decreases from 1.61 R to 1.39 R, as explained in Section 2.3., and the electrochemical characteristics are significantly altered (**Figure 3**). Evidently, the R-HEO exhibits much improved capacity retention over the first 100 cycles compared to the R-MEO(-X) compounds, thus indicating that the transition to medium entropy compounds results in significant performance decay (Figure 3a). This finding leads us to the conclusion that entropy stabilization possibly plays an important role in achieving a stable conversion reaction mechanism.[22] The Coulombic efficiencies corroborate this interpretation by showing the highest values for R-HEO.[22] A complete cell failure within approximately ten cycles is observed for R-MEO(-Co), indicating the importance of Co in the system (Figure 3a). The significance of certain elements, like Co and Mg, to achieve stable cycling performance has also been observed by Qiu et al.[40] The extraction of constituent cations leads to completely different effects on the electrochemical behavior. For example, a much lower lithiation potential is found when Cu is removed from the R-HEO (Figure 3b), while a two-step oxidation with delithiation is seen when Zn is absent.[22] Such element specific behavior may help to design or tailor electrode materials to specific user needs.

The stable cycling behavior of R-HEO observed for both micrometer- and nanometer-sized particles is in fact interesting. During the course of the initial lithiation, the XRD reflections of R-HEO vanished (**Figure 4**a), thus indicating an X-ray amorphous structure after the first half-cycle. However, no other reflections (from secondary phases) or reappearance of the initial reflections, even after subsequent delithiation, were observed. This behavior is typical of conversion electrode materials and can be explained by formation of very small and highly defective crystallites, whose sizes are often below the coherence length of X-rays. Using SAED, a rock-salt structure was clearly identified, even at the fully lithiated state, where only Li_2O and corresponding metals should be present (Figure 4a). Upon subsequent delithiation the rock-salt structure could still be observed.[22] The corresponding STEM–EDX elemental distribution maps demonstrate the homogeneity (no element segregation) of R-HEO after one complete cycle (Figure 4b). This in turn demonstrates the possibility of preserving a stable R-HEO host matrix during the entire conversion process, facilitating reintegration of metal cations in the delithiation cycle.[22] Additionally, SAED rings after the first lithiation indicate the presence of Li_2O, thereby supporting the assumption of a conversion-based reaction during cycling operation (Figure 4c). The host rock-salt structure of R-HEO can still be identified after ten cycles from the SAED pattern shown in Figure 4d. The as-synthesized R-HEO (Figure 1e) shows a well-defined lattice, while a defective structure is evident after ten cycles (indicated by red circles in Figure 4e). Consequently, an entropy-stabilized

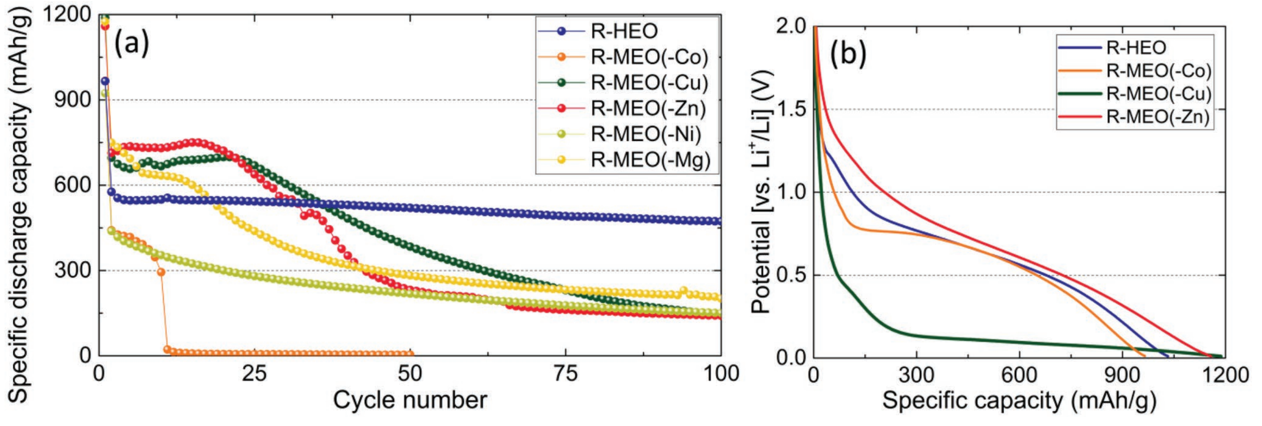

Figure 3. a) Specific capacity over 100 cycles and b) the first lithiation profiles of different compounds. a,b) Reproduced under the terms of the CC-BY 4.0 license (http://creativecommons.org/licenses/by/4.0/).[22] Copyright 2018, the authors, published by Springer Nature.

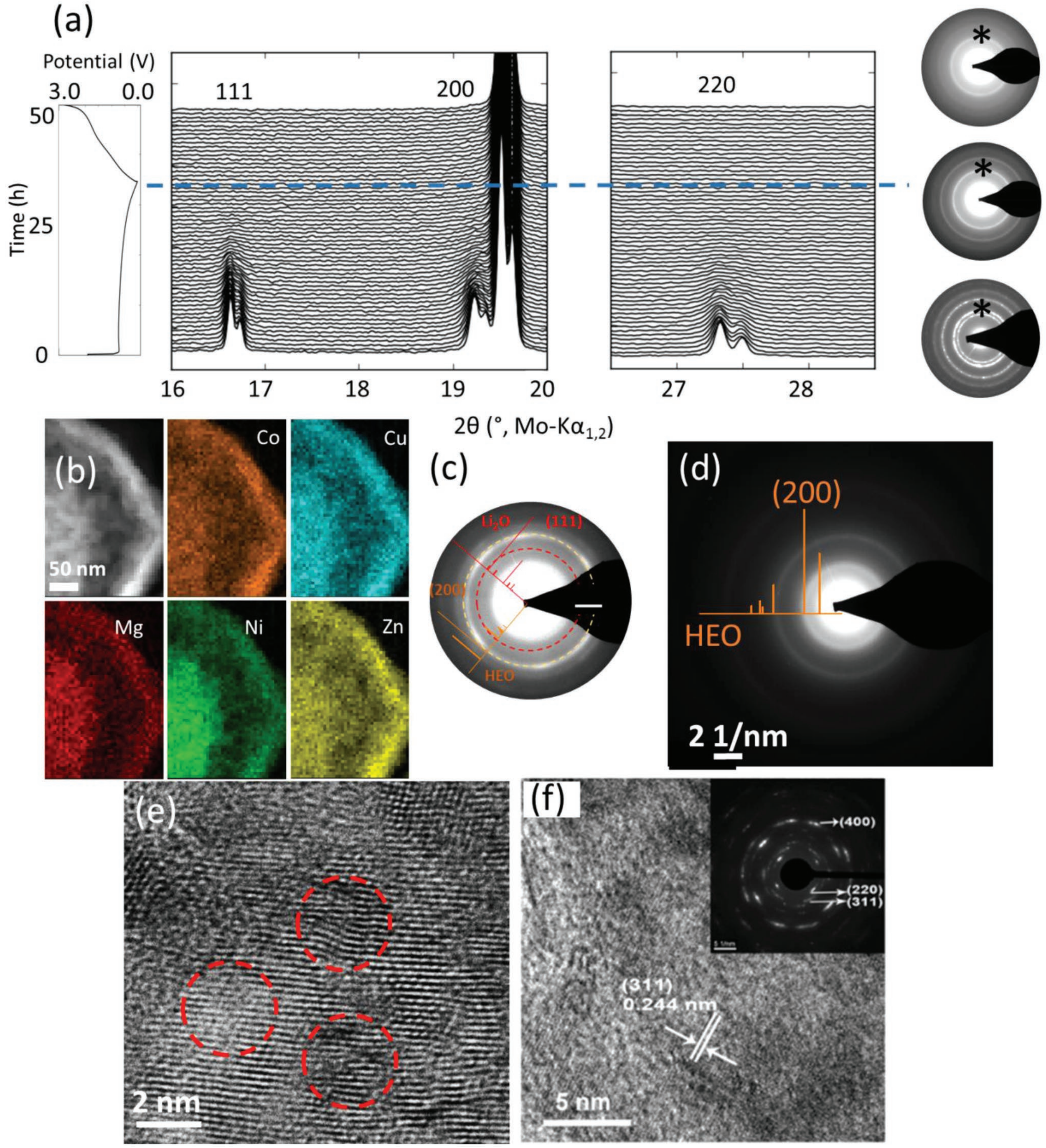

Figure 4. a) Operando XRD and SAED patterns. b) The uniform elemental distribution is evidenced by STEM–EDX. c) Formation of Li_2O visualized by SAED. d,e) Preserved rock-salt structure of R-HEO after ten cycles. f) Rock-salt structure in nanometer-sized R-HEO after 300 cycles. a–e) Reproduced under the terms of the CC-BY 4.0 license (http://creativecommons.org/licenses/by/4.0/).[22] Copyright 2018, the authors, published by Springer Nature. f) Reproduced with permission.[40] Copyright 2018, Elsevier.

conversion reaction is hypothesized,[22] wherein a host rock-salt structure is preserved by some of the constituent elements (e.g., Mg, which does not react in the given potential range) while the others participate in the redox reactions. In the case reported by Qiu et al., similar observations were made.[40] The SAED pattern in the inset of Figure 4f shows that the R-HEO undergoes crystallinity deterioration upon cycling, but small crystalline domains can still be identified after 300 cycles.[40]

The formation of secondary phases (metal or metal oxides) was not observed in both studies. The presence of a "stable" host lattice (probably inactive MgO) and sluggish diffusion effects were assumed by Qiu et al. to be the reasons for the structural integrity and the stable cycling performance.[40] Hence, both studies independently point toward a very similar reaction mechanism, where some of the constituent elements preserve the host lattice structure, while the others react to contribute to the capacity. Combining both mechanistic hypotheses,[22,40] it seems that the retention of R-HEO structure is possibly due to sluggish diffusion, preventing element segregation and formation of individual (binary) oxides.

4. Summary and Outlook

In recent years, HEOs have evolved into a new research field. The possibility of incorporating multiple cations (five or more) into a specific lattice structure opens up new ways for designing/tailoring oxide materials. The uniform distribution of cations in HEOs, among others, strengthens the hypothesis of entropy-dominated phase-stabilization effects in these chemically complex systems. Furthermore, the unique chemistry of HEOs leads to materials with exciting and unexpected properties. The multifunctional behavior of HEO is clearly evident from the fact that there are several different properties reported (dielectric, magnetic, thermal, catalytic, etc.) for a single composition of $(Co_{0.2}Cu_{0.2}Mg_{0.2}Ni_{0.2}Zn_{0.2})O$. The high Li-ion conductivities along with promising Li-storage capabilities make the rock-salt-based HEOs (R-HEOs) interesting for battery applications. It has been found that the entropy stabilization not only affects the phase stability, but also the functional properties (e.g., R-HEOs exhibit much more stable and reversible de/lithiation behavior than medium entropy oxides). The combination of high Li-ion conductivities in Li-doped R-HEO with high specific capacities observed when R-HEOs are used as an electrode (anode) material indicates the possibility of fabricating all HEO-based solid-state batteries (depending upon the possibility of designing a suitable HEO-type cathode material). Overall, the HEO concept could possibly pave the way to develop advanced oxide materials, which make use of the S_{config} structure stabilization effect to advance in the areas of thermo/mechanical engineering and semi-/superconductors, to name a few. A combination of experiments and theoretical calculations is essential for this new class of oxide systems to find the right composition regime for achieving targeted functional properties.

Acknowledgements

The authors acknowledge financial support from the Helmholtz Association and the Deutsche Forschungsgemeinschaft (HA 1344/43-1). A.S., Q.W., B.B., and H.H. appreciate the support of EnABLES, a project funded by the European Union's Horizon 2020 research and innovation program under grant agreement no. 730957.

Conflict of Interest

The authors declare no conflict of interest.

Keywords

electrochemical energy storage, fluorite, high-entropy oxides, perovskite, rock-salt

Received: September 26, 2018
Revised: February 6, 2019

---

[1] B. Cantor, I. T. H. Chang, P. Knight, A. J. B. Vincent, *Mater. Sci. Eng. A* **2004**, *375–377*, 213.
[2] J.-W. Yeh, S.-K. Chen, S.-J. Lin, J.-Y. Gan, T.-S. Chin, T.-T. Shun, C.-H. Tsau, S.-Y. Chang, *Adv. Eng. Mater.* **2004**, *6*, 299.
[3] C. M. Rost, E. Sachet, T. Borman, A. Moballegh, E. C. Dickey, D. Hou, J. L. Jones, S. Curtarolo, J.-P. Maria, *Nat. Commun.* **2015**, *6*, 8485.
[4] E. Castle, T. Csanadi, S. Grasso, J. Dusza, M. Reece, *Sci. Rep.* **2018**, *8*, 8609.
[5] J. Gild, Y. Zhang, T. Harrington, S. Jiang, T. Hu, M. C. Quinn, W. M. Mellor, N. Zhou, K. Vecchio, J. Luo, *Sci. Rep.* **2016**, *6*, 37946.
[6] T. Jin, X. Sang, R. R. Unocic, R. T. Kinch, X. Liu, J. Hu, H. Liu, S. Dai, *Adv. Mater.* **2018**, *30*, 1707512.
[7] R.-Z. Zhang, F. Gucci, H. Zhu, K. Chen, M. J. Reece, *Inorg. Chem.* **2018**, *57*, 13027.
[8] D. Bérardan, S. Franger, D. Dragoe, A. K. Meena, N. Dragoe, *Phys. Status Solidi RRL* **2016**, *10*, 328.
[9] D. Bérardan, S. Franger, A. K. Meena, N. Dragoe, *J. Mater. Chem. A* **2016**, *4*, 9536.
[10] D. Bérardan, A. K. Meena, S. Franger, C. Herrero, N. Dragoe, *J. Alloys Compd.* **2017**, *704*, 693.
[11] D. B. Miracle, O. N. Senkov, *Acta Mater.* **2017**, *122*, 448.
[12] B. S. Murty, J. W. Yeh, S. Ranganathan, *High-Entropy Alloys*, Butterworth- Heinemann, London **2014**.
[13] S. Jiang, T. Hu, J. Gild, N. Zhou, J. Nie, M. Qin, T. Harrington, K. Vecchio, J. Luo, *Scr. Mater.* **2018**, *142*, 116.
[14] J. Zhou, J. Zhang, F. Zhang, B. Niu, L. Lei, W. Wang, *Ceram. Int.* **2018**, *44*, 22014.
[15] A. Sarkar, R. Djenadic, N. J. Usharani, K. P. Sanghvi, V. S. K. Chakravadhanula, A. S. Gandhi, H. Hahn, S. S. Bhattacharya, *J. Eur. Ceram. Soc.* **2017**, *37*, 747.
[16] R. Djenadic, A. Sarkar, O. Clemens, C. Loho, M. Botros, V. S. K. Chakravadhanula, C. Kübel, S. S. Bhattacharya, A. S. Gandhi, H. Hahn, *Mater. Res. Lett.* **2017**, *5*, 102.
[17] J. Gild, M. Samiee, J. L. Braun, T. Harrington, H. Vega, P. E. Hopkins, K. Vecchio, J. Luo, *J. Eur. Ceram. Soc.* **2018**, *38*, 3578.
[18] K. Chen, X. Pei, L. Tang, H. Cheng, Z. Li, C. Li, X. Zhang, L. An, *J. Eur. Ceram. Soc.* **2018**, *38*, 4161.
[19] J. Dąbrowa, M. Stygar, A. Mikuła, A. Knapik, K. Mroczka, W. Tejchman, M. Danielewski, M. Martin, *Mater. Lett.* **2018**, *216*, 32.
[20] A. Sarkar, R. Djenadic, D. Wang, C. Hein, R. Kautenburger, O. Clemens, H. Hahn, *J. Eur. Ceram. Soc.* **2018**, *38*, 2318.
[21] Y. Sharma, B. L. Musico, X. Gao, C. Hua, A. F. May, A. Herklotz, A. Rastogi, D. Mandrus, J. Yan, H. N. Lee, M. F. Chisholm, V. Keppens, T. Z. Ward, *Phys. Rev. Mater.* **2018**, *2*, 060404.
[22] A. Sarkar, L. Velasco, D. Wang, Q. Wang, G. Talasila, L. de Biasi, C. Kübel, T. Brezesinski, S. S. Bhattacharya, H. Hahn, B. Breitung, *Nat. Commun.* **2018**, *9*, 3400.
[23] C. M. Rost, Z. Rak, D. W. Brenner, J.-P. Maria, *J. Am. Ceram. Soc.* **2017**, *100*, 2732.
[24] A. D. Dupuy, X. Wang, J. M. Schoenung, *Mater. Res. Lett.* **2019**, *7*, 60.
[25] M. Biesuz, L. Spiridigliozzi, G. Dell'Agli, M. Bortolotti, V. M. Sglavo, *J. Mater. Sci.* **2018**, *53*, 8074.

[26] E. J. Williams, *Proc. R. Soc. London, Ser. A* **1935**, *152*, 231.
[27] G. Anand, A. P. Wynn, C. M. Handley, C. L. Freeman, *Acta Mater.* **2018**, *146*, 119.
[28] H. Chen, J. Fu, P. Zhang, H. Peng, C. W. Abney, K. Jie, X. Liu, M. Chi, S. Dai, *J. Mater. Chem. A* **2018**, *6*, 11129.
[29] W. Hong, F. Chen, Q. Shen, Y.-H. Han, W. G. Fahrenholtz, L. Zhang, *J. Am. Ceram. Soc.* **2019**, *102*, 2228.
[30] J. L. Braun, C. M. Rost, M. Lim, A. Giri, D. H. Olson, G. N. Kotsonis, G. Stan, D. W. Brenner, J.-P. Maria, P. E. Hopkins, *Adv. Mater.* **2018**, *30*, 1805004.
[31] A. Sarkar, C. Loho, L. Velasco, T. Thomas, S. S. Bhattacharya, H. Hahn, R. Djenadic, *Dalton Trans.* **2017**, *46*, 12167.
[32] G. N. Kotsonis, C. M. Rost, D. T. Harris, J.-P. Maria, *MRS Commun.* **2018**, *8*, 1371.
[33] P. B. Meisenheimer, T. J. Kratofil, J. T. Heron, *Sci. Rep.* **2017**, *7*, 3.
[34] Z. Rak, C. M. Rost, M. Lim, P. Sarker, C. Toher, S. Curtarolo, J. P. Maria, D. W. Brenner, *J. Appl. Phys.* **2016**, *120*, 095105.
[35] Z. Rák, J.-P. Maria, D. W. Brenner, *Mater. Lett.* **2018**, *217*, 300.
[36] Q. Wang, Z. Wen, J. Jin, J. Guo, X. Huang, J. Yang, C. Chen, *Chem. Commun.* **2016**, *52*, 1637.
[37] Z. Gao, H. Sun, L. Fu, F. Ye, Y. Zhang, W. Luo, Y. Huang, *Adv. Mater.* **2018**, *30*, 1705702.
[38] Z. Zhang, Y. Shao, B. Lotsch, Y. Hu, L. F. Nazar, C. Nan, J. Maier, M. Armand, L. Chen, *Energy Environ. Sci.* **2018**, *11*, 1945.
[39] F. Strauss, T. Bartsch, L. de Biasi, A.-Y. Kim, J. Janek, P. Hartmann, T. Brezesinski, *ACS Energy Lett.* **2018**, *3*, 992.
[40] N. Qiu, H. Chen, Z. Yang, S. Sun, Y. Wang, Y. Cui, *J. Alloys Compd.* **2019**, *777*, 767.

Scripta Materialia 187 (2020) 43–48

Contents lists available at ScienceDirect

Scripta Materialia

journal homepage: www.elsevier.com/locate/scriptamat

High entropy oxides: The role of entropy, enthalpy and synergy

Abhishek Sarkar[a,b,*], Ben Breitung[b,*], Horst Hahn[a,b,c,d]

[a] *Joint Research Laboratory Nanomaterials – Technische Universität Darmstadt & Karlsruhe Institute of Technology, 64287 Darmstadt, Germany*
[b] *Institute of Nanotechnology, Karlsruhe Institute of Technology (KIT), Hermann-von-Helmholtz-Platz 1, 76344 Eggenstein-Leopoldshafen, Germany*
[c] *Department of Materials Science and Engineering, University of California, Irvine, USA*
[d] *Herbert Gleiter Institute of Nanoscience, Nanjing University of Science and Technology, Nanjing, China*

ARTICLE INFO

Article history:
Received 31 March 2020
Revised 7 May 2020
Accepted 7 May 2020

Keywords:
Multicomponent equiatomic systems
High entropy ceramics
Entropy-stabilization
Functional properties

ABSTRACT

This viewpoint article focuses on some of the important issues related to the emerging field of high entropy oxides (HEOs). Open queries regarding the role of entropy, enthalpy, individual elements and synergy arising from the presence of multiple elements in HEOs are discussed. In addition, a brief overview of the current state of research on HEOs is provided. Finally, we share our views on the uniqueness of HEOs by describing some features, which distinguish them from the conventional oxides.

In 2004, Cantor *et al.* [1] pioneered a new approach of materials design with the aim "to investigate the unexplored central regions" of multicomponent metallic phase diagrams. It was observed that most of the near-equimolar multicomponent alloys resulted in a significantly lower number of phases (even single phased alloys) compared to the maximum allowed by Gibbs phase rule [1]. Yeh *et al.* [2] proposed that the tendency to form a single phase solid solution can be related to the increased configurational entropy of mixing, stemming from the large number of constituent elements and their respective molar proportions. Consequently, the term "high entropy alloys (HEAs)" was coined [2]. Thus, the discovery of HEAs can be credited to two ideas [1–3]: (a) to investigate unexplored central regions of multicomponent phase diagrams, where unexpected synergies can be anticipated; (b) to precisely control the configurational entropy (by altering the number of elements and/or their proportions) to tailor the phase composition and therefore the properties. These two design concepts are now extended to other kind of materials [4–7], i.e., going beyond metallic HEAs.

Since 2004, attempts have been made to investigate non-metallic high entropy materials (HEMs) like nitrides and carbides [8–10]. However, a major leap in the research interest on non-metallic HEMs has been observed, following the first report on high entropy oxides (HEOs) by Rost *et al.* [4] in 2015. Since then, HEOs have gained significant research attention resulting in numerous compositions, crystal structures, microstructures, and most importantly, tailorable properties [11–23]. Many HEO compositions are known to exhibit exceptional properties, however, a majority of them also shows features similar to the traditional oxides. Nevertheless, research activities on HEOs are essential, as only very little is known, which is by far not sufficient to predict their overall potential. Additionally, numerous fundamental questions are yet to be clarified, for instance, the driving force behind the phase stability, the specific role of entropy, the underlying mechanisms governing the properties, the effect of the individual cations, etc. This viewpoint commentary focuses on these aforementioned issues, followed by a critical evaluation of the advantages and differences that the HEOs offer in contrast to the conventional oxides. Furthermore, from our standpoint, we attempt to provide a unified classification for HEOs which seems to be still missing. In addition, a general overview of HEOs along with some future perspectives is presented.

1. Definition and classification

HEOs represent a relatively new development compared to metallic HEAs, so a widely accepted definition for the former is not yet available. Hence, we attempt to provide a unified definition by combining reports from the existing literature on HEOs [12,14,19,24,25] and in accordance with the definition of HEAs [2,3,26]. HEOs can be defined as single phase oxide systems containing 5 or more cations, such that the configurational entropy (S_{config}) is greater than 1.5R (where R is the universal gas constant). The S_{config} for an $A_xB_yO_z$ type oxide can be calculated as

---

[*] Corresponding authors.
E-mail addresses: abhishek.sarkar@kit.edu (A. Sarkar), ben.breitung@kit.edu (B. Breitung), horst.hahn@kit.edu (H. Hahn).

https://doi.org/10.1016/j.scriptamat.2020.05.019
1359-6462/

per Eq. (1):

$$S_{\mathrm{config}} = -R\left[x\left(\sum_{a=1}^{M} x_a \ln x_a\right)_{A-site} + y\left(\sum_{b=1}^{N} y_b \ln y_b\right)_{B-site} + z\left(\sum_{o=1}^{P} z_o \ln z_o\right)_{O-site}\right] \tag{1}$$

with x_a, y_b and z_o being the mole fractions of the elements present in the A-site, B-site and O^{2-}-site (or anion site), respectively. While M, N and P are the number of cations present on A-sites, B-sites and anions on O^{2-}-sites, respectively. For an oxide system, S_{config} from O^{2-}-site is ideally zero. However, the presence of oxygen defects or other anions (like F^- in oxyfluorides [27]) can lead to an additional S_{config} contribution of the anionic sublattice. Moreover, as several oxides have only a single cation sub-lattice (like rocksalt, fluorite, etc.) Eq. (1) can be modified as follows.

$$S_{\mathrm{config}} = -R\left[x\left(\sum_{a=1}^{M} x_a \ln x_a\right)_{cation-site}\right] \tag{2}$$

It can be observed that Eq. (2) is similar to the entropy equation known for metallic HEA systems and the maximum S_{config} (for a given composition) can be reached when all the elements are present in equimolar proportion. As per Eq. (2), five or more elements in near-equiatomic proportions are required to achieve $S_{config} \geq 1.5R$. Although this "S_{config}-based" definition is typically used to classify HEOs, there are two limitations that should be kept in mind. First of all, the S_{config} calculation (based on Eqs (1) and (2)) is only valid for ideal solid solutions, which is rarely the case. Secondly, unlike in metallic systems like $Co_{20}Cr_{20}Fe_{20}Mn_{20}Ni_{20}$ where the mole fraction of each of the elements is 0.2 (resulting in $S_{config} = 1.61R$), in HEOs only the cationic mole fraction is taken into account. For instance, in $Co_{0.2}Cu_{0.2}Mg_{0.2}Ni_{0.2}Zn_{0.2}O$ the overall cationic mole fraction is 0.5 and the mole fraction of the individual cation is 0.1. However, for the "S_{config}-based" definition the overall cationic fraction is considered as 1 (such as in Eq. (2)). Furthermore, in systems like spinels, $(Co_{0.2}Cr_{0.2}Fe_{0.2}Mn_{0.2}Ni_{0.2})_3O_4$, the S_{config} calculation is not straightforward as the site occupancies of the cations (due to possible inversion) are often unknown.

Apart from this "S_{config}-based" definition, there are several other terms that are often used. In the pioneering report by Rost *et al.*, the term "entropy-stabilized oxides (ESOs)" [4] was used. To retain the significance of this term, now it is only used in special cases where the system shows a typical entropy driven phase stabilization effect (described in Section 3). Another definition often used is "multicomponent equiatomic oxides" [18,28–30], analogous to "equiatomic multicomponent alloys" used by Cantor *et al.* [1] in their first report on HEAs. This composition-based classification is rather self-explanatory and independent of the S_{config} or the entropy stabilization effect. However, at the same time it is too broad and might include many conventional systems, such as $Li(Ni_{1/3}Co_{1/3}Mn_{1/3})O_2$. Therefore, we suggest the use of the term "high entropy oxides" as a general description for oxides, which possess a $S_{config} \geq 1.5R$. Additionally, the term "entropy stabilized oxide" can be used, when a clear indication of a reversible phase transformation upon cyclic heat treatment is observed.

Before embracing the critical factors driving the phase composition or properties in HEOs, a highlight of the synthesis procedures and crystal structures possible for HEOs is provided in the following section.

2. Synthesis route and crystal structures

In our opinion, one of the key reasons for the increasing attention on HEOs is the ease and flexibility of synthesis. Currently, there are several synthesis and processing routes known for HEOs, which are listed in Table 1. HEOs typically require high synthesis temperatures, which is a major drawback for the fabrication of nanoparticulate morphology. Techniques like spray pyrolysis [31] can help in synthesis of nanocyrstalline HEOs, since the residence time at high temperatures is very short. However, aggregation of crystallites, leading to micrometer sized particles, still appears even at such short residence times. To counter this agglomeration, synthesis techniques using mechanochemistry [32] or sonochemistry [33] have been developed, which operate at lower temperatures. Similarly, in post processing, sintered bulk nanocrystalline or ultrafine grained structures can be obtained using methods such as flash sintering [34], which again needs shorter exposure to high temperatures. Epitaxial thin film deposition has also been reported for different types of HEOs [23,35,36], which certainly broadens the spectrum of applications by opening up further structure-property tailoring possibilities using strain effects between films and substrates.

Table 1
Different synthesis and processing routes of HEOs.

Product type	Techniques used	References
Powder	Conventional solid-state	[4,12]
	Mechanochemistry	[32,37]
	Spray pyrolysis	[20,29,31]
	Hydrothermal	[38]
	Co-precipitation	[31,38]
	Sonochemistry	[33]
	Solution combustion	[39]
	Solvothermal	[40]
	Polymeric steric entrapment	[41]
Pellet	Conventional sintering	[11]
	Spark plasma sintering	[25,42]
	Flash sintering	[34,43]
Thin films	Pulsed laser deposition	[23,35,44]
	Magnetron sputtering	[45]

Alongside the exploration of new synthesis techniques, several studies focus on the investigation of new compositions and crystal structure types possible for HEOs. Currently, around fifty compositions are already known. A comprehensive list of the compositions can be found in the referred review articles [19,46]. Based on their crystal structures, the reported HEOs can be categorized into 8 groups; rocksalt [4,12], fluorite [25,29], bixbyite [18,41], pyrocholore [47], magnetoplumbite [48], O3-type layered [49], perovskite [20,24] and spinel [22,50,51]. The studies reported till now hint towards the fact that all crystal structure types known for oxides can be practically achieved using the entropy-based design approach, especially when the cations are selected based on their ionic radii and oxidation state [4,31]. Nevertheless, the presence of the different cations results in structures or phase compositions, which cannot be always anticipated using Pauling's rules or Goldschmidt's tolerance factor [52]. For instance, the tolerance factor of $(Gd_{0.2}La_{0.2}Nd_{0.2}Sm_{0.2}Y_{0.2})MnO_3$ is very close to $NdMnO_3$ and $SmMnO_3$, both of which crystallize into a single phase orthorhombic structure. In contrast, the HEO-$(Gd_{0.2}La_{0.2}Nd_{0.2}Sm_{0.2}Y_{0.2})MnO_3$ exhibits a distribution of eight orthorhombic perovskites phases at room temperature [20]. Importantly, the charge state of the A-site cations in this HEO and in simple rare earth-orthomagantites are very similar. This observation indicates that the ionic radii and oxidation state are not the only factors but synergetic effect of the multiple cations might also have a strong impact on the structural parameters and can lead to rather unusual phase compositions in HEOs. These kind of features motivates exploration of new HEO compositions and crystal structures.

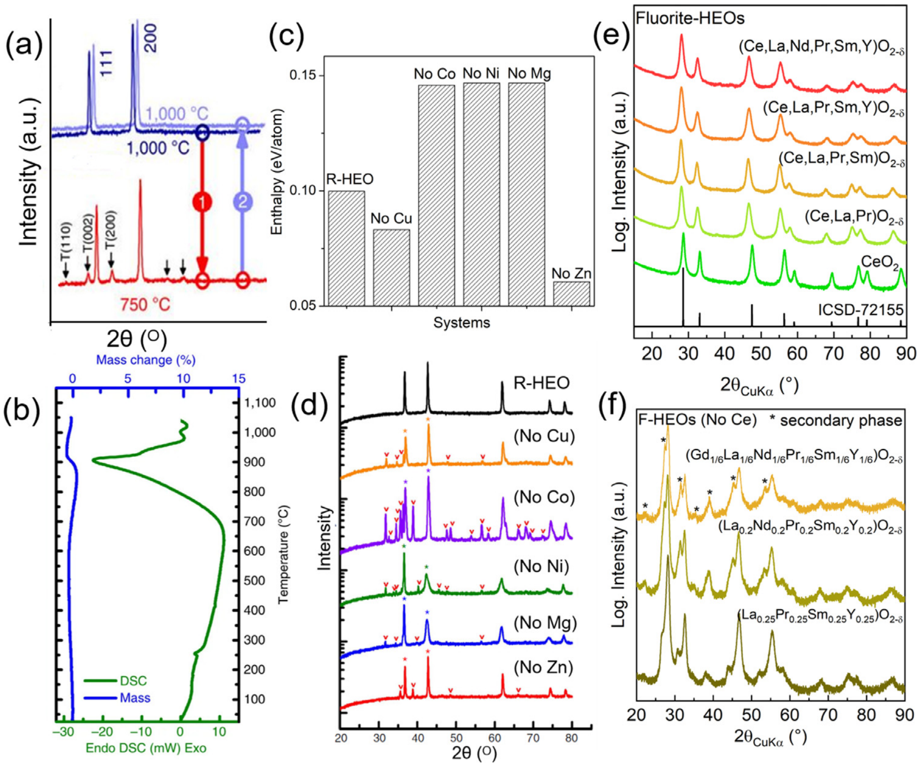

Fig. 1. Two different phase stability mechanisms in HEOs are illustrated here, (a-d) depict the scenario for entropy-stabilized oxides and (e-f) highlight the crucial role of a single cation. The reversible phase transformation and the related endothermicity upon cyclic heat treatment of entropy stabilized rocksalt-HEO (R-HEO) are shown in (a) and (b), respectively [4]. Comparison of the enthalpy penalty obtained from MD simulations (c) [53] and the XRD patterns (d) [4] of 5-cationic R-HEO and 4-cationic medium entropy oxides strengthen the entropy-mediated phase stabilization in R-HEO. (e) and (f) compare the XRD patterns of F-HEOs with and without Ce, respectively. It can be observed that Ce determines the phase composition of fluorite (F-HEOs) [29].

3. Phase stability mechanisms

The basic mechanisms behind the phase stabilities observed in HEOs can differ widely, especially when different crystal structures, but also when different compositions and the same structure are formed. Here, we demonstrate a few cases with different underlying principles. Rocksalt-HEOs (R-HEOs), such as ($Co_{0.2}Cu_{0.2}Mg_{0.2}Ni_{0.2}Zn_{0.2}O$), exhibit a typical entropy-mediated phase stabilization. This is evident from a reversible phase transformation, which can be observed upon cyclic heat treatment (Fig. 1a) and is in accordance with the Gibbs free energy Eq. (3).

$$\Delta G_{\text{mix}} = \Delta H_{\text{mix}} - T\Delta S_{\text{mix}} \tag{3}$$

The entropy (ΔS_{mix}) dominated single phase solid solution is observed at high temperatures (T), whereas enthalpy driven (ΔH_{mix}) phase segregation occurs at lower temperatures, there the free energy (ΔG_{mix}) to form a single phase is positive. The entropy-driven phase transition from multiple to a single phase at high temperature is further confirmed from the endothermic reaction, as shown in Fig. 1b [4,38]. The endothermicity is related to the presence of Zn and Cu in the ($Co_{0.2}Cu_{0.2}Mg_{0.2}Ni_{0.2}Zn_{0.2}O$)-R-HEO [4]. These cations exert enthalpic penalties for crystallization of a rocksalt structure. Hence, the exclusion of these cations from HEO should ideally favor a single phase rocksalt type solid solution (as in Fig. 1c). However, this is not the case, the 4 cationic systems without Zn or Cu are not phase pure. In fact, removing any of the constituent cations from ($Co_{0.2}Cu_{0.2}Mg_{0.2}Ni_{0.2}Zn_{0.2}O$) leads to the formation of multi-phase mixture under identical synthesis conditions (Fig. 1c,d) [4]. This is a strong indication that the role of the configurational entropy is prominent, as it decreases (to 1.39 R) when one cation is removed (Eq. (2)) from R-HEO. Molecular dynamic (MD) simulations further support this entropy-driven phase stabilization effect in R-HEO [53]. Consequently, the systems, which show a dominant role of entropy are often categorized as the “entropy-stabilized oxides (ESOs)”. Currently, only a handful of HEO systems [4,20,54–56] and a sole high entropy oxyfluoride system [27] are known to exhibit the phenomena of entropy stabilization. Definitely, the ESOs are unique especially compared to the conventional oxides.

Nevertheless, this doesn’t mean at all that the non-entropy stabilized HEOs are not interesting for further research. HEOs also show interesting phase stability mechanisms, for instance, fluorite-HEOs (F-HEOs) obtained from equiatomic combinations of Gd, Nd, Ce, La, Pr, Sm and Y usually crystallize in single phase solid solutions (Fig. 1e) with the only pre-requisite being the presence of Ce. Any F-HEO [29] system without Ce, irrespective of the number of incorporated elements (S_{config}) or synthesis temperature, always crystallizes in multiple phases (Fig. 1f). This primarily indicates that the formation of a single phase fluorite only with Gd, Nd, La, Pr, Sm and Y is not thermodynamically favorable, but can be achieved even with a low amount of Ce (e.g. 20 % of the overall cations in a 5-component system). In fact all the F-HEOs reported till date [17,18,25,28–30] include either Ce or Zr (or both), both cations are known to possess a stable 4+ oxidation state. Fluorite oxides in general favor 4+ cations, along with the cation to oxygen radius ratio between 0.73 to 1 [52]. Most likely, Ce or/and Zr act as a host, stabilizing the fluorite lattice, whereas the other cations help to achieve the appropriate effective cationic radius required to maintain an 8-fold coordination of oxygen. Hence, from these systems an important role of the single cation with a given oxidation state (like Ce^{4+}) is identified. Likewise, a struc-

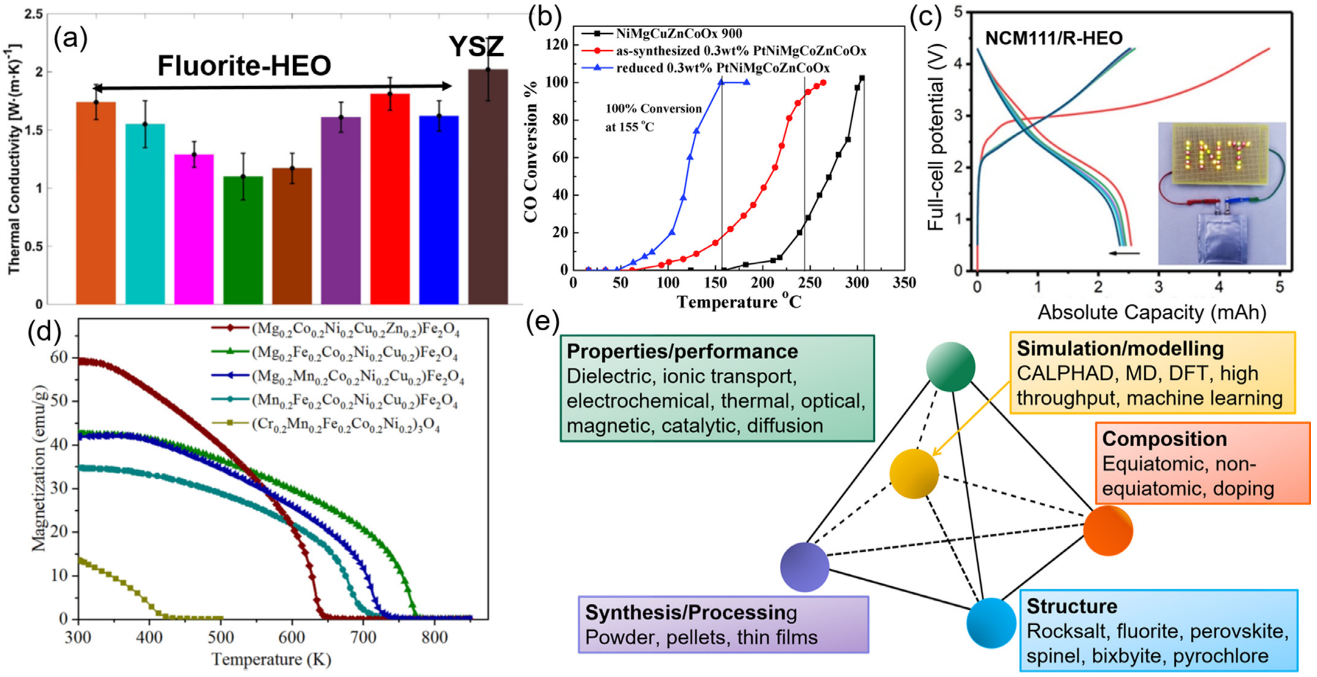

Fig. 2. The tailorable properties of HEOs are presented in (a-d), along with an overview and outlook of research on HEOs projected in form of a hyper-tetrahedron (e). A comparison of thermal conductivity between fluorite-HEO and yttria-stabilized zirconia (YSZ) is shown in (a) [6]. Catalytic activities of rocksalt-HEO and practical application of the same as an anode in a full cell Li-ion battery (with NCM111 as cathode) are shown in (b) [67] and (c) [59], respectively. Tailorable magnetic features of spinel-HEOs are shown in (d) [22].

tural transformation from a spinel type HEO (S-HEO) to R-HEO can be observed upon addition of Li$^+$, which is believed to be a result of internal charge compensation [57]. In fact such interesting effects are also observed in many of the other HEOs, for instance Ba(Zr$_{0.2}$Sn$_{0.2}$Ti$_{0.2}$Hf$_{0.2}$Ce$_{0.2}$)O$_3$ shows a transformation from a phase pure perovskite structure to a multi-phase mixture when heat treated at high temperatures [24]. This de-mixing upon increasing the temperature is actually the opposite of the entropy-stabilization phenomena observed in ESOs. Thus, these intriguing structural features observed in different HEOs certainly warrants future experimental investigations, perhaps in close combination with thermodynamic calculations.

4. Properties and underlying principles

Oxides, in general, show rich structure-composition-property relationships. Likewise, different HEOs exhibit distinct functional properties. Already a large number of properties have been studied for HEOs, such as dielectric [12,58], ionic transport [11], electrochemical [16,59–61], optical [18,62,63], magnetic [15,21,22,36,44,64–66], catalytic [32,40,67], mechanical [13] and thermal [25,68]. An exhaustive list of these properties, along with the compositions and crystal structures of the respective HEOs, can be found in some of the recent review articles [46,69,70]. The properties exhibited by HEOs are key factors that will decide their practical utilization and future prospects. Especially, the advantages of HEOs over conventional oxides need to be critically evaluated, which can be done in two ways: (a) simply, if the achieved values (of the studied properties) are improved and (b) if the underlying mechanisms governing the properties are unique and can be further utilized. Furthermore, it is also worthwhile to distinguish between the properties, which arise from the synergies stemming from the presence of multiple cations, from those, which are strongly governed by one certain constituent cation. Here, we call these “synergetic” or “element driven” properties. This distinction is not straightforward, as in many cases, there is a convolution of both effects. Nevertheless, we attempt to demonstrate these two aspects by highlighting a few scenarios, as illustrated in Fig. 2.

Thermophysical properties (Fig. 2a) of HEOs render promises for their practical application as thermal barrier coatings. Both R-HEOs [68] and F-HEOs [25] are known to exhibit lower thermal conductivities compared to their constituent parent oxides, or even to some of the commercially used materials. The reduction of the thermal conductivity in HEOs is consistent with reports about thermophysical properties in HEAs [71]. The reason for this finding can be linked with the high chemical disorder and the resulting multiple phonon scattering. Hence, in this case, a collective role of the multiple cations seems to be dominant over the individual effects, therefore synergetic properties are apparent. Likewise, the colossal dielectric susceptibility observed in R-HEOs [12,58] can also be a result of the synergetic effect. However, tailoring the structural parameters just by varying the amount of Cu in R-HEO is known to affect the dielectric susceptibility [58]. Another example is the reported catalytic property of HEOs (Fig. 2b), which is known to benefit from their high temperature stability. This can be credited to the high configurational entropy and in fact to the synergetic effect of the cations [32,40,67]. On the other hand, band gap energies of F-HEOs appear more like single element driven effects, where the presence of intermediate 4*f* energy bands of certain cations (like Pr and Ce) is found to play the determining role [20,63]. Interestingly, the amount of oxygen vacancies or the number of other cations present in the F-HEOs do not have a significant impact on their optical properties [18].

Electrochemical properties of HEOs, is another avenue, which projects substantial potential for practical applications. Li-doped R-HEOs exhibit extremely high room temperature Li-ion conductivity, which is orders of magnitudes higher than in conventional solid electrolytes, like LiPON [11]. The underlying principle behind this high Li$^+$ conduction in a closed packed rocksalt lattice is quite intriguing, given the fact that Li$^+$ (in 6 fold coordination) is actually larger than many of the transition metal cations present in the HEO. It is believed that the oxygen vacancies play a crucial role in promoting high Li^+-conductivity [11,72], however a synergetic effect cannot be neglected as none of the parent oxides (when doped with Li) are known to show such remarkable performance. Another, interesting electrochemical feature is the remarkable reversible Li-ion storage capability of R-HEOs [16,19,59,60], which show their potential as anodes in LIBs (Fig. 2c). A “partial-conversion” reaction mechanism has been identified in HEOs [16]. Unlike in conventional transition metal oxides, a complete structural conversion (from oxide to respective metals) does not happen upon lithiation, instead a rocksalt-HEO type host structure is retained throughout the cycling process. The retention of the host structure along with the fact that R-HEOs show better performance than medium entropy oxides (containing fewer cations) hints towards a link between the entropy-driven structural stability and enhanced cyclic performance in HEOs [16,19]. In addition, the role of individual cations cannot be neglected while considering the electrochemical features of HEOs, as it has been observed that the redox potentials of HEOs (vs Li^+/Li) can be significantly altered by changing the chemical compositions [16,57]. These distinct electrochemical features have motivated the research on HEOs for post-LIBs, like Na-ion [49] and Li-Sulfur batteries [73]. An improved cyclic performance, compared to the conventional oxides, has been observed in most of the cases.

Apart from these, a unique combination of synergy, composition (or role of single elements) and crystal structure can be observed in the magnetic properties of HEOs. The magnetic ordering, for instance antiferromagnetism in rocksalt- or perovskite-HEOs [21,36,44,64–66] and ferrimagnetism in spinel-HEOs [15,22], despite the chemical disorder, is appealing. In addition, exchange bias, non-collinearity and magnetocrystalline anisotropy can also be observed in single phase HEOs [21,36,44]. In general, the magnetic features of HEOs can be largely elucidated using fundamentals known for the parent systems. For instance, the Goodenough-Kanamori rules are followed, as a result a direct correlation with the tolerance factor and transition temperature can be observed even in complex perovskite-HEOs [21,36]. Simultaneously, the local interactions between the different cations also lead to distinct magnetic ordering. For instance, in $La(Co_{0.2}Cr_{0.2}Fe_{0.2}Mn_{0.2}Ni_{0.2})O_3$ antiferromagnetic order prevails, however, local Fe^{3+}-Cr^{3+} interactions might result in ferromagnetism leading to exchange bias effect [21]. Likewise, rocksalt type transition metal oxides are known to show antiferromagnetic ordering [74], while in case of spinels the resultant magnetic features (often ferrimagnetic) typically arises from the antiparallel alignment of the B and A-site spins, while the spins in the respective sites are in parallel [75]. Most of these features are strongly dependent on the composition, thus offering a vast research space for tailoring the magnetic properties (Fig. 2d) with the high entropy-based design approach.

5. Perspective

The aforementioned studies highlight the versatility of HEOs, and certainly warrant future research to identify the full potential of these materials. The current state of research along with an outlook has been presented in form of a HEO-hypertetrahedron (Fig. 2e). There are in fact numerous research possibilities using HEOs, as the synergies arising from the presence of multiple elements can practically affect all the properties associated with metal oxides. However, it is rather obvious that out of all the studied properties only a few will be highly influenced by this extreme compositional complexity and the resulting synergies. Nevertheless, the topic is still in its infancy, hence, a broad range of properties need to be investigated to comprehend the full potential of HEOs. Given their compositional immensity, several structural and chemical combinations are possible. Hence, experimentally scavenging the “sweet-spot” for specific purposes will be rather tedious and probably in many cases disappointing. Theoretical approaches like CALPHAD, MD simulations and density functional theory (DFT) calculations can provide a basic guideline for the phase equilibria, structure and (some) properties of the HEOs. However, traditional simulation approaches might still be tedious for systems with such complexity. Hence, combinatorial synthesis and high-throughput calculations with proper descriptors, can accelerate the identification or discovery of new HEOs with specific properties. Certainly, a more active cooperation between the experimental and theoretical researchers will be crucial for the advancement of HEOs. As a concluding remark, besides the perspectives already presented, it has to be stated that the field of multicomponent ceramics has grown to an extent, where unambiguous terms are necessary to describe the characteristics of the materials and properties. In the field of multicomponent oxides, materials with “just” a high configurational entropy, labeled as “high entropy oxides”, are often confused with “entropy-stabilized oxides”, which show reversible entropy-mediated phase transformations. Additionally, properties of materials can be classified into “synergetic” properties, when the interplay between the incorporated elements is the most important factor, or in “single element driven” properties, when a specific element in the multicomponent system is responsible for the properties. Regardless, of the underlying mechanisms, all these materials deserve further investigations, since the promises they offer are countless.

Declaration of Competing Interest

The authors declare that they have no known competing financial interests or personal relationships that could have appeared to influence the work reported in this paper.

Acknowledgements

AS and HH acknowledge financial support from the Deutsche Forschungsgemeinschaft (DFG) project HA 1344/43-1. HH and BB appreciate the support of EnABLES, a project funded by the European Union’s Horizon 2020 research and innovation program under grant agreement no. 730957. The authors appreciate fruitful discussions with Robert Kruk, Ralf Witte, Richard Brand, Miriam Botros, Leonardo Velasco Estrada, Subramshu S. Bhattacharya, Qingsong Wang, Mohammed Reda Chellali, Julie Schoenung and Alex Dupuy.

References

[1] B. Cantor, I.T.H. Chang, P. Knight, A.J.B. Vincent, Mater. Sci. Eng. A 375–377 (2004) 213–218.
[2] J.W. Yeh, S.K. Chen, S.J. Lin, J.Y. Gan, T.S. Chin, T.T. Shun, C.H. Tsau, S.Y. Chang, Adv. Eng. Mater. 6 (2004) 299–303.
[3] D.B. Miracle, O.N. Senkov, Acta Mater. 122 (2017) 448–511.
[4] C.M. Rost, E. Sachet, T. Borman, A. Moballegh, E.C. Dickey, D. Hou, J.L. Jones, S. Curtarolo, J.-P. Maria, Nat. Commun. 6 (2015) 8485.
[5] T. Jin, X. Sang, R.R. Unocic, R.T. Kinch, X. Liu, J. Hu, H. Liu, S. Dai, Adv. Mater. 30 (2018) 1707512.
[6] J. Gild, Y. Zhang, T. Harrington, S. Jiang, T. Hu, M.C. Quinn, W.M. Mellor, N. Zhou, K. Vecchio, J. Luo, Sci. Rep. 6 (2016) 37946.
[7] R.-Z. Zhang, F. Gucci, H. Zhu, K. Chen, M.J. Reece, Inorg. Chem. 57 (2018) 13027–13033.
[8] V. Braic, A. Vladescu, M. Balaceanu, C.R. Luculescu, M. Braic, Surf. Coatings Technol. 211 (2012) 117–121.
[9] M.-H. Hsieh, M.-H. Tsai, W.-J. Shen, J.-W. Yeh, Surf. Coatings Technol. 221 (2013) 118–123.
[10] X.C. Yang, W. Riehemann, M. Dubiel, H. Hofmeister, Mater. Sci. Eng. B 95 (2002) 299–307.
[11] D. Bérardan, S. Franger, A.K. Meena, N. Dragoe, J. Mater. Chem. A 4 (2016) 9536–9541.
[12] D. Bérardan, S. Franger, D. Dragoe, A.K. Meena, N. Dragoe, Phys. Status Solidi - Rapid Res. Lett. 10 (2016) 328–333.
[13] W. Hong, F. Chen, Q. Shen, Y. Han, W.G. Fahrenholtz, L. Zhang, J. Am. Ceram. Soc. 102 (2019) 2228–2237.

[14] J. Dąbrowa, M. Stygar, A. Mikuła, A. Knapik, K. Mroczka, W. Tejchman, M. Danielewski, M. Martin, Mater. Lett. 216 (2018) 32–36.
[15] A. Mao, H.-Z. Xiang, Z.-G. Zhang, K. Kuramoto, H. Zhang, Y. Jia, J. Magn. Magn. Mater. 497 (2020) 165884.
[16] A. Sarkar, L. Velasco, D. Wang, Q. Wang, G. Talasila, L. de Biasi, C. Kübel, T. Brezesinski, S.S. Bhattacharya, H. Hahn, B. Breitung, Nat. Commun. 9 (2018) 3400.
[17] M.R. Chellali, A. Sarkar, S.H. Nandam, S.S. Bhattacharya, B. Breitung, H. Hahn, L. Velasco, Scr. Mater. 166 (2019) 58–63.
[18] A. Sarkar, C. Loho, L. Velasco, T. Thomas, S.S. Bhattacharya, H. Hahn, R. Djenadic, Dalt. Trans. 46 (2017) 12167–12176.
[19] A. Sarkar, Q. Wang, A. Schiele, M.R. Chellali, S.S. Bhattacharya, D. Wang, T. Brezesinski, H. Hahn, L. Velasco, B. Breitung, Adv. Mater. 31 (2019) 1806236.
[20] A. Sarkar, R. Djenadic, D. Wang, C. Hein, R. Kautenburger, O. Clemens, H. Hahn, J. Eur. Ceram. Soc. 38 (2018) 2318–2327.
[21] R. Witte, A. Sarkar, R. Kruk, B. Eggert, R.A. Brand, H. Wende, H. Hahn, Phys. Rev. Mater. 3 (2019) 034406.
[22] B. Musicó, Q. Wright, T.Z. Ward, A. Grutter, E. Arenholz, D. Gilbert, D. Mandrus, V. Keppens, Phys. Rev. Mater. 3 (2019) 104416.
[23] Y. Sharma, B.L. Musico, X. Gao, C. Hua, A.F. May, A. Herklotz, A. Rastogi, D. Mandrus, J. Yan, H.N. Lee, M.F. Chisholm, V. Keppens, T.Z. Ward, Phys. Rev. Mater. 2 (2018) 060404.
[24] S. Jiang, T. Hu, J. Gild, N. Zhou, J. Nie, M. Qin, T. Harrington, K. Vecchio, J. Luo, Scr. Mater. 142 (2018) 116–120.
[25] J. Gild, M. Samiee, J.L. Braun, T. Harrington, H. Vega, P.E. Hopkins, K. Vecchio, J. Luo, J. Eur. Ceram. Soc. 38 (2018) 3578–3584.
[26] B.S. Murty, J.W. Yeh, S. Ranganathan, High-Entropy Alloys, 1st ed., Butterworth-Heinemann, London, 2014.
[27] Q. Wang, A. Sarkar, D. Wang, L. Velasco, R. Azmi, S.S. Bhattacharya, T. Bergfeldt, A. Düvel, P. Heitjans, T. Brezesinski, H. Hahn, B. Breitung, Energy Environ. Sci. 12 (2019) 2433–2442.
[28] M. Anandkumar, S. Bhattacharya, A.S. Deshpande, RSC Adv. 9 (2019) 26825–26830.
[29] R. Djenadic, A. Sarkar, O. Clemens, C. Loho, M. Botros, V.S.K. Chakravadhanula, C. Kübel, S.S. Bhattacharya, A.S. Gandhi, H. Hahn, Mater. Res. Lett. 5 (2017) 102–109.
[30] M. Pianassola, M. Loveday, J.W. McMurray, M. Koschan, C.L. Melcher, M. Zhuravleva, J. Am. Ceram. Soc. 103 (2020) 2908–2918.
[31] A. Sarkar, R. Djenadic, N.J. Usharani, K.P. Sanghvi, V.S.K. Chakravadhanula, A.S. Gandhi, H. Hahn, S.S. Bhattacharya, J. Eur. Ceram. Soc. 37 (2017) 747–754.
[32] H. Chen, W. Lin, Z. Zhang, K. Jie, D.R. Mullins, X. Sang, S.-Z. Yang, C.J. Jafta, C.A. Bridges, X. Hu, R.R. Unocic, J. Fu, P. Zhang, S. Dai, ACS Mater. Lett. 1 (2019) 83–88.
[33] F. Okejiri, Z. Zhang, J. Liu, M. Liu, S. Yang, S. Dai, ChemSusChem 13 (2020) 111–115.
[34] D. Liu, X. Peng, J. Liu, L. Chen, Y. Yang, L. An, J. Eur. Ceram. Soc. 40 (2020) 2504–2508.
[35] G.N. Kotsonis, C.M. Rost, D.T. Harris, J.-P. Maria, MRS Commun. 8 (2018) 1371–1377.
[36] Y. Sharma, Q. Zheng, A.R. Mazza, E. Skoropata, T. Heitmann, Z. Gai, B. Musico, P.F. Miceli, B.C. Sales, V. Keppens, M. Brahlek, T.Z. Ward, Phys. Rev. Mater. 4 (2020) 014404.
[37] M. Balcerzak, K. Kawamura, R. Bobrowski, P. Rutkowski, T. Brylewski, J. Electron. Mater. 48 (2019) 7105–7113.
[38] M. Biesuz, L. Spiridigliozzi, G. Dell'Agli, M. Bortolotti, V.M. Sglavo, J. Mater. Sci. 53 (2018) 8074–8085.
[39] A. Mao, H.-Z. Xiang, Z.-G. Zhang, K. Kuramoto, H. Yu, S. Ran, J. Magn. Magn. Mater. 484 (2019) 245–252.
[40] D. Wang, Z. Liu, S. Du, Y. Zhang, H. Li, Z. Xiao, W. Chen, R. Chen, Y. Wang, Y. Zou, S. Wang, J. Mater. Chem. A 7 (2019) 24211–24216.
[41] K. Tseng, Q. Yang, S.J. McCormack, W.M. Kriven, J. Am. Ceram. Soc. 103 (2020) 569–576.
[42] A.D. Dupuy, X. Wang, J.M. Schoenung, Mater. Res. Lett. 7 (2019) 60–67.
[43] A. Kumar, G. Sharma, A. Aftab, M.I. Ahmad, J. Eur. Ceram. Soc. 40 (2020) 3358–3362.
[44] P.B. Meisenheimer, T.J. Kratofil, J.T. Heron, Sci. Rep. 7 (2017) 3–8.
[45] A. Kirnbauer, C. Spadt, C.M. Koller, S. Kolozsvári, P.H. Mayrhofer, Vacuum 168 (2019) 108850.
[46] C. Oses, C. Toher, S. Curtarolo, Nat. Rev. Mater. (2020).
[47] Z. Teng, L. Zhu, Y. Tan, S. Zeng, Y. Xia, Y. Wang, H. Zhang, J. Eur. Ceram. Soc. 40 (2020) 1639–1643.
[48] D.A. Vinnik, E.A. Trofimov, V.E. Zhivulin, O.V. Zaitseva, S.A. Gudkova, A.Y. Starikov, D.A. Zherebtsov, A.A. Kirsanova, M. Häßner, R. Niewa, Ceram. Int. 45 (2019) 12942–12948.
[49] C. Zhao, F. Ding, Y. Lu, L. Chen, Y. Hu, Angew. Chemie Int. Ed. 59 (2020) 264–269.
[50] J. Dąbrowa, M. Stygar, A. Mikuła, A. Knapik, K. Mroczka, W. Tejchman, M. Danielewski, M. Martin, Mater. Lett. 216 (2018) 32–36.
[51] T. Parida, A. Karati, K. Guruvidyathri, B.S. Murty, G. Markandeyulu, Scr. Mater. (2020).
[52] Y.-M. Chiang, D.P. Birnie, W.D. Kingery, Physical Ceramics: Principles for Ceramic Science and Engineering, John Wiley & Sons, Inc., New York, 1997.
[53] G. Anand, A.P. Wynn, C.M. Handley, C.L. Freeman, Acta Mater. 146 (2018) 119–125.
[54] K. Chen, X. Pei, L. Tang, H. Cheng, Z. Li, C. Li, X. Zhang, L. An, J. Eur. Ceram. Soc. 38 (2018) 4161–4164.
[55] N. Dragoe, D. Bérardan, Science (80-.) 366 (2019) 573–574.
[56] L. Spiridigliozzi, C. Ferone, R. Cioffi, G. Accardo, D. Frattini, G. Dell'Agli, Materials (Basel) 13 (2020) 558.
[57] J. Wang, D. Stenzel, R. Azmi, S. Najib, K. Wang, J. Jeong, A. Sarkar, Q. Wang, P.A. Sukkurji, T. Bergfeldt, M. Botros, J. Maibach, H. Hahn, T. Brezesinski, B. Breitung, Electrochem 1 (2020) 60–74.
[58] D. Bérardan, A.K. Meena, S. Franger, C. Herrero, N. Dragoe, J. Alloys Compd. 704 (2017) 693–700.
[59] Q. Wang, A. Sarkar, Z. Li, Y. Lu, L. Velasco, S.S. Bhattacharya, T. Brezesinski, H. Hahn, B. Breitung, Electrochem. Commun. 100 (2019) 121–125.
[60] N. Qiu, H. Chen, Z. Yang, S. Sun, Y. Wang, Y. Cui, J. Alloys Compd. 777 (2019) 767–774.
[61] B. Breitung, Q. Wang, A. Schiele, Đ. Tripković, A. Sarkar, L. Velasco, D. Wang, S.S. Bhattacharya, H. Hahn, T. Brezesinski, Batter. Supercaps 3 (2020) 361–369.
[62] B. Cheng, H. Lou, A. Sarkar, Z. Zeng, F. Zhang, X. Chen, L. Tan, V. Prakapenka, E. Greenberg, J. Wen, R. Djenadic, H. Hahn, Q. Zeng, Commun. Chem. 2 (2019) 114.
[63] A. Sarkar, B. Eggert, L. Velasco, X. Mu, J. Lill, K. Ollefs, S.S. Bhattacharya, H. Wende, R. Kruk, R.A. Brand, H. Hahn, APL Mater. 8 (2020) 051111.
[64] J. Zhang, J. Yan, S. Calder, Q. Zheng, M.A. McGuire, D.L. Abernathy, Y. Ren, S.H. Lapidus, K. Page, H. Zheng, J.W. Freeland, J.D. Budai, R.P. Hermann, Chem. Mater. 31 (2019) 3705.
[65] M.P. Jimenez-Segura, T. Takayama, D. Bérardan, A. Hoser, M. Reehuis, H. Takagi, N. Dragoe, Appl. Phys. Lett. 114 (2019) 122401.
[66] R. Witte, A. Sarkar, L. Velasco, R. Kruk, R.A. Brand, B. Eggert, K. Ollefs, E. Weschke, H. Wende, H. Hahn, J. Appl. Phys. 127 (2020) 185109.
[67] H. Chen, J. Fu, P. Zhang, H. Peng, C.W. Abney, K. Jie, X. Liu, M. Chi, S. Dai, J. Mater. Chem. A 6 (2018) 11129–11133.
[68] J.L. Braun, C.M. Rost, M. Lim, A. Giri, D.H. Olson, G.N. Kotsonis, G. Stan, D.W. Brenner, J.-P. Maria, P.E. Hopkins, Adv. Mater. 30 (2018) 1805004.
[69] A.J. Wright, J. Luo, J. Mater. Sci. (2020).
[70] B.L. Musicó, D. Gilbert, T.Z. Ward, K. Page, E. George, J. Yan, D. Mandrus, V. Keppens, APL Mater. 8 (2020) 040912.
[71] M.-H. Chuang, M.-H. Tsai, W.-R. Wang, S.-J. Lin, J.-W. Yeh, High-Entropy Alloys, Springer International Publishing, Cham, 2016.
[72] N. Osenciat, D. Bérardan, D. Dragoe, B. Léridon, S. Holé, A.K. Meena, S. Franger, N. Dragoe, J. Am. Ceram. Soc. (2019).
[73] Y. Zheng, Y. Yi, M. Fan, H. Liu, X. Li, R. Zhang, M. Li, Z.-A. Qiao, Energy Storage Mater. 23 (2019) 678–683.
[74] C. Rödl, F. Fuchs, J. Furthmüller, F. Bechstedt, Phys. Rev. B 79 (2009) 235114.
[75] N.A. Spaldin, Magn. Mater., Cambridge University Press, Cambridge, 2010, pp. 113–129.

Bibliography

[1] J. William D. Callister, *Materials Science and Engineering An Introduction*, 7th ed. (John Wiley & Sons, Inc., July 2007), ISBN: 978-0-471-73696-7 (cit. on pp. 1, 7, 136, 137).

[2] R. Abbaschian and R. E. Reed-Hill, *Physical metallurgy principles* (Cengage Learning, 2008), ISBN: 978-0-495-08254-5 (cit. on pp. 1, 7).

[3] B. Cantor, I. Chang, P. Knight, and A. Vincent, Materials Science and Engineering: A **375-377**, 213 (2004) `10.1016/j.msea.2003.10.257` (cit. on pp. 1, 5, 7, 20).

[4] C. T. Sims, JOM **18**, 1119 (1966) `10.1007/BF03378505` (cit. on p. 1).

[5] W. L. Johnson, Current Opinion in Solid State and Materials Science **1**, 383 (1996) `10.1016/S1359-0286(96)80029-5` (cit. on p. 1).

[6] J. Yeh, S. Chen, S. Lin, J. Gan, T. Chin, T. Shun, C. Tsau, and S. Chang, Advanced Engineering Materials **6**, 299 (2004) `10.1002/adem.200300567` (cit. on pp. 1, 5, 20).

[7] B. Gludovatz, A. Hohenwarter, D. Catoor, E. H. Chang, E. P. George, and R. O. Ritchie, Science **345**, 1153 (2014) `10.1126/science.1254581` (cit. on pp. 1, 20).

[8] Y. Zhang, T. T. Zuo, Z. Tang, M. C. Gao, K. A. Dahmen, P. K. Liaw, and Z. P. Lu, Progress in Materials Science **61**, 1, ISSN: 0079-6425 (2014) `https://doi.org/10.1016/j.pmatsci.2013.10.001` (cit. on p. 1).

[9] M. C. Gao, J.-W. Yeh, P. K. Liaw, and Y. Zhang, *High-entropy alloys: fundamentals and applications* (Springer, 2016), ISBN: 9783319270135 (cit. on pp. 1, 20, 48).

[10] T. Chen, T. Shun, J. Yeh, and M. Wong, Surface and Coatings Technology **188-189**, Proceedings of the 31st International Conference on Metallurgical Coatings and Thin Films, 193, ISSN: 0257-8972 (2004) `https://doi.org/10.1016/j.surfcoat.2004.08.023` (cit. on pp. 2, 20).

[11] V. Braic, A. Vladescu, M. Balaceanu, C. R. Luculescu, and M. Braic, SURFACE & COATINGS TECHNOLOGY **211**, 117 (2012) `10.1016/j.surfcoat.2011.09.033` (cit. on pp. 2, 20).

[12] M.-H. Hsieh, M.-H. Tsai, W.-J. Shen, and J.-W. Yeh, Surface and Coatings Technology **221**, 118 (2013) `10.1016/j.surfcoat.2013.01.036` (cit. on pp. 2, 20).

[13] W. Shen, M. Tsai, K. Tsai, C. Juan, C. Tsai, J. Yeh, and Y. Chang, Journal of The Electrochemical Society **160**, C531 (2013) `10.1149/2.028311jes` (cit. on p. 2).

[14] C. M. Rost, E. Sachet, T. Borman, A. Moballegh, E. C. Dickey, D. Hou, J. L. Jones, S. Curtarolo, and J.-P. Maria, Nature Communications **6**, 8485 (2015) `10.1038/ncomms9485` (cit. on pp. 2, 3, 5, 11, 14–17, 24, 101, 102).

[15] R. Djenadic, A. Sarkar, O. Clemens, C. Loho, M. Botros, V. S. K. Chakravadhanula, C. Kübel, S. S. Bhattacharya, A. S. Gandhi, and H. Hahn, Materials Research Letters **5**, 102 (2017) `10.1080/21663831.2016.1220433` (cit. on pp. 2, 3, 17–19, 48, 101, 102).

[16] H. Eric and M. Timucin, Metallurgical Transactions B **10**, 561 (1979) `10.1007/BF02662558` (cit. on pp. 2, 14).

[17] D. Bérardan, S. Franger, D. Dragoe, A. K. Meena, and N. Dragoe, physica status solidi (RRL) - Rapid Research Letters **10**, 328 (2016) `10.1002/pssr.201600043` (cit. on pp. 2, 3, 11, 20, 24, 102).

[18] D. Bérardan, S. Franger, A. K. Meena, and N. Dragoe, Journal of Materials Chemistry A **4**, 9536 (2016) `10.1039/C6TA03249D` (cit. on pp. 2, 3, 20, 24, 101–103).

[19] Z. Gao, H. Sun, L. Fu, F. Ye, Y. Zhang, W. Luo, and Y. Huang, Advanced Materials **30**, 1705702 (2018) `10.1002/adma.201705702` (cit. on p. 2).

[20] Z. Zhang, Y. Shao, B. Lotsch, Y.-S. Hu, H. Li, J. Janek, L. F. Nazar, C.-W. Nan, J. Maier, M. Armand, and L. Chen, Energy Environ. Sci. **11**, 1945 (2018) `10.1039/C8EE01053F` (cit. on p. 2).

[21] T. Jin, X. Sang, R. R. Unocic, R. T. Kinch, X. Liu, J. Hu, H. Liu, and S. Dai, eng, Advanced Materials **30**, 1707512 (2018) `10.1002/adma.201707512` (cit. on pp. 5, 20).

[22] E. Castle, T. Csanádi, S. Grasso, J. Dusza, and M. Reece, eng, Scientific Reports **8**, 8609 (2018) `10.1038/s41598-018-26827-1` (cit. on pp. 5, 20).

[23] J. Gild, Y. Zhang, T. Harrington, S. Jiang, T. Hu, M. C. Quinn, W. M. Mellor, N. Zhou, K. Vecchio, and J. Luo, Scientific Reports **6**, 37946 (2016) `10.1038/srep37946` (cit. on pp. 5, 21).

[24] D. Miracle and O. Senkov, Acta Materialia **122**, 448 (2017) `10.1016/j.actamat.2016.08.081` (cit. on pp. 5–8, 10, 20).

[25] B. Murty, J. Yeh, and S. Ranganathan, *High-Entropy Alloys*, 1st (Butterworth- Heinemann, London, 2014), ISBN: 9780128002513 (cit. on pp. 6–8, 10, 20, 48).

[26] J. M. Park, J. Moon, J. W. Bae, M. J. Jang, J. Park, S. Lee, and H. S. Kim, Materials Science and Engineering: A **719**, 155 (2018) `10.1016/j.msea.2018.02.031` (cit. on pp. 7, 8).

[27] B. Schuh, F. Mendez-Martin, B. Völker, E. P. George, H. Clemens, R. Pippan, and A. Hohenwarter, Acta Materialia **96**, 258 (2015) `10.1016/j.actamat.2015.06.025` (cit. on p. 8).

[28] K.-Y. Tsai, M.-H. Tsai, and J.-W. Yeh, Acta Materialia **61**, 4887 (2013) `10.1016/j.actamat.2013.04.058` (cit. on p. 10).

[29] M.-H. Tsai and J.-W. Yeh, Materials Research Letters **2**, 107 (2014) `10.1080/21663831.2014.912690` (cit. on pp. 10, 11).

[30] S. V. Divinski, A. V. Pokoev, N. Esakkiraja, and A. Paul, Diffusion Foundations **17**, 69 (2018) `10.4028/www.scientific.net/DF.17.69` (cit. on p. 10).

[31] D.-H. Lee, M.-Y. Seok, Y. Zhao, I.-C. Choi, J. He, Z. Lu, J.-Y. Suh, U. Ramamurty, M. Kawasaki, T. G. Langdon, et al., Acta Materialia **109**, 314 (2016) `10.1016/j.actamat.2016.02.049` (cit. on p. 10).

[32] O. Senkov, J. Scott, S. Senkova, D. Miracle, and C. Woodward, Journal of alloys and compounds **509**, 6043 (2011) `10.1016/j.jallcom.2011.02.171` (cit. on p. 11).

[33] S. Ranganathan, Current Science, ISSN: 00113891 (2003) (cit. on p. 11).

[34] A. Sarkar, Q. Wang, A. Schiele, M. R. Chellali, S. S. Bhattacharya, D. Wang, T. Brezesinski, H. Hahn, L. Velasco, and B. Breitung, Advanced Materials **31**, 1806236 (2019) `10.1002/adma.201806236` (cit. on pp. 11, 14, 17, 18).

[35] S. Jiang, T. Hu, J. Gild, N. Zhou, J. Nie, M. Qin, T. Harrington, K. Vecchio, and J. Luo, Scripta Materialia **142**, 116 (2018) `10.1016/j.scriptamat.2017.08.040` (cit. on p. 11).

[36] Y.-M. Chiang, (1997) (cit. on pp. 12, 15, 47).

[37] C. B. Carter, M. G. Norton, et al., *Ceramic materials: science and engineering*, Vol. 716 (Springer, 2007), ISBN: 978-1-4614-3523-5 (cit. on pp. 12, 47).

[38] M. R. Chellali, A. Sarkar, S. H. Nandam, S. S. Bhattacharya, B. Breitung, H. Hahn, and L. Velasco, Scripta Materialia **166**, 58 (2019) `10.1016/j.scriptamat.2019.02.039` (cit. on pp. 14, 18).

[39] L. Xia, Z. Liu, and P. Taskinen, Journal of Alloys and Compounds **687**, 827, ISSN: 0925-8388 (2016) `https://doi.org/10.1016/j.jallcom.2016.06.191` (cit. on p. 15).

[40] P. K. Davies and A. Navrotsky, Journal of Solid State Chemistry **38**, 264, ISSN: 0022-4596 (1981) `https://doi.org/10.1016/0022-4596(81)90044-X` (cit. on p. 15).

[41] J. BULARZIK, P. DAVIES, and A. NAVROTSKY, Journal of the American Ceramic Society **69**, 453, ISSN: 1551-2916 (1986) `10.1111/j.1151-2916.1986.tb07444.x` (cit. on p. 15).

[42] G. Anand, A. P. Wynn, C. M. Handley, and C. L. Freeman, Acta Materialia **146**, 119 (2018) `10.1016/j.actamat.2017.12.037` (cit. on pp. 15, 16).

[43] E. Andrievskaya, O. Kornienko, A. Sameljuk, and A. Sayir, Journal of the European Ceramic Society **31**, 1277 (2011) `10.1016/j.jeurceramsoc.2010.05.024` (cit. on p. 18).

[44] K. M. Ryan, J. P. McGrath, R. A. Farrell, W. M. O. Neill, C. J. Barnes, and M. A. Morris, Journal of Physics: Condensed Matter **15**, L49 (2003) `10.1088/0953-8984/15/2/107` (cit. on p. 18).

[45] A. Filtschew, K. Hofmann, and C. Hess, The Journal of Physical Chemistry C **120**, 6694 (2016) `10.1021/acs.jpcc.6b00959` (cit. on pp. 19, 50).

[46] F. Zhang, Q. Jin, and S.-W. Chan, Journal of Applied Physics **95**, 4319 (2004) `10.1063/1.1667251` (cit. on p. 19).

[47] S. Praveen and H. S. Kim, Advanced Engineering Materials **20**, 1700645 (2018) `10.1002/adem.201700645` (cit. on p. 20).

[48] Z. Fan, H. Wang, Y. Wu, X. J. Liu, and Z. P. Lu, RSC Adv. **6**, 52164 (2016) `10.1039/C5RA28088E` (cit. on p. 20).

[49] M.-H. Chuang, M.-H. Tsai, W.-R. Wang, S.-J. Lin, and J.-W. Yeh, *High-Entropy Alloys*, edited by M. C. Gao, J.-W. Yeh, P. K. Liaw, and Y. Zhang (Springer International Publishing, Cham, Sept. 2016), ISBN: 978-3-319-27011-1, `10.1007/978-3-319-27013-5` (cit. on p. 20).

[50] C.-W. Tsai, S.-W. Lai, K.-H. Cheng, M.-H. Tsai, A. Davison, C.-H. Tsau, and J.-W. Yeh, Thin Solid Films **520**, 2613 (2012) `10.1016/j.tsf.2011.11.025` (cit. on p. 20).

[51] J. L. Braun, C. M. Rost, M. Lim, A. Giri, D. H. Olson, G. N. Kotsonis, G. Stan, D. W. Brenner, J.-P. Maria, and P. E. Hopkins, Advanced Materials **30**, 1805004 (2018) `10.1002/adma.201805004` (cit. on pp. 20, 24, 102, 103).

[52] H. Chen, J. Fu, P. Zhang, H. Peng, C. W. Abney, K. Jie, X. Liu, M. Chi, and S. Dai, J. Mater. Chem. A **6**, 11129 (2018) `10.1039/C8TA01772G` (cit. on p. 20).

[53] R.-Z. Zhang, F. Gucci, H. Zhu, K. Chen, and M. J. Reece, Inorganic Chemistry **57**, 13027 (2018) `10.1021/acs.inorgchem.8b02379` (cit. on pp. 20, 21).

[54] A. Sarkar, L. Velasco, D. Wang, Q. Wang, G. Talasila, L. de Biasi, C. Kübel, T. Brezesinski, S. S. Bhattacharya, H. Hahn, et al., Nature communications **9**, 3400 (2018) `10.1038/s41467-018-05774-5` (cit. on pp. 20, 27, 102, 133).

[55] J. Zhou, J. Zhang, F. Zhang, B. Niu, L. Lei, and W. Wang, Ceramics International **44**, 22014 (2018) `10.1016/j.ceramint.2018.08.100` (cit. on p. 20).

[56] L. Feng, W. G. Fahrenholtz, G. E. Hilmas, and Y. Zhou, Scripta Materialia **162**, 90, ISSN: 1359-6462 (2019) `https://doi.org/10.1016/j.scriptamat.2018.10.049` (cit. on p. 20).

[57] P. H. Mayrhofer, A. Kirnbauer, P. Ertelthaler, and C. M. Koller, Scripta Materialia **149**, 93 (2018) `10.1016/j.scriptamat.2018.02.008` (cit. on p. 21).

[58] Q. Wang, A. Sarkar, D. Wang, L. Velasco, R. Azmi, S. S. Bhattacharya, T. Bergfeldt, A. Düvel, P. Heitjans, T. Brezesinski, H. Hahn, and B. Breitung, Energy & Environmental Science **12**, 2433 (2019) `10.1039/C9EE00368A` (cit. on pp. 21, 102, 103).

[59] N. Zhou, S. Jiang, T. Huang, M. Qin, T. Hu, and J. Luo, Science Bulletin, `10.1016/j.scib.2019.05.007` (2019) `10.1016/j.scib.2019.05.007` (cit. on p. 21).

[60] Y. Qin, J.-X. Liu, F. Li, X. Wei, H. Wu, and G.-J. Zhang, Journal of Advanced Ceramics **8**, 148 (2019) `10.1007/s40145-019-0319-3` (cit. on p. 21).

[61] A. Corpuz and R. Richards, 51 `10.1021/bk-2010-1045.ch004` (cit. on p. 23).

[62] P. A. Cox, *Transition metal oxides: an introduction to their electronic structure and properties* (Oxford university press, 2010), ISBN: 978-0-191-03013-0 (cit. on p. 23).

[63] L. Duò, M. Finazzi, and F. Ciccacci, *Magnetic Properties of Antiferromagnetic Oxide Materials: Surfaces, Interfaces, and Thin Films*, Wiley Online Library: Books (Wiley, 2010), ISBN: 9783527630387 (cit. on p. 23).

[64] V. I. Anisimov, M. A. Korotin, and E. Z. Kurmaev, Journal of Physics: Condensed Matter **2**, 3973 (1990) `10.1088/0953-8984/2/17/008` (cit. on p. 23).

[65] P. Poizot, S. Laruelle, S. Grugeon, L. Dupont, and J. M. Tarascon, Nature **407**, 496 (2000) `10.1038/35035045` (cit. on pp. 23, 24, 99).

[66] K. Mizushima, P. Jones, P. Wiseman, and J. Goodenough, English (US), Materials Research Bulletin **15**, 783, ISSN: 0025-5408 (1980) `10.1016/0025-5408(80)90012-4` (cit. on p. 24).

[67] N. Nitta, F. Wu, J. T. Lee, and G. Yushin, Materials Today **18**, 252 (2015) `10.1016/j.mattod.2014.10.040` (cit. on pp. 24, 103).

[68] X. Huang, J. Tu, C. Zhang, and F. Zhou, Electrochimica Acta **55**, 8981 (2010) `10.1016/j.electacta.2010.08.039` (cit. on p. 24).

[69] D. Bérardan, A. Meena, S. Franger, C. Herrero, and N. Dragoe, Journal of Alloys and Compounds **704**, 693 (2017) `10.1016/j.jallcom.2017.02.070` (cit. on pp. 24, 102).

[70] Z. Rák, J.-P. Maria, and D. Brenner, Materials Letters **217**, 300 (2018) `10.1016/j.matlet.2018.01.111` (cit. on p. 24).

[71] K. Chen, X. Pei, L. Tang, H. Cheng, Z. Li, C. Li, X. Zhang, and L. An, Journal of the European Ceramic Society **38**, 4161 (2018) `10.1016/j.jeurceramsoc.2018.04.063` (cit. on pp. 24, 48, 102).

[72] H. Chen, W. Lin, Z. Zhang, K. Jie, D. R. Mullins, X. Sang, S.-Z. Yang, C. J. Jafta, C. A. Bridges, X. Hu, R. R. Unocic, J. Fu, P. Zhang, and S. Dai, ACS Materials Letters **1**, 83 (2019) `10.1021/acsmaterialslett.9b00064` (cit. on pp. 24, 102).

[73] M. P. Jimenez-Segura, T. Takayama, D. Bérardan, A. Hoser, M. Reehuis, H. Takagi, and N. Dragoe, Applied Physics Letters **114**, 122401 (2019) `10.1063/1.5091787` (cit. on pp. 24, 102).

[74] J. Zhang, J. Yan, S. Calder, Q. Zheng, M. A. McGuire, D. L. Abernathy, Y. Ren, S. H. Lapidus, K. Page, H. Zheng, J. W. Freeland, J. D. Budai, and R. P. Hermann, Chemistry of Materials **31**, 3705 (2019) `10.1021/acs.chemmater.9b00624` (cit. on pp. 24, 102).

[75] N. Qiu, H. Chen, Z. Yang, S. Sun, Y. Wang, and Y. Cui, Journal of Alloys and Compounds **777**, 767 (2019) `10.1016/j.jallcom.2018.11.049` (cit. on pp. 27, 102, 103).

[76] Q. Wang, A. Sarkar, Z. Li, Y. Lu, L. Velasco, S. S. Bhattacharya, T. Brezesinski, H. Hahn, and B. Breitung, Electrochemistry Communications **100**, 121 (2019) `10.1016/j.elecom.2019.02.001` (cit. on pp. 27, 103).

[77] A. D. Liyanage, S. D. Perera, K. Tan, Y. Chabal, and K. J. Balkus Jr, ACS Catalysis **4**, 577 (2014) `10.1021/cs400889y` (cit. on p. 47).

[78] S. Zha, C. Xia, and G. Meng, Journal of Power Sources **115**, 44 (2003) `10.1016/S0378-7753(02)00625-0` (cit. on p. 47).

[79] J. Goff, W. Hayes, S. Hull, M. Hutchings, and K. N. Clausen, Physical Review B **59**, 14202 (1999) `10.1103/PhysRevB.59.14202` (cit. on p. 47).

[80] R. Vassen, X. Cao, F. Tietz, D. Basu, and D. Stöver, Journal of the American Ceramic Society **83**, 2023 (2000) `10.1111/j.1151-2916.2000.tb01506.x` (cit. on p. 47).

[81] A. Sarkar, C. Loho, L. Velasco, T. Thomas, S. S. Bhattacharya, H. Hahn, and R. Djenadic, Dalton Trans. **46**, 12167 (2017) `10.1039/C7DT02077E` (cit. on pp. 48, 133).

[82] J. Gild, M. Samiee, J. L. Braun, T. Harrington, H. Vega, P. E. Hopkins, K. Vecchio, and J. Luo, Journal of the European Ceramic Society **38**, 3578 (2018) `10.1016/j.jeurceramsoc.2018.04.010` (cit. on pp. 48, 101–103).

[83] A. Prokofiev, A. Shelykh, and B. Melekh, Journal of Alloys and Compounds **242**, 41, ISSN: 0925-8388 (1996) `https://doi.org/10.1016/0925-8388(96)02293-1` (cit. on p. 50).

[84] S. Zinatloo-Ajabshir and M. Salavati-Niasari, New J. Chem. **39**, 3948 (2015) `10.1039/C4NJ02106A` (cit. on p. 50).

[85] S. Som and S. K. Sharma, Journal of Physics D: Applied Physics **45**, 415102 (2012) `10.1088/0022-3727/45/41/415102` (cit. on p. 50).

[86] B. Cheng, H. Lou, A. Sarkar, Z. Zeng, F. Zhang, X. Chen, L. Tan, V. Prakapenka, E. Greenberg, J. Wen, et al., Communications Chemistry **2**, 1 (2019) `10.1038/s42004-019-0216-2` (cit. on p. 51).

[87] R. J. Tilley, *Perovskites: structure-property relationships* (John Wiley & Sons, Inc., 2016), ISBN: 9781118935668 (cit. on p. 75).

[88] V. M. Goldschmidt, Naturwissenschaften **14**, 477, ISSN: 1432-1904 (1926) `10.1007/BF01507527` (cit. on p. 75).

[89] A. Molinari, P. M. Leufke, C. Reitz, S. Dasgupta, R. Witte, R. Kruk, and H. Hahn, Nature Communications **8**, 15339, ISSN: 2041-1723 (2017) `10.1038/ncomms15339` (cit. on p. 76).

[90] S.-W. Cheong and M. Mostovoy, Nature Materials **6**, 13, ISSN: 1476-1122 (2007) `10.1038/nmat1804` (cit. on p. 76).

[91] J. R. Mawdsley and T. R. Krause, Applied Catalysis A: General **334**, 311, ISSN: 0926860X (2008) `10.1016/j.apcata.2007.10.018` (cit. on p. 76).

[92] J. Goodenough, ed., *Localized to itinerant electronic transition in perovskite oxides* (Springer, Berlin, 2001), ISBN: 3540675221 (cit. on p. 76).

[93] E. Koep, C. Jin, M. Haluska, R. Das, R. Narayan, K. Sandhage, R. Snyder, and M. Liu, Journal of Power Sources **161**, 250, ISSN: 03787753 (2006) `10.1016/j.jpowsour.2006.03.060` (cit. on p. 76).

[94] S. J. Skinner and J. A. Kilner, Materials Today **6**, 30, ISSN: 13697021 (2003) `10.1016/S1369-7021(03)00332-8` (cit. on p. 76).

[95] C. N. R. Rao, A. K. Cheetham, and R. Mahesh, Chemistry of Materials **8**, 2421 (1996) `10.1021/cm960201v` (cit. on p. 76).

[96] M. Eibschütz, S. Shtrikman, and D. Treves, Physical Review **156**, 562 (1967) `10.1103/PhysRev.156.562` (cit. on p. 76).

[97] J. Kanamori, Journal of Physics and Chemistry of Solids **10**, 87 (1959) `10.1016/0022-3697(59)90061-7` (cit. on p. 76).

[98] P. W. Anderson, Physical Review **79**, 350 (1950) `10.1103/PhysRev.79.350` (cit. on p. 76).

[99] J. B. Goodenough, Journal of Physics and Chemistry of Solids **6**, 287 (1958) `10.1016/0022-3697(58)90107-0` (cit. on pp. 76, 78).

[100] A. Sarkar, R. Djenadic, D. Wang, C. Hein, R. Kautenburger, O. Clemens, and H. Hahn, Journal of the European Ceramic Society **38**, 2318 (2018) `10.1016/j.jeurceramsoc.2017.12.058` (cit. on pp. 78, 133).

[101] J. Dabrowa, M. Stygar, A. Mikuła, A. Knapik, K. Mroczka, W. Tejchman, M. Danielewski, and M. Martin, Materials Letters **216**, 32 (2018) `10.1016/j.matlet.2017.12.148` (cit. on pp. 101, 102).

[102] A. Sarkar, R. Djenadic, N. J. Usharani, K. P. Sanghvi, V. S. Chakravadhanula, A. S. Gandhi, H. Hahn, and S. S. Bhattacharya, Journal of the European Ceramic Society **37**, 747 (2017) `10.1016/j.jeurceramsoc.2016.09.018` (cit. on pp. 101, 102, 133).

[103] M. Biesuz, L. Spiridigliozzi, G. Dell'Agli, M. Bortolotti, and V. M. Sglavo, Journal of Materials Science **53**, 8074 (2018) `10.1007/s10853-018-2168-9` (cit. on p. 101).

[104] M. Balcerzak, K. Kawamura, R. Bobrowski, P. Rutkowski, and T. Brylewski, Journal of Electronic Materials **48**, 7105 (2019) `10.1007/s11664-019-07512-z` (cit. on pp. 101, 102).

[105] F. Okejiri, Z. Zhang, J. Liu, M. Liu, S. Yang, and S. Dai, ChemSusChem **13**, 111 (2020) `10.1002/cssc.201902705` (cit. on pp. 101, 102).

[106] A. Mao, H.-Z. Xiang, Z.-G. Zhang, K. Kuramoto, H. Yu, and S. Ran, Journal of Magnetism and Magnetic Materials **484**, 245, ISSN: 0304-8853 (2019) `https://doi.org/10.1016/j.jmmm.2019.04.023` (cit. on p. 101).

[107] A. Mao, F. Quan, H.-Z. Xiang, Z.-G. Zhang, K. Kuramoto, and A.-L. Xia, Journal of Molecular Structure **1194**, 11 (2019) `10.1016/j.molstruc.2019.05.073` (cit. on pp. 101, 102).

[108] D. Wang, Z. Liu, S. Du, Y. Zhang, H. Li, Z. Xiao, W. Chen, R. Chen, Y. Wang, Y. Zou, and S. Wang, J. Mater. Chem. A **7**, 24211 (2019) `10.1039/C9TA08740K` (cit. on pp. 101, 102).

[109] K.-P. Tseng, Q. Yang, S. J. McCormack, and W. M. Kriven, Journal of the American Ceramic Society **103**, 569 `10.1111/jace.16689` (cit. on p. 101).

[110] P. Meisenheimer, T. Kratofil, and J. Heron, Scientific reports **7**, 13344 (2017) `10.1038/s41598-017-13810-5` (cit. on p. 101).

[111] Y. Sharma, B. L. Musico, X. Gao, C. Hua, A. F. May, A. Herklotz, A. Rastogi, D. Mandrus, J. Yan, H. N. Lee, M. F. Chisholm, V. Keppens, and T. Z. Ward, Physical Review Materials **2**, 060404 (2018) `10.1103/PhysRevMaterials.2.060404` (cit. on p. 101).

[112] A. Kirnbauer, C. Spadt, C. M. Koller, S. Kolozsvári, and P. H. Mayrhofer, Vacuum **168**, 108850 (2019) `10.1016/j.vacuum.2019.108850` (cit. on p. 101).

[113] A. D. Dupuy, X. Wang, and J. M. Schoenung, Materials Research Letters **7**, 60 (2019) `10.1080/21663831.2018.1554605` (cit. on p. 101).

[114] K. Zhang, W. Li, J. Zeng, T. Deng, B. Luo, H. Zhang, and X. Huang, Journal of Alloys and Compounds **817**, 153328, ISSN: 0925-8388 (2020) `https://doi.org/10.1016/j.jallcom.2019.153328` (cit. on p. 102).

[115] D. Vinnik, E. Trofimov, V. Zhivulin, O. Zaitseva, S. Gudkova, A. Starikov, D. Zherebtsov, A. Kirsanova, M. Häßner, and R. Niewa, Ceramics International **45**, 12942, ISSN: 0272-8842 (2019) `https://doi.org/10.1016/j.ceramint.2019.03.221` (cit. on p. 102).

[116] C. Zhao, F. Ding, Y. Lu, L. Chen, and Y.-S. Hu, Angewandte Chemie International Edition **59**, 264 (2020) `10.1002/anie.201912171` (cit. on pp. 102, 103).

[117] Y. Zheng, Y. Yi, M. Fan, H. Liu, X. Li, R. Zhang, M. Li, and Z.-A. Qiao, Energy Storage Materials **23**, 678, ISSN: 2405-8297 (2019) `https://doi.org/10.1016/j.ensm.2019.02.030` (cit. on pp. 102, 103).

[118] A. Sarkar, B. Eggert, L. Velasco, X. Mu, J. Lill, K. Ollefs, S. S. Bhattacharya, H. Wende, R. Kruk, R. A. Brand, and H. Hahn, APL Materials **8**, 051111 (2020) `10.1063/5.0007944` (cit. on pp. 102, 104).

[119] R. Witte, A. Sarkar, R. Kruk, B. Eggert, R. A. Brand, H. Wende, and H. Hahn, Physical Review Materials **3**, 034406 (2019) `10.1103/PhysRevMaterials.3.034406` (cit. on pp. 102, 133).

[120] R. Witte, A. Sarkar, L. Velasco, R. Kruk, R. A. Brand, B. Eggert, K. Ollefs, E. Weschke, H. Wende, and H. Hahn, Journal of Applied Physics **127**, 185109 (2020) `10.1063/5.0004125` (cit. on p. 102).

[121] Y. Sharma, Q. Zheng, A. R. Mazza, E. Skoropata, T. Heitmann, Z. Gai, B. Musico, P. F. Miceli, B. C. Sales, V. Keppens, M. Brahlek, and T. Z. Ward, Phys. Rev. Materials **4**, 014404 (2020) `10.1103/PhysRevMaterials.4.014404` (cit. on p. 102).

[122] B. Musicó, Q. Wright, T. Z. Ward, A. Grutter, E. Arenholz, D. Gilbert, D. Mandrus, and V. Keppens, Phys. Rev. Materials **3**, 104416 (2019) `10.1103/PhysRevMaterials.3.104416` (cit. on p. 102).

[123] Z. Grzesik, G. Smoła, M. Miszczak, M. Stygar, J. Dąbrowa, M. Zajusz, K. Świerczek, and M. Danielewski, Journal of the European Ceramic Society **40**, 835 (2020) `10.1016/j.jeurceramsoc.2019.10.026` (cit. on p. 102).

[124] J. Hemberger, A. Krimmel, T. Kurz, H.-A. Krug von Nidda, V. Y. Ivanov, A. A. Mukhin, A. M. Balbashov, and A. Loidl, Phys. Rev. B **66**, 094410 (2002) `10.1103/PhysRevB.66.094410` (cit. on p. 104).

[125] G. L. Messing, S.-C. Zhang, and G. V. Jayanthi, Journal of the American Ceramic Society **76**, 2707 (1993) `10.1111/j.1151-2916.1993.tb04007.x` (cit. on pp. 133, 135).

[126] W. Y. Teoh, R. Amal, and L. Mädler, Nanoscale **2**, 1324 (2010) `10.1039/C0NR00017E` (cit. on p. 133).

[127] B. M. Kumar and S. S. Bhattacharya, Proces Appl Ceramics **6**, 165 (2012) `10.2298/PAC1203165K` (cit. on p. 133).

[128] R. Djenadic, M. Botros, and H. Hahn, Solid State Ionics **287**, 71 (2016) `10.1016/j.ssi.2016.02.008` (cit. on pp. 134, 135).

[129] "Nebulized Spray Pyrolysis", in *Essentials of Inorganic Materials Synthesis* (John Wiley & Sons, Inc., 2015) Chap. 11, pp. 97–101, ISBN: 9781118892671, `10.1002/9781118892671.ch11` (cit. on p. 134).

[130] W. Ahmed, M. J. Jackson, and M. J. Jackson, *Emerging nanotechnologies for manufacturing* (William Andrew, 2009), ISBN: 9780815519782 (cit. on p. 136).

[131] B. D. Cullity, *Elements of X-ray Diffraction* (Addison-Wesley Publishing, 1956), ISBN: 9780201610918 (cit. on p. 136).

[132] *Topas V5, General profile and structure analysis software for powder diffraction data, User's Manual* (Bruker AXS, Karlsruhe), ISBN: 8522796610 (cit. on p. 137).

[133] J. I. Goldstein, D. E. Newbury, J. R. Michael, N. W. Ritchie, J. H. J. Scott, and D. C. Joy, *Scanning electron microscopy and X-ray microanalysis* (Springer, 2017), ISBN: 9781493966769 (cit. on p. 137).

[134] D. B. Williams and C. B. Carter, *The transmission electron microscope* (Springer, 1996), pp. 3–17, ISBN: 978-0-387-76501-3 (cit. on pp. 137, 138).

[135] P. Keil and A. Jossen, Journal of Energy Storage **6**, 125, ISSN: 2352-152X (2016) `10.1016/j.est.2016.02.005` (cit. on p. 138).

[136] R. G. Compton and C. E. Banks, *Understanding voltammetry* (World Scientific, 2011), ISBN: 9781848165854 (cit. on p. 139).

[137] D. H. Evans, K. M. O'Connell, R. A. Petersen, and M. J. Kelly, Journal of Chemical Education **60**, 290 (1983) `10.1021/ed060p290` (cit. on p. 139).

[138] W. H. Weber and R. Merlin, *Raman scattering in materials science*, Vol. 42 (Springer Science & Business Media, 2013), ISBN: 9783662042212 (cit. on p. 139).

[139] J. F. Moulder, *Handbook of X-ray Photoelectron Spectroscopy: A Reference Book of Standard Spectra for Identification and Interpretation of XPS Data* (Physical Electronics Division, Perkin-Elmer Corporation, 1992), ISBN: 9780962702624 (cit. on p. 140).

[140] J. E. Penner-Hahn, Coordination Chemistry Reviews **190-192**, 1101, ISSN: 0010-8545 (1999) `https://doi.org/10.1016/S0010-8545(99)00160-5` (cit. on p. 141).

[141] E. Weschke and E. Schierle, Journal of large-scale research facilities JLSRF **4**, 1 (2018) `10.17815/jlsrf-4-77` (cit. on p. 141).

[142] E. Welter, R. Chernikov, M. Herrmann, and R. Nemausat, in , Vol. 2054, 1 (2019), p. 040002, `10.1063/1.5084603` (cit. on p. 141).

[143] V. A. Fassel, Fresenius' Zeitschrift für analytische Chemie **324**, 511 (1986) `10.1007/BF00470406` (cit. on p. 141).

[144] S. P. Tandon and J. P. Gupta, physica status solidi (b) **38**, 363 (1970) `10.1002/pssb.19700380136` (cit. on p. 142).

[145] J. Clarke and A. Braginski, *The SQUID Handbook: Applications of SQUIDS and SQUID Systems. Vol. 2* (New York: Wiley, 2006), ISBN: 978-3-527-40408-7 (cit. on p. 142).

[146] B. D. Cullity and C. D. Graham, *Introduction to magnetic materials* (John Wiley & Sons, Inc., 2009), ISBN: 978-0-471-47741-9 (cit. on p. 143).

[147] R. Nagendran, N. Thirumurugan, N. Chinnasamy, M. P. Janawadkar, and C. S. Sundar, Review of Scientific Instruments **82**, 015109 (2011) `10.1063/1.3519017` (cit. on p. 143).

[148] P. Gütlich, E. Bill, and A. X. Trautwein, *Mössbauer spectroscopy and transition metal chemistry: fundamentals and applications* (Springer Science & Business Media, 2010) (cit. on p. 143).

[149] R. L. Mössbauer, Zeitschrift für Physik **151**, 124, ISSN: 0044-3328 (1958) `10.1007/BF01344210` (cit. on p. 143).

[150] O. C. Kistner and A. W. Sunyar, Phys. Rev. Lett. **4**, 412 (1960) `10.1103/PhysRevLett.4.412` (cit. on p. 143).

Appendices

A. Experimental techniques

A.1. Synthesis techniques

Three types of techniques, flame spray pyrolysis (FSP), nebulized spray pyrolysis (NSP) and reverse co-precipitation (RCP), were used for the synthesis of high entropy oxides (HEOs). Precursor solution was prepared by dissolving high purity water soluble salts (mostly nitrates) of the constituent metallic elements in deionized water. Depending upon the HEO composition, the precursor concentration and synthesis parameters were modified to achieve single phase. Specific detail can be found in the respective articles [54, 81, 100, 102, 119] presented in Chapter 3, 4 and 5.

A.1.1. Flame spray pyrolysis

Flame spray pyrolysis (FSP) is an aerosol based synthesis technique typically used for large scale production of nanoparticles.[125, 126] A schematic of the FSP process is shown in Fig. A.1. The steps of a typical pyrolysis reaction happening in the flame [125] are as follows (also shown in Fig. A.1):

(a) First step is the evaporation of the solvent.

(b) Next step is the solute precipitation and drying.

(c) Following is the decomposition (or pyrolysis) of the precursor and nucleation of the microporous powder.

(d) The final step is growth and agglomeration/sintering of the product before it gets quenched and deposited on the powder collector.

FSP[1] used in this study consisted of a precursor delivery system, multiport diffusion burner, powder collection unit and vacuum pumping unit. The aerosol of the aqueous precursor was created using a nebulizer/atomizer and was carried to the reaction chamber using O_2 as the carrier gas. A multiport diffusion burner fueled by liquefied petroleum gas (LPG) and O_2 was used to create the flame. After pyrolysis, the powdered product was collected using a filter paper. A vacuum pump

---

[1] More information can be found in Ref. [102, 127].

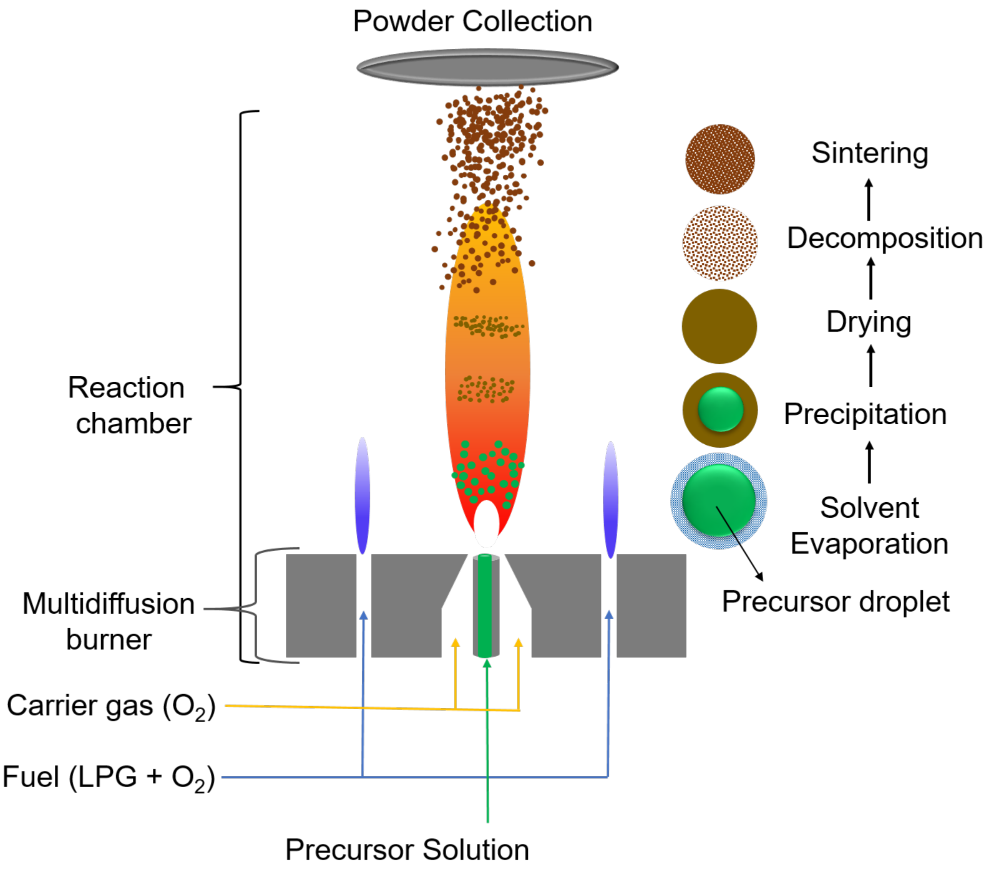

Figure A.1.: Schematic of flame spray pyrolysis process, showing the different steps of pyrolysis reaction.

positioned at the end of the process line was used to maintain a constant system pressure, which aided the powder collection and prevented over-pressure arising from the constant flow of gases.

A.1.2. Nebulized spray pyrolysis

Nebulized spray pyrolysis (NSP) is a versatile technique used for synthesis of nanoparticles and thin films[128, 129]. The basic principle of precursor pyrolysis is similar for both NSP and FSP. However, the decomposition reaction happens in a hot wall reactor instead of a flame in NSP. Hence, the resulting products can vary drastically as the time scale and temperature of the decomposition reaction are very different. A schematic of NSP system used in this dissertation is shown in Fig A.2. The setup consisted of four major parts which are as follows:

(a) **Spraying and nebulization unit**. The aqueous precursor solution was fed to a glass made nebulization chamber using a syringe pump. The precursor solution is nebulized using a transducer (TDK, NB series) operating at resonant frequency in the range of 1.6 – 1.75 MHz. The precursor mist was then carried to the pyrolysis unit using O_2 as the carrier gas.

The gas flow rate (5 standard liters per minute) was regulated using a mass flow controller (MFC in Fig. A.2).

(b) **Pyrolysis unit**. The pyrolysis zone consisted of a horizontal hot wall reactor (CTF 1200, Carbolite) which controlled the (synthesis) temperature of an alumina tube passing through it. The pyrolysis reaction[125] takes place in the alumina tube leading to the formation of powdered product (as discussed in Fig. A.1).

(c) **Collection unit**. The product so formed was collected using glass fiber filter paper (13400-100 K, Sartorius) placed inside the stainless steel based collection unit. To avoid moisture, the collection unit was moderately heated (120 °C) using a heating tape (HBS 450, Horst GmbH).

(d) **Pumping unit**. The pumping unit consisted of a vacuum pump, placed at the end of the synthesis line, connected to a butterfly valve (MKS Instruments 253B) and Baraton pressure gauge (MKS Instrument 628A). The butterfly valve was positioned after the collector (B in Fig. A.2) while the pressure gauge (P in Fig. A.2) was placed between the pyrolysis zone and the collector. The synthesis took place at a constant pressure (900 mbar) which could be adjusted using a pressure controller connected to the pressure gauge.

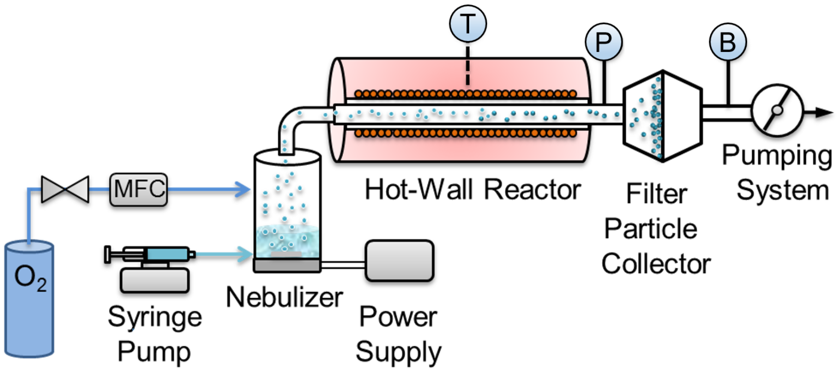

Figure A.2.: Schematic of nebulized spray pyrolysis setup. MFC, T, P and B denote the mass flow controller, temperature controller, pressure gauge and butter valve, respectively. Adapted from [128]

The phase composition, particle size and morphology of the resultant product can be manipulated by changing several parameters in a NSP setup. For instance, changing the synthesis temperature can strongly influence the product, such as low temperatures can lead to incomplete pyrolysis whereas high temperature can lead to agglomeration and sintering of the particles. Similarly, changing the nebulization speed, carrier gas flow rate or system pressure can alter the residence time of the precursor in the pyrolysis zone, hence, can influence the phase composition and degree of particle agglomeration.

A.1.3. Reverse co-precipitation

Reverse co-precipitation (RCP) is a variation of the well known co-precipitation technique [130], which is a wet chemistry based synthesis approach for producing nanomaterials. The chronology of RCP for HEO preparation is shown in Fig. A.3.

Figure A.3.: Synthesis steps followed in a reverse co-precipitation technique.

The calcination temperature was chosen based on the HEO composition, such as for rocksalt HEO it was 1000 °C while 750 °C was used for fluorite HEO.

A.2. Characterization techniques

A.2.1. X-ray diffraction

X-ray diffraction (XRD) [1, 131] technique relies on the elastic scattering of X-rays undergoing constructive interference from the periodic arrangement of atoms present in a lattice. However, when a beam of X-rays is irradiated on a material then constructive interference can occur only under highly restricted conditions, which are governed by the Bragg's law (Eqn. A.1).

$$2\,d\,\mathrm{sin}\theta = \mathrm{n}\,\lambda \tag{A.1}$$

In Eqn. A.1, d is the interplanar lattice spacing, θ is the angle between the incident X-rays and the interacting lattice plane, n (an integer) is the order of reflection, and λ is the wavelength of the incident X-rays.

XRD is one of the most frequently used nondestructive technique for characterizing materials. Information about the crystal structure can be derived from Eqn. A.1, as the d is a crystal system dependent function of the lattice parameter(s) and the Miller indices (h, k, and l) of the diffracting plane. Information regarding phase composition, preferred crystal orientations (texture), average grain size, microstrain, and crystal defects can also be obtained from XRD. Hence, it was used in a daily basis for investigating the structural features and phase compositions of HEOs. XRD patterns (both room and high temperature) were recorded in a Bruker D8 diffractometer with Bragg-Brentano geometry equipped with a Cu-K_α radiation and a Ni filter. The instrumental calibration was performed using a reference scan of $\mathrm{LaB_6}$ (NIST 660a).

Reitveld refinements of the XRD patterns were performed using TOPAS 5, Bruker[132]. The instrumental intensity distribution was determined using a reference scan of LaB6 (NIST 660a) and the microstructural parameters were refined (using two Voigt functions) to adjust the peak shapes. Thermal displacement parameters were constrained to be the same for all atoms of all phases to avoid quantification problems.

A.2.2. Scanning electron microscopy

An electron microscope operates with the same basic principles as the optical microscopes but uses electrons instead of light. In a scanning electron microscope (SEM) [1, 133] the sample surface is scanned by a pointed electron beam over an area known as the raster. The main advantage of SEM over optical microscope is the fact that wavelength of the electrons are much lower than that of visible light, thus higher magnification, better resolution and greater depth of field can be obtained. The interaction of the electron beam with the sample can result in energetic emissions, such as secondary electrons (SE), back-scattered electrons (BSE), Auger electrons and characteristic X-rays. Out of these, SE (emerging from inelastic interaction) and BSE (emerging from elastic interaction) are used for imaging. The energy of SE are very small, thus a majority of SE get absorbed and only the ones close to the surface can escape and are detected. Hence, SE are typically used for topographical information. BSE possess higher energy than SE, thus information of deeper region are obtained using BSE. Furthermore, BSE depend on atomic number, thus compositional differences can also be imaged.

Philips XL-30 and ZEISS Gemini Leo 1530 SEMs were used in this thesis. These SEMs are equipped with a field emission electron gun. Particle size distribution, morphology and elemental compostion[2] of HEOs were studied using SEM.

A.2.3. Transmission electron microscopy

The transmission electron microscope (TEM) [1, 134] was first demonstrated by Max Knoll and Ernst Ruska in 1931. Identical to SEM, TEM also uses electron beam for probing samples, however, unlike SEM, it utilizes the transmitted electrons. As a result, TEM offers additional information on crystallinity, structural parameters, stress state and magnetic domains. Furthermore, the possibility to use high energy electron (80 - 300 keV) in TEM helps to achieve much higher magnification and resolution (down to the atomic scale).

In this work[3], a FEI Titan 80-300 equipped with a CEOS image spherical aberration corrector, a high angle annular dark field (HAADF) scanning transmission electron microscopy (STEM) detector (Fischione model 3000) and a Tridiem Gatan image filter (GIF) was used. The TEM was

---

[2] Sec. A.2.4, Energy dispersive X-ray spectroscopy, for more detail.

[3] TEM/EELS measurements were performed by Dr. D. Wang, Dr. L. Velasco, Dr. X. Mu and Dr. C. Kübel from KIT.

typically operated at 300 keV. HEOs were characterized using TEM to investigate the local phase composition, crystallographic structure, elemental distribution[2] and charge states[4].

A.2.4. Energy dispersive X-ray spectroscopy

Energy dispersive X-ray spectroscopy (EDS) is a quantitative chemical analysis tool equipped within an electron microscope. The interaction of electron beam with the sample leads to the emission of characteristic X-rays, which are element specific. Thus, detection of these X-rays can help to estimate the chemical composition and distribution [134]. In EDS measurement, the characteristic X-rays enter a semiconductor detector where the X-ray energy is transferred to form electron-hole pairs. The electron-hole pairs results in electrical conduction, which can be measured. One limitation of EDS is the detection of the light elements, typically below the atomic number of Na with detectors using a Be window.

The EDX analyses in this thesis were performed either with the SEM (ZEISS Gemini Leo 1530) equipped with INCA EDS X-Ray spectrometer or with a EDAX SUTW EDX detector connected to FEI Titan 80-300 TEM. SEM-EDS was routinely performed to verify the chemical compositions, whereas TEM-EDS was used to investigate local elemental distribution of HEOs.

A.2.5. Electron energy loss spectroscopy

Electron energy loss spectroscopy (EELS) is a common accessory available in TEM. The kinetic energy change of electrons after inelastic interactions with the sample is measured in EELS [134]. This change in the energy provides structural and chemical information of the specimen. The major advantage of EELS over EDS is the possibility to detect and quantify all elements in the periodic table, especially lighter elements.

In this dissertation[3] EELS spectra were collected in TEM mode with objective aperture of 30 µm, convergence semi-angle of <0.5 mrad, dispersion 0.1 eV/channel, collection semi-angle 15 mrad, and acquisition time 5 s and in STEM mode with condenser aperture of 70 µm, convergence semi-angle 14 mrad, dispersion 0.1 eV/channel, collection semi-angle of 16 mrad, and acquisition time of 5 s. Information about the oxidation state of the elements in HEOs were obtained from EELS.

A.2.6. Galvanostatic charge-discharge cycling

A cycle of charging and discharging is a standard technique used to test the performance of a battery, such as its capacity, reversibility, redox potential(s) and operating voltage range [135]. In galvanostatic charge discharge cycling (GCDC) a constant current is applied to the cell to reach certain upper and lower cut-off voltages. During GCDC, the applied charge and discharge currents

---

[4] Sec.A.2.5, Electron energy loss spectroscopy, for more detail.

are often expressed in C-rate. A C-rate is a measure of the rate at which a battery is charged or discharged relative to its maximum capacity. For instance, a C-rate of 1C indicates the amount of current needed to completely charge or discharge battery in 1 hour. Thus, GCDC at 1C means that a complete cycle (both charge and discharge loop) will take 2 hours, likewise, C/20 means one complete cycle will take 40 hours.

In this thesis GCDC measurements were carried using a MACCOR battery cycler to investigate the capacity and cyclic stability of HEOs against Li counter electrodes. The lower and upper voltage limits (vs. Li^+/Li) were 0.01 and 3.0 V, respectively. Measurements were performed with different C-rates, such as C/20, C/10, C/5, C, 2C and 3C. The total capacity of HEOs was considered as 1000 mAh/g, thus, C/20, C/10, C/5, C, 2C and 3C meant specific currents of 50 mA/g, 100 mA/g, 200 mA/g, 1000 mA/g, 2000 mA/g and 3000 mA/g, respectively. Every GCDC measurement started with 3 initial formation cycles, where the charging and discharging were done at 50 mA/g. Formation cycles typically lead to the formation of the solid electrolyte interphase (SEI) film over the surface of the electrode. Ideally, SEI protects irreversible loss of Li and electrolyte, thus, helping in smooth cycling.

A.2.7. Cyclic voltammetry

Cyclic voltammetry (CV) [136, 137] is a versatile electrochemical technique used to investigate the reduction and oxidation processes of electrochemically active species. CV is a dynamic measurement in which the voltage applied on the working electrode is varied linearly with time at a given scan rate. Simultaneously, the current at the working electrode, which is basically the response of the voltage scan, is measured. A redox reaction in CV can be identified by a pair peaks (typically with currents of reverse polarity). In battery research, CV is used to obtain information about the redox potentials of different reactions, reaction intermediates, and stability of reaction products.

During this doctoral work, CV was performed on a Bio-logic potentiostat (VMP3) with a scan rate of 0.1 mV/s in the potential range of 0.01 - 3.0 V (vs Li^+/Li). CV was used to compare the redox reactions happening in different types of electrodes.

A.2.8. Raman Spectroscopy

Raman spectroscopy (RS) is named after nobel laureate C.V. Raman. In RS, the molecular vibration of the sample is studied using monochromatic light [138]. The light source is typically a laser in ultraviolet, visible, or infrared region. Upon interaction, the photons of the laser light are first absorbed by the sample and then re-emitted. RS is based on the inelastic scattering of these photons, where the energy of the absorbed (same as incident) photons is different from that of the re-emitted (scattered) ones. The difference in energy is transferred in form of an additional vibrational energy (with wavenumber $\tilde{\nu}$), as shown in Eqn. A.2.

$$\tilde{\nu} = \tilde{\nu}_i - \tilde{\nu}_s \tag{A.2}$$

where $\tilde{\nu}_i$ and $\tilde{\nu}_s$ are the wavenumbers of the incident and scattered photons, respectively. If the energy of the scattered photon is lower, then the transfer of vibrational energy happens from the incident photon to the sample, known as Stokes shift. The inverse is the anti-Stokes shift where energy transfer is from the sample to the photon. Both the shifts contains the same information, so the more intense Stokes shift is usually measured in RS. Raman shifts ($\tilde{\nu}$) are independent of the wavelength of the incident photon.

RS is versatile technique which can be used for studying variety of systems in all forms (solid, liquid or gaseous). In case of metal oxide, RS can be used to identify structural transition, local chemical environment/co-ordination, particle size effects, presence of defects (such as oxygen vacancies), etc. RS was used to study the oxygen vacancies and change in chemical environment of HEOs upon different types of thermal treatments. Depending upon the laser source the penetration depth can vary, thus information of both surface and bulk can be obtained. In this thesis two laser sources were used for RS, 633 nm and 785 nm. Measurements were done in the range of 300 – 1000 cm^{-1}, with a spot size $\sim 1\ \mu$m and laser power of 1 mW.

A.2.9. X-ray photoelectron spectroscopy

X-ray photoelectron spectroscopy (XPS) is based on the photoelectric effect, where a beam of X-rays is used as a irradiating source for ejecting photoelectrons [139]. When the incident monochromatic X-ray energy ($h\nu$) is higher than the sum of the electron binding energy (*B.E.*) and specimen work function (*W*), then electrons are ejected with a kinetic energy (*K.E.*) according to Eqn. A.3.

$$K.E. = h\nu - B.E. - W \tag{A.3}$$

In most of the cases the *W* of the specimen is unknown, thus the *W* of the analyzer is used, given the fact that sample and analyzer are in electrical contact. The *K.E.* is measured by electrostatic analyzer, while value of $h\nu$ and *W* are known. Hence, the value of element specific *B.E.* can be calculated, which helps to identify the elements present in a sample. The shift in *B.E.* is used to estimate the nature of chemical bonding or oxidation state of the elements. One of the drawback of the lab scale XPS technique is the fact that is highly surface sensitive, hence, provides information typically below 10 nm from the surface.

In this thesis[5], XPS was used to identify the oxidation states of the cations present in HEOs. XPS spectra were measured with a PHI 5000 spectrometer (Physical Electronics) using a monochromatic Al K_α radiation ($h\nu$ = 1486.6 eV). A charge neutralizer was used to minimize charging effects in the investigated HEOs.

---

[5] XPS measurements were performed by Dr. C. Loho (TU Darmstadt).

A.2.10. X-ray absorption spectroscopy

Similar to XPS, X-ray absorption spectroscopy (XAS) is also an element specific characterization technique which relies on the photoelectric effect [140]. In XAS, an incoming beam of X-ray interacts with an deep core level electron, which is promoted to an unoccupied state above the Fermi energy. The core-hole, which is formed due to the ejection, is then filled up by an higher level electron that decays to the core-hole emitting a fluorescent X-Ray or an Auger electron. Whenever the incident X-ray energy is larger than the binding energy, there is a sharp increase in the absorption.

In general, XAS follows the Beer-Lambert's law of absorption (Eqn. A.4), where I_0 is the incident X-ray, I_T is the transmitted X-ray, t is the sample thickness and μ is the absorption coefficient.

$$\mu t = ln(I_0/I_T) \tag{A.4}$$

Unlike XPS, both bulk and surface information of the sample can be obtained from XAS. Depending upon the thickness of the sample and the incident X-ray energy different kind of detection possibilities can be used, such as the transmission yield (TY) mode, fluorescence yield (FY) mode and the total electron yield (TEY) mode.

The obtained XAS spectrum can be divided into 2 regions: (a) one is X-ray near edge structure (XANES) typical spanning from 10 eV below the edge to 20 ev above the edge, and (b) the other is the extended X-ray fine structure (EXAFS) typically starting 50 eV above the edge. XANES is used to identify the oxidation state and the local symmetry/co-ordination of the selected element. Information about the unoccupied electronic density of states above the Fermi level can also be estimated using XANES. EXAFS, on the other hand, contains the information about the short-range order of the selected atom, including the identity of neighboring atoms, their distance from the selected atom and the number of neighboring atoms in the nearest shell.

In this thesis, XANES was used to identify the oxidation states of the constituent cations in HEOs. For the investigation of the RE $4f$ and the O $2p$ states, measurements were performed in the soft X-ray regime at the XUV diffractometer end station, located at the beamline UE46_PGM-1[141] (BESSY II, Berlin), while for the investigation of the RE $5d$ states, measurements in the hard X-ray regime have been performed at the beamline P65 [142] (PETRA III, Hamburg). For the measurements in the soft X-ray regime (O $2p$ and RE $4f$ states) the sample powder was pressed onto Indium foil to ensure electrical grounding, while the signal was measured in TEY. In the hard X-ray regime (RE-$5d$ edges), the sample powder was pressed into a pellet, while the absorption measurements were performed in transmission mode at 10 K.

A.2.11. Inductively coupled plasma - mass spectrometry

Inductively coupled plasma - mass spectrometry (ICP-MS) [143] is an elemental analysis technique capable of detecting most of the elements in the periodic table. As the name suggests, an inductively coupled plasma is used to ionize and fully decompose the sample (which is in liquid form). The ions are detected by a mass spectrometer attached to the setup. The main advantages of ICP-MS are the speed of the measurement and ability to detect and quantify trace elements (in the range of 0.01 to 0.1 μg/l) present in the sample. One major of disadvantages is the requirement of liquid sample, which in many cases necessitates the dissolution of solid samples in concentrated acids.

In this thesis[6], ICP-MS was used for the verification of the elemental composition of HEOs. An Agilent 7500cx ICPMS (Agilent, Santa Clara, USA) was used. For the preparation of the liquid specimen 10 mg of the HEOs was dissolved in HNO_3, which was diluted using deionized water. 10 μl of internal standard (10 mg/l scandium and holmium, respectively) was added to calibrate the time dependent sensitivity variation of the ICP-MS.

A.2.12. Ultraviolet-visible spectroscopy

Ultraviolet-visible (UV-Vis) spectroscopy (or spectrophotometry) is one of the important characterization tool for investigating optical and electronic properties of materials. Spectrophotometry is a quantitative measurement of the absorption/transmission/reflection (of a material) as a function of the wavelength of the illuminated light. One of the variation of UV-Vis spectroscopy is the diffuse reflectance spectroscopy (DRS), which is especially used for powders [144]. DRS usually is performed using an integrating sphere attached to the UV-Vis spectrophotometer. The interaction of incident light with a solid matter can result in four possibilities: (a) specular reflection, (b) absorption, (c) scattering (elastic/inelastic) and (d) diffuse reflection (used in DRS). From the obtained DRS spectra, optical band gaps are determined by applying the Tauc relation:

$$[F(R_\infty)h\nu] = A(h\nu - E_g) \tag{A.5}$$

where $F(R_\infty)$ is the Kubelka–Munk function, $h\nu$ is energy of incident light, A is a constant, and E_g is the band gap. The exponent n denotes the nature of the optical transitions. The values of $n = 1/2$ and $n = 2$ are used for determining direct and indirect allowed transitions, respectively.

In this thesis, band gap of HEOs were obtained using DRS method, which was performed using a Perkin Elmer Lambda 900 spectrophotometer.

A.2.13. Superconducting quantum interference device magnetometry

Superconducting quantum interference device (SQUID) magnetometer utilizes the Josephson effect for highly precise measurement of magnetic properties [145]. Josephson effect describes the flow of current through a Josephson junction (JJ), which consists of two superconductors separated by an insulator (weak link), through which the Cooper pairs can tunnel. In SQUID, two JJs are connected to form a superconduting ring. The number of such rings depends on the

---

[6] ICP-MS measurements were performed by Dr. C. Hein and Dr. R. Kautenburger from Saarland University.

type of the SQUID magnetometer. The electric current density through the JJ depends on the phase difference $\Delta\varphi$ of the two superconducting wave functions. The time derivative of $\Delta\varphi$ is correlated to the voltage across the weak link. The $\Delta\varphi$ is also influenced by the magnetic flux Φ passing through the superconducting ring. The magnetic flux can be converted into an electrical voltage. In the actual magnetometer, the sample (magnet) is repeatedly transported across a superconducting pick-up loop (that is connected to the SQUID) and output voltage is recorded as the function of sample position in the form of a flux profile. The magnetization of the sample is extracted by fitting the measured flux profile [146]. In a vibrating sample magnetometer (VSM) SQUID (as used in this thesis), the sample is vibrated with an optimum low frequency about a mean position where the slope of the flux profile is maximum. [147]

Temperature and magnetic field dependent measurements were performed on HEOs. For this purpose, a Quantum Design MPMS3 VSM SQUID[7] was used.

A.2.14. ^{57}Fe Mössbauer spectroscopy

Mössbauer spectroscopy (MS) is named after Nobel laureate R.L. Mössbauer. MS is an element-specific technique, which relies on recoilless emission and resonant absorption of γ-rays [148, 149]. In MS a solid sample is exposed to a beam of γ-rays, and a detector measures the intensity of the beam transmitted through the sample. The source of γ-rays is oscillated, hence the γ-rays reaching the absorber (i.e., the sample) is Doppler shifted. Whenever, this Doppler shifted energy of the γ-rays matches the energy of a nuclear transition in the sample it results in a resonant absorption (indicated by a peak in MS plot) [148].

Mössbauer active ^{57}Fe is a natural isotope which is around 2.2% of total Fe. ^{57}Co is used as source for ^{57}Fe MS. ^{57}Fe MS is an efficient technique for studying chemical, structural and magnetic environment of Fe in a sample. Depending upon the local environment of Fe, different types of nuclear interactions are possible [148, 150]. For instance, Fe in a magnetic environment leads to hyperfine splitting which is characterized by a sextet, Fe in a non-magnetic environment (which is centrosymmetric) results in a singlet, while non-magnetic Fe in a non-centrosymmetric environment leads to quadrupole doublet. In addition, depending upon the chemical surrounding and oxidation state of Fe, shift of the spectral lines can occur, which is known as the isomer shift.

In this thesis[8], ^{57}Fe MS was carried out in transmission mode using a ^{57}Co:Rh source. HEOs containing Fe were probed with MS to identify the magnetic and chemical environment around Fe.

---

[7] SQUID measurements were performed by Dr. R. Witte (KIT).

[8] MS measurements were performed by Dr. R. Witte (KIT).

B. Supplementary material

B.1. Supplementary information for Sec. 3.2

Supplementary Information
High entropy oxides for reversible energy storage
A. Sarkar et al

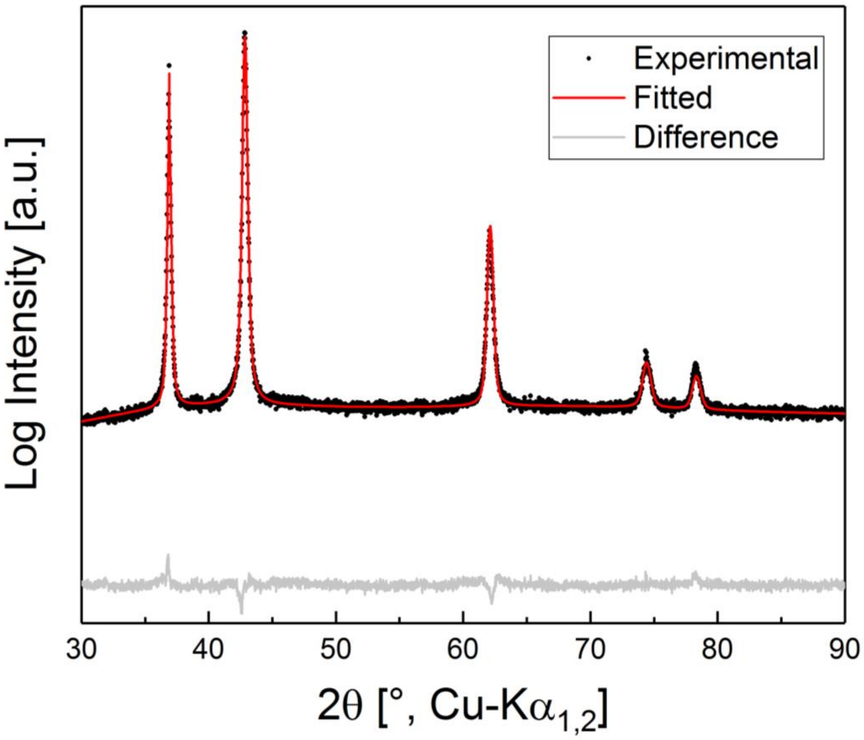

Supplementary Figure 1: Powder XRD pattern together with the corresponding Rietveld fit for TM-HEO. The goodness of fit and R_{wp} values are 1.06 and 1.39, respectively. Single phase rock-salt structure with lattice parameter of 4.2330(6) Å and average crystallite size of 36(5) nm is observed.

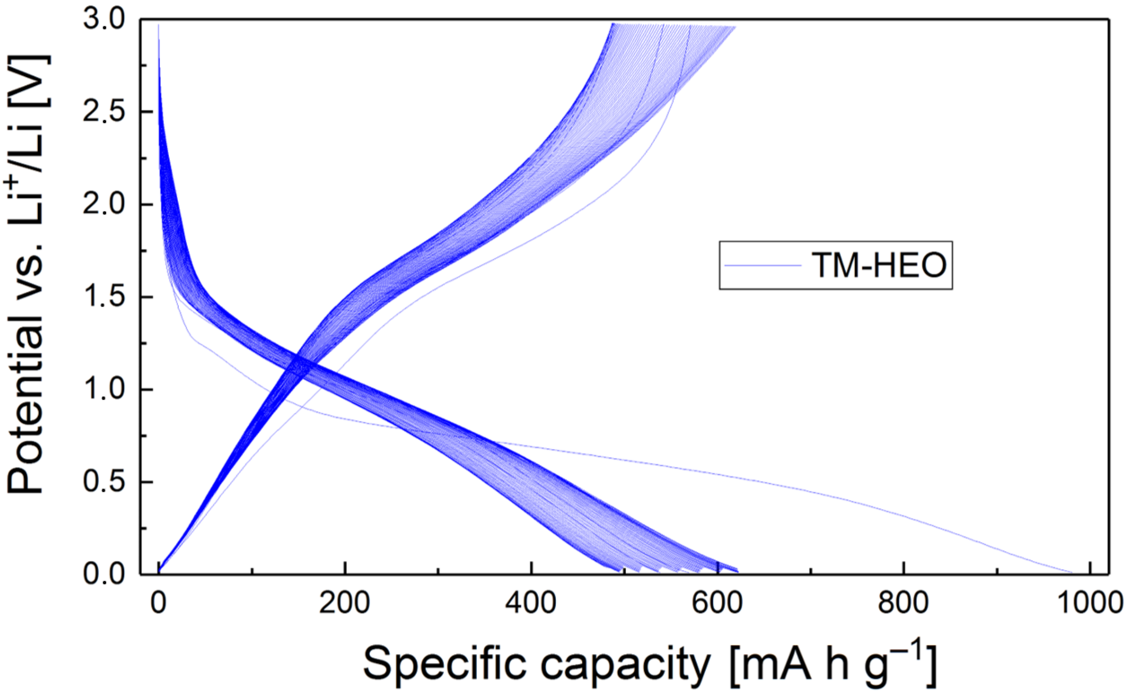

Supplementary Figure 2: First 70 voltage profiles of TM-HEO electrode operated at a current density of 200 mA/g between 0.01 and 3.0 V.

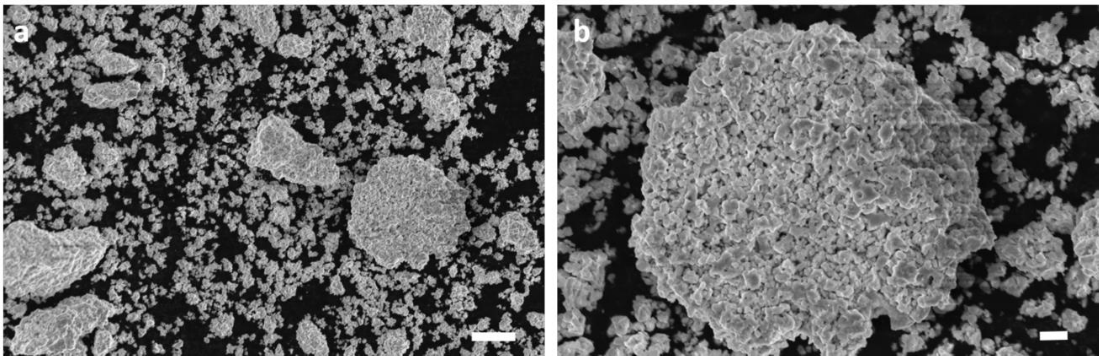

Supplementary Figure 3: SEM micrographs of sintered TM-HEO. The particles are agglomerated and larger in size. Many of the agglomerates even exceed several tens of micrometers. The scalebars are corresponding to 10 µm and 2 µm for a) and b) respectively.

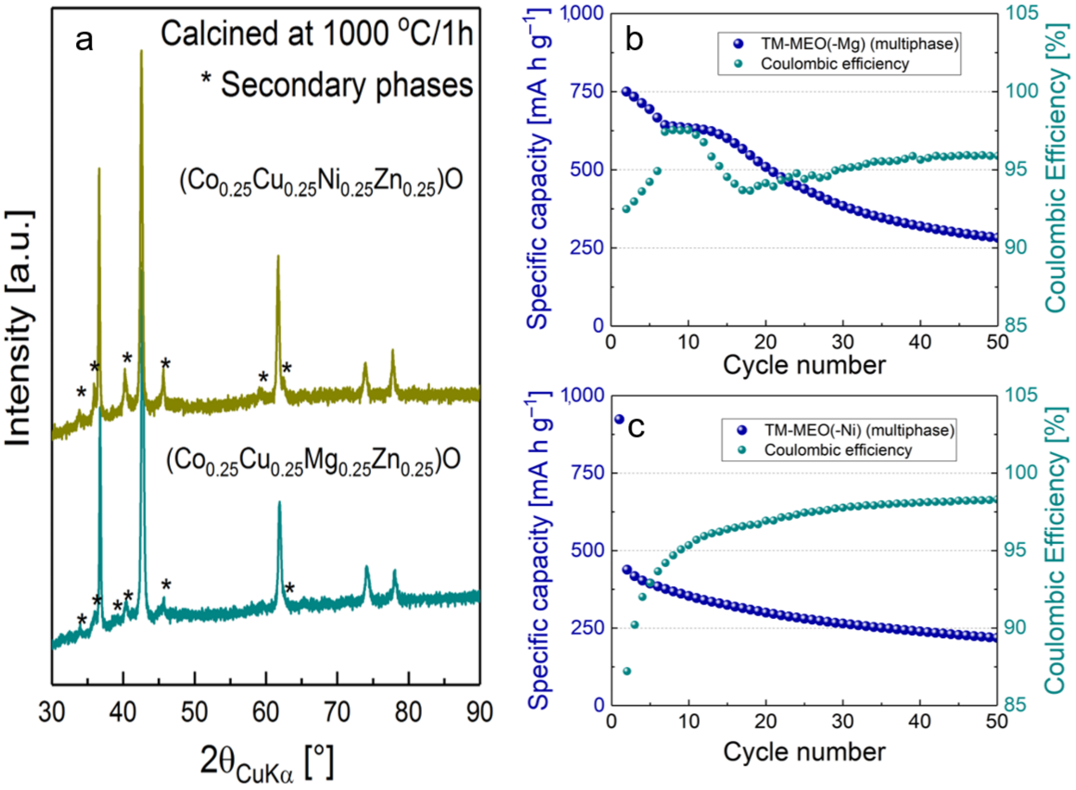

Supplementary Figure 4: Structural and electrochemical comparison of the multiphase compounds. In a) XRD patterns of multiphase compounds TM-MEO(-Ni) and TM-MEO(-Mg) are shown. These materials could not be synthesized as single phase compounds. The corresponding electrochemical characterization is shown in panels b) and c), respectively.

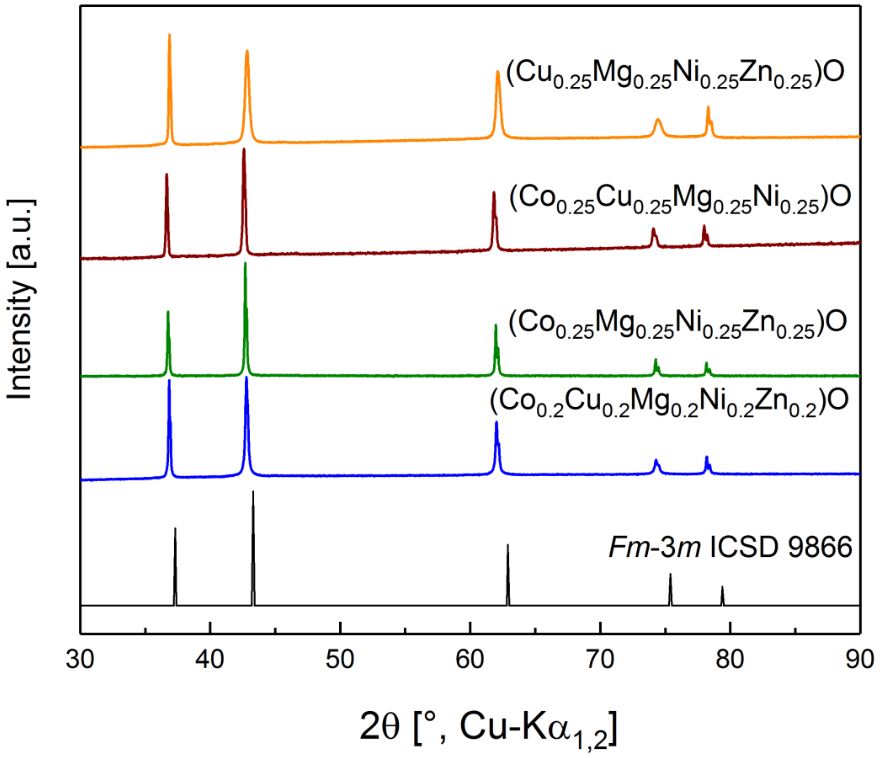

Supplementary Figure 5: Powder XRD pattern of the different materials synthesized. All of them crystallize into a single phase rock-salt structure.

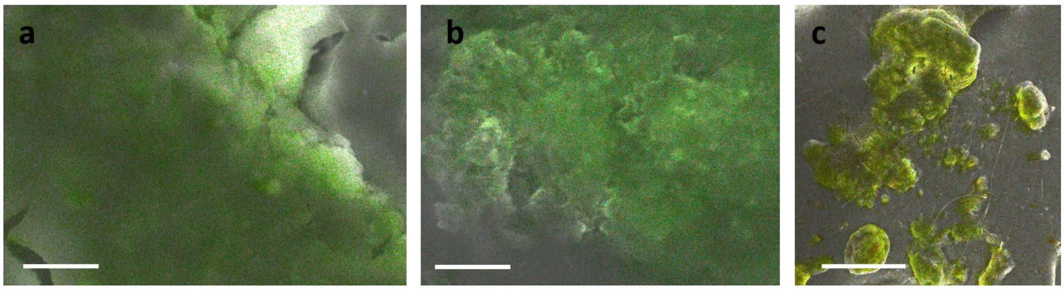

Supplementary Figure 6: EDX measurements performed on an electrode after 100 cycles. No Cu aggregation nor dendrite formation are observed. The green layer in a) and b) shows the Cu distribution. The homogenous coloring indicates that no dendrites have formed, which would appear as a higher local color intensity. In c) besides Cu (green), Ni (yellow) has been added to show the equal distribution of the different elements. The scalebars correspond to 25 µm, 10 µm and 250 µm in a, b and c respectively.

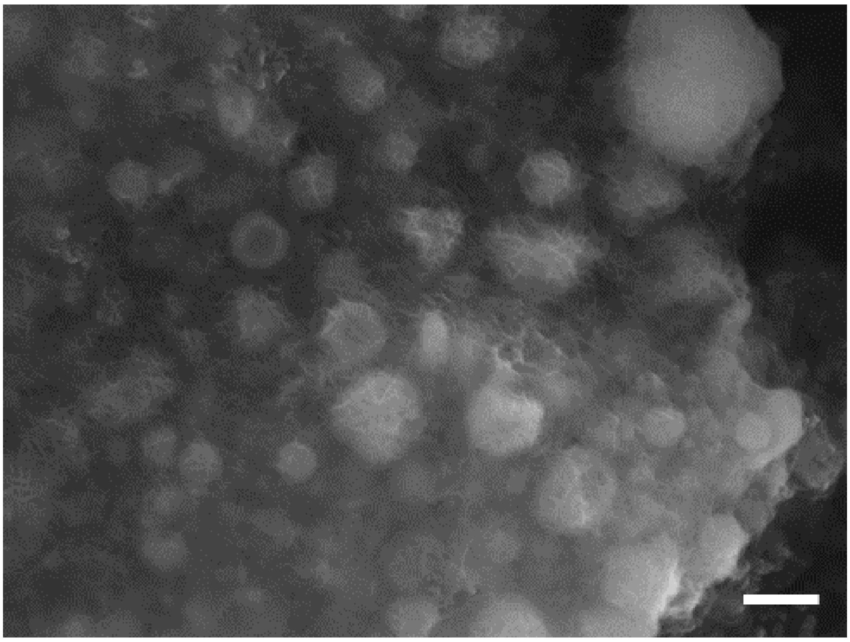

Supplementary Figure 7: SEM micrograph of the TM-HEO after several cycles, confirming that the overall morphology is maintained during cycling. This is in contrast to the typical pulverization observed for conversion-type electrodes. Scanning electron microscopy (SEM) was performed using a ZEISS Gemini Leo 1530. The scalebar corresponds to 1 µm.

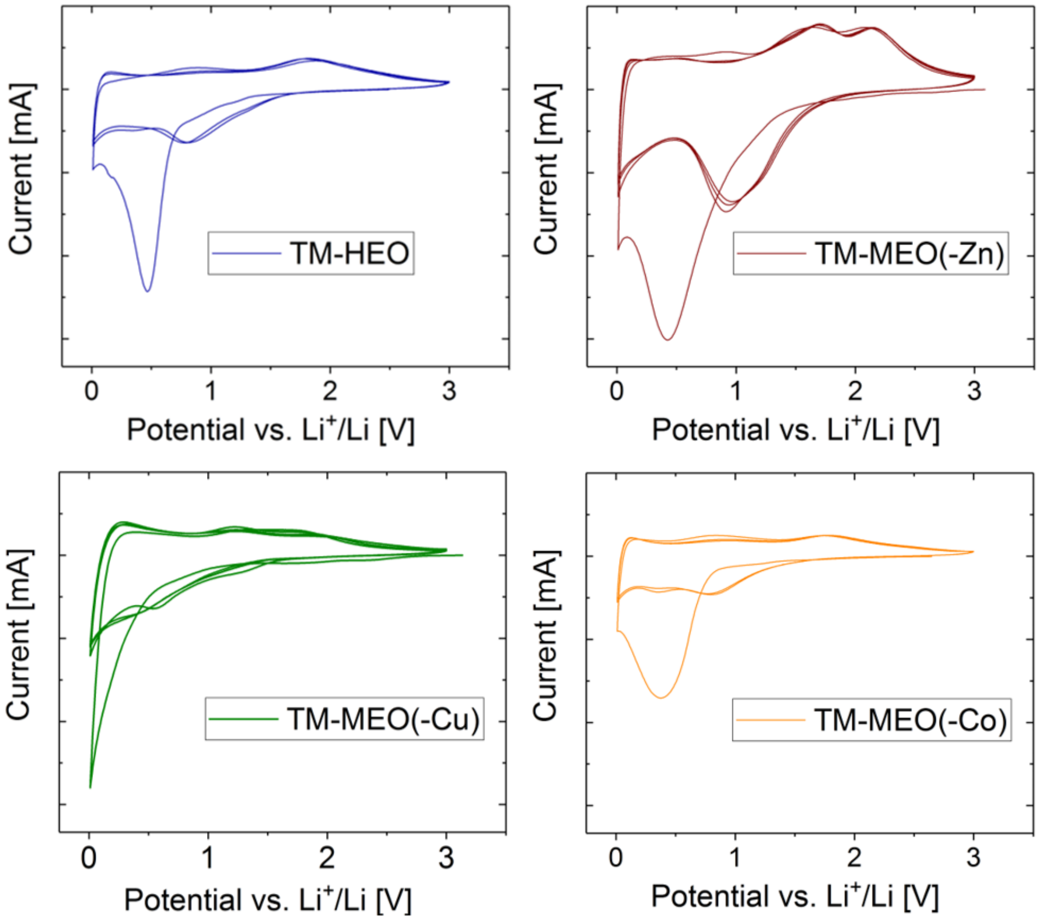

Supplementary Figure 8: Cyclic voltammograms obtained on the different single phase compounds. The curves reveal the difference in electrochemical behavior of the HEO compared to MEO. For TM-MEO(-Zn), the two anodic peaks centered around 1.7 V and 2.2 V indicate formation of NiO and CoO, respectively[2]. In the case of TM-MEO(-Cu), a distinct reduction peak at low potential appears[3].

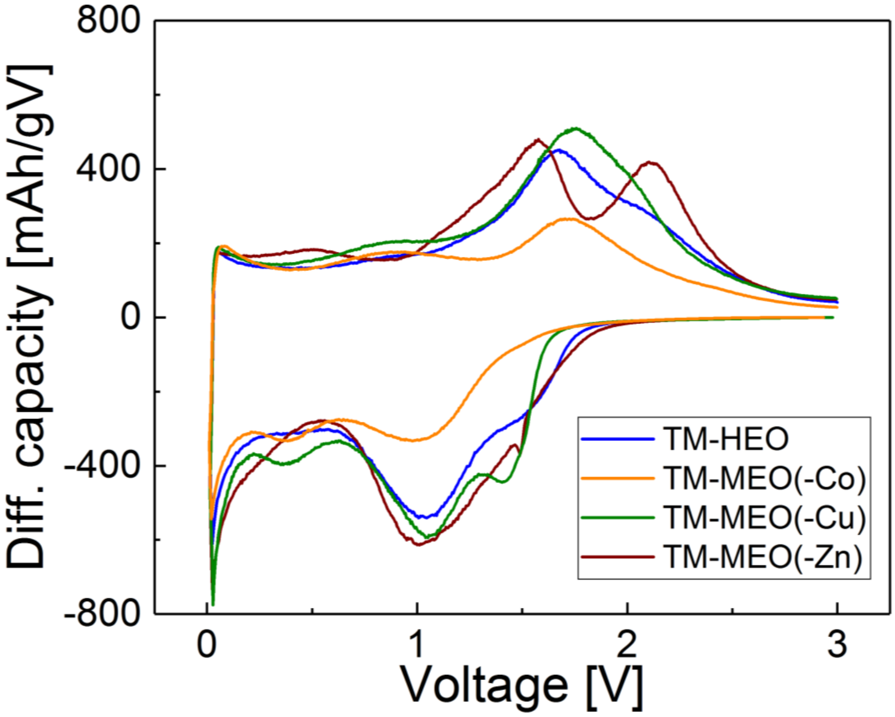

Supplementary Figure 9: Differential capacity plots for TM-HEO and the different TM-MEO compounds. It is evident that every single element has its own specific effect on the redox processes.

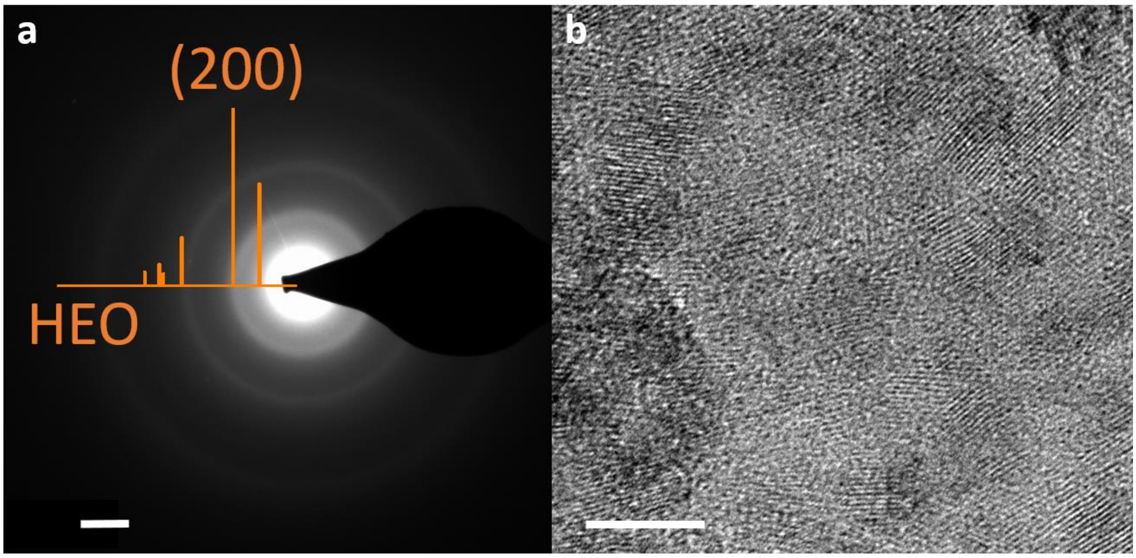

Supplementary Figure 10: TEM characterization. The SAED pattern of an electrode after 10 cycles is shown in (a), where the rock-salt structure is clearly observable. As shown, the rock-salt structure is retained, even after prolonged cycling. The presence of crystallites is clearly evident in the HR-TEM micrograph in (b). The scalebar in a) corresponds to 2 1/nm and in (b) to 5 nm.

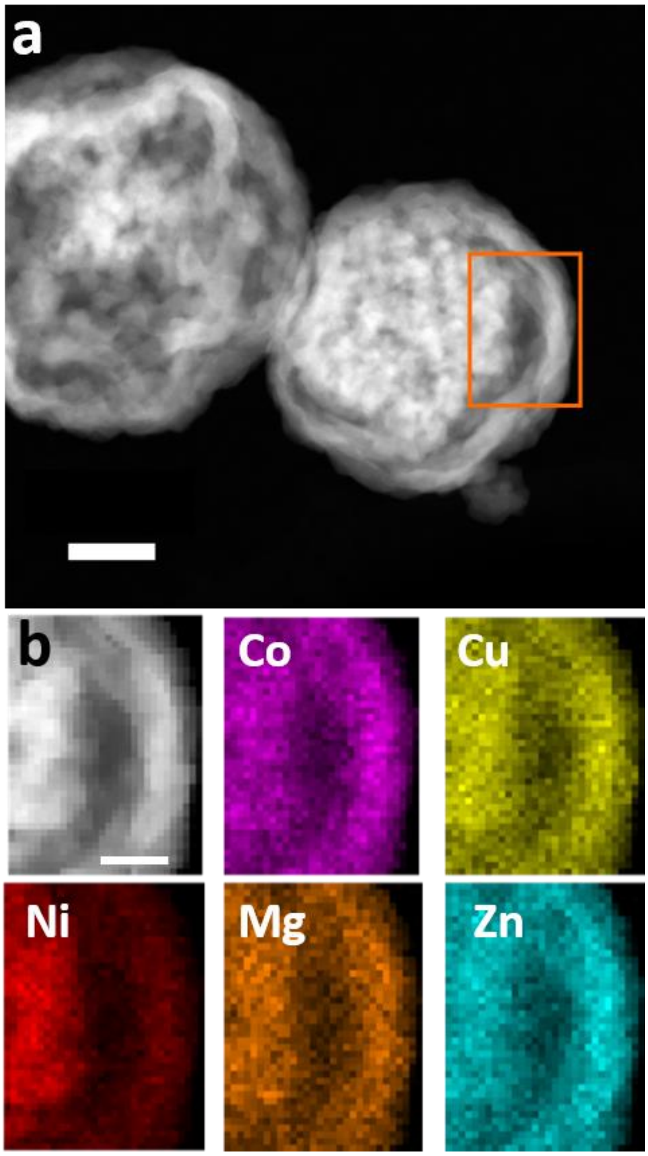

Supplementary Figure 11: STEM-EDX imaging of the as-prepared sample (orange rectangle). The scalebars in (a) and (b) correspond to 100 nm and 50 nm respectively.

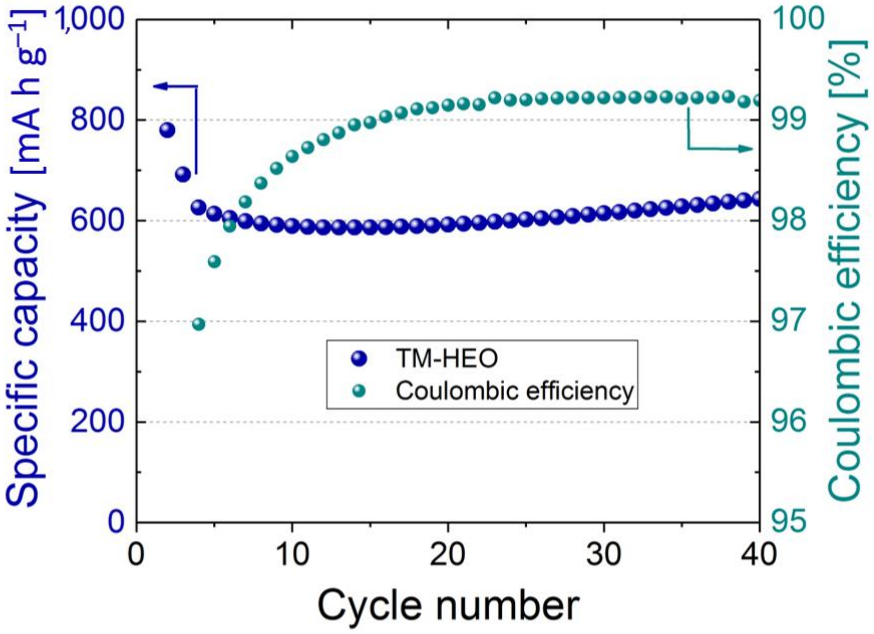

Supplementary Figure 12: Capacity retention and Coulombic efficiency of an electrode with a relatively high TM-HEO content (TM-HEO:binder:carbon black ratio of 80:10:10). The current density applied was 200 mA g^{-1}.

Supplementary Notes

The different intensity in the SAED rings displayed in Figure 3, come from a slightly different thickness of crystallites in the SAED area. The main intention to show these SAED rings is, to support the finding that a rock-salt structure is being preserved through the whole cycling process. Therefore Supplementary Figure 11a shows an SAED pattern of a 10 times cycled electrode, where it is clearly observable that the rock-salt structure can be found even after such a prolonged cycling. The nanometer-sizedcrystallites could be clearly identified in HR-TEM micrographs as can be seen in b.

Supplementary Equation 1 was used for the calculation of the theoretical capacity:

$$Q_\mathrm{m} = \frac{z*F}{M} \qquad (1)$$

Q_m represents the theoretical capacity, z the number of transferred electrons, F the Faraday constant, and M is the molar mass of the active material. The specific capacity for compounds of almost the same molecular weight and redox state is very similar (e.g. Q_m(CoO) ≈ Q_m(NiO) ≈ 715 mAh g^{-1}).

Supplementary Equation 2 was used for the calculation of the configurational entropy:

$$S_\mathrm{config} = -R[(\sum_{\mathrm{i}=1}^{\mathrm{N}} x_\mathrm{i} \ln x_i)_\mathrm{cation-site} + (\sum_{\mathrm{j}=1}^{\mathrm{N}} x_\mathrm{j} \ln x_\mathrm{j})_\mathrm{anion-site}] \qquad (2)$$

Example for TM-HEO with equimolar amount of different cations (5 cations → $x_\mathrm{j} = 0.2$):

S_config = –R(((0.2 ln 0.2) + (0.2 ln 0.2) + (0.2 ln 0.2) + (0.2 ln 0.2) + (0.2 ln 0.2))$_\mathrm{cation\text{-}site}$ + (1 ln 1)$_\mathrm{anion–site}$)
S_config = –R(5 * (0.2 ln 0.2)) = 1.61R
For the TM-MEO
S_config = –R(4 * (0.25 ln 0.25)) = 1.39 R

Supplementary Method

Room temperature powder X-ray diffraction patterns were recorded using a Bruker D8 Advance diffractometer with a Cu-Kα radiation source and a LYNEXE detector having a fixed divergence slit (0.3°). Rietveld analysis (TOPAS 5, Bruker[1]) of the XRD pattern was performed to determine the crystal structure and phase composition of the as-synthesized and thermally treated powders using the structural file of NiO (Fm-3m, ICSD 9866), which was modified according to the number and type of elements present in the refined system. The instrumental intensity distribution for the XRD data was determined using LaB_6 (NIST 660a) as a reference material. Thermal displacement parameters were constrained to be equal for all the atoms.

Supplementary References

1. *Topas V5, General profile and structure analysis software for powder diffraction data, User's Manual*. (Bruker AXS, 2015).

2. Wang, Y. F. & Zhang, L. J. Simple synthesis of CoO-NiO-C anode materials for lithium-ion batteries and investigation on its electrochemical performance. *J. Power Sources* **209,** 20–29 (2012).

3. Mueller, F. *et al.* Iron-Doped ZnO for Lithium-Ion Anodes: Impact of the Dopant Ratio and Carbon Coating Content. *J. Electrochem. Soc.* **164,** A6123–A6130 (2017).

B.2. Supplementary information for Sec. 4.1

Electronic Supplementary Material (ESI) for Dalton Transactions.

Supporting Information

Multicomponent equiatomic rare earth oxides with narrow band gap and associated praseodymium multivalency

Abhishek Sarkar,[1,2] Christoph Loho,[2] Leonardo Velasco,[1] Tiju Thomas,[3] Subramshu S. Bhattacharya,[3] Horst Hahn,[1,2,4] and Ruzica Djenadic[2,4,†]*

[1]Institute of Nanotechnology, Karlsruhe Institute of Technology, Hermann-von-Helmholtz-Platz 1, 76344 Eggenstein-Leopoldshafen, Germany

[2]Joint Research Laboratory Nanomaterials – Technische Universität Darmstadt and Karlsruhe Institute of Technology, Alarich-Weiss-Str. 2, 64287 Darmstadt, Germany

[3]Department of Metallurgical and Materials Engineering, Indian Institute of Technology Madras, Chennai-600036, India

[4]Helmholtz Institute Ulm – Electrochemical Energy Storage, Helmholtzstr. 11, 89081 Ulm, Germany

*Corresponding author: abhishek.sarkar@kit.edu, horst.hahn@kit.edu

Table S1. Summary of results obtained from the Rietveld refinement of as-synthesized ME-REOs: fraction of main phase, i.e., fluorite (*f*), lattice parameter (*a*), and crystallite size (*D*).

Oxides	*f* [wt. %]	*a* [Å]	*D* [nm]
As-synthesized, ($Fm\bar{3}m$)			
CeO_2	100	5.4135(1)	15.7(3)
$(Ce,Pr)O_{2-\delta}$	100	5.4392(3)	6.8(1)
$(Ce,La,Pr)O_{2-\delta}$	100	5.5203(2)	10.5(2)
$(Ce,La,Pr,Y)O_{2-\delta}$	100	5.4962(3)	6.8(2)
$(Ce,La,Pr,Sm)O_{2-\delta}$	100	5.5276(3)	7.8(2)
$(Ce,La,Pr,Sm,Y)O_{2-\delta}$	100	5.5071(4)	7.5(2)
$(Ce,La,Nd,Pr,Sm,Y)O_{2-\delta}$	100	5.4998(1)	–[a]
$(Ce,Gd,La,Nd,Pr,Sm,Y)O_{2-\delta}$	97.1	5.5168(4)	–[a]
Calcined, ($Ia\bar{3}$)			
$(Ce,La,Pr,Sm,Y)O_{2-\delta}$	100	10.9567(2)	28.8(7)
$(Ce,La,Nd,Pr,Sm,Y)O_{2-\delta}$	100	10.9319(3)	31.0(1)
$(Ce,Gd,La,Nd,Pr,Sm,Y)O_{2-\delta}$	100	10.9625(2)	34.0(2)

[a]*main contribution to peak broadening arises from strain*

Oxidation state of Pr and lattice parameter variation with respect to cationic radii. Figure S1 shows variation of the lattice parameters of the different multicomponent equiatomic rare earth oxides (ME-REOs) with respect to average cationic radii, *r*, which is calculated by taking an average of the ionic radii[1] of all the cations, considering their oxidation (either 3+ or 4+) state and coordination number (8). The values of the average cationic radii of all the ME-REO systems are given in Table S2. The changes in the lattice parameter are often linearly related to the average cationic size (which is dependent on the valence state) in accordance with Vegard's law. The same trend is also observed in ceria based (or related) systems.[2] Conversely, the average radii of the cations (and hence, their valence state) can also be deduced if the variation of the lattice parameter is known. In order to get a better picture regarding the actual oxidation state of Pr three cases are considered: (a) Pr is considered to be in only 4+ state, (b) Pr is considered to in a mixed 3+/4+ oxidation state with ratio of 3+ to 4+ is same as in Pr_6O_{11} and (c) where Pr is considered to be in only 3+ state. The oxidation state of all the other cations are kept constant, i.e., Ce^{4+}, Gd^{3+}, La^{3+}, Nd^{3+}, Sm^{3+}, Y^{3+}. From the Fig S1 (a) – (c), it can clearly be seen that

Vegard's law, i.e., a linear trend is followed only in case (b) where Pr is assumed to be in a mixed oxidation state. This result is in good agreement with the XPS result and hence, it can be stated that Pr is a multivalent state with Pr^{3+}: Pr^{4+} ratio being same as in Pr_6O_{11}, i.e., 1: 2.

Table S2. Values of the average cationic radii of ME-REOs where in (a) Pr is considered only in 4+ state (b) Pr is in multivalent (3+/4+) state with Pr^{3+} : Pr^{4+} is 1 : 2 (c) Pr is in only 3+ state.

Oxides	Average cationic radii, *r*, [Å]		
	Case (a)	Case (b)	Case (c)
CeO_2	0.970	0.970	0.970
$(Ce,Pr)O_{2-\delta}$	0.965	1.050	0.993
$(Ce,La,Pr)O_{2-\delta}$	1.019	1.075	1.042
$(Ce,La,Pr,Y)O_{2-\delta}$	1.042	1.085	1.056
$(Ce,La,Pr,Sm)O_{2-\delta}$	1.025	1.067	1.037
$(Ce,La,Pr,Sm,Y)O_{2-\delta}$	1.036	1.070	1.048
$(Ce,La,Nd,Pr,Sm,Y)O_{2-\delta}$	1.039	1.067	1.043
$(Ce,Gd,La,Nd,Pr,Sm,Y)O_{2-\delta}$	1.037	1.061	1.055

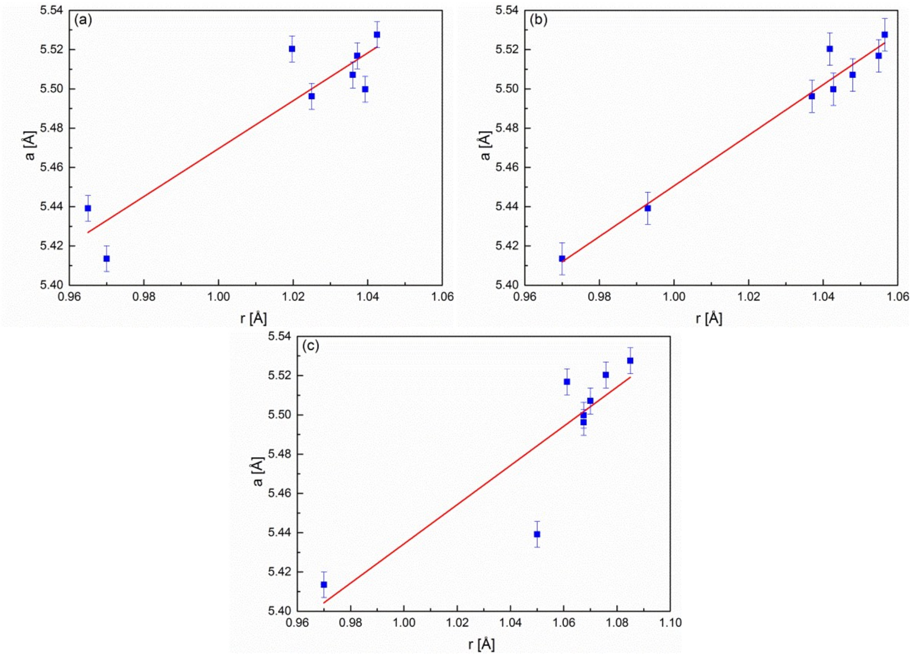

Figure S1. Variation in lattice parameters of different ME-REOs as a function of average cationic radii where Pr is considered to be only in 4+ oxidation state in (a), in a mixed (3+,4+) oxidation state (b) and only in 3+ oxidation state (c).Vegard's law is followed only in case (b).

ME-REOs without Pr. Three ME-REO systems without Pr are synthesized under the same conditions that are used for the synthesis of ME-REOs with Pr. The XRD patterns of these three systems are shown in Figure S2a. Two of the systems (Ce,La,Sm)$O_{2-\delta}$ and (Ce,La,Sm,Y)$O_{2-\delta}$ crystallize as single phase fluorite type structure with lattice parameters 5.5457(0) Å and 5.5144(0) Å, respectively. In other systems, containing 5 cations (Ce,La,Nd,Sm,Y)$O_{2-\delta}$, a small amount (~ 4.5 wt. %) of secondary La_2O_3 type phase alongside the main fluorite type phase (a = 5.5232(1) Å) is observed. Except for Ce all the RE elements in these three systems are expected to be in 3+ oxidation state justifying the selection of the non-stoichiometric formula. All the systems show strong absorption only below 450 nm and the direct band gap are in the range of 2.91 – 3.04 eV (see Figure S2b). The difference in the band gap between these systems and ceria is around 0.30 – 0.15 eV which can be because of the presence of oxygen vacancies in these systems.

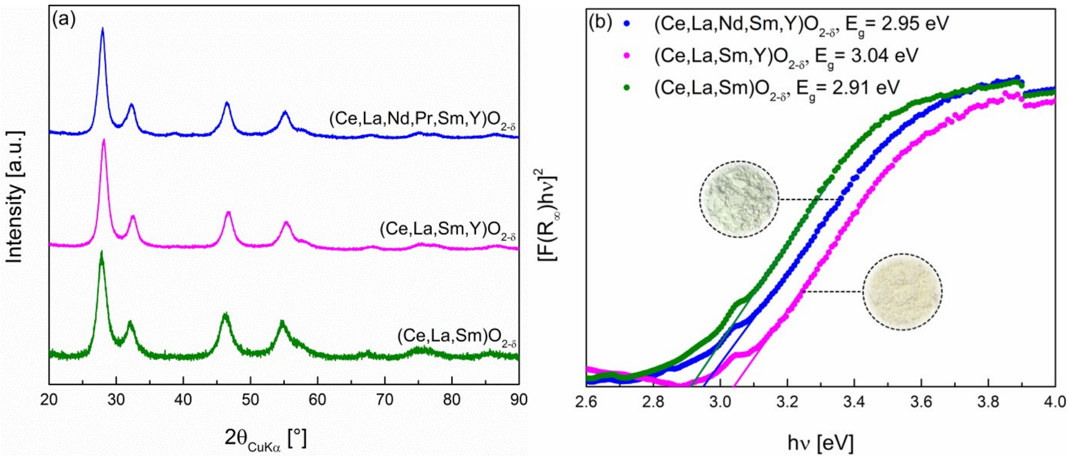

Figure S2. XRD patterns (a) and Tauc plots (b) for ME-REOs without Pr. The XRD pattern confirms the phase purity of the systems while the Tauc plots show that the band gap of these ME-REOs without Pr are in the range of 2.91 – 3.04 eV.

References

(1) Shannon, R. D. Revised Effective Ionic Radii and Systematic Studies of Interatomic Distances in Halides and Chalcogenides. *Acta Crystallogr. Sect. A* **1976**, *32* (5), 751–767.

(2) Omar, S.; Wachsman, E. D.; Nino, J. C. Higher Conductivity Sm3+ and Nd3+ Co-Doped Ceria-Based Electrolyte Materials. *Solid State Ionics* **2008**, *178* (37–38), 1890–1897.

B.3. Supplementary information for Sec. 4.2

Role of intermediate 4f states in tuning the band structure of high entropy oxides

Abhishek Sarkar,[1,2,a] Benedikt Eggert,[3] Leonardo Velasco,[2] Xiaoke Mu,[2] Johanna Lill,[3] Katharina Ollefs,[3] Subramshu S. Bhattacharya,[4] Heiko Wende,[3] Robert Kruk,[2] Richard A. Brand,[2,3] and Horst Hahn[1,2,b]

[1] *Joint Research Laboratory Nanomaterials – Technische Universität Darmstadt and Karlsruhe Institute of Technology, Otto-Berndt-Str. 3, 64287, Darmstadt, Germany*

[2] *Institute of Nanotechnology, Karlsruhe Institute of Technology, Hermann-von-Helmholtz-Platz 1, 76344 Eggenstein-Leopoldshafen, Germany*

[3] *Faculty of Physics and Center for Nanointegration Duisburg-Essen (CENIDE), University of Duisburg-Essen, Lotharstr. 1, 47057 Duisburg, Germany*

[4] *Nano Functional Material Technology Centre (NFMTC), Department of Metallurgical and Materials Engineering, Indian Institute of Technology Madras, 600036 Chennai, India*

Additional information to the main manuscript is compiled in this supplementary material. It includes the Rietveld refinements of the XRD patterns, TEM-EDS maps, Raman spectra (of vacuum heat treated F-HEO and bixbyite HEO) and X-ray absorption spectra of La and Sm L_3 edges.

---

[a] Electronic mail: abhishek.sarkar@kit.edu

[b] Electronic mail: horst.hahn@kit.edu

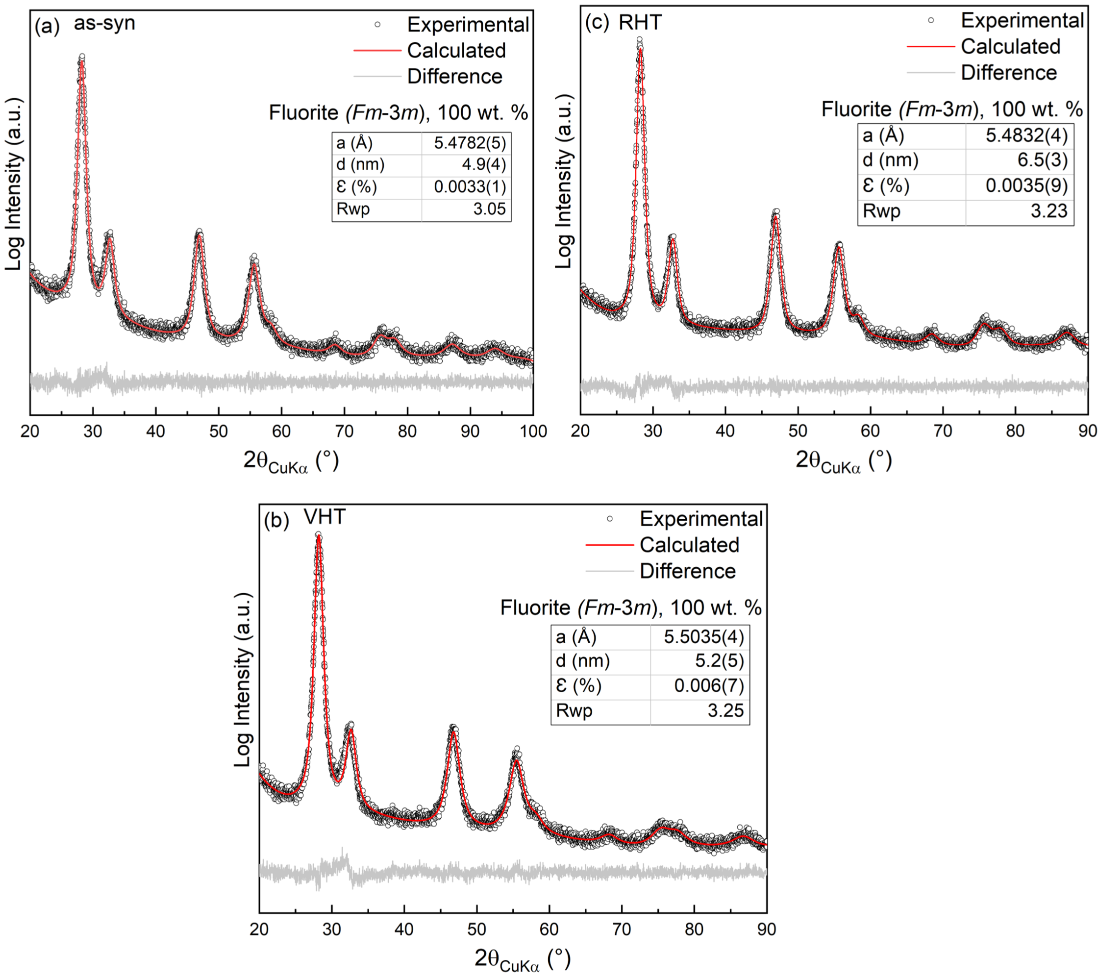

Figure SI1. Rietveld refinement of the XRD patterns (a) as-synthesized (b) vacuum heat treated (VHT) (c) reheat treated (RHT). The 4*a* site refined using equal occupation of all the cations.

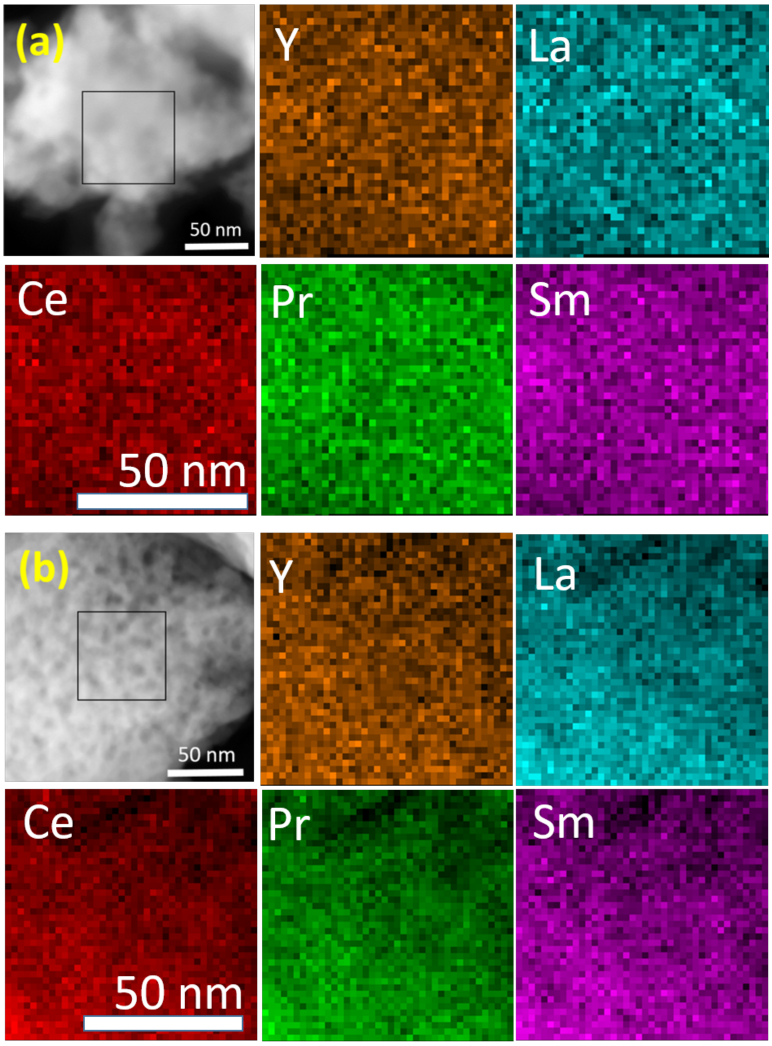

Figure SI2. Homogeneous distribution of the constituent elements of the (a) as-synthesized and (b) VHT samples was confirmed from STEM-EDS.

I. RAMAN SPECTROSCOPY OF F-HEO: VHT

In the Raman spectra (Figure SI3), two characteristics bands centered at ~452 cm^{-1} and ~570 cm^{-1} can be observed for all three variants of F-HEO (as-synthesized, vacuum heat treated (VHT) and air reheat treated (RHT)), where the latter corresponds to the presence of oxygen vacancies[1,2]. Irrespective of the heat treatment La, Sm and Y are present in 3+ oxidation state, hence oxygen vacancies (V_O) is observed in all the three variants of F-HEO. However, a shift of the center of the the V_O band along with it change in relative intensity can be observed upon VHT, which indicate an increase in 3+ cation or more V_O. The ratio of the integral intensity of the V_O band (A_{V_O}) to the integral intensity of the F_{2g} vibrational mode ($A_{F_{2g}}$) portrays the relative oxygen vacancy concentration. The inset in Figure SI3 displays the relatively amount of oxygen vacancies (i.e., $A_{V_O}/A_{F_{2g}}$), which is higher in VHT system, while as-synthesized sample and the RHT sample exhibit comparable amount of oxygen vacancies.

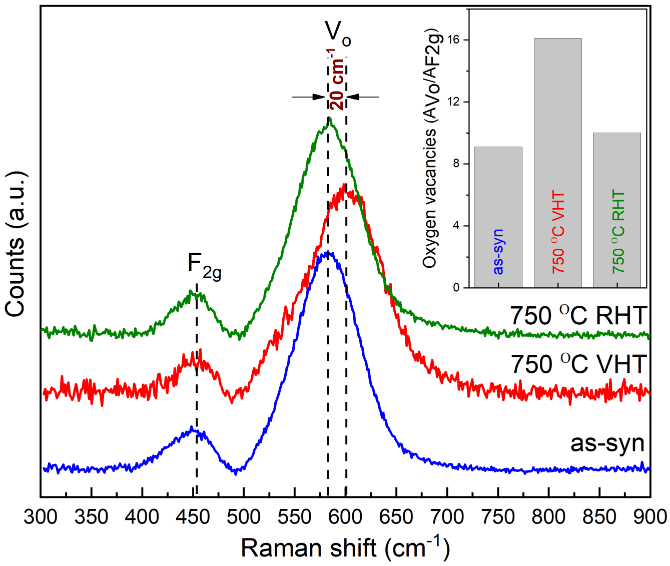

Figure SI3. Raman spectra of the F-HEO $(Ce_{0.2}La_{0.2}Pr_{0.2}Sm_{0.2}Y_{0.2})O_{2}$-$\delta$ obtained using a 785 nm excitation source. The F_{2g} vibration mode lies at 452 cm^{-1}. An additional broad band (~580 cm^{-1}) is observed for the different heat treatments, which is related to the oxygen vacancies (Vo) present in the structure. The inset displays the ratio of $A_{V_O}/A_{F_{2g}}$, which indicates that the amount of oxygen vacancies increases for the VHT sample.

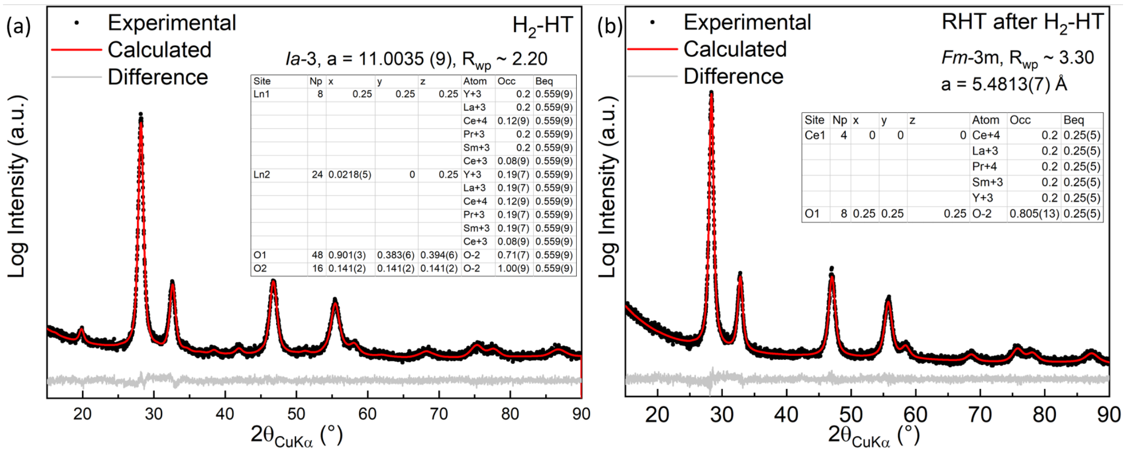

Site	Np	x	y	z	Atom	Occ	Beq
Ln1	8	0.25	0.25	0.25	Y+3	0.2	0.559(9)
					La+3	0.2	0.559(9)
					Ce+4	0.12(9)	0.559(9)
					Pr+3	0.2	0.559(9)
					Sm+3	0.2	0.559(9)
					Ce+3	0.08(9)	0.559(9)
Ln2	24	0.0218(5)	0	0.25	Y+3	0.19(7)	0.559(9)
					La+3	0.19(7)	0.559(9)
					Ce+4	0.12(9)	0.559(9)
					Pr+3	0.19(7)	0.559(9)
					Sm+3	0.19(7)	0.559(9)
					Ce+3	0.08(9)	0.559(9)
O1	48	0.901(3)	0.383(6)	0.394(6)	O-2	0.71(7)	0.559(9)
O2	16	0.141(2)	0.141(2)	0.141(2)	O-2	1.00(9)	0.559(9)

Site	Np	x	y	z	Atom	Occ	Beq
Ce1	4	0	0	0	Ce+4	0.2	0.25(5)
					La+3	0.2	0.25(5)
					Pr+4	0.2	0.25(5)
					Sm+3	0.2	0.25(5)
					Y+3	0.2	0.25(5)
O1	8	0.25	0.25	0.25	O-2	0.805(13)	0.25(5)

Figure SI4. Rietveld fit confirming the structural transition to (a) bixbyite structure upon H_2-HT of F-HEO followed by reversal to (b) fluorite structure upon subsequent RHT in air.

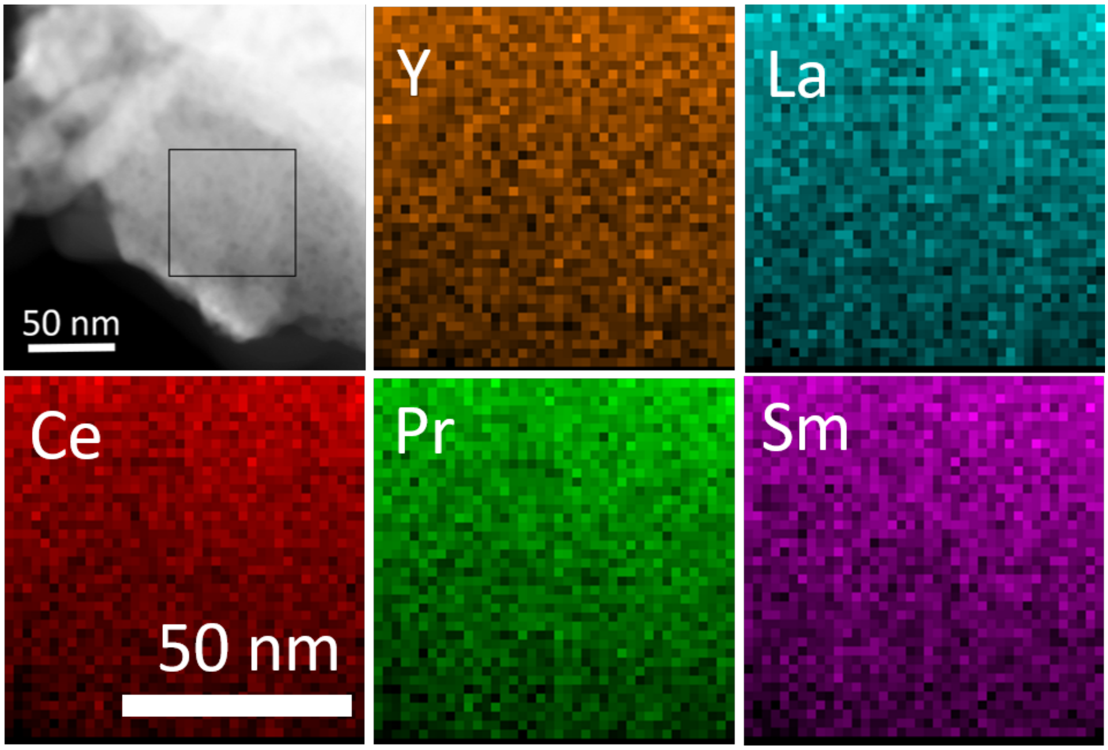

Figure SI5. Homogeneous distribution of the constituent elements of the H_2-HT sample was confirmed from STEM-EDS.

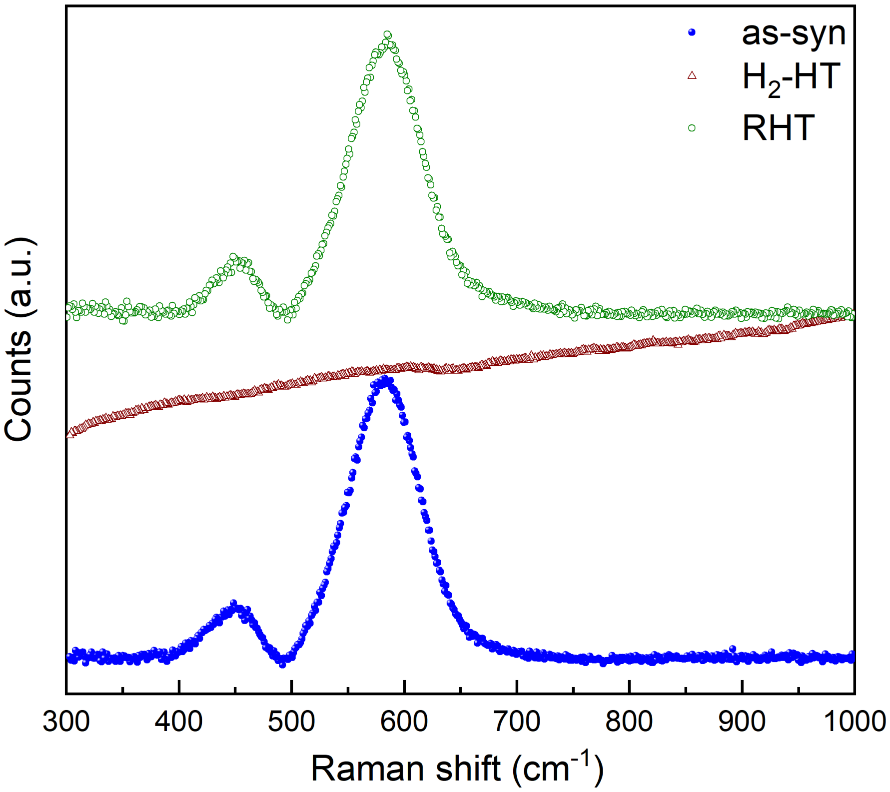

Figure SI6. H_2-HT sample seems to Raman inactive when probed with infrared (785 nm) laser.

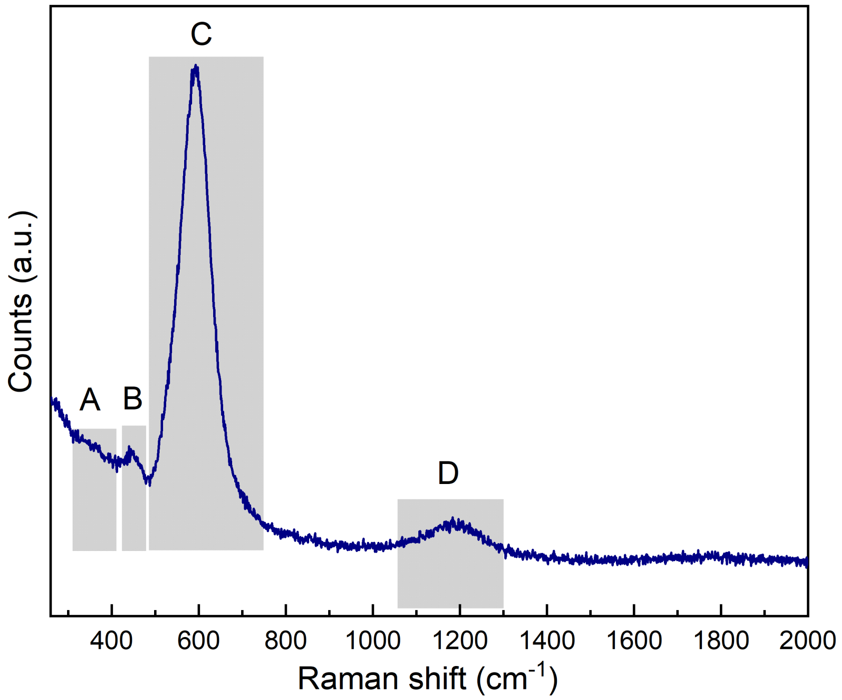

Figure SI7. Raman spectra, using 532 nm laser, of the bixbyite type $(Ce_{0.2}La_{0.2}Pr_{0.2}Sm_{0.2}Y_{0.2})O_{2-\delta}$. The bands at 358 cm^{-1}, 451 cm^{-1}, 580 cm^{-1} and 1180 cm^{-1} can be identified (as mentioned in main text). However, the bands at 1338 cm^{-1} and 1610 cm^{-1}, which can be seen in bixbyite variant formed upon H_2-HT, are not observed

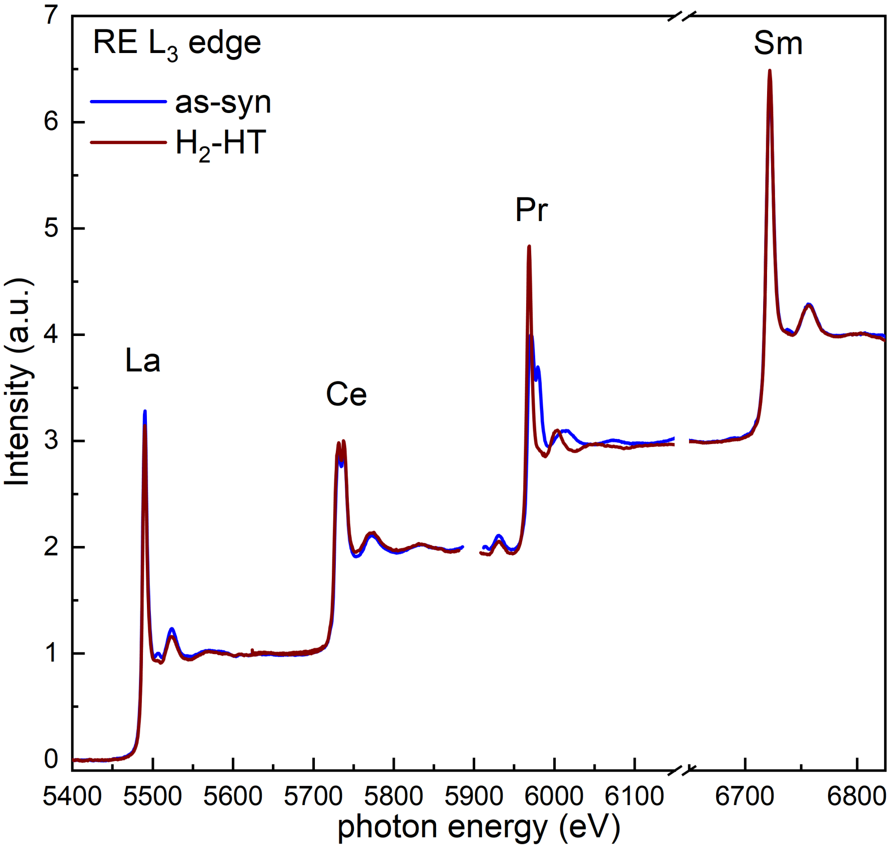

Figure SI8. XAS spectra of RE L_3 edges for the as-synthesized and H_2-heat treated sample. The peak for $E = 5930$ eV originates from the La L_2 edge.

REFERENCES

[1]M. Guo, J. Lu, Y. Wu, Y. Wang, and M. Luo, Langmuir **27**, 3872 (2011).

[2]A. Filtschew, K. Hofmann, and C. Hess, Journal of Physical Chemistry C **120**, 6694 (2016).

B.4. Supplementary information for Sec. 5.1

Supplementary Information

Rare earth and transition metal based entropy stabilized perovskite type oxides

Abhishek Sarkar,[a,b] Ruzica Djenadic,[b,c,†] Di Wang,[a,d] Christina Hein,[e] Ralf Kautenburger,[e]*
Oliver Clemens,[a,f] and Horst Hahn,*[a,b,c]*

[a]Institute of Nanotechnology, Karlsruhe Institute of Technology, Hermann-von-Helmholtz-Platz 1, 76344 Eggenstein-Leopoldshafen, Germany

[b]Joint Research Laboratory Nanomaterials – Technische Universität Darmstadt and Karlsruhe Institute of Technology, Alarich-Weiss-Str. 2, 64287 Darmstadt, Germany

[c]Helmholtz Institute Ulm – Electrochemical Energy Storage, Helmholtzstr. 11, 89081 Ulm, Germany

[d]Karlsruhe Nano Micro Facility, Karlsruhe Institute of Technology, Hermann-von-Helmholtz-Platz 1, 76344 Eggenstein-Leopoldshafen, Germany

[e]WASTe Group, Inorganic Chemistry, Saarland University, Campus Dudweiler, Am Markt Zeile 5, D-66125 Saarbrücken, Germany

[f]Materials Design by Synthesis Group, Technische Universität Darmstadt, Alarich-Weiss-Str. 2, 64287 Darmstadt, Germany

*Corresponding author: abhishek.sarkar@kit.edu, oliver.clemens@nano.tu-darmstadt.de, horst.hahn@kit.edu

[†](R.D.) Heraeus Deutschland GmbH & Co. KG, Heraeusstr. 12 – 14, 63450 Hanau, Germany.

Table S1. Oxidation state, co-ordination number (CN) and corresponding cationic radii (r_c).[1]

Element	**Oxidation**	**CN**	**r_c [Å]**
Gd	3+	XII	1.10
La	3+	XII	1.36
Nd	3+	XII	1.27
Sm	3+	XII	1.24
Y	3+	XII	1.07
Co	3+	VI	0.54^{LS}, 0.61^{HS}
Cr	3+	VI	0.61
Fe	3+	VI	0.54^{LS}, 0.64^{HS}
Mn	3+	VI	0.58^{LS}, 0.64^{HS}
Ni	3+	VI	0.56^{LS}, 0.60^{HS}

LS - low spin, HS - high spin

Table S2. Space groups of various perovskites oxides based on rare earth (A-site) and transition metal (B-site) elements showing that they can adopt different crystal structures.[2]

System	Space group (number)
$GdCoO_3$	*Pbnm* (62)
$GdCrO_3$	*Pbnm* (62)
$GdFeO_3$	*Pbnm* (62)
$GdMnO_3$	*Pbnm* (62)
$GdNiO_3$	*Pbnm* (62)
$LaCoO_3$	$R\bar{3}ch$ (167)
$LaCrO_3$	*Pbnm (62)* $Pm\bar{3}m$ *(221)*
$LaFeO_3$	*Pbnm* (62)
$LaMnO_3$	$R\bar{3}ch$ (167) *Pnma* (62)
$LaNiO_3$	$R\bar{3}ch$ (167) $Pm\bar{3}m$ (221)
$NdCoO_3$	*Pbnm* (62) $Pm\bar{3}m$ (221)
$NdCrO_3$	*Pbnm* (62)
$NdFeO_3$	*Pbnm* (62)
$NdMnO_3$	*Pbnm* (62)
$NdNiO_3$	*Pbnm* (62)
$SmCoO_3$	$Pm\bar{3}m$ (221) *Pbnm* (62)
$SmCrO_3$	$Pm\bar{3}m$ (221) *Pbnm* (62)
$SmFeO_3$	*Pbnm* (62)
$SmMnO_3$	*Pbnm* (62)
$SmNiO_3$	*Pbnm* (62)
$YCoO_3$	*Pbnm* (62)
$YCrO_3$	*Pbnm* (62)
$YFeO_3$	*Pbnm* (62) $P6_3/mmc$ (194)
$YMnO_3$	$P6_3cm$ (185)
$YNiO_3$	$P12_1/n1$ (14)

Table S3. Operating parameters and analytical conditions of the ICP-MS

ICP-MS	**Agilent 7500cx**
RF Power	1550 W
Cooling/auxiliary gas	15.0/1.05 L min^{-1}
Dwell times	300 ms (3 x 100 ms) per mass
Helium gas flow for reaction mode	4.3 ml min^{-1}
Repetition	3 times
Samples	
ICP standards	Certipur® (Merck)
Analysed isotopes (reaction mode)	^{52}Cr, ^{56}Fe
Analysed isotopes (default mode)	^{55}Mn, ^{59}Co, ^{60}Ni, ^{89}Y, ^{139}La, ^{146}Nd, ^{147}Sm, ^{157}Gd
Internal standards	^{45}Sc, ^{165}Ho

Table S4. Actual composition of the ME-POs based on ICP-MS analysis, showing that all cations in are present in desired stoichiometry. The compositions of all the elements are measured in triplicate and normalized in a way that the sum of the A-site stoichiometry is fixed to 1.

System	**Gd**	**La**	**Nd**	**Sm**	**Y**	**Co**	**Cr**	**Fe**	**Mn**	**Ni**
$(5A_{0.2})CoO_3$	0.198(9)	0.201(6)	0.194(3)	0.202(2)	0.205(6)	0.990(66)	-	-	-	-
$La(5B_{0.2})O_3$	-	1.000(22)	-	-	-	0.212(8)	0.207(11)	0.202(8)	0.216(10)	0.206(6)
$Nd(5B_{0.2})O_3$	-	-	1.000(14)	-	-	0.216(10)	0.203(12)	0.202(1)	0.208(13)	0.210(9)
$Sm(5B_{0.2})O_3$	-	-	-	1.000(63)	-	0.200(13)	0.186(9)	0.188(8)	0.201(12)	0.201(1)
$(5A_{0.2})(5B_{0.2})O_3$	0.198(2)	0.200(3)	0.196(8)	0.202(2)	0.204(3)	0.210(3)	0.194(8)	0.197(7)	0.209(8)	0.208(2)

Table S5. Elemental composition based on EDS analysis of SEM micrographs showing that all cations in all three the systems are present in equiatomic amounts.

System	Gd	La	Nd	Sm	Y	Co	Cr	Fe	Mn	Ni
$(5A_{0.2})CoO_3$	10.1	10.8	10.0	10.2	11.0	47.8	-	-	-	-
$(5A_{0.2})CrO_3$	10.4	11.0	10.7	10.6	9.1	-	48.2	-	-	-
$(5A_{0.2})FeO_3$	10.8	10.9	10.3	10.6	9.3	-	-	48.1	-	-
$(5A_{0.2})MnO_3$	10.0	10.0	10.9	9.9	9.7	-	-	-	49.5	-
$(5A_{0.2})NiO_3$	9.9	9.8	9.2	9.8	10.2	-	-	-	-	51.1
$Gd(5B_{0.2})O_3$	48.8	-	-	-	-	10.2	10.6	10.2	10.5	9.7
$La(5B_{0.2})O_3$	-	49.0	-	-	-	10.2	10.6	10.3	9.5	10.3
$Nd(5B_{0.2})O_3$	-	-	48.9	-	-	10.3	10.6	9.1	11.2	9.9
$Sm(5B_{0.2})O_3$	-	-	-	50.1	-	9.5	9.9	10.5	10.9	9.1
$Y(5B_{0.2})O_3$	-	-	-	-	50.5	10.0	10.0	9.9	9.9	9.7
$(5A_{0.2})(5B_{0.2})O_3$	9.0	10.3	9.7	9.9	10.7	10.5	10.2	9.5	10.1	10.1

$5A_{0.2} = Gd_{0.2}La_{0.2}Nd_{0.2}Sm_{0.2}Y_{0.2}$, $5B_{0.2} = Co_{0.2}Cr_{0.2}Fe_{0.2}Mn_{0.2}Ni_{0.2}$

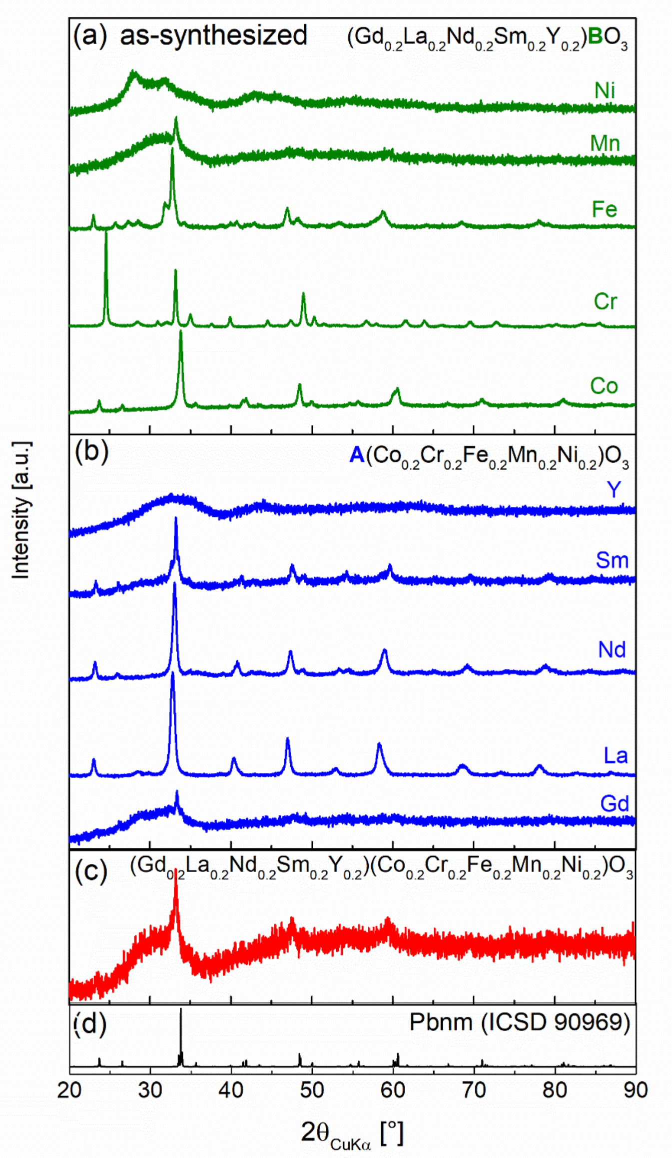

Figure S1. XRD patterns of as-synthesized ME-PO powders: (a) (5A0.2)BO3, B = Co, Cr, Fe, Mn, or Ni, (b) A(5B0.2)O3, A = Gd, La, Nd, Sm, or Y, (c) (5A0.2)(5B0.2)O3, and (d) simulated orthorhombic perovskite (Pbnm) pattern (ICSD 23823).

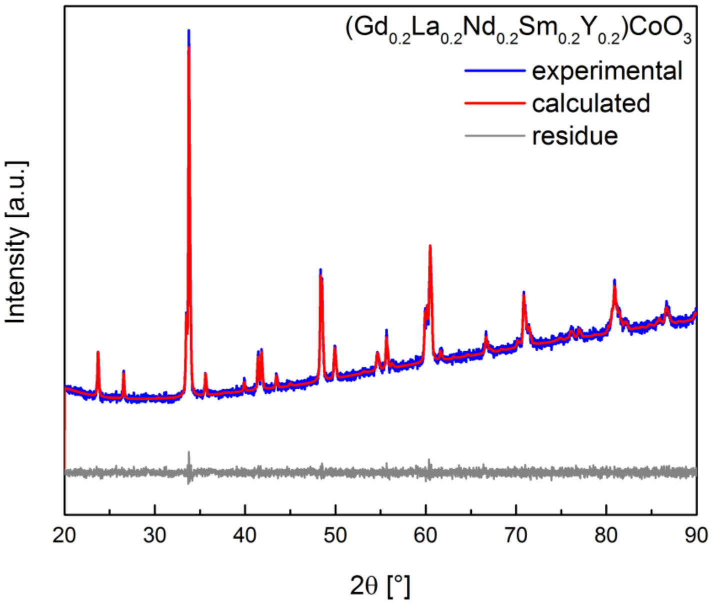

Figure S2. XRD pattern together with Rietveld fit of (5A$_{0.2}$)CoO$_3$, confirming the phase purity (of the perovskite structure) of the powder.

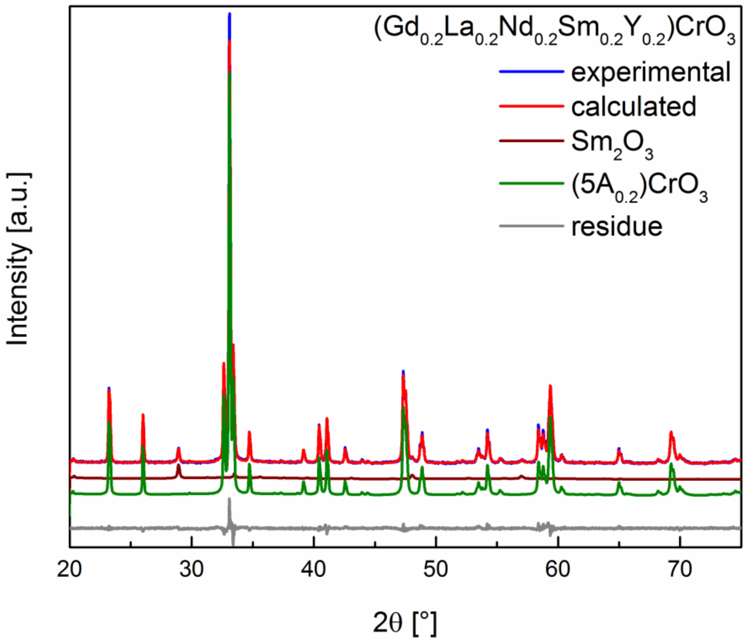

Figure S3. XRD pattern together with Rietveld fit of (5A$_{0.2}$)CrO$_3$, confirming the presence of small amount (~ 3 wt.%) of secondary Sm$_2$O$_3$-type phase along with the major perovskite phase.

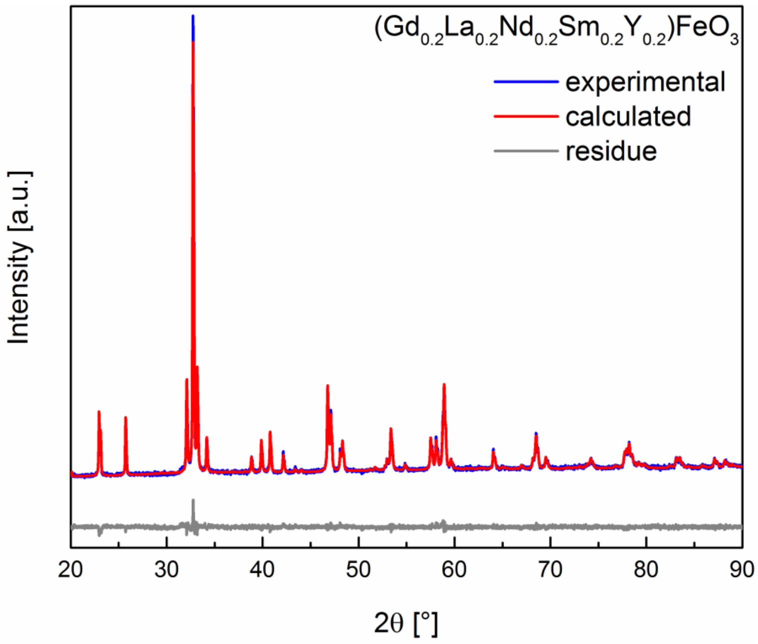

Figure S4. XRD pattern together with Rietveld fit of $(5A_{0.2})FeO_3$, confirming the presence of a single perovskite (*Pbnm*) phase.

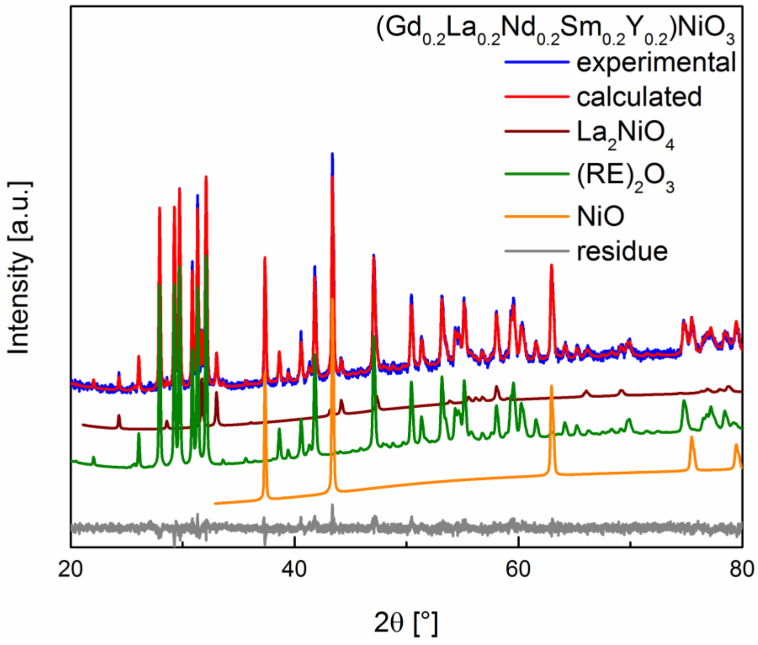

Figure S5. XRD pattern together with Rietveld fit of $(5A_{0.2})NiO_3$, where three different phases, tetragonal, monoclinic and rocksalt, are observed.

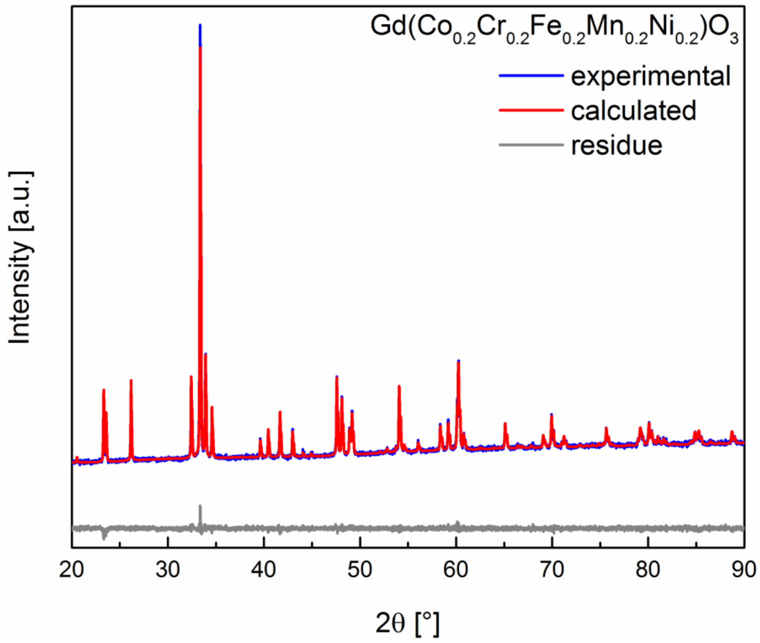

Figure S6. XRD pattern together with Rietveld fit of $Gd(5B_{0.2})O_3$, confirming the presence of a single perovskite (*Pbnm*) phase.

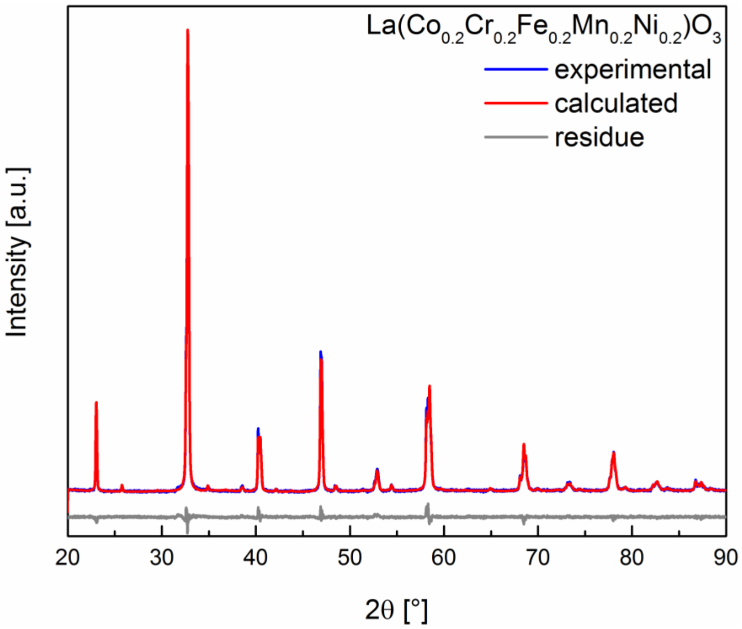

Figure S7. XRD pattern together with Rietveld fit of $La(5B_{0.2})O_3$, confirming the presence of a single perovskite (*Pbnm*) phase

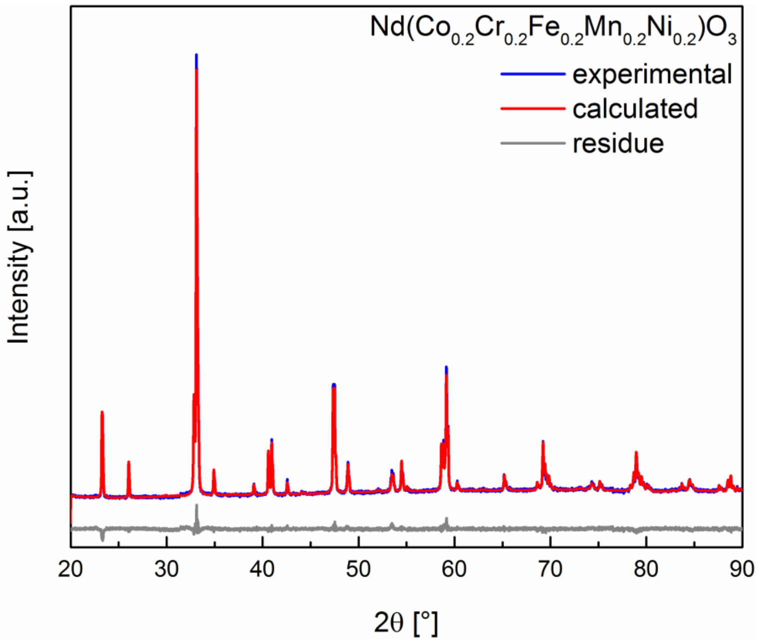

Figure S8. XRD pattern together with Rietveld fit of Nd(5$B_{0.2}$)O_3, confirming the presence of a single perovskite (*Pbnm*) phase.

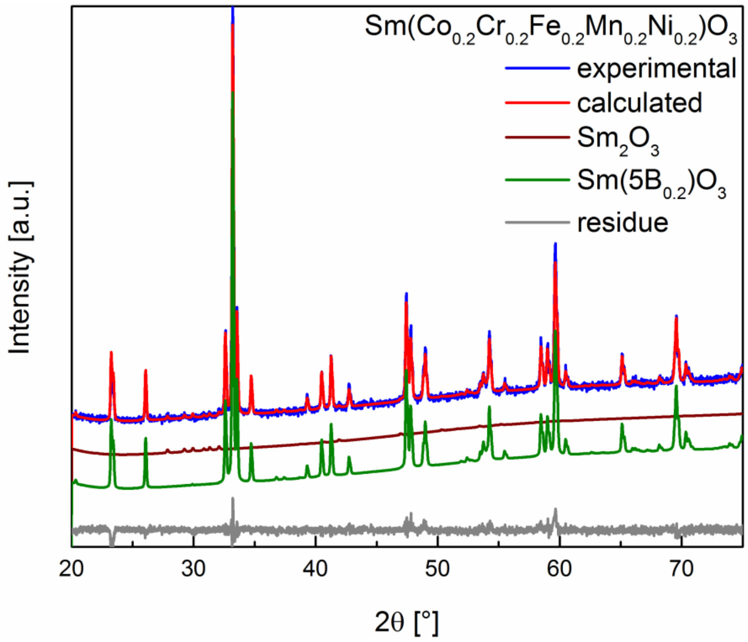

Figure S9. XRD pattern together with Rietveld fit of Sm(5$B_{0.2}$)O_3, where small amount of secondary Sm_2O_3 phase alongside the major perovskite phase was observed.

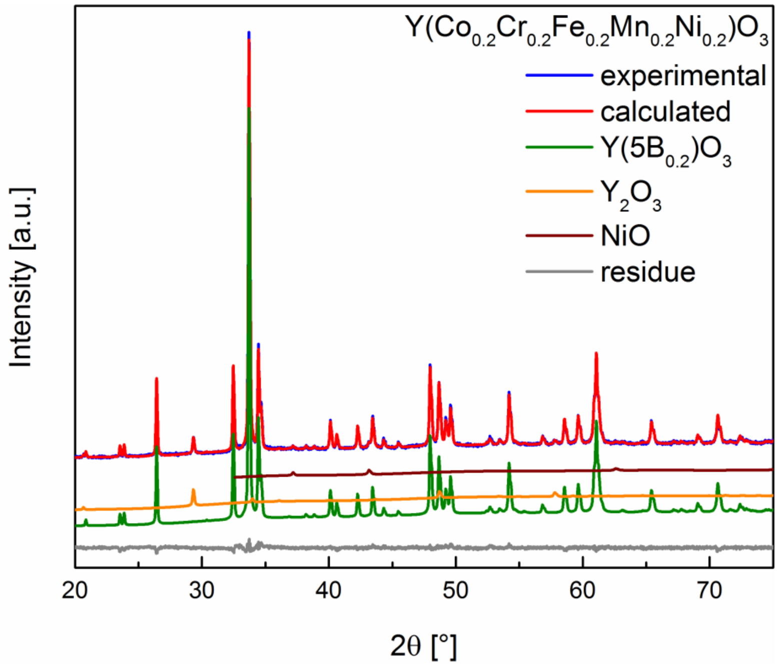

Figure S10. XRD pattern together with Rietveld fit of $Y(5B_{0.2})O_3$, where two secondary phases (Y_2O_3 and NiO) alongside the major perovskite phase was observed.

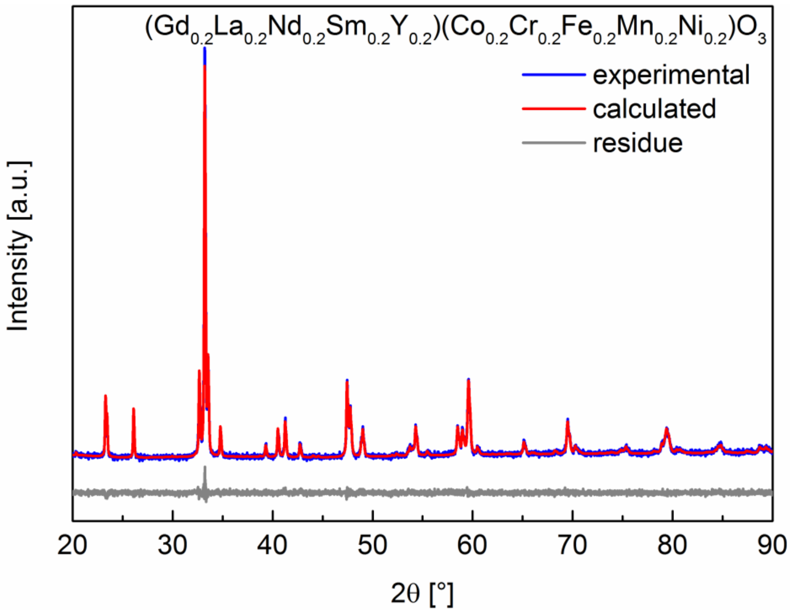

Figure S11. XRD pattern together with Rietveld fit of $(5A_{0.2})(5B_{0.2})O_3$, confirming the phase purity (*Pbmn*) of the highly complex 10 cationic system.

Table S6. Structural data for 8 phase perovskite mixtures observed in $(5A_{0.2})MnO_3$ system obtained from Rietveld refinement: space group (SG) along with prototype structures of secondary phases, phase fraction (*f* in wt.%) and lattice parameters (*a*, *b*, *c* in Å).

SG	*f*	*a*	*b*	*c*
Pbnm	25.6(1)	5.3658(4)	5.7521(4)	7.5250(5)
Pbnm	25.2(1)	5.3661(9)	5.7697(9)	7.5136(1)
Pbnm	25.1(5)	5.3656(2)	5.7345(2)	7.5364(3)
Pbnm	7.8(1)	5.3654(1)	5.7169(2)	7.5478(2)
Pbnm	7.7(2)	5.3651(2)	5.6993(3)	7.5593(3)
Pbnm	3.0(1)	5.3649(5)	5.6817(6)	7.5707(5)
Pbnm	2.8(1)	5.3647(1)	5.6641(6)	7.5821(8)
Pbnm	2.8(1)	5.3644(8)	5.6465(6)	7.5936(1)

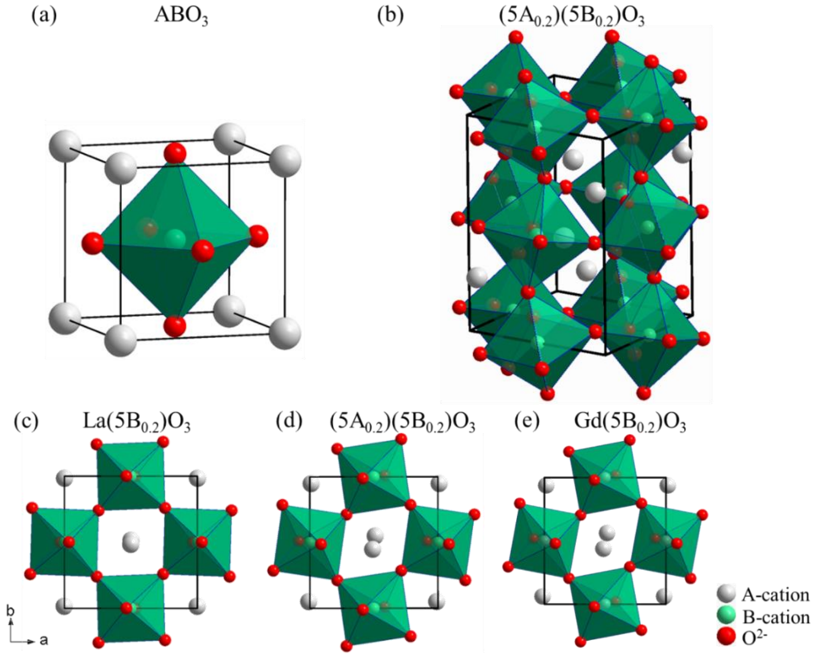

Figure S12. Schematic of crystal structure of an ideal cubic perovskite, ABO_3 ($Pm\bar{3}m$) (a) and $(5A_{0.2})(5B_{0.2})O_3$ (b) as a representative orthorhombic (*Pbnm*) ME-PO systems. The increasing magnitude of tilting the BO_6 polyhedra observed in ME-POs along [001] axis in: $La(5B_{0.2})O_3$ (c), $(5A_{0.2})(5B_{0.2})O_3$ (d), and $Gd(5B_{0.2})O_3$ (e).

Table S7. M-O bond distances (error ~ 0.01Å) for different ME-POs obtained from Rietveld analysis the corresponding XRD patterns.

$(5A_{0.2})CoO_3$		**$(5A_{0.2})CrO_3$**		**$(5A_{0.2})FeO_3$**		**$(5A_{0.2})MnO_3$**		**$Gd(5B_{0.2})O_3$**		**$La(5B_{0.2})O_3$**		**$Nd(5B_{0.2})O_3$**		**$Sm(5B_{0.2})O_3$**		**$Y(5B_{0.2})O_3$**		**$(5A_{0.2})(5B_{0.2})O_3$**	
A-O distances																			
O1	2.29	O1	2.32	O1	2.35	O1	2.21	O1	2.30	O2	2.57	O1	2.29	O1	2.38	O1	2.22	O1	2.35
O2	2.34	O2	2.40	O2	2.39	O2	2.47	O1	2.37	O2	2.57	O2	2.44	O1	2.44	O2	2.27	O2	2.43
O2	2.34	O2	2.40	O2	2.39	O2	2.47	O2	2.43	O1	2.57	O2	2.44	O2	2.48	O2	2.27	O2	2.43
O1	2.43	O1	2.47	O1	2.43	O2	2.53	O2	2.43	O2	2.57	O1	2.49	O2	2.48	O1	2.30	O1	2.46
O2	2.54	O2	2.58	O2	2.59	O2	2.53	O2	2.58	O2	2.57	O2	2.55	O2	2.59	O2	2.48	O2	2.51
O2	2.54	O2	2.58	O2	2.59	O2	2.64	O2	2.58	O1	2.66	O2	2.55	O2	2.59	O2	2.48	O2	2.51
O2	2.61	O2	2.66	O2	2.69	O2	2.64	O2	2.59	O1	2.82	O2	2.73	O2	2.62	O2	2.63	O2	2.70
O2	2.61	O2	2.66	O2	2.69	O1	2.68	O2	2.59	O2	2.84	O2	2.73	O2	2.62	O2	2.63	O2	2.70
O1	3.02	O1	3.09	O1	3.11	O1	3.26	O1	3.07	O2	2.84	O1	3.14	O1	3.06	O1	3.12	O1	3.11
O1	3.02	O1	3.12	O1	3.26	O1	3.43	O1	3.32	O1	2.94	O1	3.17	O1	3.15	O1	3.14	O1	3.14
O2	3.05	O2	3.31	O2	3.42	O2	3.43	O2	3.33	O2	3.01	O2	3.29	O2	3.25	O2	3.51	O2	3.32
O2	3.05	O2	3.31	O2	3.42	O2	2.21	O2	3.33	O2	3.01	O2	2.29	O2	3.25	O2	3.51	O2	3.32
B-O distances																			
O2	1.92	O2	1.97	O1	1.98	O1	1.98	O1	1.95	O1	1.94	O2	1.95	O2	1.94	O1	1.96	O2	1.95
O2	1.92	O2	1.97	O1	1.98	O1	1.98	O1	1.95	O1	1.94	O2	1.95	O2	1.94	O1	1.96	O2	1.95
O1	1.93	O1	1.97	O2	1.99	O2	1.96	O2	1.96	O2	1.94	O1	1.99	O1	1.95	O2	1.98	O1	1.96
O1	1.93	O1	1.97	O2	1.99	O2	1.96	O2	1.96	O2	1.94	O1	1.99	O1	1.95	O2	1.98	O1	1.96
O2	1.93	O2	1.98	O2	2.02	O2	2.14	O2	1.99	O2	1.96	O2	2.00	O2	1.98	O2	1.99	O2	1.98
O2	1.93	O2	1.98	O2	2.02	O2	2.14	O2	1.99	O2	1.96	O2	2.00	O2	1.98	O2	1.99	O2	1.98

$5A_{0.2} = Gd_{0.2}La_{0.2}Nd_{0.2}Sm_{0.2}Y_{0.2}$, $5B_{0.2} = Co_{0.2}Cr_{0.2}Fe_{0.2}Mn_{0.2}Ni_{0.2}$

Effective coordination number (ECoN)

The effective coordination number (ECoN) for the cations are calculated based on the formulation proposed by Hoppe:[3]

$$ECoN = \sum_{i=1}^{n} e^{\left[1-\left\{\frac{(f_{MO})_i}{f_{MFIR}}\right\}^6\right]} \qquad \text{(S1)}$$

where f_{MO} and f_{MFIR} are the fictive and the mean fictive ionic radii, respectively, and are calculated as follows:

$$f_{MO} = (M \rightarrow O) \cdot [\frac{r_M}{r_M + r_O}] \qquad \text{(S1)}$$

$$f_{MFIR} = \frac{\sum_{i=1}^{n} (f_{MO})_i \cdot e^{\left[1-\left\{\frac{(f_{MO})_i}{(f_{MO})_{i=1}}\right\}^6\right]}}{\sum_{i=1}^{n} e^{\left[1-\left\{\frac{(f_{MO})_i}{(f_{MO})_{i=1}}\right\}^6\right]}} \qquad \text{(S2)}$$

where $(M \rightarrow O)$ stands for the bond distance between a cation and a neighboring oxygen ion (see Table S7), r_M and r_O are the cation and oxygen ion radii, respectively (see Table S1). The value of n should be theoretically infinite. However, due to negligible contribution of the far off ions n is fixed to 12 for calculation of the ECoN(A) and to 6 for calculation of the ECoN(B).

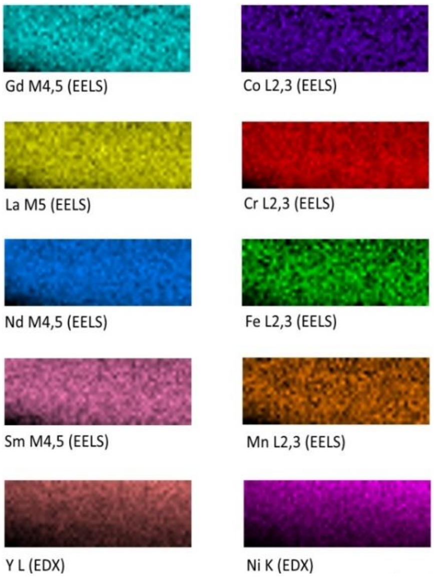

Figure S13. EELS and EDX elemental maps showing homogenous distribution of elements in $(5A_{0.2})(5B_{0.2})O_3$.

Table S8. Structural data for the $(5A_{0.2})MnO_3$ systems at different temperatures (T) obtained from Rietveld refinement: space group (SG), phase fraction (*f* in wt.%) and lattice parameters (*a*, *b*, *c* in Å).

T [°C]	SG	*f*	*a*	*b*	*c*
30 (before HTXRD)	*Pbnm*	42.3(1)	5.3658(4)	5.7396(4)	7.5352(5)
	Pbnm	40.9(1)	5.3670(9)	5.7637(9)	7.5201(1)
	Pbnm	16.8(5)	5.3633(2)	5.6916(2)	7.5652(3)
400	*Pbnm*	81.4(4)	5.3927(2)	5.6662(2)	7.6216(3)
	Pbnm	17.5(4)	5.3888(7)	5.6287(5)	7.6616(8)
	Pbnm	1.1(9)	5.3240(5)	5.8440(5)	7.9560(6)
500	*Pbnm*	86.4(4)	5.4011(2)	5.6488(2)	7.6487(2)
	Pbnm	13.6(4)	5.3978(8)	5.6129(5)	7.6887(9)
600	*Pbnm*	93.0(4)	5.4111(2)	5.6260(2)	7.6778(2)
	Pbnm	7.0(4)	5.4093(1)	5.5945(9)	7.7188(1)
700	*Pbnm*	97.4(3)	5.4214(1)	5.5992(1)	7.7040(1)
	Pbnm	2.6(3)	5.4170(3)	5.6800(2)	7.7440(3)
800	*Pbnm*	98.3(3)	5.4340(7)	5.6016(8)	7.7255(1)
	Pbnm	1.7(3)	5.4470(2)	5.5731(1)	7.7660(9)
900	*Pbnm*	100	5.4450(6)	5.6046(7)	5.7435(1)
1000	*Pbnm*	100	5.4611(7)	5.6037(7)	7.7680(1)
30 (after HTXRD)	*Pbnm*	37.2(1)	5.3656(4)	5.7449(8)	7.5317(7)
	Pbnm	31.7(2)	5.3657(9)	5.7678(9)	7.5191(1)
	Pbnm	31.1(8)	5.3654(1)	5.7220(2)	7.5444(2)

High Temperature X-Ray Diffraction (HT-XRD)

The structural parameters obtained from the Rietveld analysis for the $(5A_{0.2})(5B_{0.2})O_3$ systems, at different temperatures, are summarized in Table S8. It was observed that the orthorhombic distortion in the ME-POs was maintained even at higher temperatures (till 1000 °C). However, linear expansion of the lattice parameters and a decrease in the metric distortion form the cubic structure was observed with increasing the temperature.

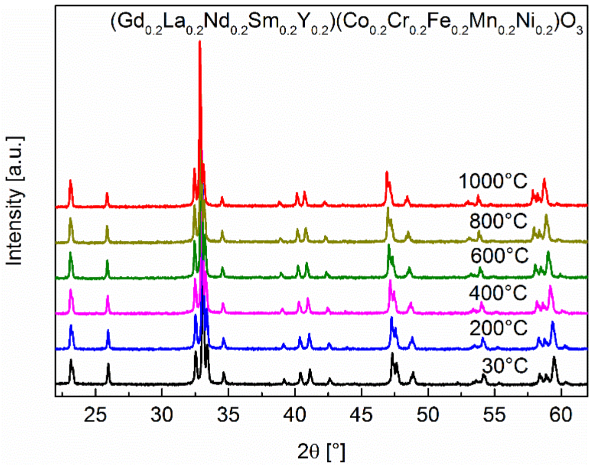

Figure S14: In situ HT-XRD patterns of $(5A_{0.2})(5B_{0.2})O_3$ at different temperatures indicating no phase separation or change in the lattice symmetry.

Table S9. Structural data for the 10 cationic $(5A_{0.2})(5B_{0.2})O_3$ systems at different temperatures (T) obtained from Rietveld refinement: space group (SG), phase fraction (f in wt.%), lattice parameters (a, b, c, $a_{ps.cubic}$ in Å), and degree of metric distortion (ε in %).

T [°C]	SG	f	a	b	c	$a_{ps.cubic}$	ε
30	*Pbnm*	100	5.3614(7)	5.5012(7)	7.6309(1)	3.832	0.63
200	*Pbnm*	100	5.3738(5)	5.5087(4)	7.6478(9)	3.839	0.61
400	*Pbnm*	100	5.3915(6)	5.5219(5)	7.6717(9)	3.850	0.58
600	*Pbnm*	100	5.4097(5)	5.5361(5)	7.6972(1)	3.862	0.56
800	*Pbnm*	100	5.4280(3)	5.5483(4)	7.7216(2)	3.874	0.53
1000	*Pbnm*	100	5.4454(4)	5.5579(1)	7.7444(3)	3.884	0.50

$a_{ps.cubic}$ is the pseudo-cubic lattice parameter calculated using Eq. 4.

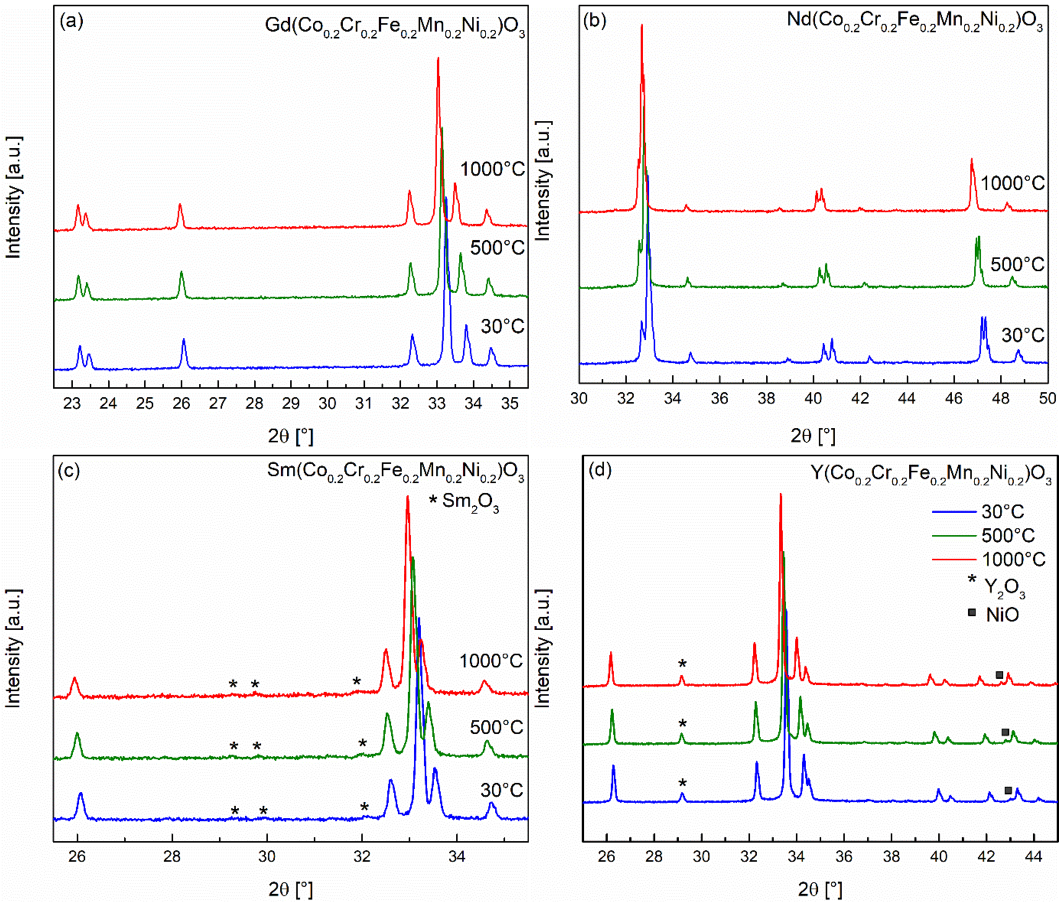

Figure S15. In situ HT-XRD pattern (at 30 °C, 500 °C and 1000 °C) of the different ME-PO systems with multiple cations on the B site where (a) $Gd(Co_{0.2}Cr_{0.2}Fe_{0.2}Mn_{0.2}Ni_{0.2})O_3$; (b) $Nd(Co_{0.2}Cr_{0.2}Fe_{0.2}Mn_{0.2}Ni_{0.2})O_3$; (c) $Sm(Co_{0.2}Cr_{0.2}Fe_{0.2}Mn_{0.2}Ni_{0.2})O_3$ and (d) $Y(Co_{0.2}Cr_{0.2}Fe_{0.2}Mn_{0.2}Ni_{0.2})O_3$. No changes other than lattice expansion at higher temperatures were observed in the systems.

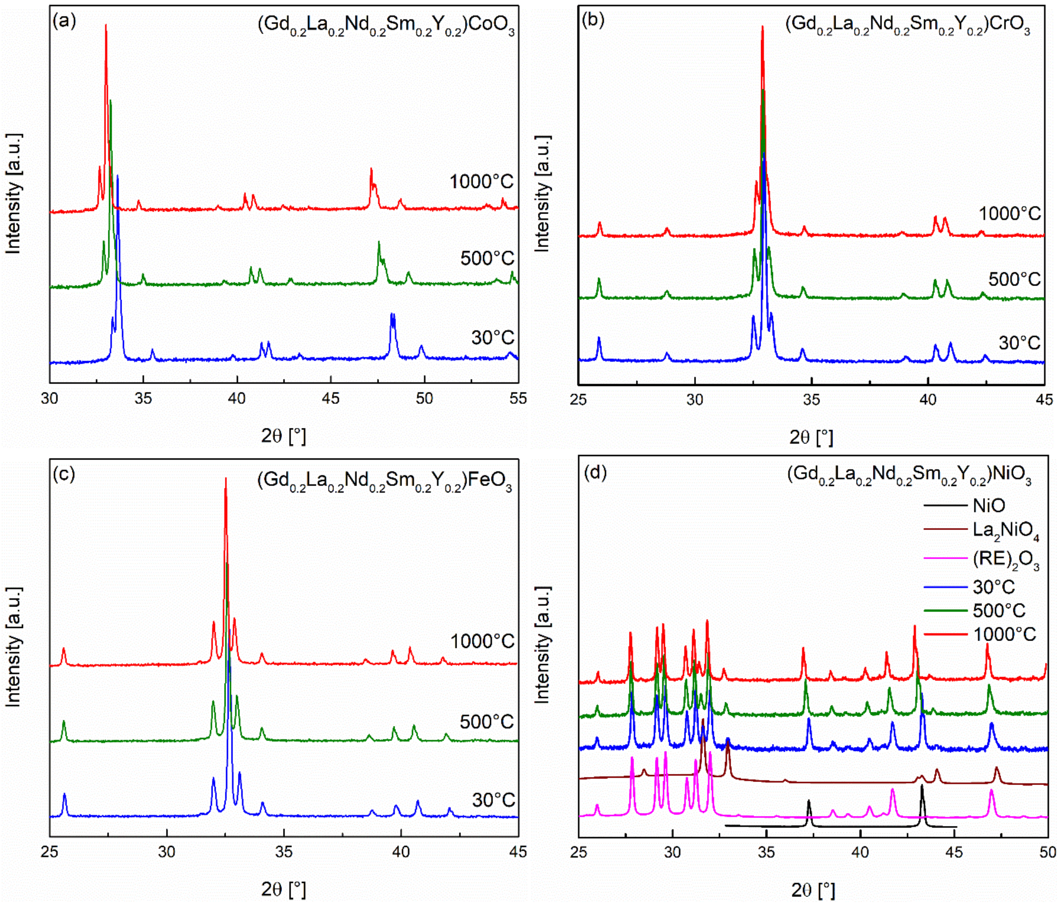

Figure S16. In situ HT-XRD pattern (at 30 °C, 500 °C and 1000 °C) of the different ME-PO systems with multiple cations on the A site where (a) $(Gd_{0.2}La_{0.2}Nd_{0.2}Sm_{0.2}Y_{0.2})CoO_3$; (b) $(Gd_{0.2}La_{0.2}Nd_{0.2}Sm_{0.2}Y_{0.2})CrO_3$; (c) $(Gd_{0.2}La_{0.2}Nd_{0.2}Sm_{0.2}Y_{0.2})FeO_3$ and (d) $(Gd_{0.2}La_{0.2}Nd_{0.2}Sm_{0.2}Y_{0.2})NiO_3$. No changes other than lattice expansion at higher temperatures were observed in the systems.

Table S10. Structural data for the La(5B$_{0.2}$)O$_3$ systems at different temperatures (T) obtained from Rietveld refinement: space group (SG), phase fraction (*f* in wt.%), lattice parameters (*a*, *b*, *c* in Å) and metric strain (*ε*).

T [°C]	**SG**	***f***	***a***	***b***	***c***	***ε* [%]**
30 (before HTXRD)	*Pbnm*	100	5.4656(6)	5.5101(5)	7.7424(9)	0.198
100	*Pbnm*	100	5.4687(1)	5.5152(1)	7.7480(1)	0.214
125	*Pbnm* $R\bar{3}ch$	84.6(4) 15.4(4)	5.4994(1) 5.5161(3)	5.5166(1) -	7.7517(2) 13.2842(1)	0.223 0.460
140	*Pbnm* $R\bar{3}ch$	39.5(4) 60.5(4)	5.4707(1) 5.5175(1)	5.5179(1) -	7.7536(2) 13.2863(4)	0.223 0.463
150	*Pbnm* $R\bar{3}ch$	19.2(3) 80.8(3)	5.4717(1) 5.5180(1)	5.5189(2) -	7.7550(2) 13.2903(3)	0.227 0.457
175	*Pbnm* $R\bar{3}ch$	5.4(3) 94.6(3)	5.4721(5) 5.5194(9)	5.5193(5) -	7.7556(7) 13.2966(3)	0.228 0.451
300	*Pbnm* $R\bar{3}ch$	3.2(3) 96.8(3)	5.4790(7) 5.5272(1)	5.5263(7) -	7.7653(1) 13.3344(3)	0.265 0.413
450	$R\bar{3}ch$	100	5.5369(7)	-	13.3799(2)	0.368
600	$R\bar{3}ch$	100	5.5474(5)	-	13.4260(1)	0.326
750	$R\bar{3}ch$	100	5.5578(5)	-	13.4699(1)	0.288
900	$R\bar{3}ch$	100	5.5675(5)	-	13.5124(1)	0.250
1050	$R\bar{3}ch$	100	5.5767(4)	-	13.5541(1)	0.211
30 (after HTXRD)	*Pbnm*	100	5.4653(1)	5.5106(9)	7.7438(2)	0.204

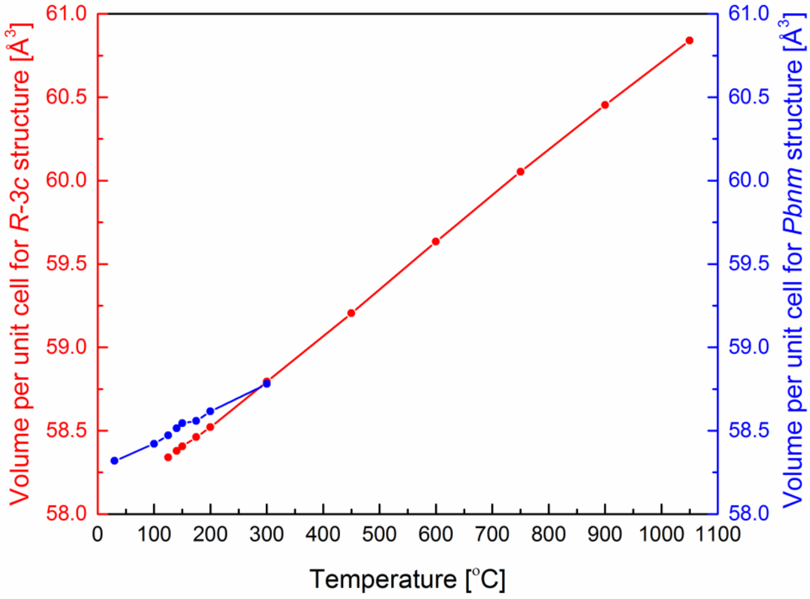

Figure S17: Volume change of the trigonal ($R\overline{3}ch$) and the orthorhombic (*Pbnm*) unit cell of $La(5B_{0.2})O_3$ system with increasing temperature.

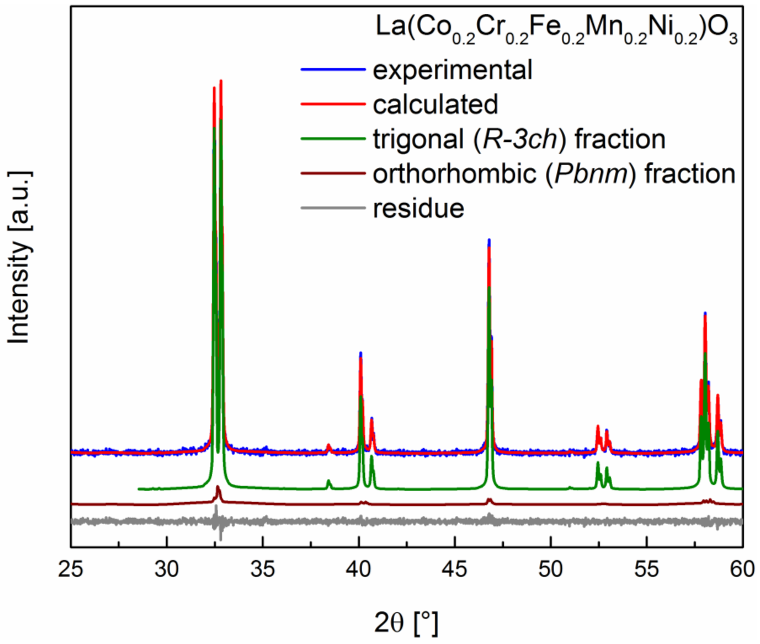

Figure S18. In-situ HTXRD pattern together with Rietveld fit of $La(5B_{0.2})O_3$ at 300 °C. A major (96.2 wt.%) trigonal phase along with a minor (3.8 wt.%) orthorhombic phase are adequately required to fit the pattern. Above this temperature only the trigonal phase is observed.

References

(1) Shannon, R. D. Revised Effective Ionic Radii and Systematic Studies of Interatomic Distances in Halides and Chalcogenides. *Acta Crystallogr. Sect. A* **1976**, *32* (5), 751–767 DOI: 10.1107/S0567739476001551.

(2) Springer Materials (online database) http://materials.springer.com (accessed Mar 14, 2017).

(3) Hoppe, R. Effective Coordination Numbers (ECoN) and Mean Fictive Ionic Radii (MEFIR). *Zeitschrift für Krist.* **1979**, *150* (1–4), 23–52 DOI: 10.1524/zkri.1979.150.1-4.23.

B.5. Supplementary information for Sec. 5.2

Supplementary information: High entropy oxides: An emerging prospect for magnetic rare earth - transition metal perovskites

Ralf Witte,[1,*] Abhishek Sarkar,[1,2] Robert Kruk,[1] Benedikt Eggert,[3] Richard A. Brand,[1,3] Heiko Wende,[3] and Horst Hahn[1,2]

[1]*Institute of Nanotechnology, Karlsruhe Institute of Technology, 76344 Eggenstein-Leopoldshafen, Germany*

[2]*KIT-TUD-Joint Research Laboratory Nanomaterials, Technical University Darmstadt, 64287 Darmstadt, Germany*

[3]*Faculty of Physics and Center for Nanointegration Duisburg-Essen (CENIDE), University of Duisburg-Essen, Lotharstr. 1, 47048 Duisburg, Germany*

(Dated: February 18, 2019)

Abstract

Additional information to the main manuscript is compiled in this supplementary material. First results of structural investigations are presented. Then further additional results of AC and DC magnetometry are shown. Results of temperature and field dependent Mössbauer spectra are presented and the deduced hyperfine parameters are given. Finally low temperature hysteresis measurements are shown.

I. RESULTS OF X-RAY DIFFRACTION AND STRUCTURAL DETAILS

Table I. Structural data for the PE-HEO systems obtained from Rietveld refinement: space group (SG) along with prototype structures of secondary phases, phase fraction (f in wt.%) lattice parameters (a, b, c in Å, and β in °) and goodness of fit (GoF).

PE-HEO	SG	f [wt.%]	a [Å]	b [Å]	c [Å]	β [°]	GoF
$Gd(5B_{0.2})O_3$	*Pbnm*	100	5.2958(6)	5.5303(6)	7.5708(9)	-	1.25
$La(5B_{0.2})O_3$	*Pbnm*	100	5.4656(6)	5.5101(5)	7.7424(9)	-	1.19
$Nd(5B_{0.2})O_3$	*Pbnm*	100	5.4087(6)	5.4760(6)	7.6718(8)	-	1.47
$Sm(5B_{0.2})O_3$	*Pbnm*	98.3(3)	5.3523(6)	5.5024(6)	7.6178(9)	-	1.42
	$C2/m$ (Sm_2O_3)	1.7(3)	14.236(1)	3.6400(3)	8.7290(1)	100.4(1)	
$Y(5B_{0.2})O_3$	*Pbnm*	94.7(1)	5.2255(6)	5.5361(7)	7.4977(1)	-	1.44
	Ia-3 (Y_2O_3)	3.2(7)	10.597(1)	-	-	-	
	Fm-3*m*(NiO)	2.1(1)	4.2021(1)	-	-	-	
$(5A_{0.2})(5B_{0.2})O_3$	*Pbnm*	100	5.3614(7)	5.5012(7)	7.6309(1)	-	1.45

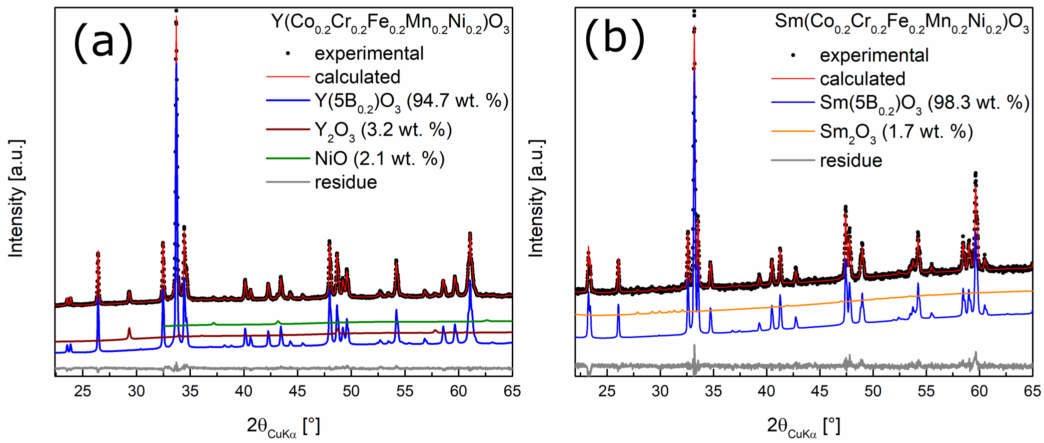

Figure 1. X-ray diffraction data with Rietveld refinment for the two compounds which contains minor secondary phases, (a) $Y(5B_{0.2})O_3$ and (b) $Sm(5B_{0.2})O_3$.

Fig. 1 present the X-ray diffraction results for the two PE-HEO compounds, which have a minor addition of secondary phases. It is clear from the refinements, that it is indeed a matter of minority phases, as the reflections are barely visible. The respective weight fractions of the additional phases are tabulated in Tab. I.

II. HYSTERESIS MEASUREMENTS OF LA(5B$_{0.2}$)O$_3$

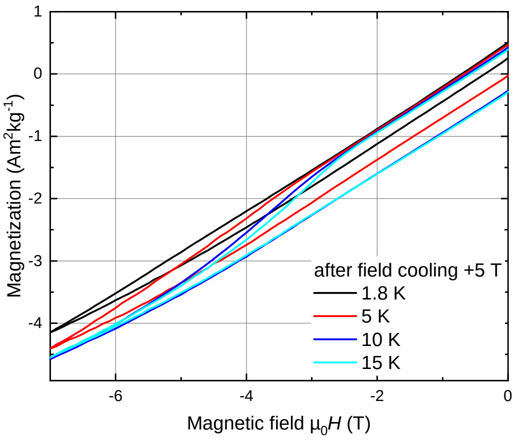

Figure 2. View of the negative branch of hysteresis measurements at low temperatures after field cooling in +5 T magnetic field. Measurements below 10 K show still an opening at the maximum attainable field, hence they are so-called minor loops.

Hysteresis measurements of the La(5B$_{0.2}$)O$_3$ compound at T=1.8, 5, 10, 15 K after field cooling in +5 T are plotted in Fig.2. The magnified view of the negative branch of the hysteresis loops clearly indicates minor loops and the maximum negative field of $\mu_0 H$=7 T is not sufficient to reverse the magnetization completely. As pointed out in the literature[1], minor loops necessarily lead to the observation of exchange bias effects. We therefor limited ourselves to the analysis of the 10 K data.

In order to distinguish between a horizontal or vertical exchange bias shift, which is not directly obvious from the data, when curves do not show a clear coercive field, we calculated the derivative of the magnetization with respect to the magnetic field. In this representation a horizontal shift along the field axis, would be directly visible. However as can be seen from Fig.3, there is no such difference between hysteresis measurements with

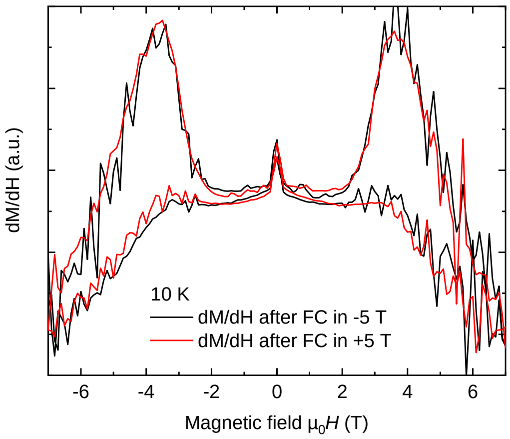

Figure 3. Derivative of the magnetization with respect to the field dM/dH at 10 K after field cooling in ±5 T magnetic field. The overlapping curves provide no evidence for a horizontal, cooling field dependent shift.

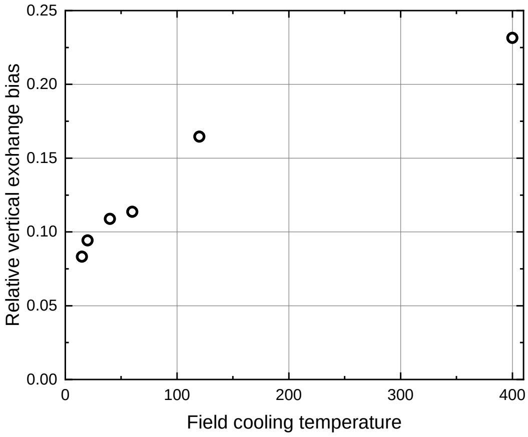

Figure 4. The relative magnitude of the vertical shift with respect to the remnant magnetization at 10 K, as function field cooling temperature T_{FC}.

$\mu_0 H_{\mathrm{FC}} = \pm 5\,\mathrm{T}$, hence a horizontal exchange bias can be ruled out.

The vertical shift was studied as function of the field cooling temperature T_{FC}, i.e. the temperature from which on the magnetic field was applied during cooling to 10 K. Fig. 4 plots the relative vertical shift with respect to the remnant magnetization. As discussed in the main text a reduction of the shift is observed if applying the field directly below the transition temperature, however if using even lower temperature it reduces significantly but remains present. This observation leads to the conclusion that magnetic order sets in gradually, hence on a local scale a variation of transition temperatures exists.

III. AC SQUID MAGNETOMETRY

Temperature dependent ac (alternating current) SQUID (Supraconducting quantum interference device) magnetometry measurements were performed on the $La(5B_{0.2})O_3$ compound using different excitation frequencies and small ac magnetic field of $\mu_0\Delta H$ of 0.5 mT. The fact that no frequency dependent shift is found in the m‘ rules out a possible spin glass arrangement of the magnetic moments, while the featureless m“ (please mark the different y-scale) points towards a predominantly antiferromagnetic spin arrangement with no or very little energy dissipation across the transition.

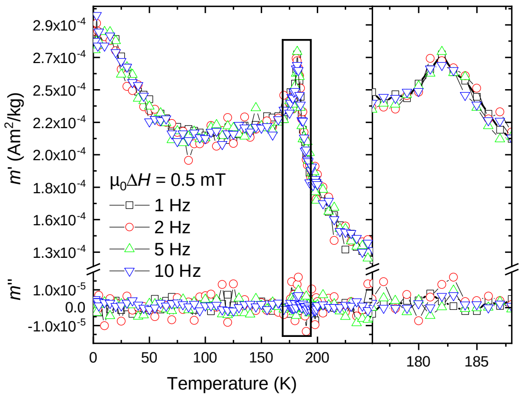

Figure 5. Temperature dependent ac SQUID magnetometry for the $La(5B_{0.2})O_3$ compound.

IV. RESULTS OF MÖSSBAUER SPECTROSCOPY

Table II. Mössbauer hyperfine parameters obtained from fitting a sextet to low temperature Mössbauer spectra: centre shift δ, quadrupole splitting ΔE_Q, Lorentzian linewidth Γ, magnetic hyperfine field B_{HF}, Gaussian broadening σ, A2:A3 area ratio of second to third line. δ is given with respect to bcc-Fe at room temperature. Parameters labeled with an asterisks * have been held fixed in the refinement.

	δ (mm/s)	$\Delta E_Q (mm/s)$	Γ (mm/s)	B_{HF} (T)	σ (T)	A2:A3	Area (%)
100 K	0.46(5)	0.15(6)	0.35(6)	37(1)	6.6(5)	2*	63(3)
	0.44(1)	0.06(3)	0.4*	42.4(1)	2*	2*	37(2)
50 K	0.47(3)	-	0.50(8)	42(1)	4.5(5)	2*	41(4)
	0.456(6)	-	0.30(3)	47.3(5)	2*	2*	59(6)
12 K	0.45(1)	-0.04(1)	0.42(2)	49.5(5)	2.0(1)	2*	100
4.3 (0 T)	0.46(2)	-0.03(1)	0.4(2)	49.8(5)	1.7(1)	2*	100
4.3 (5 T)	0.46(2)	-0.08(5)	0.35(8)	50.0(2)	2.8(0.1)	2.9(1)	100

Temperature dependent Mössbauer spectra are presented in Fig. 3 of the main article and the fits are described there. In Tab. II we provide the hyperfine parameters obtained from the fits.

Fig. 6 presents results for the measurements in a magnetic field of 5 T applied parallel to the γ radiation at 4.3 K. The arrows indicate the second and fifth lines, which increase in intensity in the magnetic field, resulting in a area ratio of first:second:third line of 3:3:1. This shows a rotation of the magnetic moments towards a perpendicular orientation with respect to the magnetic field. such a behavior would be expected expected for an AFM material, however a possible canting of the moments will help in aligning them. However the fact that the magnetic moments do not orient fully perpendicular shows that there exist retention forces. This could be related either to exchange interaction related effects, such as strong coupling of the AFM to the FM regions discussed in the text (which would align parallel to the field), large frustration of the system or to the presence of a strong magnetocrystalline anisotropy. The slight broadening of the lines as evidenced by the increase in Gaussian linewidth may indicate a slight distribution of canting angles, as the respective projection of

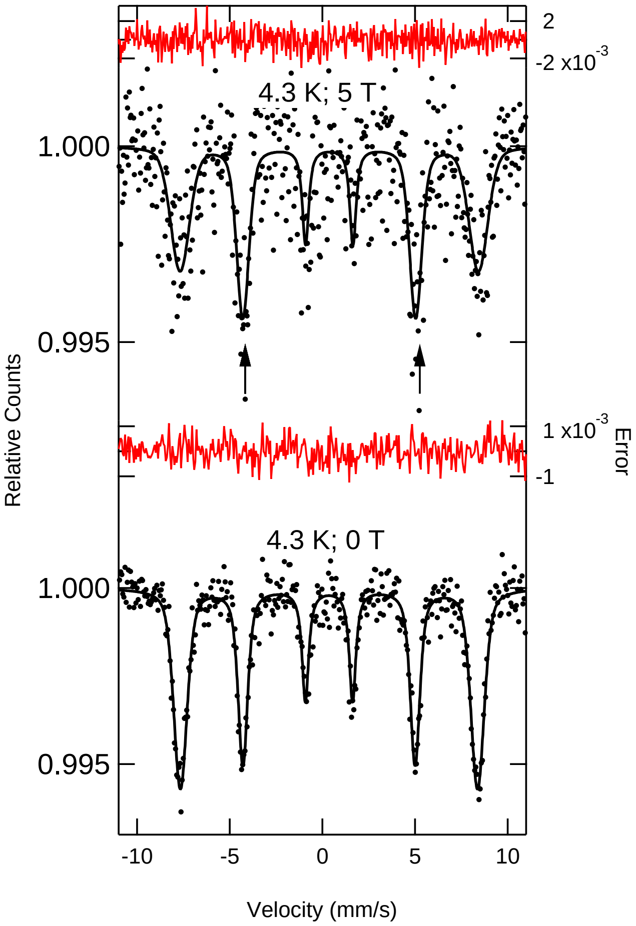

Figure 6. Low temperature Mössbauer spectra as function of external magnetic field applied parallel to the γ direction. The arrows indicate the change in intensity of the second and fifth line.

magnetic moment and external field on the magnetic hyperfine field might change slightly.

The presence of two magnetic components, AFM and FM cannot be observed in the spectra as i) only very small part of the sample is coupling FM, ii) the FM regions are not necessarily always Fe containing regions and iii) the low signal to noise ratio of the measurement.

V. LOW TEMPERATURE HYSTERESIS MEASUREMENTS

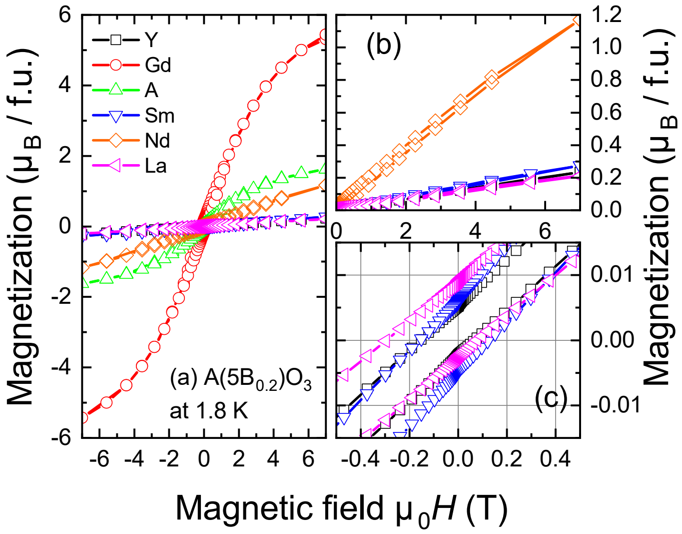

Figure 7. (a) Magnetization of $A(5B_{0.2})O_3$ with A= Gd, La, Nd, Sm, Y and $(5A_{0.2})$ as function of magnetic field, measured at 1.8 K. (b) Magnified view on the positive branch for A=La, Nd, Sm, Y. (c) Magnified view on the central part of the hysteresis for A=La, Nd, Y, showing exchange bias. The legend in (a) applies to all subfigures and the the x-axis is in all cases the magnetic field.

In Fig.7 (a) we give a synopsis of $M(\mu_0 H)$measurements for all compounds; (b) presents the positive branch of the hysteresis for the A=Y, Sm, Nd and La compounds; (c) is a magnified view around zero magnetic field. It is clear that the Gd compound shows the largest magnetization, but it is also evident that it is not possible to saturate the magnetization in the applied field. A complete interpretation is beyond the scope of this manuscript due to the complexity of the possibly present magnetic exchange interactions. However it is known that the crystal field interaction of Gd^{3+} is negligible due to the vanishing angular momentum (L=0) of the ion[2], which results in a very small magnetic anisotropy. Moreover the Gd^{3+}-Gd^{3+} interactions are small and in most Gd compounds, e.g. $GdFeO_3$ the weak ferromagnetic behavior originates from the Dzyaloshinskii-Moriya (DM) interaction with the canted moment of the AFM Fe sublattice[2]. This results in a weak additional ferromagnetic component. However in the $GdCrO_3$ compound one can observe different temperature regimes in which either Cr^{3+}-Cr^{3+}, Cr^{3+}-Gd^{3+} or the Gd^{3+}-Gd^{3+} interactions dominate, leading to different magnetic behaviors at each temperature[3]. What remains is that in the case of Gd^{3+} these interactions are small and the coupling to the TM ion sublattice is weak.

The compound $Y(5B_{0.2})O_3$ (RE ions without magnetic moment) shows the linear like behavior similar to the $La(5B_{0.2})O_3$ compound, which is discussed in the main manuscript. In agreement with the temperature dependent measurements (discussed in the main text) a higher $M(\mu_0 H)$ is reached, as expressed by the larger slope of curve. It seems thus that the structural variation between the two compounds (octahedral tilting, bond angles) impacts mostly on the magnetic exchange and thus the magnetic transition temperature.

The Nd and Sm compound both show a strongly non saturating behavior, which might be linked to the stronger crystal field coupling of these trivalent ions, which strengthens the coupling to the TM magnetic sublattice. The $M(\mu_0 H)$ curve measured for the compound with a mixture of the five RE elements on the A-site $(5A_{0.2})(5B_{0.2})O_3$ shows probably a mixture of the behavior of the individual RE elements compounds, as the RE^{3+}-RE^{3+} is very weak and they thus behave as if they were virtually isolated, or only linked to their nearest TM neighbors.

---

[*] ralf.witte@kit.edu

[1] J. Geshev, Journal of Magnetism and Magnetic Materials **320**, 600 (2008).

[2] M. Das, S. Roy, and P. Mandal, Physical Review B **96**, 174405 (2017).

[3] A. Jaiswal, R. Das, K. Vivekanand, T. Maity, P. M. Abraham, S. Adyanthaya, and P. Poddar, Journal of Applied Physics **107**, 013912 (2010).

List of Figures

List of Tables

List of acronyms and symbols

AFM Antiferromagnetic

APT Atom Probe Tomography

bcc Body Centered Cubic

BSE Backscattered Electrons

CN Coordination Number

CV Cyclic Voltammetry

EDX Energy-Dispersive X-ray Spectroscopy

EELS Electron Energy Loss Spectroscopy

eV electronvolt

EXAFS Extended X-Ray Absorption Fine Structure

fcc Face Centered Cubic

FSP Flame Spray Pyrolysis

F-HEO Fluorite type High Entropy Oxide

FM Ferromagnetic

G_{mix} Gibbs free energy of mixing

GCDC Galvanostatic Charge Discharge Cycling

H_{mix} Enthalpy of mixing

HAADF High Angle Annular Dark Field

HEA High Entropy Alloy

HEB High Entropy Boride

HEC High Entropy Carbide

HEN High Entropy Nitride

HEO High Entropy Oxide

HEOF High Entropy Oxyfluoride

H_2-HT Hydrogen Heat Treatment

ICP-MS Inductively Coupled Plasma Mass Spectrometry

kJ mol^{-1} kilo joule per mole

LIB Lithium Ion Battery

LiPON Lithium Phosphorus Oxynitride

mAh/g milliampere hour per gram

MEO Medium Entropy Oxide

NCM Lithium Nickel Manganese Cobalt Oxide

P-HEO Perovskite High Entropy Oxide

R Universal gas constant

RCP Reverse Co-precipitation

RE Rare Earth

R-HEO Rocksalt High Entropy Oxide

RHT Re-heat Treatment

S_{config} Configurational Entropy

S_{mix} Entropy of mixing

SE Secondary Electron

SEM Scanning Electron Microscopy

STEM Scanning Transmission Electron Microscopy

SQUID Superconductive Quantum Interference Device

t Tolerance Factor

T Temperature

TEM Transmission Electron Microscopy

TM Transition Metal

TM Transition Metal Oxide

UV-Vis Ultraviolet Visible

VHT Vacuum Heat Treatment

V_O Oxygen Vacancies

V Volts

XANES X-ray Absorption Near Edge Structure

XAS X-ray Absorption Spectroscopy

XPS X-ray Photoelectron Spectroscopy

XRD X-ray Diffraction

YSZ Yttria Stabilized Zirconia

Personal data

Name:	Abhishek Sarkar
Date of birth:	18.07.1992
Place of birth:	Kalyani
Citizenship:	Indian

Scientific Education

August 2010– June 2014	Bachelor of Technology (B. Tech.) in Metallurgical and Materials Engineering at National Institute of Technology (NIT) Durgapur, India Bachelor's thesis: High temperature oxidation behavior of microalloyed steel in dry air. Supervised by Prof. Dr. Swapan Kumar Mitra
July 2014 – May 2016	Master of Technology (M. Tech.) in Metallurgical and Materials Engineering at Indian Institute of Technology (IIT) Madras, Chennai, India Master's thesis: Synthesis and characterization of equiatomic multicomponent oxide systems. Supervised by Prof. Dr. Subramshu Shekar Bhattacharya and Prof. Dr.-Ing. Horst Hahn
June 2016 – present	Doctoral studies in Material Science and Engineering at Technische Universität Darmstadt, Germany Doctoral thesis: High Entropy Oxides: Structure and Properties. Supervised by Prof. Dr.-Ing. Horst Hahn

Scientific Career

September 2015 – March 2016	Guest student at Institute of Nanotechnology, Karlsruhe Institute of Technology (INT, KIT) under DAAD-IIT Master Sandwich Fellowship
June 2016 – August 2018	Research associate at INT - KIT
August 2018 – present	Research associate at Technische Universität Darmstadt, working at INT - KIT

Publications

1. High entropy oxides: The role of entropy, enthalpy and synergy
   A. Sarkar, B. Breitung, H. Hahn, *Scripta Materialia* (2020)
   10.1016/j.scriptamat.2020.05.019

2. Role of intermediate $4f$ states in tuning the band structure of high entropy oxides
   A. Sarkar, B. Eggert, L. Velasco, X. Mu, J. Lill, K. Ollefs, S.S. Bhattacharya, H. Wende, R. Kruk, R.A. Brand, H. Hahn, *APL Materials* 8, 051111 (2020), 10.1063/5.0007944

3. Magnetic properties of rare-earth and transition metal based perovskite type high entropy oxides
   R. Witte, A. Sarkar, L. Velasco, R. Kruk, R.A. Brand, B. Eggert, K. Ollefs, E. Weschke, H. Wende, H. Hahn *Journal of Applied Physics* 127 185109 (2020), 10.1063/5.0004125

4. Spinel to rock-salt transformation in high entropy oxides with Li incorporation
   J. Wang, D. Stenzel, R. Azmi, S. Najib, K. Wang, J. Jeong, A. Sarkar, Q. Wang, P.A. Sukkurji, T. Bergfeldt, M. Botros, J. Maibach, H. Hahn, T. Brezesinski, B. Breitung *Electrochem* 1 60–74 (2020), 10.3390/electrochem1010007

5. Gassing Behavior of High-Entropy Oxide Anode and Oxyfluoride Cathode Probed Using Differential Electrochemical Mass Spectrometry
   B. Breitung, Q. Wang, A. Schiele, Đ. Tripković, A. Sarkar, L. Velasco, D. Wang, S.S. Bhattacharya, H. Hahn, T. Brezesinski, *Batteries & Supercaps* 3, 4 (2020), 10.1002/batt.202000010

6. Multi-anionic and -cationic compounds: new high entropy materials for advanced Li-ion batteries
   Q. Wang, A. Sarkar, D. Wang, L. Velasco, R. Azmi, S. S. Bhattacharya, T. Bergfeldt, A. Düvel, P. Heitjans, T. Brezesinski, H. Hahn, B. Breitung, *Energy & Environmental Science* 12, 2433 (2019), 10.1039/C9EE00368A

7. Pressure-induced tuning of lattice distortion in a high-entropy oxide
   B. Cheng, H. Lou, A. Sarkar, Z. Zeng, F. Zhang, X. Chen, L. Tan, V. Prakapenka, E. Greenberg, J. Wen, R. Djenadic, H. Hahn, Q. Zeng, *Communications Chemistry* 2, 114 (2019), 10.1038/s42004-019-0216-2

8. High-Entropy Oxides: Fundamental Aspects and Electrochemical Properties
   A. Sarkar, Q. Wang, A. Schiele, M. R. Chellali, S. S. Bhattacharya, D. Wang, T. Brezesinski, H. Hahn, L. Velasco, B. Breitung, *Advanced Materials* 31, 1806236 (2019)
   10.1002/adma.201806236

9. On the homogeneity of high entropy oxides: An investigation at the atomic scale
   M. R. Chellali, A. Sarkar, S. H. Nandam, S. S. Bhattacharya, B. Breitung, H. Hahn and L. Velasco, *Scripta Materialia* 166, 58 (2019), 10.1016/j.scriptamat.2019.02.039

10. High-entropy oxides: An emerging prospect for magnetic rare-earth transition metal perovskites
R. Witte, A. Sarkar, R. Kruk, B. Eggert, R. Brand, H. Wende, H. Hahn, *Physical Review Materials* 3, 034406 (2019), `10.1103/PhysRevMaterials.3.034406`

11. High entropy oxides as anode material for Li-ion battery applications: A practical approach
Q. Wang, A. Sarkar, Z. Li, Y. Lu, L. Velasco, S. S. Bhattacharya, T. Brezesinski, H. Hahn, B. Breitung, *Electrochemistry Communications* 100, 121 (2019), `10.1016/j.elecom.2019.02.001`

12. High entropy oxides for reversible energy storage
A. Sarkar, L. Velasco, D. Wang, Q. Wang, G. Talasila, L. de Biasi, C. Kübel, T. Brezesinski, S. S. Bhattacharya, H. Hahn and B. Breitung, *Nature Communications* 9, 3400 (2018), `10.1038/s41467-018-05774-5`

13. Rare earth and transition metal based entropy stabilised perovskite type oxides
A. Sarkar, R. Djenadic, D. Wang, C. Hein, R. Kautenburger, O. Clemens and H. Hahn, *Journal of the European Ceramic Society* 9, 2318 (2018), `10.1016/j.jeurceramsoc.2017.12.058`

14. Multicomponent equiatomic rare earth oxides with a narrow band gap and associated praseodymium multivalency
A. Sarkar, C. Loho, L. Velasco, T. Thomas, S. S. Bhattacharya, H. Hahn and R. Djenadic, *Dalton transactions* 46, 12167 (2017), `10.1039/C7DT02077E`

15. Nanocrystalline multicomponent entropy stabilised transition metal oxides
A. Sarkar, R. Djenadic, J. N. Usharani, K. Sanghvi, V. S. K Chakravadhanula, A. S. Gandhi, H. Hahn, S. S. Bhattacharya, *Journal of the European Ceramic Society* 37, 747 (2017), `10.1016/j.jeurceramsoc.2016.09.018`

16. Multicomponent equiatomic rare earth oxides
R. Djenadic, A. Sarkar, O. Clemens, C. Loho, M. Botros, V. S. K Chakravadhanula, C. Kübel, S. S. Bhattacharya, A. S. Gandhi, and H. Hahn, *Materials Research Letters* 5, 102 (2017), `10.1080/21663831.2016.1220433`

Patents applied

1. Elektrodenmaterial, Verfahren zu dessen Herstellung und dessen Verwendung
B. Breitung, A. Sarkar, T. Brezesinski, L. Velasco and H. Hahn, **DE102018100928**, Filed on 17.01.2018

2. Multianionic and multicationic high-entropy materials
Q. Wang, A. Sarkar, B. Breitung and H. Hahn, **DE10201810074.0**, Filed on 20.12.2018

Conferences and workshops (as presenter)

1. High entropy oxides characterized by Ga-jet XRD
   A. Sarkar, Q. Wang, B. Breitung, and H. Hahn
   STOE User Meeting 2019, 6–7 September 2019, *Darmstadt* (Germany), Invited talk.
2. Recent developments on High Entropy Oxides
   A. Sarkar, Indo-German Workshop On Recent Advances in Nanoscience and Nanotechnology, March 25–27, 2019, *Chennai* (India), Oral presentation.
3. High entropy oxides with tailorable properties- Fundamental aspects and prospects
   A. Sarkar, L. Velasco, B. Breitung, S. S. Bhattacharya and H. Hahn, European Materials Research Society (E-MRS), 17–20 September 2018, *Warsaw* (Poland), Invited talk.
4. Electrochemical properties of transition metal based high entropy oxides
   A. Sarkar, L. Velasco, D. Wang, G. Talasila, L. de Biasi, T. Brezesinski, S. S. Bhattacharya, H. Hahn and B. Breitung, European Materials Research Society (E-MRS), 18–22 June 2018, *Strasbourg* (France), Oral presentation.
5. Multicomponent equiatomic rare earth oxides
   A. Sarkar, R. Djenadic and H. Hahn
   12th Conference for Young Scientists in Ceramics, CYSC-2017, October 18-21, 2017, *Novi Sad* (Serbia), Oral presentation.
6. Multicomponent equiatomic oxides
   A. Sarkar, R. Djenadic, M. Shams, M. Brotos, O. Clemens, S. Lebedkin, T. Thomas, S. S. Bhattacharya and H. Hahn
   European Materials Research Society (E-MRS), 19–22 September 2016, *Warsaw* (Poland), Oral presentation.

Acknowledgments

Firstly, I would like to express my sincere gratitude to my supervisor, Prof. Horst Hahn, without whom this work would have never been possible. I am highly grateful for his continuous guidance and the amount of time he spent with me solving numerous scientific problems. Importantly, he gave me the freedom, opportunity and encouragement to explore new ideas, which helped me grow as an independent researcher.

I am indebted to my master's supervisor and current collaborator, Prof. S.S. Bhattacharya from IIT Madras. He has always been an unfailing source of inspiration.

I would like to thank my co-referee, Prof. Jürgen Janek, and the other members of the my doctoral examination committee, Prof. Wolfgang Ensinger and Prof. Wolfgang Donner, for the time devoted in evaluating my work.

I would like to thank Dr. Robert Kruk for the numerous stimulating discussions we had. I admire his in-depth knowledge and the ability to teach the most complex things in a simple manner.

I am extremely lucky to have the expert advice of Dr. Richard Brand. He is an outstanding teacher. I would like to thank Prof. Oliver Clemens for instructing me the basics of XRD and Rietveld refinement. I am grateful to Dr. Ben Breitung for introducing me to the exciting field of electrochemistry and lithium ion batteries. I always enjoyed and learnt from the vibrant scientific discussions we had. I especially acknowledge Dr. Ralf Witte, a superb scientist, who performed the magnetic measurements and, simultaneously, taught me the basics of SQUID magnetometry and Mössbauer spectroscopy. Dr. Qingsong Wang is an invaluable scientist, I thank him for the numerous scientific discussions we had. I am grateful to our TEM specialists at INT, in particular Dr. Di Wang, Dr. Leonardo Velasco, Dr. Xioake Mu and Prof. Dr. Christian Kübel. A special mention goes to Dr. Leonardo Velasco for the exciting scientific discussions we had in our office. I will always be thankful to Dr. Ruzica Djenadic, who taught me the NSP process and supervised my work during the initial months of my PhD. The highly-skilled hands of Martin Limbach kept our labs alive. Prof. Ashutosh Gandhi, Prof. Tiju Thomas, Dr. Torsten Brezesinski, Dr. Issac Ibrahim, Dr. Virgil Provenzano, Dr. Vladimir Šepelák, Dr. Julia Ivanisenko, Dr. Sree Harsha Nandam, Dr. Mithun Palit, Dr. Reda Chellali, Dr. Suresh Kumar Garlapati, Dr. Alexander Benes, Dr. Shiv Prakash Singh, Dr. Soumabha Bag, Dr. Christoph Loho and Nandhini JU are gratefully acknowledged for the fruitful discussions. Special mention goes to our master students, Saurabh Bopte, Gopichand Talasila, Pavan Kumar Mannava, Mukti Ranjan Mohapatra, Janhavika Sonar, Chintakindi Hrushikesh and Kante Mohan Veerraju, for supporting the synthesis efforts.

I would like to thank my collaborators, Dr. Christina Hein and Dr. Ralf Kautenburger from the Saarland University for the ICP-MS studies. I would like to acknowledge the constant support of Prof. Heiko Wende's group, especially Benedikt Eggert, from University of Duisburg-Essen. Their experience was of great importance during the beamtime at DESY and BESSY.

I am grateful to Renate Hernichel, Birgit Limmer, Hartmut Speck, Anna Navickas and Christine Fischer for taking utmost care of the various administrative and official matters.

The financial support by Deutsche Forschungsgemeinschaft (DFG) under Grant No. HA 1344/43-1 is gratefully acknowledged.

I would like to thank all the current and former members of the Hahn group for making our lunch and coffee breaks delightful. The La Clusaz trips are unforgettable.

I would like to express my deepest gratitude to my family and friends for their enduring support and understanding. Finally, I would like to mention my parents, Renuka Sarkar and Prasanta Kumar Sarkar, and my wife, Lipika Sarkar, for their endless sacrifices.